

DOCTORAL THESIS

Upcycling Li-Ion Battery Waste into Sustainable Electrocatalysts for Zinc-Air Battery Application

Reio Praats

TALLINN UNIVERSITY OF TECHNOLOGY
DOCTORAL THESIS
66/2025

Upcycling Li-Ion Battery Waste into Sustainable Electrocatalysts for Zinc-Air Battery Application

REIO PRAATS



TALLINN UNIVERSITY OF TECHNOLOGY

School of Engineering

Department of Materials and Environmental Technology

National Institute of Chemical Physics and Biophysics, Laboratory of Chemical Physics

This dissertation was accepted for the defence of the degree 07/07/2025

Supervisor:

Dr. Kerli Liivand

National Institute of Chemical and Physics and Biophysics

Tallinn, Estonia

Co-supervisor:

Dr. Ivar Kruusenberg

National Institute of Chemical and Physics and Biophysics

Tallinn, Estonia

Opponents:

Dr. Tim-Patrick Fellingner

BAM Federal Institute for Materials Research and Testing

Berlin, Germany

Associate Professor Cristina Pozo Gonzalo

Institute of Carboquímica, Spanish National Research Council

Zaragoza, Spain

Defence of the thesis: 29/09/2025, Tallinn

Declaration:

Hereby I declare that this doctoral thesis, my original investigation and achievement, submitted for the doctoral degree at Tallinn University of Technology has not been submitted for doctoral or equivalent academic degree.

Reio Praats

signature



European Union
European Regional
Development Fund



Investing
in your future



Copyright: Reio Praats, 2025

ISSN 2585-6898 (publication)

ISBN 978-9916-80-369-1 (publication)

ISSN 2585-6901 (PDF)

ISBN 978-9916-80-370-7 (PDF)

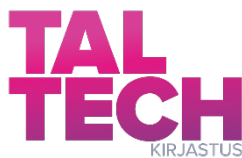
DOI <https://doi.org/10.23658/taltech.66/2025>

Praats, R. (2025). *Upcycling Li-Ion Battery Waste into Sustainable Electrocatalysts for Zinc-Air Battery Application* [TalTech Press]. <https://doi.org/10.23658/taltech.66/2025>

TALLINNA TEHNIKAÜLIKOO
DOKTORITÖÖ
66/2025

Liitiumioonakude jäätmete väärindamine ressursitõhusateks katalüsaatormaterjalideks tsink-õhk akude tarvis

REIO PRAATS



Contents

List of publications	7
Author's contribution to the publications	8
Introduction	9
Abbreviations	11
1 Literature overview	13
1.1 Li-ion batteries recycling	13
1.1.1 Overview of Li-ion batteries	13
1.1.2 Current state of Li-ion battery recycling	14
1.1.3 Recycling graphite from Li-ion batteries	16
1.2 Oxygen reduction and oxygen evolution reactions	18
1.2.1 Oxygen reduction reaction	18
1.2.2 Oxygen evolution reaction	18
1.3 Metal-air batteries from zinc-air battery perspective	19
1.4 Bifunctional oxygen electrocatalysts	20
1.4.1 Metal-nitrogen-carbon materials as bifunctional oxygen electrocatalysts	22
1.4.2 Oxygen electrocatalysts from end-of-life Li-ion batteries	25
2 Aims of the study	27
3 Experimental	28
3.1 Preparation of black mass leach residue	28
3.2 Purification of carbon nanotubes	28
3.3 Synthesis of reduced graphene oxide	29
3.4 Synthesis of nitrogen doped black mass leach residue	29
3.5 Synthesis of nitrogen doped black mass leach residue/carbon nanotubes composite materials	30
3.6 Synthesis of nitrogen doped black mass leach residue/reduced graphene oxide composite materials	30
3.7 Details of electrochemical experiments	31
3.7.1 Preparation of electrodes and details of the rotating disc electrode measurements	31
3.7.2 Details of zinc-air battery measurements	31
3.8 Physicochemical characterisation methods	32
4 Results and discussion	34
4.1 Physicochemical characterisation of battery derived precursor materials	34
4.2 Investigation of transition metal and nitrogen co-doped black mass leach residue for ORR/OER applications	38
4.3 Investigation of transition metal and nitrogen co-doped black mass leach residue and CNT composites for ORR/OER applications	45
4.4 Investigation of transition metal and nitrogen co-doped black mass leach residue and rGO composites for ORR/OER applications	58
4.5 Black mass leach residue derived oxygen electrocatalysts for zinc-air battery applications	71
Conclusions	78
Novelty and further research	80
References	81

Acknowledgements.....	98
Abstract.....	99
Lühikokkuvõte.....	100
Appendix 1	101
Appendix 2	113
Appendix 3	127
Curriculum vitae.....	147
Elulookirjeldus.....	149

List of publications

The list of author's publications, based on which the thesis has been prepared:

- I **R. Praats**, A. Chernyaev, J. Sainio, M. Lundström, I. Kruusenberg, K. Liivand, Supporting critical raw material circularity – upcycling graphite from waste LIBs to Zn–air batteries, *Green Chemistry* 26 (2024) 2874–2883.
- II **R. Praats**, J. Sainio, M. Vikberg, L. Klemettinen, B.P. Wilson, M. Lundström, I. Kruusenberg, K. Liivand, Utilizing waste lithium-ion batteries for the production of graphite-carbon nanotube composites as oxygen electrocatalysts in zinc–air batteries, *RSC Sustainability* 3 (2025) 546–556.
- III **Praats, R.**; Sainio, J.; Vikberg, M.; Klemettinen, L.; Wilson, B. P.; Lundström, M.; Kruusenberg, I.; Liivand, K. A Pathway to Circular Economy-Converting Li-Ion Battery Recycling Waste into Graphite/rGO Composite Electrocatalysts for Zinc–Air Batteries, *Batteries* 11 (2025) 165.

Author's contribution to the publications

Contribution to the papers in this thesis are:

- I The author was responsible for carrying out the materials synthesis, physico-chemical characterisation (X-ray diffraction analysis, N₂ adsorption-desorption analysis) and all the electrochemical characterisation experiments and its data analysis. The author was responsible for the interpretation of all testing results, except the Raman spectroscopy and X-ray photoelectron spectroscopy, and was primarily responsible for writing the manuscript.
- II The author was responsible for carrying out the materials synthesis, physico-chemical characterisation (X-ray diffraction analysis, N₂ adsorption-desorption analysis) and all the electrochemical characterisation experiments and its data analysis. The author was responsible for the interpretation of all testing results, except the Raman spectroscopy and X-ray photoelectron spectroscopy and was primarily responsible for writing the manuscript.
- III The author was responsible for carrying out the materials synthesis, physico-chemical characterisation (X-ray diffraction analysis, N₂ adsorption-desorption analysis, atomic adsorption spectroscopy) and all the electrochemical characterisation experiments and its data analysis. The author was responsible for the interpretation of all testing results, except the X-ray photoelectron spectroscopy and was primarily responsible for writing the manuscript.

Introduction

Recent geopolitical developments in the world have intensified the focus of the world leaders to find solutions for emerging energy crisis. The need for fossil fuels have already decreased from 82% in 2013 to 80% in 2023 in global energy mix [1]. This transition is largely driven by the growing deployment of renewable energy technologies—such as wind and solar power. Supported by advancements in usage of energy storage and carrier technologies, such as Li-ion batteries (LIBs) and fuel cell systems [1]. Among these developments, the rapid growth in the production and use of LIBs has been particularly noteworthy. LIBs have become the most common energy carrier used in everyday portable electronics as well as in larger scale in electric vehicles and in energy storage systems. Although the market for LIBs has experienced exponential growth in recent years, recent data suggests that the pace of expansion is beginning to stabilise [2]. This enormous rise in LIB market size will lead to shortage of critical raw materials like Li, Co, Ni, Mn, Cu, and natural graphite, all of which are essential components of LIBs [3]. In addition, the extraction and processing of critical raw materials for Li-ion batteries are geographically concentrated, raising concerns about supply chain vulnerability. For instance, approximately 33% of the world's lithium is mined in Australia, yet 57% of its global refining takes place in China. Similarly, 66% of cobalt is mined in Congo DR, while 74% is refined in China. In the case of graphite, China dominates both mining (82%) and the production of battery-grade material (93%) [4]. This data highlights China's dominant role in refining of battery grade materials. Together with the popularity of LIBs has been the development and growth of battery recycling industry to increase the circularity of materials, which reduces the environmental effect of mining and secures the supply chain by reusing secondary materials again for LIBs or finding new applications for them [5,6]. While some of the LIB battery materials are already industrially recycled, the graphite which comprises approximately 10–24 wt% of LIBs is still discarded [7].

This thesis explores the potential of utilising graphite and impurity metals within LIB black mass leach residues for electrocatalyst synthesis. These metals are conventionally incorporated into electrocatalysts by using pure metal salts; however, this study investigates their direct integration from recycling waste to reduce the need for pure materials. To achieve this, two different black mass leach residues were employed as precursors for electrocatalyst synthesis—an approach that, to the best of our knowledge, has not been previously explored for oxygen electrocatalyst production. In this work, a combination of ball milling and pyrolysis was used to incorporate metals from the leach residue into a carbon matrix, along with nitrogen from dicyandiamide as a heteroatom dopant. The synthesised electrocatalysts were electrochemically evaluated for their performance towards oxygen reduction reaction and oxygen evolution reaction using the rotating disc electrode method, as well as their practical application in zinc-air batteries to increase their activity and stability. Comprehensive physicochemical characterisation was conducted to connect the electrochemical activity with the catalyst materials structural and compositional properties. This thesis, along with the associated published research, demonstrates that instead of discarding leach residue by burning, it can be repurposed as a precursor for active and stable bifunctional oxygen electrocatalysts which is comparable with

state-of-the-art catalyst materials reported in the literature as well as with the commercial 20% PtRu/C catalyst material. This work serves as a prime example of circular economy principles, transforming recycling waste into high-value functional materials.

The thesis is based on three published research papers, and the findings have been presented at different conferences.

Abbreviations

Explanations of abbreviations used in the thesis—the table.

AAS	Atomic absorption spectroscopy
AEM	Adsorbate evolution mechanism
BET	Brunauer–Emmett–Teller theory
CNT	Carbon nanotubes
CoPc	Cobalt phthalocyanine
CRM	Critical raw material
DCDA	Dicyandiamide
DFT	Density functional theory
$E_{1/2}$	Half-wave potential
EoL	End-of-life
E_{OER}	Oxygen evolution reaction potential where 10 mA cm^{-2} is achieved
E_{onset}	Oxygen reduction reaction onset potential, where current density is 0.1 mA cm^{-2}
E_{sp}	Specific energy density
EV	Electric vehicle
FC	Fuel cell
FWHM	Full-width half-maximum
GDL	Gas diffusion layer
GO	Graphene oxide
HRTEM	High-resolution transmission electron microscopy
j	Current density
LCO	Lithium Cobalt oxide
LFP	Lithium Iron Phosphate
LIB	Lithium-ion battery
LMNO	Lithium Manganese Nickel oxide
LMO	Lithium Manganese oxide
LNCO	Lithium Nickel Cobalt oxide
LSV	Linear-sweep voltammetry
LSV	Linear sweep voltammetry
MAB	Metal-air battery
M-N-C	Metal-nitrogen-carbon
NCA	Lithium Nickel Cobalt Aluminium oxide
NMC	Lithium Nickel Manganese Cobalt oxide
OCP	Open-circuit potential
OER	Oxygen evolution reaction
ORR	Oxygen reduction reaction
Pd	Power density

PSD	Pore size distribution
PVDF	Polyvinylidene fluoride
PVP	Polyvinylpyrrolidone
RDE	Rotating disk electrode
rGO	Reduced graphene oxide
RHE	Reversible hydrogen electrode
SE	Secondary electron
SEI	Solid electrolyte interphase
SEM-SE	Scanning electron microscope equipped with secondary electron detection
SEM-EDS	Scanning electron microscopy and energy dispersive X-ray spectroscopy
SHE	Standard hydrogen electrode
SSA	Specific surface area
TEM-EDS	Transmission electron microscopy and energy dispersive X-ray spectroscopy
ZAB	Zinc-air battery
XPS	X-ray photoelectron spectroscopy
XRD	X-ray diffraction analysis
ΔE	Bifunctionality parameter
ΔE_{ZAB}	Potential window of charge-discharge cycling in zinc-air battery testing

1 Literature overview

1.1 Li-ion batteries recycling

1.1.1 Overview of Li-ion batteries

Since their commercialisation in 1991, the production and utilisation of Li-ion batteries (LIBs) have grown exponentially [8,9]. A typical LIB cell consists of several key components: a cathode, an anode, a separator, current collectors, an electrolyte, and an external casing made of plastic or metal as demonstrated on Figure 1.1 The cathode serves as a positive electrode and is typically composed of Li-transition metal oxides as an active material coated onto Al current collector. Originally the LIB cathode active material was made of lithium cobalt oxide (LCO), but nowadays many different variants are used such as lithium nickel manganese oxide (LNMO), lithium manganese oxide (LMO), lithium nickel manganese cobalt oxide (NMC), lithium nickel cobalt aluminium oxide (NCA), lithium nickel cobalt oxide (LNCO) or lithium iron phosphate (LFP) [10,11]. While having differences in chemical composition, crystal structure and electrochemical properties their working principle is similar. The cathode active material determines the key parameters of LIBs—energy density, durability and thermal stability. The anode, acting as the negative electrode, is made of graphite—natural, synthetic, or a mixture of both, which is coated onto Cu current collector. Graphite, thanks to its layered structure and weak van der Waals forces in between the layers allows Li^+ to intercalate between the graphene sheets during charging and de-intercalate when discharged. The binder, typically polyvinylidene fluoride (PVDF), is combined with a conductive carbon additive to bind the active material to the current collector while enhancing the electrical conductivity of the electrode. The separator is a non-conductive porous polymer material, such as polypropylene or polyethylene, which physically separates the cathode and anode to prevent short circuits, while enabling Li^+ to flow freely between the electrodes during charge and discharge cycles. The electrolyte, which helps the Li^+ to move more efficiently, consists of lithium salt, such as lithium hexafluorophosphate (LiPF_6), dissolved in a mixture of organic solvents (e.g., ethylene carbonate and dimethyl carbonate). To ensure structural integrity and safety under various operating conditions the components are enclosed in a protective plastic or metal casing [8]. In summary, the composition of a lithium-ion battery cell is as follows: cathode active material 23–41 wt%, graphite for 10–24 wt%, electrolyte for 10–18 wt%, copper for 10–17 wt%, aluminum for 3–8 wt%, separator for 2–5 wt%, and binder with conductive carbon for 2–5 wt% [12–14]. By connecting multiple LIB cells in series, parallel, or a combination of both, the overall voltage and capacity of the battery pack can be adjusted to meet specific requirements. This approach enables the design of larger battery modules and packs, making LIBs suitable for a wide range of portable and stationary applications: starting from portable everyday electronics like laptops and smart phones to EVs and larger stationary energy storage modules making LIBs currently the most popular and steady energy storage option in the world [1,8]. In 2023, the global production capacity of EV batteries reached 2.2 TWh, while the demand was only 0.75 TWh. Although this excess capacity may seem sufficient, projections suggest that demand will increase 4 to 7 times by 2030, depending on the model used [1]. The increasing demand for critical battery minerals has already surpassed the current supply capabilities, resulting in a resource deficit. This shortage highlights the necessity for developing alternative ways to acquire battery materials beyond those obtained from known deposits [5]. In addition, mining and refining of the minerals have significant environmental impacts: they produce large

CO₂ emissions, which contribute to global warming and, consequently, affect wildlife, groundwater, landscapes, and finally have issues with bad working conditions and child labour [5,15]. Addressing this challenge is crucial for ensuring the long-term sustainability of battery production and mitigating supply chain vulnerabilities.

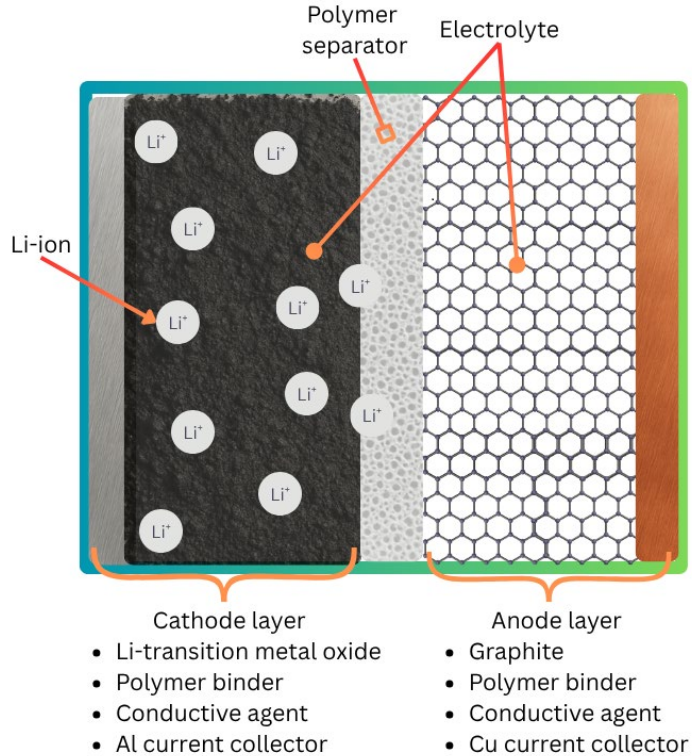


Figure 1.1 A scheme of Li-ion battery cell.

1.1.2 Current state of Li-ion battery recycling

The rapid expansion in production of LIBs is directly linked to the growing number of end-of-life (EoL) LIBs, which must be efficiently recycled to recover critical and strategic materials such as Li, Co, Ni, Mn, Al, Cu, and graphite, which are essential for sustainable battery manufacturing [3,5,16]. The improper disposal of EoL LIBs poses a substantial environmental risk. Due to the presence of heavy metals and organic electrolytes, these batteries can contaminate wildlife, groundwater, and the broader ecosystem if not properly managed [17]. Moreover, the loss of already mined resources compounds the environmental hazards associated with LIBs, highlighting the need for sustainable recycling and disposal practices. Data on the production, mining, and recycling of LIBs and critical raw materials indicate that these activities are heavily concentrated in specific geographical regions, particularly in China. For example, in 2023, China held about 66% of worlds 380 000 tons recycling capacity, while Europe had only a share of 16% [15]. This concentration poses a risk to the supply chains stability of battery resources in other regions, such as Europe and the America [16]. To mitigate this issue, one potential solution is to advance and expand LIB recycling technologies, reducing

dependence on primary resource extraction and enhancing supply chain resilience. However, recycling LIBs presents significant challenges due to their complex structure and the diverse chemistry, particularly in cathode active materials [17]. Recycling facilities typically receive batteries of varying shapes, sizes, and chemistries, resulting in highly heterogeneous waste streams. This variability necessitates complex recycling processes capable of handling all battery types, further complicating the recycling process for industrial facilities [7]. Currently, LIB recycling methods are classified into three main categories: direct recycling, pyrometallurgical processing, and hydrometallurgical processing with mechanical pre-treatment [6,16–19].

Direct recycling is a process in which anode and cathode materials are separated from each other and processed individually. Li-transition metal oxides are directly treated for reuse, eliminating the need to recover each metal separately. Solid-state sintering and various re-lithiation methods are employed to regenerate cathode active materials, restoring their electrochemical performance and structural properties [20]. Direct recycling also aims to recover graphite, separator and electrolyte, however achieving this at large scale remains challenging. This approach is considered the most environmentally friendly, as it requires fewer chemicals, and less energy compared to other recycling methods [21]. However, manual disassembly of batteries is labour-intensive and time consuming, significantly increasing operational costs. While promising, this recycling method is currently under development and is primarily utilised in the lab scale [20,21].

Mechanical pre-treatment serves as a preliminary step for hydrometallurgical or pyrometallurgical treatment. For the pretreatment of pyrometallurgical processing, the batteries are first collected, sorted, and larger packs are manually dismantled, but the whole battery cells can be directly sent to smelting furnaces [15]. The goal of mechanical processing before hydrometallurgical recycling is to prepare the black mass for the leaching of metals from cathode active material. LIBs are first collected and fully passivated, either with physical or chemical methods e.g. thermal treatment, using external circuits, salt-water baths, cryogenic methods, or crushing in inert gas or liquid media to ensure safe handling [6,22]. The discharged batteries are then shredded into smaller pieces in two steps. Initial crushing leaves larger particles, while secondary crushing produces battery cell powder, after which various physical separation techniques, such as sieving, eddy current separation, flotation, ultrasonic cleaning, pneumatic, and/or magnetic separation, as well as heat-treatment are employed to remove plastics, casings and current collectors (Cu and Al) from the battery active materials [19]. The remaining smallest fraction, concentrated of cathode and anode active materials, is referred to as black mass. This mechanical pre-treatment significantly enhances recycling efficiency by removing some of the materials before further hydrometallurgical processing [15].

Pyrometallurgical processing utilises high-temperature treatment to recover selected metals from EoL LIBs, primarily Co, Ni, and Cu, while electrolyte, plastic and graphite are lost during the process and Li, Al and Mn will produce the leftover slag, which needs additional hydrometallurgical treatment to recover Li from it, while Al and Mn will go to waste [6,19]. In this process, black mass or whole battery cells are fed into a smelting furnace, where two distinct thermal stages occur. In the first stage called calcination (up to 500 °C), electrolytes and organic solvents decompose and evaporate. In the second stage (1400–1700 °C), the remaining materials undergo high-temperature smelting, leading to the formation of metal alloys containing Co, Ni, and Cu, while the graphite is burned off and other remaining components are incorporated into a slag byproduct [23]. Compared to hydrometallurgical processing, pyrometallurgy is less chemically intensive

and generates less wastewater. However, it has several drawbacks, including the release of toxic gases, the loss of valuable materials such as Li, Mn, Al and graphite, and high energy consumption, making it a less sustainable recycling approach [17,19].

Hydrometallurgical processing is a solution-based recycling method in which black mass, the product of mechanical pre-treatment, is subjected to acid leaching [19,24]. This approach is currently the most widely adopted method for LIB recycling due to its high recovery efficiency and the ability to obtain metal compounds with high purity [6]. It is efficient for recovering metals such as Li, Co, Ni, and Mn, while offering less energy-intensive and lower capital cost alternative compared to pyrometallurgy [16,17,19]. For efficient leaching various inorganic acids (e.g., H_2SO_4 , HCl , and HNO_3) and reducing agent (e.g. H_2O_2), are used to dissolve the metal components from black mass, forming a pregnant leach solution. The efficiency of the leaching process is affected by different factors, including concentration of acid, leaching temperature, solid-liquid ratio and the content of reduction agent [6,25]. These dissolved metals are subsequently purified and separated using different techniques to obtain high-purity metal salts for battery, or other applications [25]. This process begins with the impurity (Cu, Al, Fe, F, and P) removal, e.g. by using H_3PO_4 and continues by the separation of Co, Ni, and Mn using solvent extraction or ion-exchange. Finally, the metallic salts are precipitated by crystallisation techniques [18]. Despite its advantages regarding the metal recovery efficiency and capital cost, it still has some drawbacks. The process is complex and produces a high amount of wastewater, which leads to higher operational costs and requires additional treatment to reduce the risk of environmental pollution and leaching produces some toxic gases [19]. Furthermore, a significant drawback common for all current industrial recycling methods is the loss of graphite, which is typically discarded or burned rather than recovered for reuse or repurposed for other applications [12,26].

1.1.3 Recycling graphite from Li-ion batteries

Due to its unique combination of metallic and non-metallic properties, graphite has been utilised for nearly a thousand years. In modern times, it has high demand and applications across various industries [12]. Naturally occurring graphite is found in the Earth's crust, primarily within metamorphic and igneous rocks, with its formation conditions influencing its distinctive structure [27]. Synthetic graphite, in contrast, is produced from petroleum coke or pitch coke tar through a high-temperature graphitisation process $> 2800\text{ }^\circ\text{C}$. This process is highly energy-intensive, making synthetic graphite production costly. As an allotrope of carbon, graphite is typically gray in color, extremely soft (1–2 on the Mohs hardness scale), and has a density of 2.26 g cm^{-3} . It exhibits excellent thermal and electrical conductivity, along with high stiffness, strength, chemical inertness, and its structure stays stable at temperatures up to $3600\text{ }^\circ\text{C}$ [28]. The structure of graphite consists of graphene sheets arranged in a layered configuration, held together by weak van der Waals forces, which arise due to the delocalised π -orbitals. Each graphene layer is composed of sp^2 -hybridised carbon atoms arranged in a hexagonal lattice. The weak van der Waals interactions between these layers enable them to slightly slide, making graphite an excellent lubricant [29]. Additionally, natural graphite is classified into three categories based on its crystalline and structural characteristics: flake (crystalline), vein (lump), and microcrystalline (amorphous). Among these, modified flake graphite (called spherical graphite) is predominantly used in LIB anode materials due to its superior electrochemical properties thanks to more dense lattice packing [27,28].

The demand for graphite is increasing in parallel with the growth of LIB production, necessitating a higher supply of graphite. Currently, most natural graphite is extracted in a few key countries, including China, Mozambique, India, and Brazil, with China accounting for 93% of the global mining and production of spherical graphite (battery-grade graphite) [4]. In contrast, synthetic graphite is more costly and energy-intensive to produce, making natural graphite the preferred choice for the LIB industry [12]. Due to its critical role in battery production, natural graphite has been classified as a critical raw material (CRM) by both the United States and the European Union [4,30,31]. Given the rising demand for LIB anode materials, ensuring a stable supply of battery-grade graphite is essential. One promising solution to mitigate supply chain risks and enhance sustainability is the recycling of EoL LIBs, which enables the recovery of graphite that has already been mined or synthesised, as graphite accounts for about 15% of total LIB cost [32]. Graphite recycling has received significantly less attention compared to cathode active material recycling, primarily due to its lower value compared to battery metals and the challenges associated with purifying and restoring it to the required level [33]. However, research on graphite recycling from spent LIBs has been steadily increasing. In current industrial recycling processes, graphite is largely treated as a waste fraction. In hydrometallurgical recycling, it is either landfilled or incinerated [34], while in pyrometallurgical recycling, it serves as a reductant in carbothermic reduction [32]. Both approaches result in significant material losses and are not considered sustainable solutions. The waste of hydrometallurgical recycling, black mass leach residue consists primarily of graphite, but also contains various impurities, including residual cathode metals, current collector materials, plastics and organic compounds [34,35]. The composition of this residue varies depending on the specific hydrometallurgical process and the chemistry of the batteries being used. Additionally, recycling of spent graphite is affected by solid electrolyte interphase (SEI) formation on the anode, which inhibits Li intercalation, and Li trapped within the graphite layers in the form of LiC_x compounds [36]. At the laboratory scale, several strategies have been explored for graphite recycling. One of the options is direct recycling where the graphite is reconditioned for reuse as LIB anode active material [37–39]. For direct recycling, manual disassembly of batteries is required to achieve the highest graphite purity among all recycling methods. Though effective, this method is not easily scalable due to the workforce needed for manual dismantling and material separation. Additionally, current industrial-scale recycling strategies typically involve shredding batteries, resulting in a mixture of all battery components [16]. The presence of impurities in the regenerated graphite anode poses significant safety concerns, as they can negatively impact battery performance and stability [40]. One such impurity is the PVDF binder, which can be removed by dissolution in *N,N*-dimethylformamide or high-temperature thermal treatment. However, both techniques present notable drawbacks: *N,N*-dimethylformamide is a toxic solvent posing environmental and health risks, while thermal treatment releases harmful gases and increases the overall energy demand of the recycling process [41]. To address the removal of the SEI and trapped Li, a simple water-washing method has been developed at the laboratory scale. This process converts most of the Li into Li_2CO_3 , facilitating its removal [42,43]. Despite these advancements, the purity and scalability of recycled graphite may still be insufficient for direct reuse in LIB anodes [33].

An alternative approach to utilising recycled graphite involves its application as an potential anode material in other electrochemical energy storage systems, such as

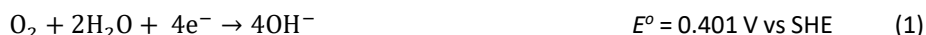
Na-ion [44], K-ion [45] or Li-S batteries [46]. Beyond direct reuse, another promising strategy is upcycling, wherein Spent graphite is transformed into high-value functional materials. One such method is chemical oxidation to produce graphene oxide (GO), which has potential applications in energy storage, electronics, and composite materials [47]. Furthermore, recycled graphite has been explored for use in supercapacitors [48,49], electrochemical sensors [50], adsorption materials for heavy metal pollutants [51], gas storage [52,53], and as catalyst materials [54–58]. This work aims to develop a sustainable approach for repurposing waste graphite from hydrometallurgical LIB recycling, contributing to a more circular and resource-efficient battery industry.

1.2 Oxygen reduction and oxygen evolution reactions

1.2.1 Oxygen reduction reaction

The oxygen reduction reaction (ORR) is a fundamental electrochemical process utilised in energy conversion devices such as fuel cells (FCs) and metal-air batteries (MABs) for electrical energy generation, as well as in the industrial production of H₂O₂. The ORR mechanism is inherently complex due to the high energy barrier associated with O₂ reduction, necessitating the use of highly efficient catalyst materials to facilitate rapid reaction kinetics. In an alkaline environment, the ORR proceeds via two primary reaction pathways [59]:

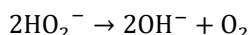
Direct 4-electron reduction:



Or via 2 step 2-electron reduction:



Or catalytic decomposition



In electrochemical energy conversion devices, the 4-electron (4e⁻) pathway is preferred, as the formation of HO₂⁻ intermediates in the 2-electron (2e⁻) pathway can reduce overall efficiency and contribute to the degradation of both the catalyst material and the structural components of FCs and MABs. However, the 2-electron pathway plays a crucial role in the selective electrochemical production of H₂O₂, where controlled formation of O₂⁻ and HO₂⁻ intermediates is desirable for high-yield H₂O₂ generation [60,61].

1.2.2 Oxygen evolution reaction

The oxygen evolution reaction (OER) plays a crucial role in the advancement of green energy technologies, including electrolyzers and reversible MABs [62–64]. Due to its multi-step nature involving various reaction intermediates, OER is inherently slow, presenting a significant challenge for researchers aiming to enhance its efficiency. A fundamental approach to understanding and accelerating this reaction is the adsorbate evolution mechanism (AEM), which is the most widely accepted reaction pathway involving four sequential electron transfer steps. For the AEM, a theoretical overpotential of 370 ± 100 mV vs. RHE has been proposed at a current density of 10 mA cm⁻².

The mechanism follows four consecutive proton-coupled electron transfer steps, as described in Equations (4)–(7) [65]:

Step 1 – Formation of adsorbed hydroxyl species:



Step 2 – oxidation of adsorbed hydroxyl to adsorbed oxygen:



Step 3 – formation of hydroperoxide intermediate:



Step 4 – oxygen molecule formation and desorption:



Reaction equations (4) – (7) make up the overall reaction (8).



This mechanism is also proposed for the metal-nitrogen-carbon (M-N-C) type catalyst materials [65–67] as is studied in this thesis.

1.3 Metal-air batteries from zinc-air battery perspective

Although LIBs are currently the most widely used electrochemical energy storage devices, several challenges associated with their performance, resource availability, and sustainability, as discussed in previous chapters, highlight the need for alternative technologies. One promising approach to mitigate these issues is the development of next-generation electrochemical storage systems. Among these, MABs present a compelling alternative due to their exceptionally high theoretical energy density (1353–11429 Wh kg⁻¹), environmental sustainability, and relatively simple design and fabrication process [61]. Unlike LIBs, MABs do not rely on CRMs as much, making them a more sustainable option [68]. MABs function as a hybrid between conventional batteries and fuel cells. A typical MAB consists of a metal anode (e.g., Fe, Zn, Mg, Al, Li, Na, or K), an air cathode (comprising a gas-diffusion layer, oxygen electrocatalyst, and current collector), and a liquid electrolyte (which can be aqueous or non-aqueous) and a separator. The presence of an air cathode, which enables oxygen intake from the atmosphere, significantly reduces the overall weight of the battery while increasing its energy storage capacity compared to LIBs [61]. As this thesis focuses on zinc-air batteries (ZABs), Figure 1.2 illustrates a typical ZAB cell configuration and reaction equations (1) (or (2) and (3)), and (9)–(12) demonstrate the reactions happening in ZAB during discharge in alkaline medium [68].



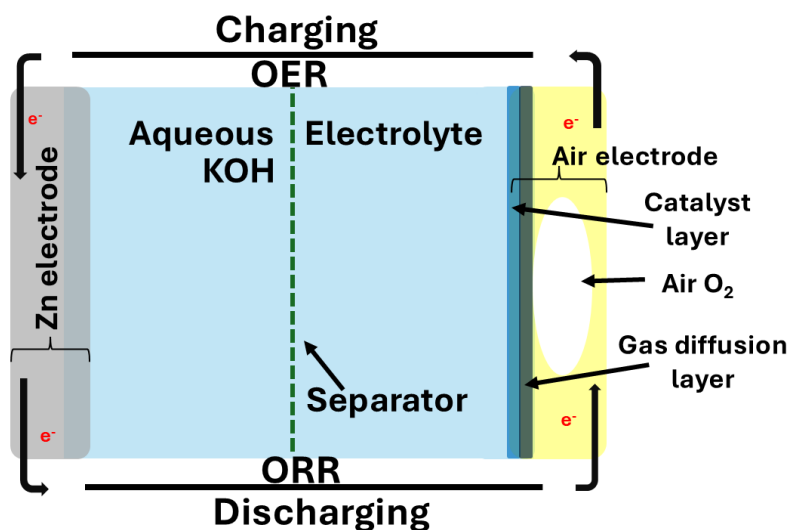


Figure 1.2 A scheme of typical zinc-air battery.

During discharging a Zn anode is oxidised to Zn(II) as per equation (9) and electrons are transferred via external circuit to air cathode where oxygen is reduced into OH^- as per equation (1) or via (2) and (3). During the charging process, these reactions are reversed, where ZnO is electrochemically reduced to metallic Zn, depositing onto the Zn electrode, while OER by equation (8) facilitates the release of O_2 at the electrolyte-electrode interface [61,68]. The ZAB has a theoretical energy density of 1353 Wh kg^{-1} with an open-circuit potential (OCP) of 1.65 V. However, in practical applications, the energy density reaches up to 800 Wh kg^{-1} , with OCP values typically below 1.65 V [61]. Several challenges hinder the performance of ZABs, both on the Zn electrode and air electrode side. The challenges on the Zn electrode include Zn corrosion due to the hydrogen evolution as a parasitic side reaction, the formation of zinc dendrites, which can cause short circuits, and the accumulation of a ZnO layer, which impedes the charging process [69]. Another major challenge for ZABs is the sluggish oxygen reduction and evolution kinetics at the air electrode, which is largely due to the low stability and activity of bifunctional oxygen electrocatalysts. These challenges contribute to the reduced efficiency and stability of ZABs [61,68,70]. To overcome these limitations, the development of more active and durable bifunctional oxygen electrocatalysts is essential to ensure long-term performance in the demanding ZAB environment to mitigate the global energy storage issues for green energy technologies.

1.4 Bifunctional oxygen electrocatalysts

As discussed in the previous chapter, one of the major challenges hindering the commercialisation of rechargeable ZABs is the sluggish kinetics of the ORR during discharge and the OER during charge at the air electrode [68,71]. These kinetic limitations can be addressed by developing cost-effective, highly active, and durable bifunctional oxygen electrocatalysts that can efficiently facilitate both reactions. The ORR and OER proceed through multiple sequential steps, including the adsorption of reactants, the surface reaction, and the desorption of products which follow the Sabatier principle—an optimal binding strength for reaction intermediates should be neither too strong

nor too weak [72]. Each of these steps is critical in determining the overall efficiency and catalytic performance of the electrocatalyst. The processes begin with the adsorption of oxygen-containing species onto the active sites of the catalyst. This step requires energy consumption to form bonds between the reactants and the catalyst surface. The strength of this adsorption plays a crucial role, as excessively strong binding can hinder product desorption and block active sites, whereas weak binding may prevent the effective activation of reaction intermediates, reducing catalytic efficiency [73–75]. Following adsorption, the surface reaction occurs, where the adsorbed reactants undergo electrochemical transformations facilitated by the catalyst's active centres. The reaction kinetics in this step are strongly influenced by the electronic structure of the catalyst, as well as its surface area and porosity, which control reactant accessibility and mass transport [76]. A highly efficient catalyst must be capable of stabilising key reaction intermediates, such as $\ast\text{O}$, $\ast\text{OH}$, and $\ast\text{OOH}$, while maintaining a balanced interaction that minimises energy losses and overpotentials [76,77]. Once the reaction is complete, the final product must be desorbed from the catalyst surface to free up active sites for subsequent catalytic cycles. Efficient desorption ensures that the catalyst is sustaining long-term activity [76]. The overall electrocatalytic performance of a material can be significantly enhanced by optimising its active site density, electronic properties, and structural features.

Currently, noble metal-based catalysts serve as the benchmark for individual ORR and OER processes. For instance, Pt/C is an excellent catalyst for ORR but exhibits negligible OER activity [78]. Conversely, RuO_2 demonstrates outstanding OER activity but performs poorly in ORR [79–81]. Although combining these two types of catalysts can enhance bifunctional activity, such an approach introduces significant challenges. The harsh electrochemical environment of ZABs, including high electrode potentials and the presence of reactive oxygen species, can lead to oxidation and corrosion of the active sites, thereby compromising catalyst activity and stability [61,82]. Furthermore, the reliance on noble metals remains a fundamental drawback due to their high cost and scarce availability in the Earth's crust [82]. Therefore, for practical and scalable ZAB applications, developing noble-metal-free, bifunctional oxygen electrocatalysts for the air electrode is essential. To address this need, a variety of noble-metal-free electrocatalysts have been explored, including carbon-based composites [83], modified carbon materials [84–87], and non-carbon materials such as transition metal oxides [88–90], nitrides [91,92], and sulfides [93].

Historically, carbon-supported noble-metal-free electrocatalysts were primarily investigated for ORR applications. However, with the emergence of rechargeable MABs and water electrolyzers, these materials are increasingly being evaluated for OER as well [71,87,94–96]. The development of noble-metal-free electrocatalysts for oxygen-related reactions began with the pioneering work of Jasinski in 1964, who first demonstrated the electrocatalytic activity of cobalt phthalocyanine (CoPc) for ORR [97]. Initially, CoPc was deposited on a nickel substrate, but subsequent work revealed improved catalytic performance when supported on carbon black, thus laying the foundation for carbon-supported metal-based electrocatalysts [98]. A significant milestone was achieved in 1989, when Yeager and co-workers introduced a novel approach that moved beyond the use of well-defined MN_4 macrocyclic complexes like CoPc. Instead, they utilised polyacrylonitrile as a nitrogen and carbon source, combined with cobalt and iron acetates as metal precursors, to synthesise Co/Fe-N-C catalysts [99]. This marked a major shift toward flexible and scalable synthesis strategies for preparing M-N-C type

electrocatalysts. Since these foundational studies, extensive research has focused on both advancing synthesis methods and unravelling the reaction mechanisms of ORR and OER in non-precious metal catalysts [65,74,94,100–104]. Although the ORR and OER share certain mechanistic similarities, OER generally requires significantly higher overpotentials and involves more complex reaction intermediates, which impose greater energetic and structural demands on the catalyst, necessitating materials capable of stabilising high-valent metal-oxo species throughout the reaction pathway [65,74]. For this reason, metals and metal oxides are commonly employed as OER catalysts [65,74]. This thesis focuses on carbon-supported, nitrogen- and metal-doped (M-N-C) materials, therefore the following section will provide a detailed overview of the development and design of these bifunctional oxygen electrocatalysts.

1.4.1 Metal-nitrogen-carbon materials as bifunctional oxygen electrocatalysts

To enhance bifunctionality, various synthesis strategies have been developed, targeting both carbon-based and non-carbon-based materials, as well as their hybrid composites, to harness synergistic effects [61,105]. Among these, M–N–C catalysts have garnered significant research attention, as their efficient metal utilisation and nitrogen doping contribute to a more uniform distribution of active sites, thereby enhancing reaction kinetics and ensuring long-term stability under electrochemical conditions [76,106]. The synthesis of M–N–C catalysts typically involve various doping strategies, most of which begin with the preparation of a precursor mixture, where the precursors are mixed by either sonication or mechanical stirring in liquid phase or through grinding and dry mixing if the synthesis is conducted in the solid phase [76,107]. The main challenges associated with M–N–C catalysts are the migration of metal species during electrochemical operation and metal agglomeration during synthesis if the metal content is too high, both of which lead to a decline in catalytic activity [106,108]. The rational control of the metal species and the choice of carbon support material is crucial to avoid agglomeration [109]. To mitigate the migration issue, high-temperature pyrolysis under inert gas environment can promote the binding to the carbon matrix or encapsulation of metal species within carbon shells or micropores, thereby preventing their mobility [110–113]. However, while micropore encapsulation can improve stability of active species, it is not always desirable, as oxygen molecules may flood the pores, therefore hindering the mass transportation of reactant species [114]. Additional acid leaching step can be incorporated into the synthesis process to address this issue. Acid leaching removes less stable metal species while simultaneously opening pores, thereby improving mass transport and enhancing the accessibility of active sites [115,116]. This step is often followed by a second pyrolysis stage, which effectively removes excess oxygen species, further refining the catalyst's structure and electrocatalytic performance [115].

A carbon support (e.g., graphite [117–119], graphene [120–124], CNTs [92,125–129], carbon aerogels [130–134], metal-organic frameworks (MOFs)) [112,135] plays a crucial role in the final catalyst structure and performance. One of the main functions of carbon support material is providing a high surface area and porosity for the uniform dispersion and anchoring of active sites, especially within micropores and efficient transportation of reactants to catalytic sites by meso- and macropores. Secondly, the carbon support offers high electrical conductivity to promote efficient electron transfer during electrochemical reactions as well as structural stability and corrosion resistance, which are essential to withstand the harsh electrochemical environment encountered during ZAB operation [114,136,137].

Graphite and graphitic carbon serve as carbon support materials due to their highly crystalline structure, which provides excellent electrical conductivity and stability in oxidising environments. These properties enhance electron transfer for redox reactions while ensuring long-term durability in electrochemical applications. However, one of the primary limitations of using graphite as a support material is its low surface area and porosity, with minimal defect density, which restricts the number of accessible catalytic sites and hinders mass transport within the carbon matrix [119,138].

Carbon nanotubes (CNTs) are one-dimensional, tubular-shaped carbon nanostructures that serve as effective support materials for oxygen electrocatalyst synthesis. CNTs are particularly valued for their exceptional electrical conductivity, enabling efficient electron transfer during redox reactions, even at low catalyst loadings. Thanks to their mesoporosity, CNTs facilitate efficient reactant transport to and from active sites, improving catalyst's performance [139]. Defect sites at the tube ends and outer walls provide anchoring points for metal nanoparticles and heteroatom dopants, preventing particle agglomeration and ensuring a highly dispersed distribution of active sites. Since CNT synthesis typically involves the use of metal catalysts, residual metal impurities are often present in the final product [140]. To eliminate these impurities and enhance the material's suitability for electrocatalytic applications, an acid purification step is required [115,116]. This treatment not only removes residual metals but also introduces oxidative functional groups on the CNT surface, facilitating further surface modifications and improving the interaction with catalytic species [139,141–143].

Reduced graphene oxide (rGO) is a two-dimensional carbon support material derived from graphite through chemical oxidation methods [144,145]. During oxidation, oxygen-containing functional groups are introduced onto graphene sheets, creating a high density of defects that could serve as anchoring sites for active centres. This tunability makes rGO an attractive candidate for oxygen electrocatalysts, as it allows for heteroatom doping and enhanced metal-support interactions. Additionally, rGO offers an increased surface area and improved porosity, facilitating a higher density of active sites and more efficient mass transport of reactants within the catalyst structure [146]. However, a major drawback of rGO is its tendency for graphene sheets to restack due to van der Waals interactions, which reduces the effective surface area and hinders mass transport [57,147].

Among the various strategies to enhance the performance of electrocatalysts, heteroatom doping has proven to be an effective approach for tuning the electronic structure of carbon-based materials and generating active sites. Common heteroatoms used for doping include N [127,148–150], S [151–153], P [154,155], and B [156,157]. However, as nitrogen is the most widely used heteroatom in electrocatalyst design and is employed throughout this thesis, the following overview focuses on nitrogen doping. Although nitrogen atoms have a similar atomic radius to carbon, their higher electronegativity allows them to form strong C–N bonds by attracting electrons from neighbouring carbon atoms [158]. This electron redistribution induces local charge and spin density variations, which are critical for creating active sites, generating structural defects, and improving both ionic and mass transport properties of the material [159]. Moreover, nitrogen doping enhances the electrical conductivity of carbon frameworks and promotes the adsorption of O₂ molecules to carbon atoms which are bonded with N atoms, both of which are essential for reducing the energy input for efficient oxygen reactions [159]. In the electrocatalyst research community, four main nitrogen species are typically identified within nitrogen-doped carbon materials: pyridinic-N, pyrrolic-N,

graphitic-N, and oxidised nitrogen (N–O) [159]. Among these, pyridinic-N is generally regarded as the most active site for the ORR [156,160], and more recently, it has also been suggested to play a key role in the OER [149]. Despite this knowledge, the exact mechanisms by which different nitrogen species contribute to catalytic activity remain under debate. This uncertainty is partly due to the difficulty in controlling the formation and distribution of specific nitrogen functionalities during synthesis [161]. As a result, electrocatalysts often feature a mixture of nitrogen species, as it is well-established that nitrogen doping significantly improves the electrocatalytic performance of carbon-based materials [158,159,161].

Doping with transition metals, typically first-row transition metals such as Fe [133, 162–164], Co [86,102,104,122,165–167], Ni [168–171], and Mn [126,172,173], is a widely adopted strategy for enhancing the electrocatalytic performance of carbon-based materials as well as they are more cost-effective and have more abundance on Earth than noble metals. Transition metals are incorporated into electrocatalysts primarily due to their ability to modify the electronic structure of carbon supports, thereby facilitating the adsorption and activation of oxygen-containing intermediates [106]. One of the main reasons for employing Fe, Co, Ni, and Mn is their partially filled d-orbitals, which influence the charge distribution within the carbon framework and therefore help to optimise the binding energy of oxygen intermediates (*O, *OH, and *OOH), facilitating a more favourable reaction pathway with reduced overpotentials [76,174]. Transition metals typically coordinate with nitrogen atoms embedded within the carbon matrix, forming metal-nitrogen coordination complexes (M–N_x sites), which are recognised as one of the primary active sites for ORR and OER [106,175]. A linear correlation exists between the O₂ binding energy on M–N₄ clusters and the electronic structure of the d-orbitals of the transition metals. The spin-up and spin-down electron channels are balanced in Ni–N₄ clusters, unlike in Co–N₄ and Fe–N₄, resulting in differences in oxygen adsorption behaviour. While Ni–N₄ clusters exhibit weak oxygen adsorption, Co–N₄ and Fe–N₄ clusters demonstrate superior oxygen-binding capabilities, making them more active for oxygen electrocatalysis [175]. Additionally, among the nitrogen coordination configurations, Co–N₄ complexes are considered the most efficient for bifunctional oxygen electrocatalysis. In terms of catalytic selectivity, Fe- and Co-based transition metal catalysts are the most effective for ORR, whereas OER activity is predominantly catalysed by Co-based active sites [76]. This distinction highlights the importance of transition metal selection in designing highly efficient bifunctional oxygen electrocatalysts. Interestingly, metals such as Co and Ni have also been shown to catalyse the formation of CNTs and onion-like carbon structures during high-temperature pyrolysis [66,167,168,176]. These nanostructures often encapsulate metal nanoparticles, which introduce structural defects within the carbon matrix and generate additional active sites and enhance the efficiency of heteroatom doping (e.g., nitrogen incorporation) [66,176]. They also contribute to greater catalyst stability by physically confining metal active sites within carbon shells, effectively preventing metal leaching and nanoparticle agglomeration under electrochemical conditions [177]. Furthermore, electrocatalysts containing Co–N₄ clusters in combination with metallic Co nanoparticles have been shown to exhibit enhanced ORR activity, as the presence of metallic Co facilitates modulation of the electron distribution within the Co–N₄ sites, thereby optimising oxygen adsorption and catalytic performance [178]. Thus, the incorporation of transition metals not only creates highly active catalytic sites but also contributes to the structural and electronic optimisation of the overall catalyst material.

1.4.2 Oxygen electrocatalysts from end-of-life Li-ion batteries

While a wide range of applications—such as supercapacitors, Zn-ion batteries, and catalysts for water purification—have been explored for graphite-based materials recovered from EoL LIBs, one particularly promising route is their upcycling into oxygen electrocatalysts [12,47,179,180]. This chapter provides an overview of oxygen electrocatalysts derived from EoL LIB anode materials, focusing on their application in enhancing the ORR, OER, or as bifunctional oxygen catalysts. Graphite is a highly suitable carbon support material and an effective precursor for the synthesis of GO, which can be further utilised as a carbon matrix in oxygen electrocatalyst synthesis. Liivand and Kazemi demonstrated that nitrogen-doped rGO, derived from graphite, exhibited superior ORR performance compared to commercial N-rGO, with E_{onset} of 0.867 V vs RHE and 0.797 V vs RHE, respectively [58]. When combined with cobalt sourced from the cathode active material, the electrocatalytic activity can be further enhanced due to the incorporation of Co and the formation of Co nanoparticle-catalysed bamboo carbon nanotubes, which contribute to improved catalyst stability [117]. Ruan et al. recovered graphite from EoL LIBs to synthesise an Fe- and N-doped graphite catalyst (G-PANI-Fe), which exhibited a half-wave potential ($E_{1/2}$) of 0.800 V vs RHE in 0.1 M KOH [181]. While their approach involved introducing an external Fe source, a more sustainable strategy would be to exploit transition metals already present in the LIB cathodes, thereby minimising the need for additional resources. In further work, they prepared N-doped rGO from EoL LIB-derived graphite, which showed comparable ORR activity and stability to commercial Pt/C in 0.1 M KOH [182]. Bejigo et al. recycled both cathode and anode materials from EoL LIBs for ORR electrocatalyst synthesis. After manual dismantling, the cathode was leached using citric or tartaric acid and H_2O_2 , while the anode graphite was purified via sonication and water washing. The graphite was then converted to GO using a modified Hummer's method. In one study, a Co_3O_4 /rGO nanocomposite was obtained by mixing Co leachate with GO and pyrolyzing the mixture, yielding an $E_{1/2}$ of 0.865 V vs RHE in 1 M KOH [183]. In a second study, Co leachate, GO, and a nitrogen source were combined to synthesise a catalyst with an $E_{1/2}$ of 0.888 V vs RHE, confirming strong ORR activity [184].

In addition to ORR catalysts, cathode active materials from EoL LIBs have been explored as precursors for OER catalysts. Bian et al. developed a porous Co-based catalyst from $LiCoO_2$, achieving an E_{OER} at 10 mA cm⁻² of 1.504 V vs RHE and 20-hour stability at an overpotential of 0.300 V [185]. A similar M-CoO-based catalyst exhibited E_{OER} at 10 mA cm⁻² of 1.569 V vs RHE with 12-hour stability in 1 M KOH, attributed to CoO surface sites promoting OH⁻ adsorption [186]. Cui et al. used a mixture of NCM111 and graphite, yielding a E_{OER} at 10 mA cm⁻² of 1.550 V vs RHE, demonstrating the suitability of mixed cathode/anode materials as both active and support components [187]. While these studies confirm that $LiCoO_2$ can be repurposed into effective OER catalysts, this practice raises economic concerns. High-value cathode active materials are typically targeted for recovery and reuse in battery manufacturing, rather than diverted into new applications. Nevertheless, alternatives like $LiNi_{0.5}Co_{0.2}Mn_{0.3}O_2$ and $LiNi_{0.8}Co_{0.1}Mn_{0.1}O_2$ have also been studied. Chen et al. synthesised a borided electrocatalyst (NCMB) from cathode leachate, achieving E_{OER} at 10 mA cm⁻² of 1.482 V vs RHE, with *in situ* formation of CoOOH and NiOOH active sites during operation [188]. Kotkar et al. used microwave-assisted leaching of mixed anode and cathode materials to recover metals and prepare r-Co(OH)₂, which showed remarkable OER performance with E_{OER} at 10 mA cm⁻² of 1.361 V vs RHE, outperforming commercial IrO_2 [189].

Beyond monofunctional catalysts, bifunctional oxygen electrocatalysts have also been synthesised from EoL LIB materials. A notable example includes a Co–N–C catalyst derived from LCO and wood chips, synthesised via NH_3 -assisted calcination, which achieved a peak power density of 225 mW cm^{-2} and operated for 160 hours at 10 mA cm^{-2} , aided by its multichannel anisotropic structure and abundant Co–N_x sites [190]. In another study, plasma-treated leach residue from cathode active material served as the ZAB air electrode, reaching a peak power density of 92 mW cm^{-2} . Despite lower performance than commercial catalysts, the material showed successful metal (Ni, Mn, Co) and heteroatom (C, N) incorporation into the carbon matrix [191]. One of the best-performing ZAB catalysts was reported by Zheng et al., who synthesised a Ni/Ni–Co–Mn–O_x (N/NMCO) electrocatalyst using EoL NMC cathode material and carbothermal shock treatment. Their catalyst achieved a peak power density of 137 mW cm^{-2} , approximately 30% higher than the commercial Pt/C + IrO₂ catalyst [192]. Liivand et al. [57] developed a bifunctional oxygen catalyst using industrial hydrometallurgical LIB recycling residue as a precursor for GO synthesis. They also utilised the residual transition metals in the leachate and incorporated nitrogen doping, resulting in a ZAB air electrode that reached a peak power density of 112.8 mW cm^{-2} and remained stable for 66 hours. This strategy demonstrates a sustainable, scalable route by avoiding additional purification steps and reusing heterogeneous recycling waste. Finally, a metal-free, nitrogen-doped graphene oxide catalyst was synthesised from manually extracted LIB graphite, achieving a ZAB peak power density of approximately 120 mW cm^{-2} . In addition to oxygen electro reactions, they utilised their NG7 material for lithium storage applications [193].

2 Aims of the study

The growing volume of end-of-life lithium-ion batteries underscores the urgent need for efficient and sustainable recycling strategies to recover critical and strategic raw materials, underutilised graphite among them. Simultaneously, the development of alternative energy storage systems, like metal-air batteries, is essential to reduce the CO₂ emission as well as the dependence on traditional Li-ion batteries and improve overall resource sustainability.

Based on these challenges the objectives of this PhD work are formulated as follows:

- To develop an upcycling pathway to the graphite rich black mass leach residue from hydrometallurgical Li-ion battery recycling, thereby reducing recycling waste, supporting circular economy principles, and promoting the responsible use of strategic resources.
- To design and synthesise sustainable bifunctional oxygen electrocatalysts for zinc-air battery applications, contributing to the advancement of alternative energy storage solution.

Based on the literature overview and research aims, the following focused hypotheses are proposed:

- The graphite-rich leach residue from Li-ion battery recycling can be directly reused as a carbon matrix for the synthesis of functional materials, eliminating the need for additional purification steps.
- The residual transition metals present in the leach residue can serve as precursors for the formation of electrocatalytically active sites, reducing reliance on pure metals salts and increasing cost competitiveness and the sustainability of electrocatalysts, while enabling the production of efficient bifunctional oxygen electrocatalysts for both the oxygen reduction reaction and oxygen evolution reaction.
- The activity and stability of the electrocatalysts can be improved by increasing the specific surface area and porosity through the incorporation of an additional carbon source alongside the graphite-rich leach residue.
- The synthesised battery-derived bifunctional oxygen electrocatalysts will exhibit good electrochemical performance in next-generation energy storage devices, such as zinc-air batteries.

3 Experimental

This chapter provides detailed descriptions of the materials synthesis procedures, along with the physicochemical and electrochemical characterisation methods used, as described in the associated publications [I-III]. The block flow scheme of the catalyst materials synthesis studied within this thesis is visualised on Figure 3.1.

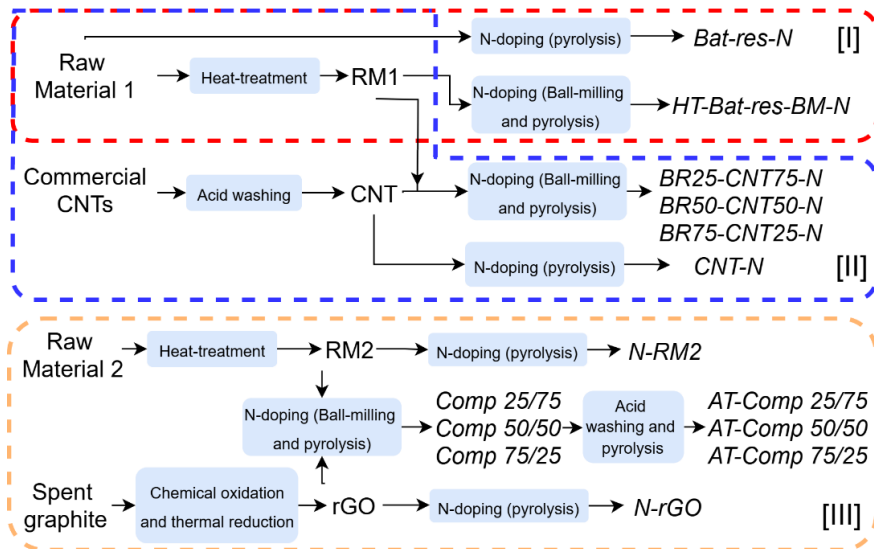


Figure 3.1. Flowsheet of the synthesis of catalyst materials studied in this thesis.

3.1 Preparation of black mass leach residue

In this thesis, two different black mass leach residues (Raw Materials) were used for the synthesis of battery-derived catalyst materials. Both Raw Materials originated from the same black mass, which was obtained through an industrial pre-treatment process—combination of crushing, magnetic separation, and sieving processes of pre-sorted LIBs. The < 500 μm fraction, enriched in Co and containing Ni, Mn, Cu, and Al, was used for leaching. All leaching experiments were conducted under same conditions: 2 M H_2SO_4 as the lixiviant, at 60 $^\circ\text{C}$, with a solid-to-liquid ratio of 200 g L^{-1} for a duration of 3 hours. The only variable was the reductant used: for Raw Material 1 (used in [I] and [II]), both Cu and Al were added to enhance leaching, whereas for Raw Material 2 (used in [III]), only Cu was used. During both treatments, most cathode metals were leached out, leaving behind a graphite-rich waste fraction [34]. In addition, both Raw Materials contained impurities such as plastics, separator, binder and traces of undissolved metals (Co, Ni, Al, Mn, Cu), albeit in different concentrations.

3.2 Purification of carbon nanotubes

CNTs (>95%, XFM13, XFANO, China) were utilised in the synthesis of composite catalyst material in [II] to enhance its conductivity and structure. Prior to use, the CNTs underwent a well-established purification process as described by [116]. The purification involved treating the CNTs with a 1:1 mixture of 0.5 M H_2SO_4 and 0.5 M HNO_3 for 2 hours

at 50 °C, followed by an additional 3 hours at 80 °C. After treatment, the CNTs were washed with Milli-Q water until a neutral pH (pH = 7) was reached and then dried under vacuum.

3.3 Synthesis of reduced graphene oxide

Graphene oxide (GO) in [III] was synthesised using manually extracted spent graphite from EoL LIBs. For that used iPhone batteries (APN: 616-00036, LiCoO₂ as cathode active material), were collected from local repair shops and submerged in a 5% NaCl solution to ensure complete discharge, allowing for safe dismantling. During dismantling the anode, cathode and separator were separated, after which the anodes were immersed in water to enhance the detachment of graphite from the copper foil. The recovered graphite was subsequently filtered, dried, and used as a precursor for graphene oxide synthesis via chemical oxidation process (classical Hummer's method) [57]. First, 4 g of graphite was weighed into a 1 L three-neck flask, followed by the addition of 100 mL of concentrated H₂SO₄ (95%, VWR, USA). The mixture was sonicated in an ultrasonic bath for 1 hour. The flask was then placed in an ice bath on a magnetic stirrer to maintain a low temperature, while 2 g of NaNO₃ (> 99.5%, Merck, Germany) was added, followed by the gradual addition of 12 g of KMnO₄ (> 98%, Stanlab, Poland). After adding KMnO₄, the reaction mixture was heated to 35 °C and maintained at this temperature for 18 hours. Once the reaction was complete, the flask was placed back in an ice bath, and 160 mL of Milli-Q water along with 40 mL of 30% H₂O₂ (VWR, USA) were carefully added. To remove metal impurities, the mixture was treated with 10% HCl (VWR, USA) and subsequently washed with water using centrifugation until a nearly neutral pH was achieved. The resulting GO was collected and dried. For the reduction of GO to rGO, the dried GO was weighed into a pyrolysis boat and reduced at 800 °C under an Ar atmosphere for 1 hour.

3.4 Synthesis of nitrogen doped black mass leach residue

In [I], Raw Material 1 was used either directly or after undergoing a heat treatment process to remove organic impurities and binder for synthesis of the catalyst material. For the heat treatment, the Raw Material 1 underwent flash pyrolysis at 800 °C for one hour in an Ar atmosphere (99.999%, Elme Messer), resulting in a material designated as RM1. To introduce nitrogen into the Raw Material 1 or RM1 (referred as HT-Bat-res in [I]), dicyandiamide (DCDA, Sigma-Aldrich, Germany) and polyvinylpyrrolidone (PVP, Sigma-Aldrich, Germany, Mw: 40,000) in a ratio of 1:20:0.1, respectively, were used. A homogeneous Raw Material 1:DCDA:PVP mixture in ethanol was achieved through sonication for two hours. Secondly, a mixture of RM1:DCDA:PVP was subjected to ball milling for two rounds of 30 minutes each, using 4 grams of 0.5 mm ZrO₂ balls in a mixture of ethanol and water (2:1) as the medium. Subsequently, the dried mixtures were subjected to flash pyrolysis for two hours at 800 °C under an Ar atmosphere, resulting in a catalyst named as Bat-res-N (N-doped Raw material 1) or HT-Bat-res-BM-N (ball-milled and N-doped RM1). Emphasis was placed on ensuring the repeatability of the synthesis process, therefore, at least three distinct syntheses per catalyst material were performed, demonstrating good repeatability.

3.5 Synthesis of nitrogen doped black mass leach residue/carbon nanotubes composite materials

In [II], two different carbon materials: Raw Material 1 and commercially available multi-walled CNTs were used for the synthesis of catalysts and preparation of the final composite materials. Both starting materials underwent a different pre-treatment step prior to their combination. The Raw Material 1 went through the same pyrolysis step as described in chapter 3.4 (referred as BR within [II]), while the CNTs pre-treatment was described in chapter 3.3. A mixture of carbon materials (*RM1* + CNT), nitrogen source dicyandiamide (DCDA, Sigma-Aldrich, Germany) and polyvinylpyrrolidone (PVP, Sigma Aldrich, Germany, Mw: 40,000), in a weight ratio of 1:20:0.1, in 3 ml of ethanol/water (2:1) was prepared. This mixture was then ball-milled with 5 mm ZrO₂ balls at 400 rpm for a total of one hour (in two separate 30-minute sessions with a 5-minute pause in between them). The resultant homogeneous material was then dried before being pyrolyzed at 800 °C for 2 hours under an Ar atmosphere. The ratio between carbon materials (*RM1* to CNT) was varied: 25–75 wt%, 50–50 wt%, and 75–25 wt%. The acquired catalysts were named *BR25–CNT75–N*, *BR50–CNT50–N*, and *BR75–CNT25–N*, respectively. For comparison, a nitrogen-doped CNT reference material (*CNT–N*) was prepared by mixing CNTs with DCDA and PVP in the same weight ratio as previously used. The mixture was sonicated for 2 hours and subsequently pyrolyzed under identical conditions.

3.6 Synthesis of nitrogen doped black mass leach residue/reduced graphene oxide composite materials

In [III], firstly the Raw Material 2 was heat-treated at 800 °C for one hour in an Ar atmosphere (99.999%, Elme Messer), resulting in a material designated as *RM2*. This was done similarly to Raw Material 1 to remove organic impurities and binder from the Raw Material 2. For the catalyst synthesis, a mixture consisting of *RM2*, a nitrogen source (dicyandiamide, DCDA, Sigma-Aldrich, Germany), and polyvinylpyrrolidone (PVP, Sigma-Aldrich, Germany, Mw: 40,000) in a weight ratio of 1:20:0.1 was prepared using 3 ml of an ethanol/water solution (2:1). This mixture was ball-milled with 5 mm ZrO₂ balls at 400 rpm for one hour, divided into two 30-minute sessions with a 5-minute pause in between. Afterward, a specific amount of rGO was added to the mixture, which was then placed in an ultrasonic bath for 2 hours. The resulting homogeneous material was dried and pyrolyzed at 800 °C for 2 hours under an Ar atmosphere. The ratio of *RM2* to rGO was varied, with compositions of 25 wt%-75 wt%, 50 wt%-50 wt%, and 75 wt%-25 wt%, respectively. The resulting nitrogen doped *RM2*/reduced graphene oxide (*RM2*/rGO) catalysts were named *Comp 25/75*, *Comp 50/50*, and *Comp 75/25*. For comparison, *N-rGO* and *N-RM2* reference materials were also prepared by mixing either rGO or *RM2* with DCDA and PVP in the same weight ratio. The mixtures were sonicated for 2 hours and subsequently pyrolyzed under identical conditions as those used for the composite catalysts. Additionally, *Comp 25/75*, *Comp 50/50*, and *Comp 75/25* underwent acid treatment with a 1:1 solution of 0.5 M H₂SO₄ and 0.5 M HNO₃, first at 50 °C for 2 hours, then at 80 °C for 3 hours. The catalyst materials were subsequently washed with Milli-Q water until a neutral pH (pH = 7) was reached and dried under vacuum. Finally, the catalyst materials were pyrolyzed again at 800 °C for 1 hour under an Ar atmosphere to remove excess oxygen groups from acid treatment. The final catalysts were named *AT-Comp 25/75*, *AT-Comp 50/50*, and *AT-Comp 75/25*.

3.7 Details of electrochemical experiments

3.7.1 Preparation of electrodes and details of the rotating disc electrode measurements

The ORR and OER were analysed utilising the rotating disc electrode (RDE) technique with a Gamry 1010E potentiostat/galvanostat, within a three-electrode system. The reference electrode employed was Ag/AgCl (3M KCl), while a graphite rod acted as the counter electrode for ORR and a platinum wire for OER. A glassy carbon (GC, $S = 0.2 \text{ cm}^2$) electrode, coated with the catalyst material, functioned as the working electrode. The RDE setup incorporated an Origalys speed control unit and rotator, with rotation speeds ranging from 3600 to 400 rpm.

The catalyst ink was prepared at concentrations of either 4 mg ml^{-1} ([I] and [III]) or 2 mg ml^{-1} ([II]) in ethanol, with either $1 \mu\text{l}$ ([I] and [II]) or $4 \mu\text{l}$ ([III]) of 5 wt% Nafion™ solution per milligram of catalyst serving as an ionomer. Five $4 \mu\text{l}$ aliquots of the catalyst ink were applied to the cleaned GC electrodes, resulting in a catalyst loading of 0.4 mg cm^{-2} ([I] and [III]) or 0.2 mg cm^{-2} ([II]). In [II], for better comparison, the loading of CNT-N was set to 0.1 mg cm^{-2} . All recorded potentials were converted to reversible hydrogen electrode values using the Nernst equation for the OER potential:

$$E(\text{RHE}) = E_{\text{Ag/AgCl}} + 0.059 \text{ pH} + E^0_{\text{Ag/AgCl}} \quad (13)$$

ORR tests were conducted in an oxygen-saturated 0.1 M KOH solution (Elme Messer Gaas, 99.999%) at room temperature, with a continuous O_2 gas flow over the solution. All experiments were controlled using Gamry Instruments Framework software. OER measurements were performed in a N_2 -saturated 1 M KOH solution (Elme Messer Gaas, 99.999%) at room temperature, under similar constant gas flow conditions as the ORR tests.

To account for system ohmic resistance, iR -drop compensation was applied to the OER polarisation curves. The resistance was determined from electrochemical impedance spectroscopy data collected over a frequency range of 100 kHz to 0.1 Hz at open circuit potential. The real part of the impedance, derived from the Nyquist plot at the point where the imaginary component was zero, was used as the resistance value. To evaluate electrocatalytic activity, at least three sets of RDE measurements were performed for each synthesised catalyst material, with each set employing three electrodes.

The bifunctionality parameter ΔE was calculated by using equation (14):

$$\Delta E = E_{\text{OER}} - E_{1/2} \quad (14),$$

where ΔE is the calculated bifunctionality parameter, E_{OER} is the potential value where the OER polarisation curves exhibits 10 mA cm^{-2} , and $E_{1/2}$ is the ORR polarisation curve half-wave potential.

3.7.2 Details of zinc-air battery measurements

The bifunctionality of all synthesised catalyst materials was evaluated using a custom-made zinc-air battery test cell. The air electrode, with an active surface area of 0.79 cm^2 ([I]) or 1.038 cm^2 ([II] and [III]), comprised a gas diffusion layer (GDL, Sigracet 28BC by SGLCarbon, Germany) and a catalyst layer, with a loading of 1 mg cm^{-2} , coated on the GDL. In [II], for better comparison, the CNT-N material had a final loading of 0.5 mg cm^{-2} , matching the CNT loading used in the studies of the composite material. A titanium mesh served as the air electrode current collector. A commercial catalyst

consisting of 20% PtRu (1:1 ratio) on carbon support (20% PtRu/C, FuelCellstore, USA) was utilised as a benchmark catalyst material for the air electrode. The ZAB cell employed an electrolyte solution of 6 M KOH + 0.2 M Zn(Ac)₂ and a polished zinc plate (1 mm, 99.9%) as the counter electrode. ZAB tests were conducted at room temperature using a PGSTAT30 potentiostat/galvanostat (Metrohm Autolab, The Netherlands) controlled by NOVA 2.1.5 software. The charge-discharge cycling involved alternating 30-minute charge and discharge processes at a current density of 10 mA cm⁻² ([I] and [II]) or 5 mA cm⁻² ([III]). Specific energy density (E_{sp}) and capacity were determined through complete discharge tests with a current density of either 10 mA cm⁻² ([I]) or 5 mA cm⁻² ([II] and [III]), calculated based on the consumed zinc mass using equation (15) for specific capacity and (16) for specific energy density. At least three separate ZAB cells were tested for each catalyst material to evaluate the maximum discharge power density.

$$\text{Specific capacity (mAh g}^{-1}\text{)} = \frac{\text{Discharge current (mA)} \times \text{time (h)}}{\text{m of consumed Zn (g)}} \quad (15)$$

$$E_{sp}(\text{Wh kg}^{-1}) = \frac{\text{Discharge current (mA)} \times \text{time (h)} \times \text{average discharge voltage (V)}}{\text{m of consumed Zn (g)}} \quad (16)$$

3.8 Physicochemical characterisation methods

Microstructural analysis for studies [I] and [II] was conducted using a MIRA3 scanning electron microscope (SEM, Tescan, Czech Republic) equipped with secondary electron (SE) detection, operated at an acceleration voltage of 5 kV. Elemental mapping was performed using an UltraDry Silicon Drift Energy-Dispersive Spectrometer (EDS) (Thermo Fisher Scientific, USA) at an acceleration voltage of 10 kV. For study [III], microstructural imaging was carried out using a JSM-IT800HL scanning electron microscope (JEOL, Japan) under SE mode at 5 kV and a beam current of 54 pA. Elemental mapping was performed using an Aztec Live Premium Ultim Max 100 EDS system (Oxford Instruments, UK) at 15 kV and 1.4 nA beam current. The beam was calibrated using a pure copper cathode as a reference. Quantitative EDS maps were acquired at 400× magnification with a 512-pixel resolution, scanning each region eight times with a 200 μs dwell time per pixel.

Atomic Absorption Spectroscopy (AAS) (iCE 3000, Thermo Fisher Scientific Inc., Germany) was used to quantify the concentrations of residual battery metals (mg g⁻¹) in Raw Material 1 and Raw Material 2. Each sample was leached in aqua regia prior to analysis and the leaching procedure was repeated three times per material to ensure reproducibility. The reported values represent the mean of the three independent measurements, with the standard deviation (± mg g⁻¹) used to reflect the reproducibility of the leaching process.

The crystallinity and phase composition of the materials were analyzed using powder X-ray diffraction (XRD) with a PANalytical X'Pert³ Powder XRD system (Malvern Panalytical, UK). The measurements were conducted with Cu Kα radiation (λ = 1.54182 Å), applying a step size of 0.04° at 45 kV and 40 mA.

High-resolution transmission electron microscopy (HRTEM) images were obtained with a double aberration-corrected microscope equipped with a 200 kV field-emission gun and X-ray EDS detector (JEOL JEM-2200FS, JEOL Ltd, Japan).

Raman spectroscopy was performed using a Renishaw inVia™ Confocal Raman Microscope (Renishaw, UK) with a 532 nm excitation laser focused through a 50× Leica microscope objective. Scattered light was collected in 180° backscattering geometry,

and a 2400 L mm⁻¹ diffraction grating was used for spectral dispersion, detected via a CCD detector. Spectra were deconvoluted using OriginPro software, applying the Voigt function for peak fitting.

Nitrogen adsorption-desorption isotherms were obtained using an Anton Paar NovaTouch LX4 system (Austria) at 77 K to evaluate the specific surface area (SSA) and porosity. SSA was calculated using the Brunauer–Emmett–Teller (BET) method over a relative pressure (P/P_0) range of 0.05–0.3. In study [III], density functional theory (DFT) surface area (S_{DFT}) was determined using the Quenched Solid DFT model for slit/cylindrical/spherical pores via Quantachrome TouchWin software. Pore size distribution (PSD) was analysed using the Non-Local DFT method via SAIEUS software (Micromeritics, USA).

X-ray photoelectron spectroscopy (XPS) was carried out with a Kratos Axis Ultra spectrometer with monochromate Al K α -radiation using a pass energy of 40 eV, X-ray power of 150 W ([I] and [II]) or 195 W ([III]) and an analysis area of approximately 700 μm * 300 μm . The C 1s sp² peak at 284.5 eV served as the reference for binding energy calibration. Elemental composition was calculated from high-resolution core-level spectra after Shirley background subtraction, using instrument-specific sensitivity factors. Spectral fitting was carried out in CasaXPS software using a Gaussian-Lorentzian (GL 30) peak shape, with the exception of the sp² carbon, which was modeled with an asymmetric line shape. Full width at half maximum (FWHM) values were constrained to be equal for most peaks within a fit, excluding those for sp² carbon and N-oxide peaks.

4 Results and discussion

4.1 Physicochemical characterisation of battery derived precursor materials

The leach residue generated from hydrometallurgical recycling of black mass is highly heterogeneous, as it retains a variety of residual additives even after the leaching process. This chapter presents the physicochemical characterisation of precursor materials from LIBs used in papers [I–III]. The same precursor was employed in papers [I] and [II] (Raw Material 1), while paper [III] utilised two different graphite-based precursors derived from EoL LIBs (Raw Material 2 and manually separated spent graphite from EoL LIBs). The characterisation of the resulting nitrogen-doped bifunctional oxygen electrocatalyst materials is described in subsequent chapters.

The compositional heterogeneity of metal residues in both Raw Materials was confirmed by the AAS analysis, presented in Table 4.1. These values represent the average of three independent aqua regia leaching experiments. Among the analysed metals, Co showed the highest concentration for both, Raw Material 1 being at $120.5 \pm 13.6 \text{ mg g}^{-1}$ and Raw Material 2 at $185.7 \pm 19.6 \text{ mg g}^{-1}$. The concentration for Cu was $48.4 \pm 13.2 \text{ mg g}^{-1}$ for Raw Material 1 and $2.2 \pm 0.2 \text{ mg g}^{-1}$ for Raw Material 2 while for the other metals the concentrations had similar values as presented in Table 4.1. These compositional differences are attributed to the distinct hydrometallurgical recycling processes used to obtain these two residues, as detailed in reference [34]. The key distinction in the leaching conditions lies in the use of current collectors as reductants. In the preparation of Raw Material 1, both Cu (2 g/100 g of black mass) and Al (2.5 g/100 g) were added as reductants, replacing the commonly used H_2O_2 to enhance Co leaching efficiency. In contrast, the preparation of Raw Material 2 involved only Cu (2 g/100 g), which proved less effective in enhancing Co leaching kinetics. This variation in reductant species accounts for the observed differences in Co and Cu concentrations between the two residues.

Table 4.1. Metal content of Raw Material 1 and Raw Material 2 based on AAS measurements.

Element	Li (mg g^{-1})	Co (mg g^{-1})	Mn (mg g^{-1})	Ni (mg g^{-1})	Cu (mg g^{-1})	Fe (mg g^{-1})
Raw Material 1	11.0 ± 3.6	120.5 ± 13.6	12.0 ± 1.8	8.4 ± 1.5	48.4 ± 13.2	1.8 ± 0.9
Raw Material 2	8.9 ± 0.4	185.7 ± 19.6	13.2 ± 0.5	7.7 ± 0.3	2.2 ± 0.2	1.2 ± 0.2

The Raw Material 1 ([I] and [II]) and Raw Material 2 ([III]) were also analysed using SEM-EDS (Figure 4.1 and Figure 4.2, Table 4.2). Both precursor materials were found to be primarily composed of carbon, along with metal residues from cathode active materials—namely Co, Ni, and Mn—as well as Cu and Al from current collectors, F from the PVDF binder and traces of Si commonly used as conductive additive for LIB anodes.

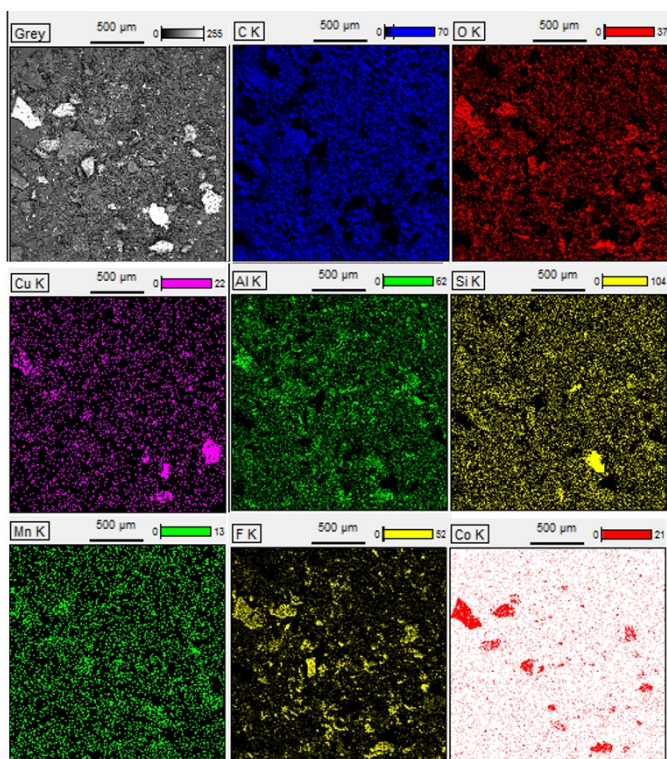


Figure 4.1. SEM-EDS map of Raw Material 1. The elemental composition data is acquired from the whole area shown on the figure above.

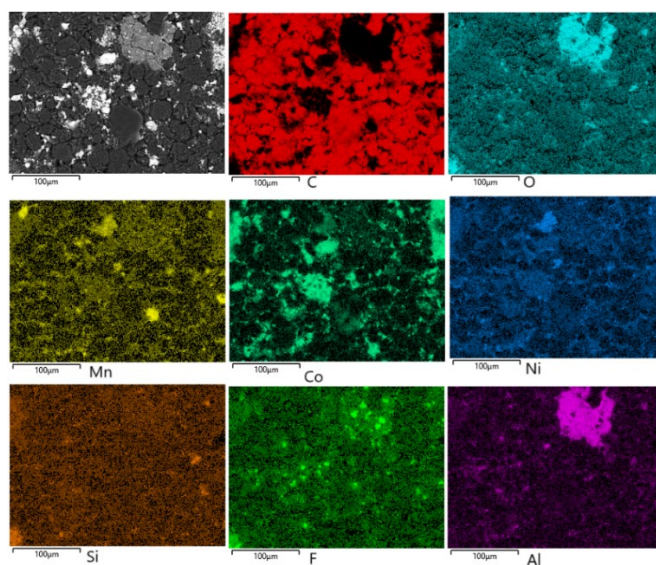


Figure 4.2. SEM-EDS map of Raw Material 2. The elemental composition data is acquired from the whole area shown on the figure above.

Elemental mapping revealed notable differences in the distribution and morphology of these elements between the two samples. Raw Material 1 displayed a more homogeneous elemental distribution, with Co appearing in more dispersed regions. In contrast, Raw Material 2 exhibited more concentrated Co agglomerates, showing the higher Co concentration, as determined also by AAS analysis. Similarly, a distinct Al_2O_3 agglomerate was observed in Raw Material 2, whereas Al and O were less prominent and more dispersed in case of Raw Material 1. Cu was only found in Raw Material 1, being consistent with the AAS results, where the Cu concentration for Raw Material 2 was much lower. Overall, the SEM-EDS analysis confirmed that both Raw Materials have heterogeneous nature with most prominent metal specie being Co. These findings are consistent with the compositional differences and leaching efficiencies discussed in the AAS results, highlighting the impact of differing leaching conditions on the final composition of the residues.

Table 4.2. Elemental composition of Raw Material 1 and Raw Material 2 based on SEM-EDS mappings. Data acquired from Figure 4.2.

Element	Raw Material 1 (wt%)	Raw Material 2 (wt%)
C	79.6	81.4
O	15.1	5.4
Co	0.8	8.5
Mn	0.1	0.6
Ni	-	0.4
Al	0.4	1.4
Cu	0.4	-
Si	0.3	0.1
F	3.1	2.0

The corresponding XRD diffractograms (Figure 4.3a) confirmed the presence of the heterogeneity of both Raw Materials. The XRD analysis identified graphite as the predominant carbon phase in both samples, evidenced by a sharp peak at $26.5^\circ 2\theta$, corresponding to the (002) plane of highly ordered graphitic carbon (ICDD: 96-900-8570). For Raw Material 1, additional peak was detected for the de-lithiated form of LiCoO_2 , namely $\text{Li}_{1.44}\text{Co}_3\text{O}_6$ (ICDD: 96-155-0393), as well as peaks for LiMn_2O_3 (ICDD: 96-151-3968), and Co_4O_4 (ICDD: 96-900-8619), Cu (ICDD: 96-901-2044) and Al_2O_3 (ICDD: 00-010-0173). A peak for SiO_2 (ICDD: 96-900-5033), often used as an anode additive to enhance cell stability and energy density, was also detected [24]. For Raw Material 2 reflections suggested the presence of residual cathode active materials, including LiCoO_2 (ICDD: 98-016-4323), metallic cobalt ($\text{Co}(0)$) (ICDD: 98-062-2443), and manganese oxide (MnO) (ICDD: 96-101-0899). As was discussed by Chernyaev et al. [34], Cu is a more effective reductant for LiCoO_2 than Al, as evidenced by the appearance of $\text{Co}(0)$ in the XRD pattern. However, the Cu content in Raw Material 2 was insufficient to fully reduce LiCoO_2 , which remained partially unreacted. In contrast, the leaching process that produced Raw Material 1 involved both Cu and Al as reductants. Although Al contributed to unwanted side reactions—reflected in the broader variety of residual

species detected—the combination of Cu and Al proved more effective overall in extracting Co, resulting in a lower Co concentration in the Raw Material 1, as shown in Table 4.1.

To facilitate comparison, Raw Material 2 was further processed via heat-treatment, followed by nitrogen doping and pyrolysis at 800 °C to produce *N*-RM2. The XRD diffractogram of *N*-RM2 (N-doped RM2) retained similar features. However, the LiCoO_2 peak was no longer present, having been reduced to metallic Co during thermal treatment. This transformation likely occurred via a carbothermic reduction mechanism, facilitated by the high carbon content of the precursor [194]. Additionally, aluminothermic reduction may have contributed due to the presence of residual Al from the current collector, although in lower concentrations [195]. The heterogeneous composition is representative of typical black mass leach residues produced by hydrometallurgical recycling, as complete extraction of active materials from the black mass is rarely achieved [34,57]. From an electrocatalyst synthesis perspective, the presence of these residual metals can be advantageous, as they can serve as *in situ* dopants. Although doping via pure metal salts allows for more precise control over composition, the use of EoL LIB-derived precursors offers a more sustainable and cost-effective alternative, allowing direct incorporation of functional elements without additional chemical inputs. Figure 4.3b presents the XRD diffractograms of the manually extracted EoL graphite (experimental data described in section 3.3), as well as the synthesised GO, rGO, and N-rGO. The recovered graphite exhibited no detectable crystalline impurities, showing only sharp peaks associated with pure graphite. In contrast, the GO sample displayed a characteristic (001) diffraction peak between 10–12°, along with broad peaks near 20–30°, both indicative of increased interlayer spacing due to the introduction of oxygen-containing functional groups. The rGO and N-rGO samples showed weakened (001) peaks and intensified broad peaks in the 20–30° range, suggesting partial restacking of graphene sheets following reduction.

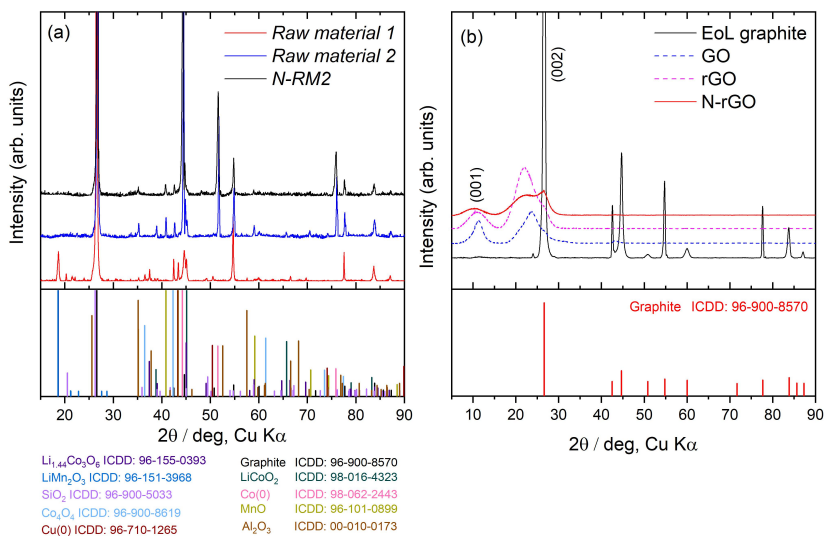


Figure 4.3 XRD diffractograms of (a) Raw Material 1, Raw material 2, and N-RM2 with standard cards; (b) EoL LIB graphite, GO, rGO and N-rGO with standard card.

4.2 Investigation of transition metal and nitrogen co-doped black mass leach residue for ORR/OER applications

The leach residue from industrially produced black mass, obtained after hydrometallurgical treatment of EoL LIBs, was selected as a carbon and metal precursor for the synthesis of a nitrogen-doped ORR/OER electrocatalyst. The detailed synthesis procedure for the catalyst materials discussed in this section are described in sections 3.1 and 3.4. The inspiration to this work came from our work groups previous study, in which EoL LIB recycling residue was successfully used as a precursor for *in situ* metal doping and GO synthesis, yielding an active Bat-N-rGO oxygen electrocatalyst [57].

Figure 4.4 shows SEM micrographs of the studied catalyst materials. The Raw Material 1 (Figure 4.4a) exhibits roundish particles with sizes ranging from approximately 25 to 50 μm , consistent with the spherical graphite typically used in LIB anodes [27]. After heat treatment (RM1, Figure 4.4b), the particles appear smaller and more uniformly distributed. This is attributed to the decomposition and removal of the polymeric binder, previously holding the graphite particles together. The nitrogen-doped samples (*Bat-res-N*, Figure 4.4c, and *HT-Bat-res-BM-N*, Figure 4.4d) display a distinctly more compact and rougher surface structure, confirming successful incorporation of nitrogen into the carbon matrix. Additionally, ball-milling in the preparation of *HT-Bat-res-BM-N* has significantly reduced particle size and improved particle uniformity compared to *Bat-res-N*. Both nitrogen-doped materials exhibit flatter, thinner, and less spherical morphologies compared to the initial Raw Material 1, indicating notable changes in surface structure due to doping and mechanical treatment. Table 4.3 shows that the highest relative increase in metal content was observed for the *HT-Bat-res-BM-N* material. This indicates the successful incorporation of Co-N-C species into the carbon framework, facilitating the stabilisation of metallic Co within the bulk [165].

Table 4.3 Elemental composition of RM1, *Bat-res-N* and *HT-Bat-res-BM-N* based on SEM-EDX mapping.

Element	RM1 (Wt%)	<i>Bat-res-N</i> (Wt%)	<i>HT-Bat-res-BM-N</i> (Wt%)
C	82.9	80.8	75.8
O	13.4	15.3	18.6
Co	2.0	2.3	3.4
Mn	0.2	0.3	0.4
Ni	-	0.2	0.2
Al	0.4	0.5	0.5
Cu	0.5	0.5	0.5

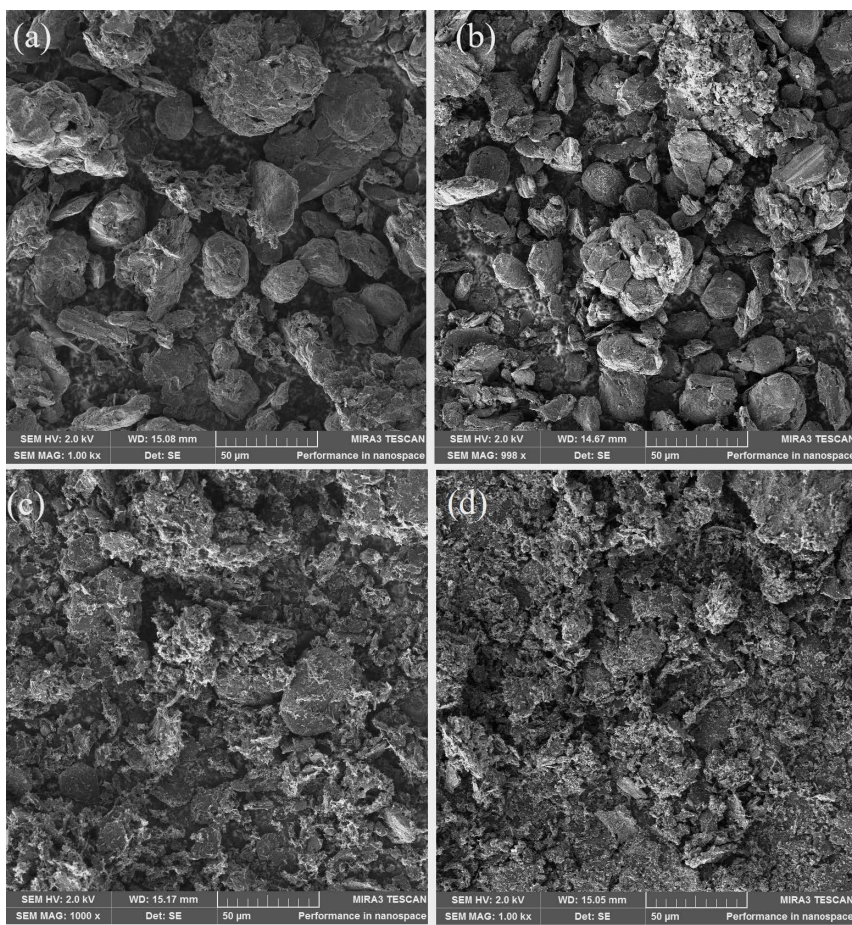


Figure 4.4. SEM micrographs of (a) Raw material 1, (b) RM1, (c) Bat-res-N and (d) HT-Bat-res-BM-N catalyst materials using 1000x magnification.

This observation aligns well with the results obtained from XRD diffractograms (Figure 4.5a), which showed an increase in the intensity of metallic cobalt (Co(0), ICDD: 96-901-1624) peaks following nitrogen doping, while for the RM1 the Co was either in Co_4O_4 (ICDD: 96-900-8619) or Co(0) form. This further confirms that the nitrogen doping step promotes the reduction of Co and its effective incorporation into the carbon matrix. Additionally, the XRD diffractograms reveal the presence of cobalt carbide ($\text{Co}_{0.01}\text{Co}$, ICDD: 98-061-7394), suggesting the formation of CNTs. The growth of CNTs typically occurs in the presence of Co nanoparticles, which subsequently become encapsulated within these CNT structures [57,168,176]. Furthermore, a distinct peak corresponding to Cu (ICDD: 96-901-2044) was identified in the diffractograms of the RM1, Bat-res-N, and HT-Bat-res-BM-N samples, confirming residual Cu content in these materials.

The carbon lattice structure was analysed using Raman spectroscopy (Figure 4.5b) to evaluate structural changes in the carbon framework. Two prominent peaks were observed: the first-order G-band ($\sim 1580\text{ cm}^{-1}$), indicative of ordered sp^2 carbon structures, and the D-band ($\sim 1350\text{ cm}^{-1}$), which arises from structural defects [196]. The intensity ratio (I_D/I_G) serves as a primary metric for assessing the relative degree of order or disorder in carbon-based materials [143]. In this study, each step of the synthesis progressively increased the degree of graphitisation and reduced the level of surface defects in the carbon lattice. However, it is important to note that the D-band intensity is influenced not only by topological defects and vacancies but also by the presence of impurities within the carbon matrix [197]. Therefore, the observed reduction in the D-band intensity during this study is likely due to the removal of impurities such as binder residues, organic contaminants, and oxygen-containing functional groups. Specifically, the heat treatment of the Raw Material 1 decreased the I_D/I_G ratio from 0.72 to 0.50 in the *RM1* sample. Further decreases in the I_D/I_G ratio were observed for the nitrogen-doped materials, attributed primarily to the incorporation of graphitic nitrogen into the carbon lattice. This doping promotes a more ordered and crystalline structure [160]. Additionally, the presence of Co and CoO species can act as catalytic active sites, further facilitating the formation of well-ordered graphitic structures [198].

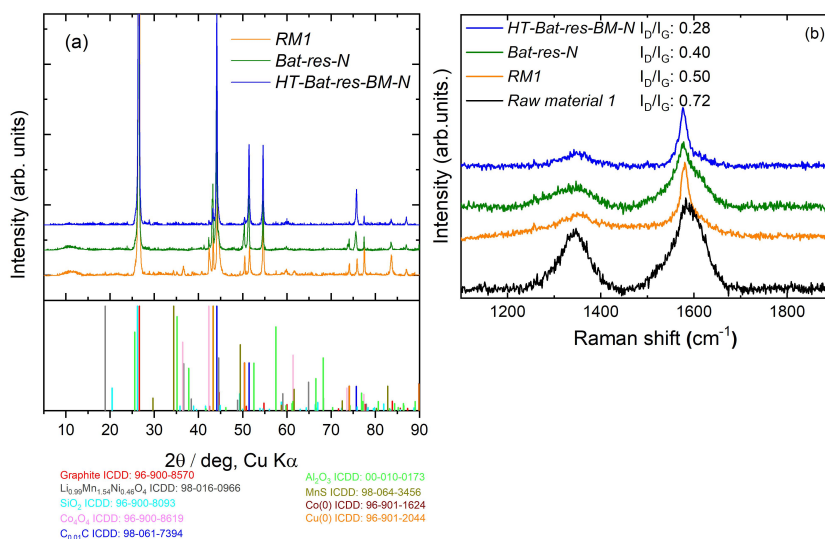


Figure 4.5. (a) XRD diffractograms of *RM1*, *Bat-res-N* and *HT-Bat-res-BM-N*, (b) Raman spectra of Raw material 1, *RM1*, *Bat-res-N* and *HT-Bat-res-BM-N*.

The N_2 physisorption was used to calculate the SSA of the catalyst materials by using BET theory. The observed trend in SSA is closely connected by the structural differences noted in the Raman spectroscopy results. Each successive synthesis step led to a significant increase in SSA, indicating a progressive enhancement in material porosity. The Raw material 1 exhibited a low SSA of $2.4\text{ m}^2\text{ g}^{-1}$, which increased to $9.9\text{ m}^2\text{ g}^{-1}$ after heat treatment (*RM1*). Further increases were observed following nitrogen doping, with *Bat-res-N* reaching $36.9\text{ m}^2\text{ g}^{-1}$, and the highest SSA of $46.8\text{ m}^2\text{ g}^{-1}$ obtained for the *HT-Bat-res-BM-N* sample. This increase in surface area and porosity is highly beneficial for electrocatalyst performance, as it provides a greater number of accessible sites for

anchoring catalytically active species and promotes more efficient mass transport of reactants and products throughout the catalyst structure. Such improvements are particularly important for oxygen electrocatalysis, where high surface accessibility and porosity are critical for enhancing overall catalytic activity and stability [136].

The extent of nitrogen doping in the *Bat-res-N* and *HT-Bat-res-BM-N* materials was evaluated using XPS. In addition to the primary elements—carbon, nitrogen, and oxygen—various residual elements originating from the LIBs were also detected, including Co, Li, Mn, Ni, Al, and Cu. Figure 4.6 presents the deconvoluted C 1s, N 1s, and Co 2p spectra.

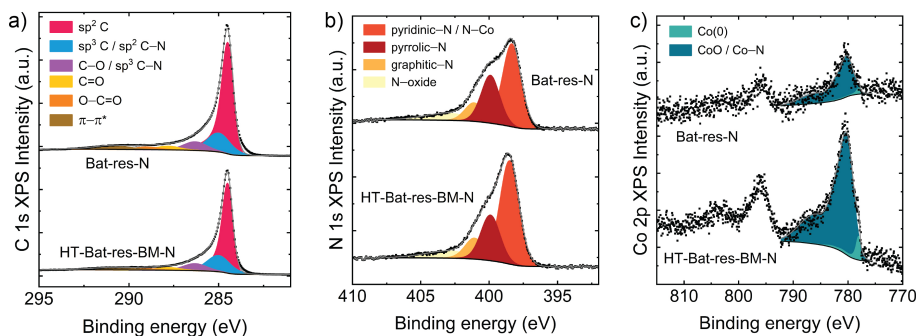


Figure 4.6. X-ray photoelectron spectra of the *Bat-res-N* and *HT-Bat-res-BM-N* samples: (a) C 1s region, (b) N 1s region and (c) Co 2p region.

The C 1s spectrum (Figure 4.6a) exhibits a main asymmetric peak at 284.5 eV, attributed to sp^2 -hybridised carbon, with additional contributions from C–C, C–O, and C–N bonding. The surface nitrogen content and detailed peak fitting results are summarised in Table 4.4. Among the samples, *HT-Bat-res-BM-N* displayed a higher nitrogen content, which is attributed to its increased SSA and smaller graphite particle size, both of which facilitate enhanced nitrogen incorporation during doping. The N 1s spectrum (Figure 4.6b) was deconvoluted into four distinct nitrogen configurations: pyridinic-N/N–Co, pyrrolic-N, graphitic-N, and N-oxide, based on established fitting parameters [57]. Pyridinic-N accounted for 50% of the total nitrogen in *Bat-res-N* and 55% in *HT-Bat-res-BM-N*. The Co 2p spectrum (Figure 4.6c) was fitted to two main oxidation states: metallic Co and Co(II). The Co(II) signal likely represents contributions from both CoO and Co–N coordination environments [169,199]. A comparison between surface metal concentrations determined by XPS (Table 4.4) and bulk elemental composition obtained from SEM-EDX (Table 4.3) revealed notable differences. For instance, in *HT-Bat-res-BM-N*, Co was present at 0.4 at% on the surface (XPS) compared to 0.8 at% (3.4 wt%) in the bulk (SEM-EDX), whereas Al showed the opposite trend, with 2.1 at% (XPS) versus 0.2 at% (0.5 wt%, SEM-EDX). These differences suggest that elements such as Al, Mn, and Li are more concentrated on the material surface, while Co is more uniformly incorporated into the carbon matrix forming Co–N–C sites.

Table 4.4. The atomic percentages (at%) of the elements for Bat-res-N and HT-Bat-res-BM-N samples including peak fitting results based on XPS data. The error associated with each value is roughly $\pm 10\%$ of the value.

Element	Bat-res-N	HT-Bat-res-BM-N
C - of which	77.1	74.2
sp ² C	57 %	55 %
sp ³ C/ sp ² C-N	21 %	24 %
C-O-C/C-OH/ sp ³ C-N	9 %	10 %
C=O	4 %	4 %
O-C=O	3 %	2 %
$\pi-\pi^*$	6 %	5 %
O	12.4	13.9
N - of which	5.6	6.4
Pyridinic-N	50 %	55 %
Pyrrolic-N	29 %	24 %
Graphitic-N	11 %	11 %
N-oxide	10 %	9 %
Al	2.1	2.1
Mn	0.5	0.9
Li	1.4	0.6
Co - of which	0.1	0.4
Co(0)	6 %	8 %
CoO / Co-N	94 %	92 %
Zr	-	0.2
Cu	0.3	0.2
Ni	0.1	0.1
F	0.3	0.9
S	0.1	0.1

The electrochemical characterisation of the synthesised catalyst materials was performed using the RDE technique to evaluate both ORR and OER activities. The experimental details are provided in Section 3.7.1. The linear sweep voltammetry (LSV) curves for ORR are presented in Figure 4.7a, and the corresponding electrochemical performance parameters are summarised in Table 4.5. A progressive improvement in ORR activity was observed with each synthesis step, as indicated by increasing onset potentials (E_{onset}). Among the nitrogen-doped catalysts, *HT-Bat-res-BM-N* exhibited superior performance compared to *Bat-res-N*, with an E_{onset} of 0.890 V vs RHE, which is 15 mV higher than that of *Bat-res-N*. The same material also achieved a half-wave potential ($E_{1/2}$) of 0.795 V vs RHE and a limiting current density (j) of 4.81 mA cm⁻², highlighting its improved electrocatalytic activity.

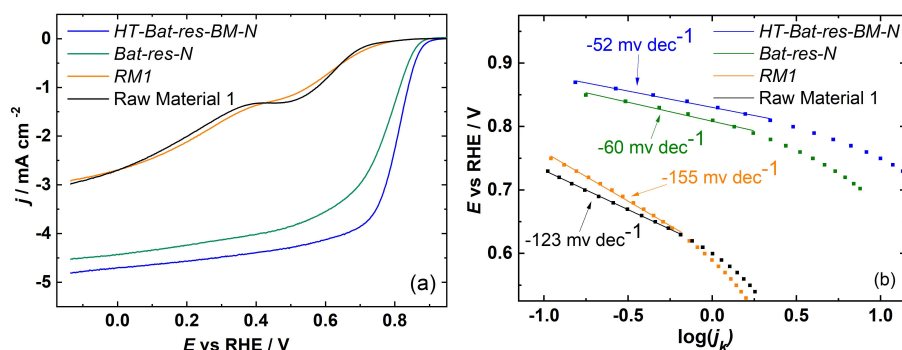


Figure 4.7. (a) ORR polarisation curves at 1600 rpm in O₂ saturated 0.1 M KOH solution for catalysts studied in section 4.2, (b) ORR Tafel slopes for *Bat-res-N* and *HT-Bat-res-BM-N*.

The number of electrons transferred per oxygen molecule (n)—presented in Table 4.5—was calculated to evaluate the ORR mechanism. For *Bat-res-N*, the n value at the end of the plateau area of ORR polarisation curve was 3.6, indicating that the ORR followed a mixed 2 + 2 e⁻ transfer pathway. In contrast, *HT-Bat-res-BM-N* exhibited an n value of 4.1, suggesting that the ORR proceeded predominantly via a direct 4 e⁻ transfer mechanism. The corresponding calculations and data supporting these values are provided in the supplementary information of paper [I]. The Tafel slopes presented in Figure 4.7b indicate that *HT-Bat-Res-BM-N* and *Bat-res-N* exhibit similar values of -52 mV dec⁻¹ and -60 mV dec⁻¹, respectively. Notably, these values are comparable to those typically reported for Pt-based catalysts, suggesting that the rate-determining step in the oxygen reduction reaction is likely associated with the initial O₂ adsorption and reduction process [200]. The enhanced ORR performance of the nitrogen-doped materials is primarily attributed to the increased surface area and effective nitrogen doping, particularly the formation of pyridinic-N species during pyrolysis, which are known to serve as highly active sites for ORR. Additionally, the ball-milling step, performed using 0.5 mm ZrO₂ balls, further reduced the graphite particle size, improving the dispersion of active sites and enhancing surface area, which increased the ORR activity of *HT-Bat-res-BM-N* over *Bat-res-N*.

Table 4.5. Electrochemical characteristics for Raw material 1, RM1, Bat-res-N and HT-Bat-res-BM-N.

Catalyst	ORR				OER	ΔE (V)
	E_{onset} (V vs. RHE)	$E_{1/2}$ (V vs. RHE)	j (mA cm ⁻²)	n	E_{OER} (V) @ 10 mA cm ⁻²	
Raw material 1	0.745	0.327	2.98	-	1.648	1.321
RM1	0.767	0.370	2.92	-	1.675	1.305
Bat-res-N	0.875	0.755	4.53	3.6	1.759	1.004
HT-Bat-res-BM-N	0.890	0.795	4.81	4.1	1.648	0.853

Figure 4.8a and Table 4.5 present a comparison of the OER activity for the synthesised catalyst materials. Among the tested samples, the *HT-Bat-res-BM-N* catalyst exhibited the highest performance, with an $E_{\text{OER}} = 1.648$ V vs RHE at 10 mA cm⁻². In contrast, *RM1* and *Bat-res-N* required higher potentials of 1.675 V and 1.759 V vs RHE, respectively, to reach the same current density. Interestingly, the Raw material 1 also demonstrated relatively good OER activity, achieving $E_{\text{OER}} = 1.648$ V vs RHE at 10 mA cm⁻². This activity is attributed to its higher content of residual metals and metal oxides, as confirmed by the XRD diffractogram shown in Figure 4.3a. In particular, the presence of Co₃O₄, which contains cobalt in mixed oxidation states (Co(II) and Co(III)), which is often associated with enhanced OER activity [127]. The OER Tafel slope (Figure 4.8b) for *Bat-res-N* and *HT-Bat-res-BM-N* was 140 mV dec⁻¹ and 119 mV dec⁻¹, respectively. For the Raw Material 1 and *RM1* the Tafel slope values were of 71 mV dec⁻¹ and 97 mV dec⁻¹, respectively. The increase of Tafel slopes for N-doped materials could indicate that mass-transfer is the rate limiting step and the effective electrode surface area is lower [75].

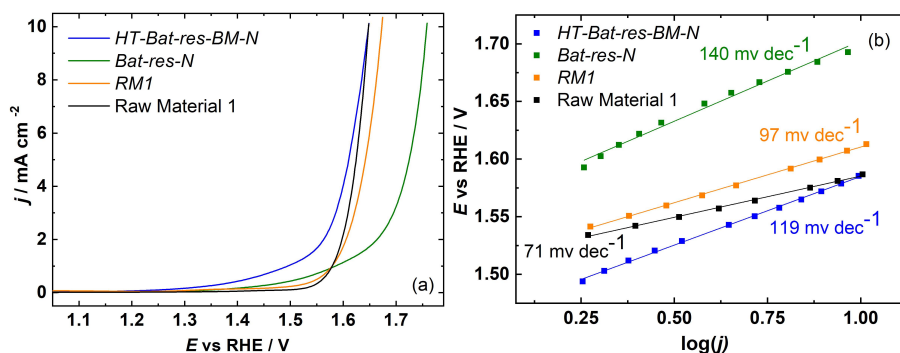


Figure 4.8. RDE electrochemical characteristics for materials studied in section 4.2: (a) OER polarisation curves at 1600 rpm in N₂-saturated 1 M KOH solution and (b) OER Tafel slopes for Raw Material 1, RM1, Bat-res-N and HT-Bat-res-BM-N.

The bifunctionality parameter ΔE for *HT-Bat-res-BM-N* was determined to be 0.853 V, which is significantly lower than that of all other catalysts investigated in this study as presented in table 4.5. The superior bifunctional oxygen electrocatalytic activity of *HT-Bat-res-BM-N* is likely due to the formation of electrochemically active Co–N–C sites and metallic Co(0) during synthesis. The presence of multiple transition metals within the catalyst may also contribute to a synergistic effect, enhancing both ORR and OER performance. However, the specific mechanisms underlying these synergistic interactions in multi-metallic electrocatalysts remain the subject of ongoing investigations [126,201].

4.3 Investigation of transition metal and nitrogen co-doped black mass leach residue and CNT composites for ORR/OER applications

In this study, the same Raw Material 1 was used as precursor as in section 4.2. The objective was to enhance the electrocatalytic activity of the material by improving its electron transfer efficiency, porosity, and SSA. To achieve this, CNTs were incorporated as spacers between the graphitic structures of *RM1*. This approach is intended to increase surface area and porosity, while simultaneously enhancing the overall electrical conductivity of the composite. It is well established that the combination of CNTs with other carbon-based materials can significantly improve both the bifunctional oxygen electrocatalytic activity and the stability of the resulting catalysts. Within the composite, CNTs function as electron-conducting bridges, facilitating charge transport across the surface and promoting better interaction with the catalytic active sites [129]. The synthesis procedure followed a similar approach to that used in the previous study in paper [I]; however, the mass ratio of *RM1* to CNT was varied, as detailed in Section 3.5 and illustrated in Figure 3.1

The synthesised materials were first analysed using XRD to investigate their crystallographic structure. The diffractograms of the *RM1*/CNT composite materials and the *CNT-N* sample are presented in Figure 4.9.

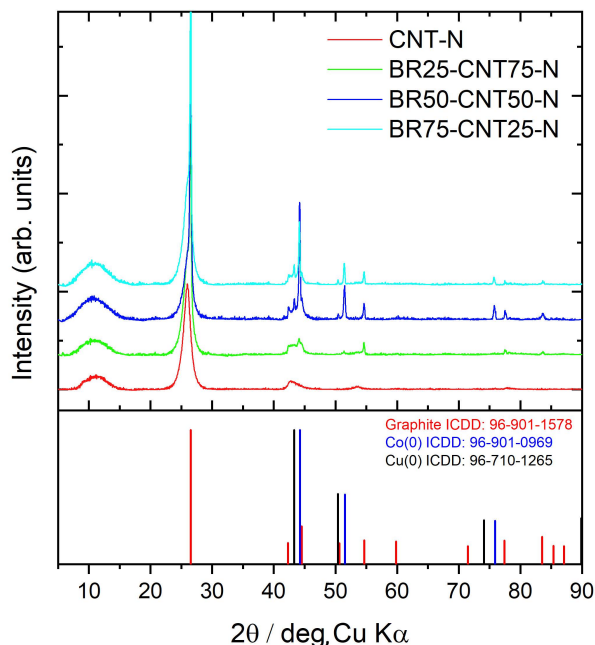


Figure 4.9. XRD diffractograms of CNT-N, and RM1/CNT composites.

The most prominent peak, observed at $2\theta = 26.5^\circ$, corresponds to the (002) plane of graphitic carbon. A progressive decrease in the intensity of this peak with increasing CNT content indicates that the (002) peak is primarily associated with the graphitic content of the RM1. Therefore, a lower intensity suggests a reduced proportion of RM1 in the composite. The XRD pattern of pure CNT-N did not exhibit any detectable metal-related peaks, indicating the absence of crystalline metallic or metal oxide phases, due to the acid purification step of CNT before the synthesis of composite materials as described in section 3.2. In contrast, the composite materials revealed distinct peaks corresponding to metallic Co(0), while no signals associated with Co_4O_4 were observed as it was for RM1 (Figure 4.5). This suggests that cobalt-containing compounds such as LiCoO_2 and Co_4O_4 were successfully reduced to metallic cobalt during the nitrogen doping and high-temperature treatment, consistent with the carbothermic and aluminothermic reduction processes discussed previously in Section 4.2 (paper [I]) for the *Bat-res-N* and *HT-Bat-res-BM-N* materials.

SEM-SE micrographs in Figure 4.10 provide insight into the surface morphology of the synthesised materials.

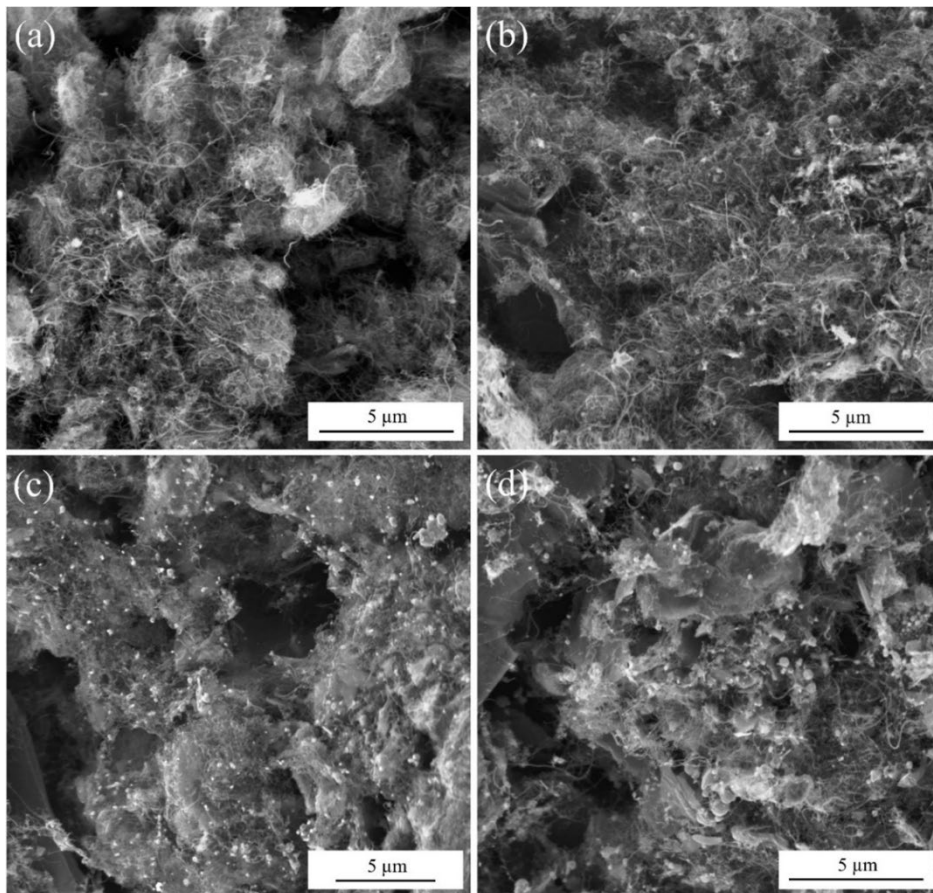


Figure 4.10. SEM-SE micrographs of (a) CNT-N, (b) BR25-CNT75-N, (c) BR50-CNT50-N, and (d) BR75-CNT25-N.

The CNT-N sample (Figure 4.10a) exhibits a uniform and extensive network of carbon nanotubes, as expected. In the BR25-CNT75-N composite (Figure 4.10b), a similarly well-developed CNT network is visible, although larger embedded particles—attributable to the RM1—can also be observed. In contrast, the BR50-CNT50-N (Figure 4.10c) and BR75-CNT25-N (Figure 4.10d) samples display a less pronounced CNT network, while lighter particles dispersed on the surface become increasingly evident on the surface. The Co nanoparticles (lighter dots) in BR50-CNT50-N are uniformly dispersed as can be seen in Figure 4.10c. Elemental analysis using SEM-EDS (Table 4.6) confirmed the presence of several metal species within the composites. Among these, Co exhibited the highest surface concentration across all composite samples. Additionally, trace amounts of Ni, Mn, Al, Cu, and Zr were detected. While the former four elements originate from the leach residue used as the precursor, the presence of Zr is attributed to the use of ZrO₂ milling balls during the ball-milling stage of synthesis. The incorporation of small

quantities of Zr is unavoidable, as the mechanical forces exerted during milling inevitably lead to abrasion of the milling media. However, previous studies—such as by Ratso et al.—have shown that this minor contamination does not significantly affect the electrocatalytic activity of the resulting material [107]. The metal content—particularly Co—was higher in the composite materials compared to the N-doped materials discussed in the previous section. This enhancement is attributed to the presence of the CNT network, which likely facilitated more effective dispersion and incorporation of Co nanoparticles. Additionally, the CNT network contributed to the formation of a more porous structure compared to *Bat-res-N* and *HT-Bat-res-BM-N*, further supporting metal integration. Overall, the metal concentration based on SEM-EDS mapping is very approximate as it only scans very small surface area of the material, therefore other methods are needed for better metal content analysis.

The surface morphology and elemental composition of the catalyst materials were further investigated using TEM-EDS. The TEM micrographs presented in Figure 4.11 confirm the observations made from SEM analysis: a uniformly distributed CNT network is clearly visible in *CNT-N*, while the composite materials exhibit larger agglomerates (50–100 nm) of metal-containing particles and graphitic carbon structures, most prominently in *BR75-CNT25-N*. Further analysis of *BR25-CNT75-N* using TEM-EDS (Figure 4.12) reveals a mixture of smaller (10–30 nm) and larger (50–100 nm) particles. Elemental mapping indicates the presence of C, O, Cu, Co, and Fe—all originating from the *RM1*. In the case of *BR50-CNT50-N* TEM-EDS on Figure 4.13 shows regions with a high concentration of Co and C. Notably, EDS1 shows a Co nanoparticle encapsulated within a CNT, while EDS2 reveals a broader region enriched with both C and Co. Cobalt is well known to catalyse the formation of bamboo carbon nanotubes, with Co nanoparticles becoming encapsulated during the growth process [66]. This encapsulation significantly

Table 4.6 Elemental composition for the RM1/CNT composite materials and CNT-N based on SEM-EDX mapping.

Element	<i>CNT-N</i> (Wt%)	<i>BR25-CNT75-N</i> (Wt%)	<i>BR50-CNT50-N</i> (Wt%)	<i>BR75-CNT25-N</i> (Wt%)
C	98.9	92.3	80.5	81.2
O	-	-	2.5	2.5
Co	-	5.5	11.2	8.4
Mn	0.1	0.7	1.8	3.3
Ni	-	-	1.3	0.9
Al	1.0	1.2	1.3	1.6
Cu	-	-	1.1	1.6
Zr	-	-	0.3	0.5

enhances the stability of the metal species under electrochemical conditions, due to favourable charge redistribution in the carbon matrix, thereby promoting the adsorption of oxygen intermediates during ORR and OER [76]. Some bamboo carbon nanotubes with encapsulated Co nanoparticles were also observed in *BR75-CNT25-N* (Figure 4.14);

however, the material was dominated by larger, irregular *RM1* particles containing both carbon and metal species. These findings suggest that the *BR50-CNT50-N* composition provides the most optimal balance in terms of uniform surface morphology and Co nanoparticle encapsulation, resulting in enhanced stability and catalytic site preservation within the electrocatalyst.

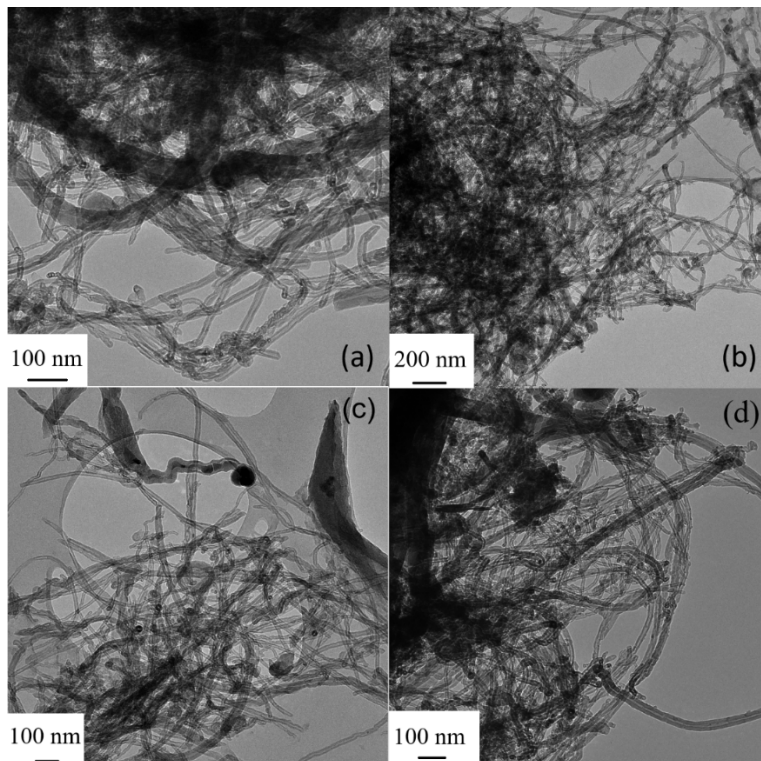


Figure 4.11. TEM micrographs of (a) *CNT-N*, (b) *BR25-CNT75-N*, (c) *BR50-CNT50-N*, and (d) *BR75-CNT25-N*.

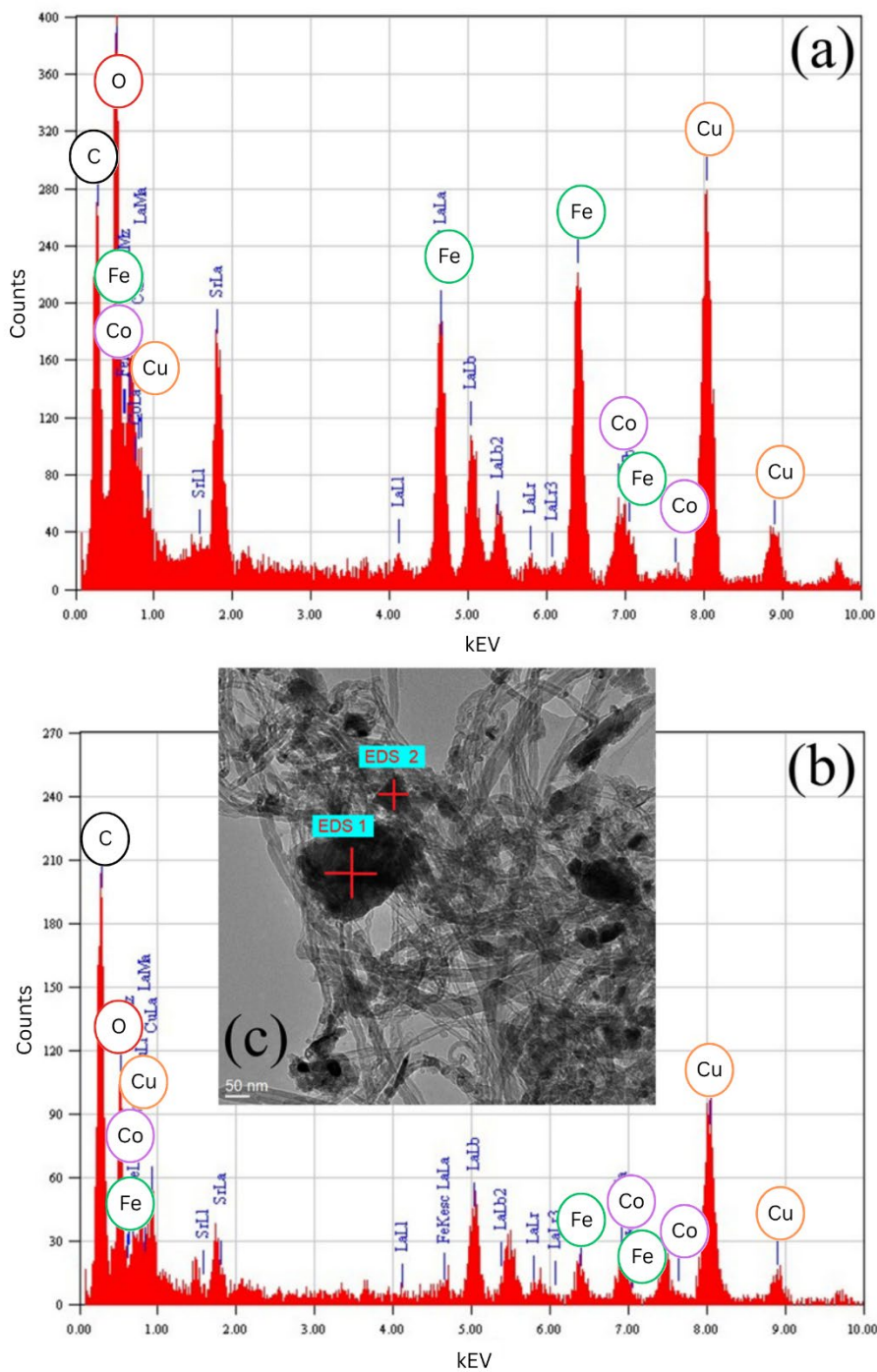


Figure 4.12. TEM-EDS of locations (a) EDS1 and (b) EDS2 as indicated on the TEM micrograph (c) of BR25-CNT75-N sample.

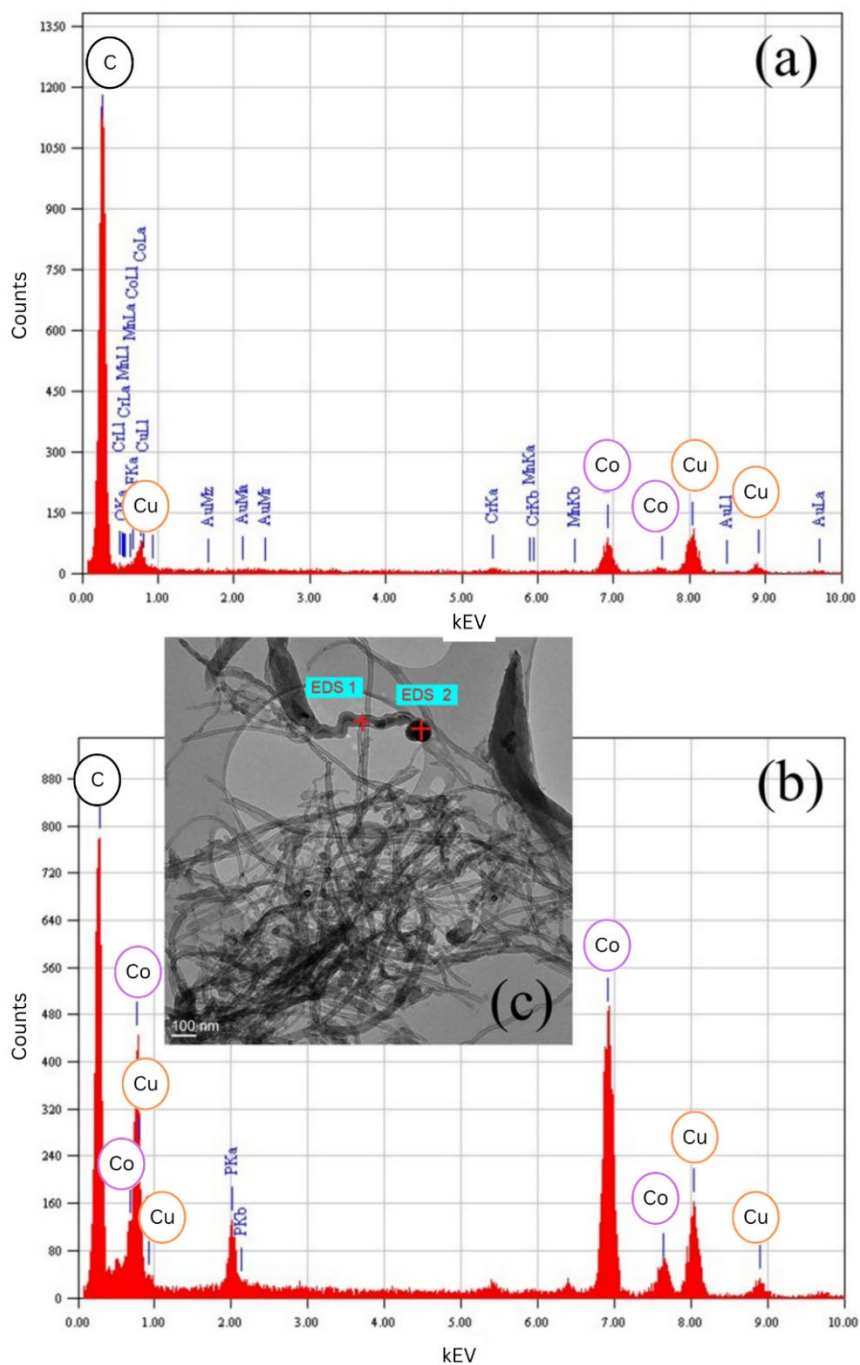


Figure 4.13. TEM-EDS of locations (a) EDS1 and (b) EDS2 as indicated on the TEM micrograph (c) of BR50-CNT50-N sample.

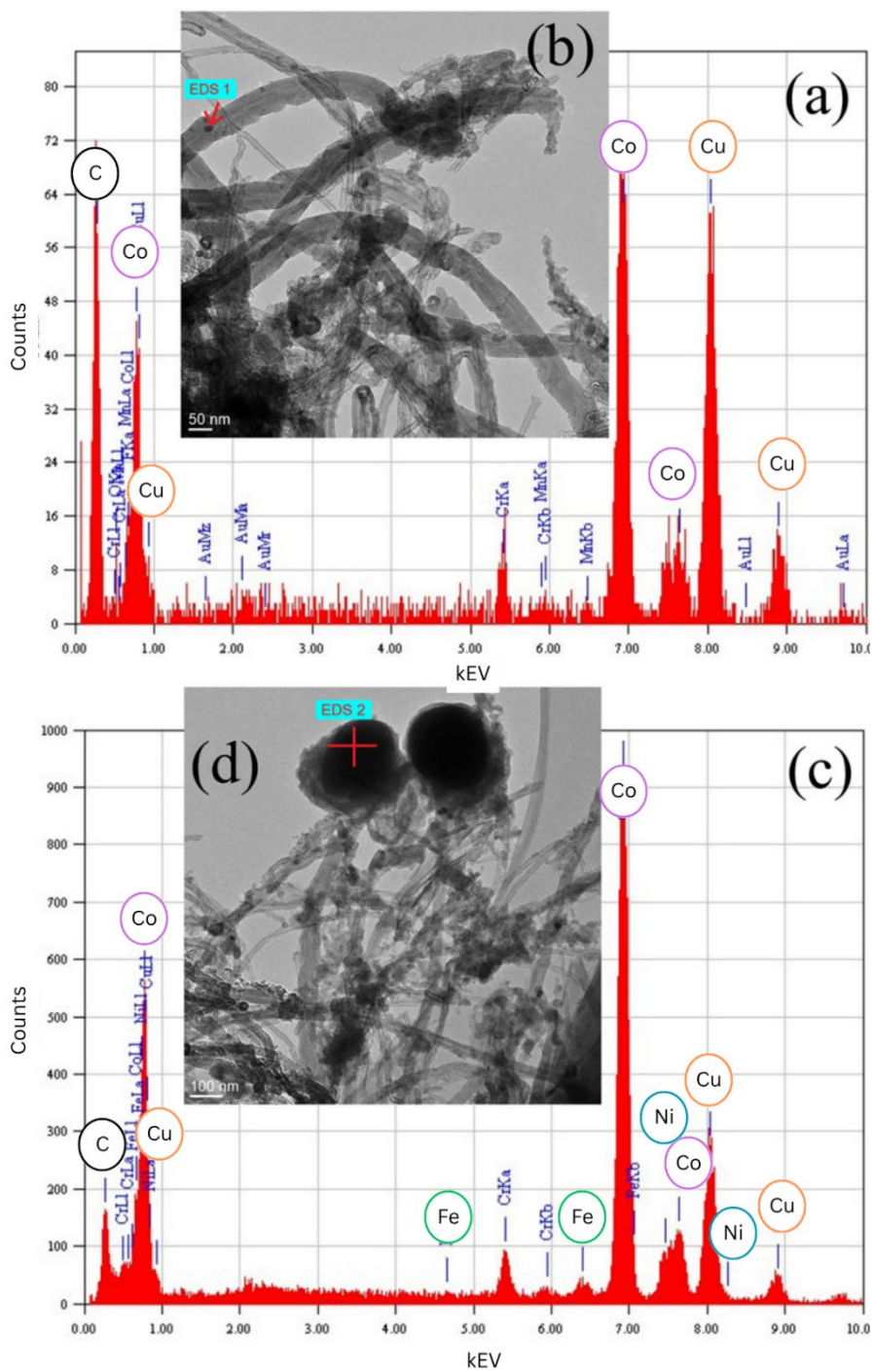


Figure 4.14. TEM-EDS of locations (a) EDS1 as indicated on the TEM micrograph (b); (c) EDS2 as indicated on the TEM micrograph (d) of BR75-CNT25-N sample.

In addition, to characteristic G-band ($\sim 1580\text{ cm}^{-1}$) and D-band ($\sim 1350\text{ cm}^{-1}$) typically observed in Raman spectra of carbon materials, the G'-band at 2700 cm^{-1} is seen (Figure 4.15a), which is an overtone of D-band. Furthermore, a shoulder for G-band at 1620 cm^{-1} associated with D'-band and broad combination mode of D+D' band at around 2950 cm^{-1} are also present. Chemical purification step of CNTs usually leads to defects, therefore the I_D/I_G ratio increases, while the following heat-treatment and modification steps partially restore the structural order and the I_D/I_G ratio decreases [143]. CNT had I_D/I_G ratio of 0.89, while for *CNT-N* it was 0.67, indication improved structural ordering. Nitrogen doping results in slight downshifts of G and D'-bands from 1580 cm^{-1} to 1575 cm^{-1} and from 1620 cm^{-1} to 1615 cm^{-1} , respectively. The degree of graphitisation was slightly higher in materials with greater *RM1* content, while no significant shifts in Raman peak positions were observed among the *RM1/CNT* composites. When compared to the *HT-Bat-res-BM-N* material, the composites exhibited a higher I_D/I_G ratio, indicating a more defect-rich structure, which is attributed to the CNT incorporation, with higher CNT content further contributing to the formation of structural defects.

The SSA of the composite materials showed a notable increase compared to the Raw Material 1. Among the composites, the SSA exhibited a positive correlation with CNT content, as detailed in Table 4.7. Similar trend was observed for the pore size distribution (PSD, Figure 4.15b), which shows that the materials containing higher concentration of CNT had gradually increasing mesoporosity, especially on the 10 nm pore size range. Overall, the pore sizes were similar to all composites with differences only in the concentration of the pores. The SSA of *BR50-CNT50-N* and *HT-Bat-res-BM-N* (discussed in Section 4.2 and paper [I]) are comparable, at $42.1\text{ m}^2\text{ g}^{-1}$ and $46.8\text{ m}^2\text{ g}^{-1}$, respectively. In contrast, the *CNT-N* sample exhibited the highest SSA, reaching $63.2\text{ m}^2\text{ g}^{-1}$. The CNT before nitrogen doping had a SSA of $92.6\text{ m}^2\text{ g}^{-1}$, showing that the nitrogen doping can reduce the SSA by increasing the material density, blocking of the pores or due to graphitisation at high temperatures. While *BR50-CNT50-N* and *HT-Bat-res-BM-N* show similar SSA values, the incorporation of CNTs in the *BR50-CNT50-N* plays an important role as spacers between graphitic layers, which improves structural integrity [202]. Furthermore, SEM-EDS mapping revealed that Co integration was more pronounced in the CNT-containing composites than in *HT-Bat-res-BM-N*. This higher metal content can also reduce the overall SSA in composites [115].

Table 4.7. BET specific surface areas for the Raw material 1, CNT, CNT-N, and RM1/CNT composites.

Name of the sample	Raw material 1	CNT	CNT-N	BR25-CNT75-N	BR50-CNT50-N	BR75-CNT25-N
S_{BET} (m^2/g)	2.9	92.6	63.2	52.9	42.1	27.1

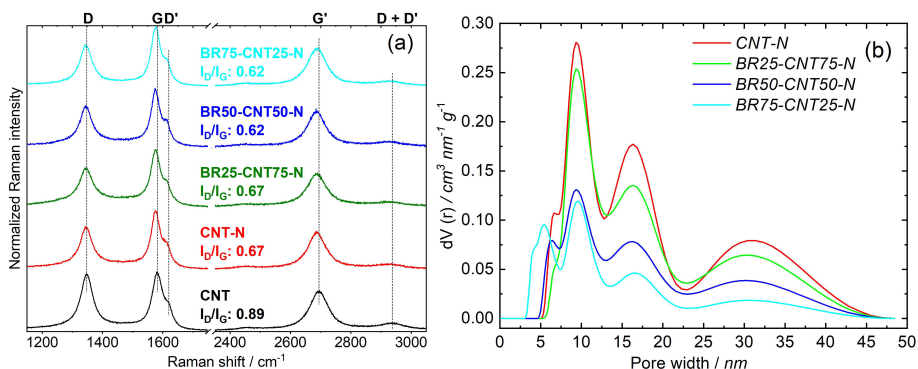


Figure 4.15. (a) Raman spectra and (b) N_2 adsorption-desorption isotherms of RM1/CNT composites and CNT-N.

The XPS analysis was used for the study of chemical composition of the materials (Figure 4.16). The fitting of the data was done similarly to section 4.2. Elemental composition derived from XPS is presented in Table 4.8, which shows that the composites contained C, O, N, Co, Mn, Ni, Al and Cu. Analysis of the XPS N 1s spectra (Figure 4.16a) revealed that the predominant nitrogen configuration across all samples was pyridinic-N. The relative distribution of nitrogen species was largely consistent among the materials, with the exception of *BR50-CNT50-N*, which exhibited a slightly higher proportion of graphitic-N and N-oxide, and a lower content of pyrrolic-N compared to the other samples. The N-doping level of materials was quite different. In general, higher SSA and a greater number of defects facilitate enhanced nitrogen incorporation during pyrolysis. However, it is important to note that total nitrogen content does not directly correlate with electrocatalytic performance. Instead, the nature and distribution of specific nitrogen species, particularly pyridinic-N and graphitic-N, are more critical in determining the oxygen reduction and evolution activity of the electrocatalysts [139,159]. Overall, the nitrogen doping levels decreases and oxygen doping level increases when going from *CNT-N* to *BR75-CNT25-N*. Compared to *HT-Bat-res-BM-N*, the CNT-containing composites exhibited higher carbon content and lower oxygen content. Although *BR50-CNT50-N* and *BR75-CNT25-N* had lower total nitrogen content than *HT-Bat-res-BM-N*, the relative distribution of nitrogen species remained comparable, with pyridinic-N being the most abundant in each case. The Co 2p spectra Figure 4.16b, can be solely explained by the presence of Co-N peak. Among the composite materials, *BR50-CNT50-N* exhibited the highest Co content, consistent with results from SEM-EDS and TEM-EDS. Overall, the incorporation of Co-species were higher for the RM1/CNT composite catalysts, while the other metals had lower concentrations compared to the *HT-Bat-res-BM-N*. These findings indicate that a balanced ratio of RM1 and CNTs facilitates a more uniform dispersion of Co species, while higher RM1 content leads to larger agglomerates due to poorer metal distribution. A more homogeneous distribution of Co nanoparticles increases the electrochemically active surface area and is beneficial for enhancing the overall electrocatalytic performance of the material [164].

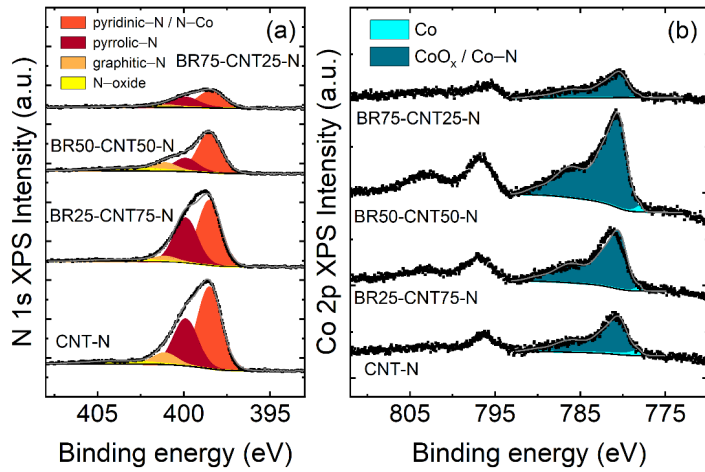


Figure 4.16. X-ray photoelectron spectra (a) N1 s region and (b) Co 2p region of the RM1/CNT composite materials.

Table 4.8. The atomic percentages (at%) of the elements for the RM1/CNT composites and CNT-N with the peak fitting results based on the XPS data.

Element	CNT-N	BR25-CNT75-N	BR50-CNT50-N	BR75-CNT25-N
C - of which	88.0	86.5	87.2	88.7
sp ² C	65 %	61 %	60 %	74 %
sp ³ C/ sp ² C-N	15 %	18 %	20 %	11 %
C-O-C/C-OH/ sp ³ C-N	8 %	7 %	8 %	6 %
C=O	5 %	6 %	4 %	2 %
O-C=O	2 %	3 %	2 %	2 %
$\pi-\pi^*$	5 %	5 %	6 %	6 %
O	3.2	3.9	5.6	6.2
N - of which	8.1	7.8	4.7	2.2
pyridinic-N	55 %	53 %	58 %	54 %
Pyrrolic-N	32 %	37 %	19 %	32 %
Graphitic-N	8 %	5 %	12 %	7 %
N-oxide	5 %	5 %	11 %	7 %
Co	0.3	0.5	0.8	0.2
Mn	-	0.2	0.3	0.3
Al	0.2	0.6	0.8	1.8
Cu	-	0.2	0.3	0.3
Ni	-	0.1	0.1	0.1
Na	0.2	0.2	0.2	0.2

The ORR activity of composite catalysts was tested in 0.1 M KOH solution with Raw Material 1 and CNT-N used for comparison, (Figure 4.17a). The highest $E_{onset} = 0.914$ V vs RHE was demonstrated by the *BR50-CNT50-N*, while others showed lower values as can be seen from Table 4.9. *CNT-N* and Raw Material 1 showed E_{onset} of 0.884 and 0.757 V vs RHE, respectively, demonstrating that the unique structure of composites and nitrogen doping has had positive effect on the onset values. Similarly, the $E_{1/2}$ values for *BR50-CNT50-N* were the highest recording at 0.830 V vs RHE. The ORR polarization curves revealed similar profiles for *CNT-N* and *BR25-CNT75-N*, both of which failed to achieve a distinct diffusion-limited plateau. The N-doped materials in section 4.2 also exhibited similar gradually increasing current density values. In contrast, *BR50-CNT50-N* reached its maximum j value at approximately 0.7 V vs RHE, indicating a more efficient ORR process compared to other composite catalysts and *HT-Bat-res-BM-N*. Out of the composites the *BR75-CNT25-N* showed the lowest ORR activity due to the insufficient amount of CNT spacer which reduced the SSA compared to other composites, as well as higher concentration Al, which is electrocatalytically less active than transition metals like Co, Ni and Fe [121,203]. The influence of CNT addition to the composite conductivity was measured using EIS (details shown in paper [II]). From the fitted and calculated charge transfer values it is possible to conclude that the addition of CNT produces a composite catalyst material which has a much better conductivity than the initial Raw Material 1.

Figure 4.17b presents the E vs n plots for the *RM1/CNT* and *CNT-N* catalyst materials. The polarisation curves at varying rotating speeds and corresponding Koutecky-Levich plots can be seen in paper [II]. The n values for *BR50-CNT50-N* material were around 3.6 over the studied potential range, therefore the oxygen was reduced either *via* direct $4 e^-$ or $2+2 e^-$ mechanism. For the other materials the n values were gradually decreasing at higher potentials which indicates ORR mechanisms which lead to more H_2O_2 formation. This behavior may be influenced by the presence of defects in the carbon matrix, like ether or carboxylic acid sites, which could promote the formation of hydrogen peroxide [204,205]. The enhanced electrocatalytic activity of *BR50-CNT50-N* is attributed to the synergistic formation of catalytically active sites, including pyridinic-N functionalities and transition metal-based active sites derived from Co, Ni, and Mn [148,160].

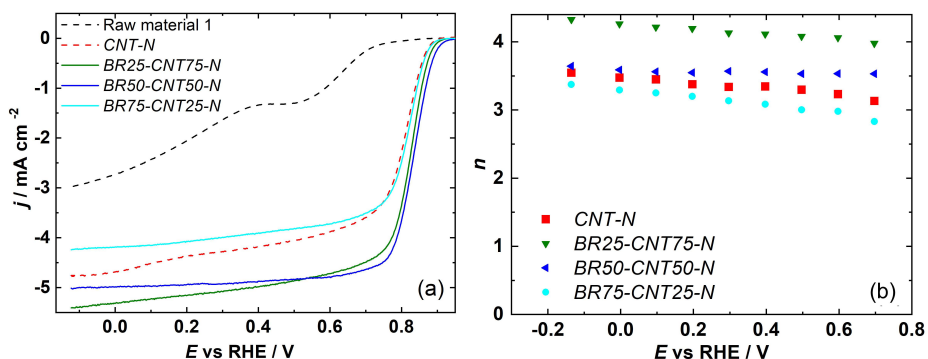


Figure 4.17. Comparative (a) ORR polarisation at 1600 rpm in O_2 saturated 0.1 M KOH solution, and (b) E vs n plot calculated derived from Koutecky-Levich plot for the *RM1/CNT* composites and *CNT-N* materials.

Table 4.9. Electrochemical characteristics of Raw Material 1, CNT-N and their corresponding composite materials.

Catalyst	ORR			OER	ΔE (V)
	E_{onset} (V vs. RHE)	$E_{1/2}$ (V vs. RHE)	j (mA cm ⁻²)	E_{OER} @ 10 mA cm ⁻²	
Raw material 1	0.757	0.342	2.96	1.660	1.318
CNT-N	0.884	0.797	4.76	-	-
BR75-CNT25-N	0.888	0.811	4.23	1.628	0.817
BR50-CNT50-N	0.914	0.830	5.02	1.629	0.799
BR25-CNT75-N	0.898	0.816	5.41	1.643	0.827

The highest electrocatalytic activity towards OER was observed for the *BR50-CNT50-N* catalyst, which exhibited an $E_{OER} = 1.628$ V at 10 mA cm⁻², as presented in Figure 4.18 and Table 4.9. A similar potential was also recorded for *BR75-CNT25-N*, while all other samples displayed higher potentials, indicating lower OER performance. The improved OER activity in the *BR50-CNT50-N* and *BR75-CNT25-N* composites can be attributed to their higher *RM1* content, which provides a greater abundance of transition metals and metal oxides (primarily Co, but also Ni, and Mn). These species are effectively incorporated into the carbon matrix, where they act as additional active sites alongside pyridinic-N functionalities, thus enhancing the OER performance. The encapsulation and integration of Co nanoparticles within the carbon matrix in the composite materials protect the active sites from leaching, thereby enhancing catalyst durability. The Raw Material 1 also demonstrated relatively good OER activity; however, its E_{OER} value was notably higher than that of the composites. This performance is likely due to the presence of metal species in the Raw Material 1, but unlike in the composites, these are not embedded in or stabilised by the carbon lattice. As a result, the metal species in the Raw Material 1 are more susceptible to leaching under harsh electrochemical conditions, leading to reduced stability and catalytic longevity. Furthermore, the lower SSA and absence of N-containing functional groups also contribute to its inferior OER performance.

The bifunctionality parameter ΔE was the lowest for the *BR50-CNT50-N* ($\Delta E = 0.799$ V). This represents a 54 mV improvement compared to the *HT-Bat-res-BM-N* catalyst discussed in the previous section ($\Delta E = 0.853$ V), while having lower loading of the catalyst on the working electrode (0.2 mg cm⁻² vs 0.4 mg cm⁻², respectively). The reduced ΔE value for *BR50-CNT50-N* clearly indicates a more efficient overall oxygen electrocatalytic performance. These results demonstrate that the incorporation of CNTs into the graphite matrix enhances the bifunctional electrocatalytic activity, likely due to improved electronic conductivity, structural stability, and more efficient dispersion of active sites.

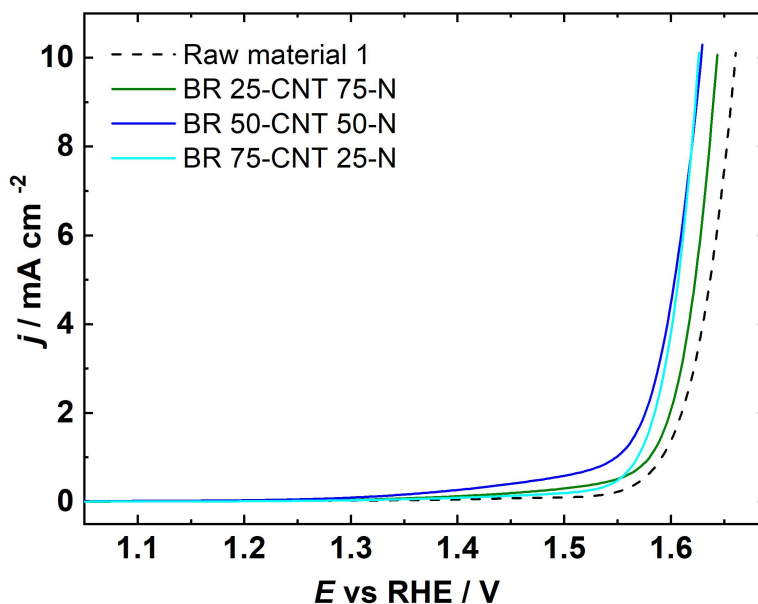


Figure 4.18. OER polarisation curves of Raw Material 1 and the RM1/CNT composite materials at 1600 rpm in N_2 saturated 1 M KOH solution.

4.4 Investigation of transition metal and nitrogen co-doped black mass leach residue and rGO composites for ORR/OER applications

The incorporation of CNTs into N-doped leach residue/CNT composite materials was found to enhance both the electrical conductivity and electrocatalytic activity of the catalysts. However, the improvement in SSA was relatively modest, and it is important to note that CNTs are not derived from LIB waste, thereby limiting the overall sustainability of the material. To address this limitation, study [III] focuses on the use of a more sustainable approach by utilising Raw Material 2, a leach residue with a higher Co content, as described in Section 4.1. In addition, a manually extracted spent graphite from EoL LIBs was employed as the precursor for reduced graphene oxide (rGO) synthesis, which was subsequently combined with Raw Material 2 to form a nitrogen-doped *RM2/rGO* composite catalyst. The primary objective of this work was to enhance the sustainability of the electrocatalyst by increasing the proportion of LIB-derived components, while simultaneously improving the bifunctional oxygen electrocatalytic activity. Detailed procedures for the synthesis and the naming of the *RM2/rGO* catalyst materials are provided in Sections 3.3 and 3.6 and illustrated in Figure 3.1.

XRD diffractograms (Figure 4.19) indicated that in addition to the graphitic carbon (002) plane, a broad peak around 20 to 25° implies that more amorphous carbon species are present. This is indicative of amorphous carbon species and is attributed to the incorporation of rGO into the composites, as it was absent in the materials discussed in earlier sections of this work. Notably, this peak was not visible in the *Comp 75/25* but became apparent after acid treatment in *AT-Comp 75/25*, suggesting that the rGO structure has a greater influence following this process. Furthermore, LiCoO_2 from Raw

Material 2 was successfully reduced into metallic Co(0), with peaks at 44.2°, 51.5°, and 75.8°, demonstrating a successful incorporation of Co(0) species into the composites. When comparing the *Comp*-series catalysts to their *AT-Comp* counterparts, the Co(0) (002) and (001) peaks demonstrate a noticeable decrease in the intensity due to the removal of less stable species during the acid treatment, especially evident comparing *Comp* 75/25 and *AT-Comp* 75/25.

The SEM micrograph in Figure 4.20a for the *Comp* 25/75 show a rough surface with layered structure, characteristic to rGO. The acid treated counterpart *AT-Comp* 25/75 (Figure 28d) showed similar layered structure, but with less heterogeneity on the surface structure. SEM micrographs of *Comp* 50/50 (Figure 4.20b) and *AT-Comp* 50/50 (Figure 28e) have more heterogeneous surface structure. Tubular structures, identified as CNTs, are visible in both samples, suggesting that the Co and Ni nanoparticles present in the system acted as catalysts for CNT formation during the pyrolysis process. Similar structures are observed for the *Comp* 75/25 (Figure 4.20c) and *AT-Comp* 75/25 (Figure 4.21f), although with much less tubular structures. This indicates that for the synthesis of CNT the optimal concentration of Co and Ni was in *Comp* 50/50. SEM-EDS mapping (Table 4.10) identified various elements present in the composites, which include Co, Ni, Mn, Al and Si, with Co being the most abundant metal within the catalysts. In the *Comp*-series the Co content was in relation with the RM2 content within the material, as expected. For the acid treated catalysts, the highest Co content was for the *AT-Comp* 50/50, which is an indication that the Co was encapsulated into the carbon structures within the material, increasing the resistance to leaching. Overall, these results underscore the beneficial role of acid treatment in improving the structural integrity and stability of the electrocatalyst materials.

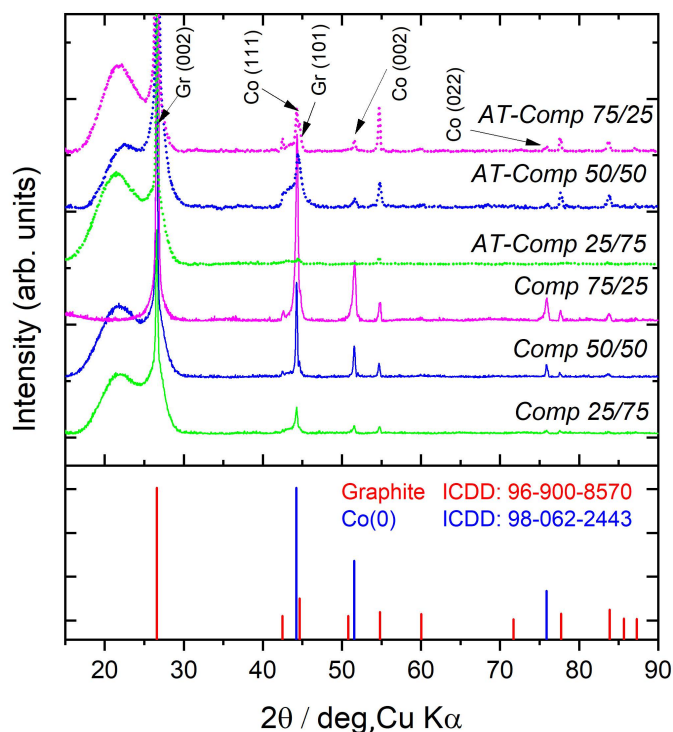


Figure 4.19. XRD diffractogram of RM2/rGO composites.

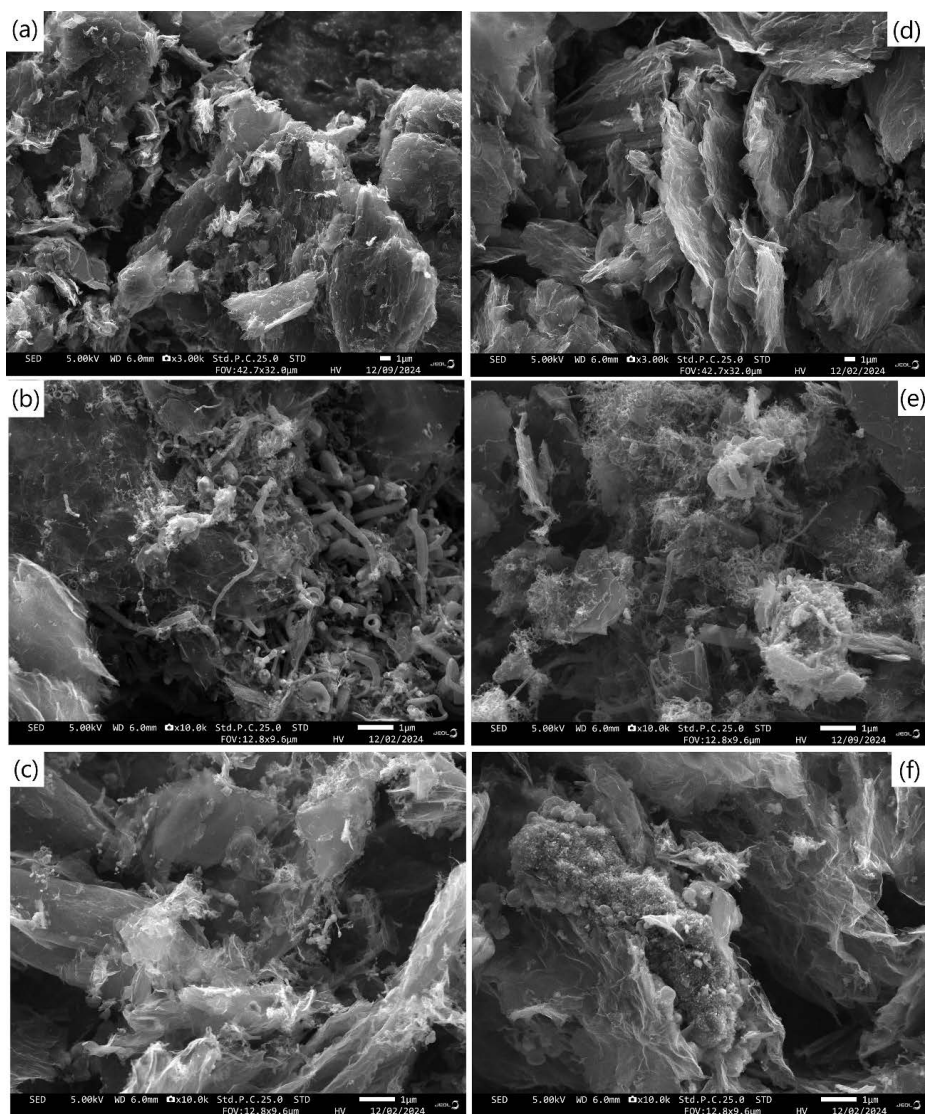


Figure 4.20. SEM micrographs of (a) Comp 25/75, (b) Comp 50/50, (c) Comp 75/25, (d) AT-Comp 25/75, (e) AT-Comp 50/50, and (f) AT-Comp 75/25.

Table 4.10. Elemental compositions RM2/rGO composite materials based on quantitative SEM-EDS mapping (wt%). Elements with concentrations below 0.1 wt% are not shown.

Sample name	Comp 25/75	Comp 50/50	Comp 75/25	AT-Comp 25/75	AT-Comp 50/50	AT-Comp 75/25
C	88.6	87.6	83.9	91.7	90.6	89.1
O	6.8	7.1	4.0	5.3	4.9	7.8
Al	0.2	0.2	0.4	0.1	0.4	0.2
Si	0.2	0.5	0.4	0.3	0.3	0.2
Mn	0.3	0.5	1.4	0.2	0.4	0.4
Co	1.9	2.6	8.2	1.0	2.2	1.0
Ni	0.2	0.2	0.7	0.2	0.2	0.2
F	-	-	-	-	-	-
Na	0.6	0.4	0.2	0.3	0.2	0.3
S	0.2	0.4	0.2	0.5	0.2	0.4

HR-TEM micrographs on Figure 4.21a and 4.21d for the *Comp* 25/75 and *AT-Comp* 25/75, respectively, show rGO sheets with minimal incorporation of other species. Figure 4.21b for *Comp* 50/50 and 4.21e for *AT-Comp* 50/50 show the bamboo carbon nanotubes and other spherical carbonaceous areas.

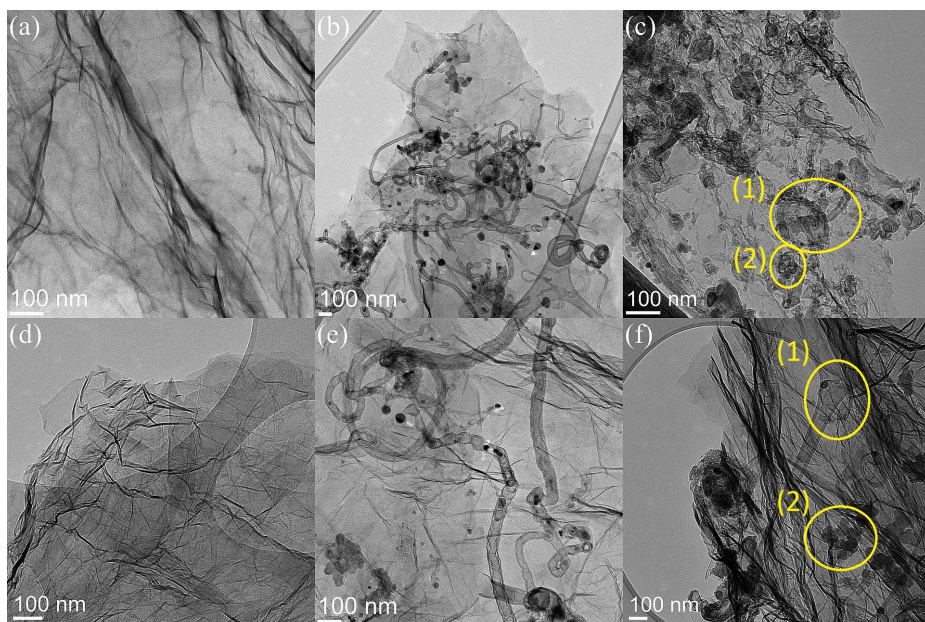


Figure 4.21. TEM micrographs of (a) *Comp* 25/75, (b) *Comp* 50/50, (c) *Comp* 75/25, (d) *AT-Comp* 25/75, (e) *AT-Comp* 50/50, and (f) *AT-Comp* 75/25.

In Figure 4.22 the TEM micrograph with EDS data for *AT-Comp* 50/50 confirms the structure and composition of the composites. EDS 1 identifies a Co nanoparticle positioned at the tip of a bamboo carbon nanotubes, while EDS 2 shows a Co nanoparticle fully encapsulated within a CNT. Additionally, EDS 3 and 4 highlight onion-like spherical carbonaceous regions surrounding Co and Cu particles. Similar structures are seen for the *Comp* 75/25 (Figure 4.21c, locations 1 and 2) and *AT-Comp* 75/25 (Figure 4.21f, locations 1 and 2), though with less CNTs and higher abundance of spherical carbon structures. Both encapsulation methods form the protective shells around Co nanoparticles, therefore making them more resistant to leaching under harsh conditions. Based on the TEM micrographs these structures are missing from the *Comp* 25/75 and *AT-Comp* 25/75. While acid treatment refined the morphology of all treated composites, its impact was most pronounced in *AT-Comp* 75/25, where the removal of less stable species is evident from both TEM micrographs and SEM-EDS analyses. This refinement not only enhances structural uniformity but is also likely to contribute to improved long-term stability in electrocatalytic applications.

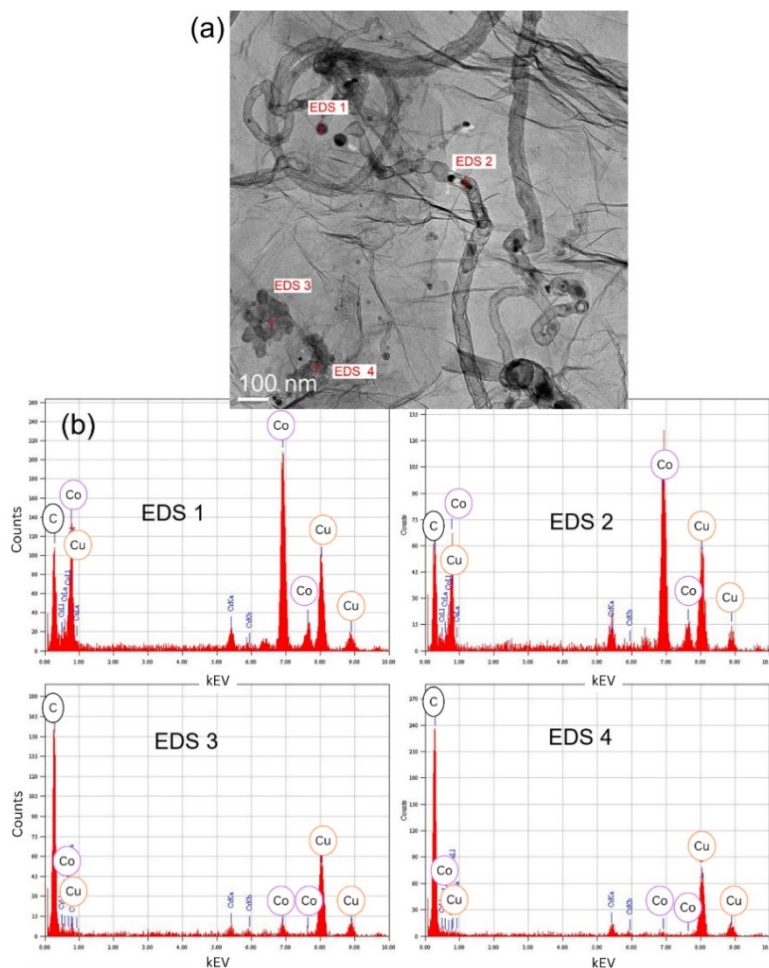


Figure 4.22. HR-TEM (a) micrograph with (b) EDS spectra of selected locations for the *AT-Comp* 50/50.

Raman spectroscopy was employed to assess the structural properties of the Raw Material 2, rGO, and composite materials (Figure 4.23), with particular attention to the effects of rGO incorporation and acid treatment on defect density and graphitic ordering. The Raman spectra of the composite samples exhibit characteristic peaks corresponding to the D-band (1350 cm^{-1}), G-band (1580 cm^{-1}), as well as indications to G' band (2700 cm^{-1}) and D + D' band (2950 cm^{-1}), reflecting various structural irregularities and carbon hybridisations [196]. In rGO and composites the G-band has shifted to a slightly higher wavenumber, indicating to the oxygenation of sp^2 carbons which leads to the formation of sp^3 carbons [206]. The I_D/I_G ratio of Raw Material 2 has lower value compared to the rGO and composites, indicating a higher degree of structural order, common for graphitic structures. The rGO sample, in contrast, displayed a higher I_D/I_G ratio, indicating to a more defect rich structure due to the presence of oxygen containing functional groups introduced during the synthesis of the material. This also contributes to the overall defect density of the composites. The I_D/I_G ratio of acid-treated composites have seen a slight reduction compared to their non-acid treated counterparts, which indicates that some of the structural ordering has been restored during the synthesis processes, by removing of oxygenated groups and non-stable forms of metals [116]. Compared to materials studied in previous sections, the composites exhibited much higher I_D/I_G ratio, due to the incorporation of defect rich rGO. The *HT-Bat-res-BM-N* was composed only graphite as carbon matrix, while the *RM1/CNT* materials were composites of graphite and CNTs as carbon matrix, both of which have higher structural ordering than rGO [196,207].

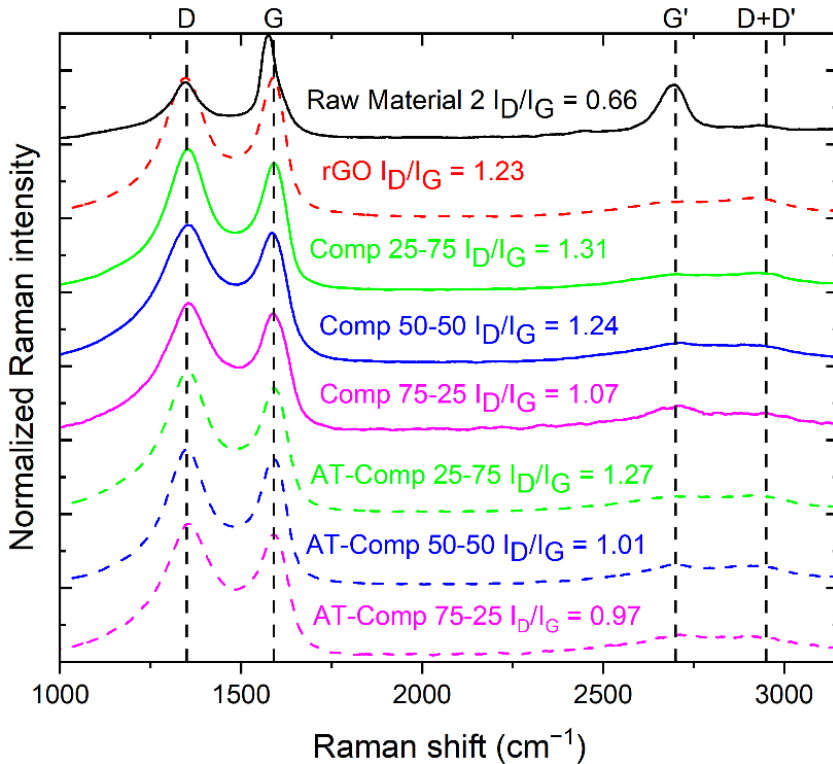


Figure 4.23. Raman analysis of the Raw Material 2, rGO and RM2/rGO composites.

One of the objectives of incorporating the rGO was to increase its SSA and porosity, thereby increasing the ability to host more active sites and improving mass transport properties. Table 4.11 contains the SSA data from the N₂ adsorption-desorption isotherms (Figure 4.24a and 4.24b) of RM2/rGO composites as well as for the Raw Material 2, *N*-RM2, rGO and *N*-rGO. The isotherms show a type IV(a) and II characteristics with H3 type hysteresis loop, indicating to a presence of meso- and macroporous structures (PSD data on Figure 4.24c and 4.24d) composed of finer mesopores and slit-like pores, which have been formed from layered structures and plate-like particles [202]. *N*-RM2 and *Comp* 75/25 display type II isotherms, which suggests that these materials are primarily macroporous. Across the composite series, an increase in rGO content led to a corresponding increase in SSA, which was further enhanced by acid treatment. The post acid-treatment increase is attributed to the unbonded metal species, which opens additional surface area and pore volume. The difference between the DFT and BET surface areas suggest that the adsorption of N₂ occurs in meso- and macropores rather than micropores. Moreover, PSD data indicate an increase in the volume of smaller mesopores in the *AT-Comp* series compared to their *Comp*-series counterparts. In addition, the increase in SSA and volume of smaller mesopores indicates to the pore opening without the degradation of the pores, thereby preserving the structural integrity of the material [110]. Compared to the materials discussed in previous sections, the RM2/rGO composites demonstrate significantly higher SSA, primarily due to the inherently higher SSA of rGO used as one of the carbon precursors. Furthermore, this incorporation notably shifted the pore size distribution toward smaller mesopores (4–13 nm), whereas RM1/CNT composites exhibited most mesopores in the 10–20 nm range. This refinement in pore structure contributes to a more well-defined porous network that facilitates efficient mass transport of reactant gases to active sites. Additionally, as discussed previously, higher surface area enables the incorporation of a greater number of catalytically active sites, which is expected to enhance the overall electrocatalytic activity of the materials.

Table 4.11. BET and DFT specific surface areas for Raw material 2, *N*-RM2, rGO, *N*-rGO and RM2/rGO composites.

Sample name	S _{BET} (m ² /g)	S _{DFT} (m ² /g)
Raw Material 2	1.9	2.7
<i>N</i> -RM2	51.3	37.9
rGO	280.5	239.8
<i>N</i> -rGO	211.7	188.5
<i>Comp</i> 25/75	149	126.5
<i>Comp</i> 50/50	77.7	64.5
<i>Comp</i> 75/25	63.5	52.9
<i>AT-Comp</i> 25/75	183.3	156
<i>AT-Comp</i> 50/50	124.6	105.6
<i>AT-Comp</i> 75/25	90.1	75.0

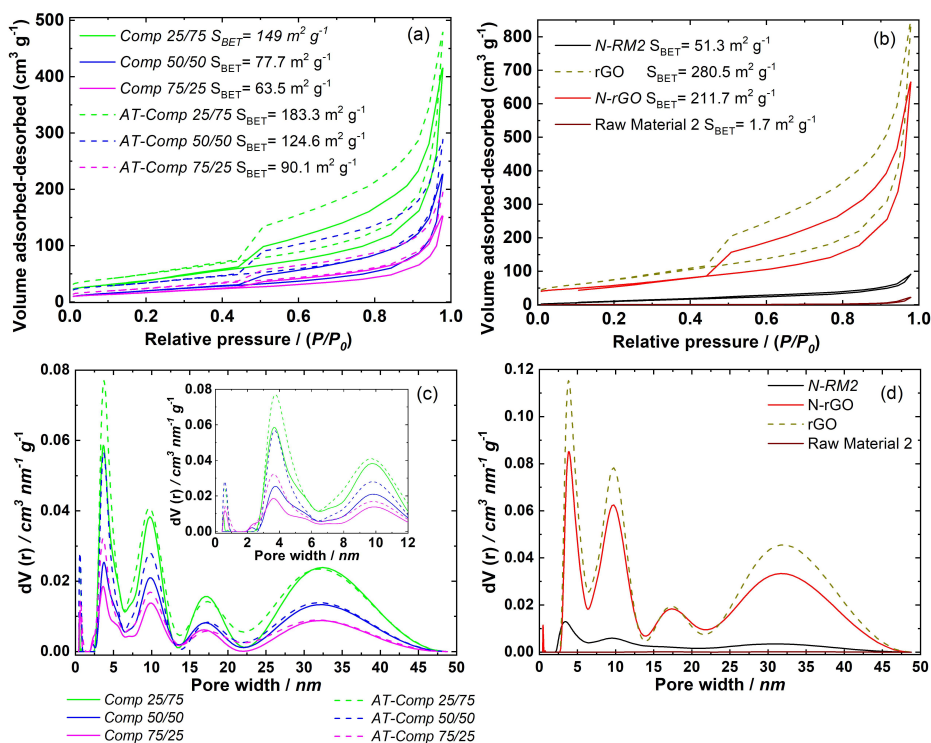


Figure 4.24. N_2 adsorption-desorption isotherms for the (a) RM2/rGO composites, (b) Raw Material 2, N-RM2, rGO and N-rGO; Pore size distribution data for the (c) RM2/rGO composites, (d) Raw Material 2, N-RM2, rGO and N-rGO.

Figure 4.25 presents the XPS spectra of C 1s, N 1s and Co 2p region. The C 1s spectra (Figure 4.25a), upon deconvolution, reveal the presence of various carbon bonding environments, with the sp^2 -hybridised carbon contributing the dominant peak, indicating a high degree of graphitic character in the composites. According to the fitting of N 1s spectra (Figure 4.25b), the majority of N is in pyridinic form for all the composites, consistent with the trends observed for *HT-Bat-res-BM-N* and *BR50-CNT50-N*, which were previously identified as the most active bifunctional electrocatalysts in their respective studies. There were much larger differences in the doping level of N, probably due to the addition of defect rich and higher SSA rGO, where nitrogen species can incorporate. For the *Comp*-series catalysts, the at% of N increases relative to the increase of rGO in the composites, a trend that correlates with the increase in SSA, providing more sites for nitrogen incorporation. For the *AT-Comp* series the doping level decreased for all the composites due to the removal of less stable N-species, with the *AT-Comp 50/50* having the smallest decrease. This enhanced stability is likely due to the encapsulated Co-species which change the electronic structure of surrounding carbon matrix and thereby mitigating the removal of N-species. The *BR50-CNT50-N* catalyst exhibited 4.7 at% nitrogen, which is comparable to the levels observed across the *AT-Comp* series. As observed in previous analyses (Sections 4.2 and 4.3 and papers [I] and [II]), Co was identified in two chemical states: metallic Co(0) and Co–N coordination species (Figure 4.25c). The relative proportions of these states varied across the samples, with Co(0)

comprising 25–44% of the total cobalt content. Acid treatment generally reduced the proportion of Co(0), with the most significant decrease observed for *AT-Comp 75/25*. Compared to samples studied in previous sections the *RM2/rGO* composites had higher Co(0) content, which has increased probably due to the encapsulation and better distribution of metallic species in the smaller mesopores provided by the *RM2/rGO* composites. Detailed peak fitting results for the C 1s, N 1s, and Co 2p spectra and at% of the elements found in the composites are summarised in Table 4.12.

Table 4.12. Elemental composition (at%) of *RM2/rGO* composite samples measured with XPS, including peak fitting results.

Element	Comp 25/75	Comp 50/50	Comp 75/25	AT-Comp 25/75	AT-Comp 50/50	AT-Comp 75/25
C - of which	86.8	86.0	86.9	89.2	88.1	89.9
sp ² C	62 %	58 %	62 %	56 %	57 %	60 %
sp ³ C / sp ² C-N	12 %	20 %	17 %	21 %	17 %	19 %
C-O-C / C-OH / sp ³ C-N	15 %	13 %	9 %	12 %	17 %	11 %
C=O	5 %	3 %	4 %	4 %	4 %	3 %
O-C=O	1 %	2 %	2 %	3 %	2 %	2 %
π - π *	5 %	4 %	6 %	4 %	3 %	5 %
O	5.0	5.7	4.9	5.0	5.7	4.2
N - of which	7.2	6.4	6.2	5.0	5.4	4.8
Pyridinic-N	59 %	55 %	55 %	52 %	53 %	52 %
Pyrrolic-N	20 %	18 %	20 %	21 %	19 %	19 %
Graphitic-N	11 %	13 %	11 %	13 %	14 %	14 %
N-oxide	10 %	14 %	14 %	14 %	14 %	15 %
Co - of which	0.3	0.3	0.2	0.3	0.3	0.2
Co(0)	28 %	35 %	44 %	25 %	33 %	32 %
Co-N / CoO _x	72 %	65 %	56 %	75 %	67 %	68 %
Mn	0.2	0.4	0.7	0.2	0.2	0.5
Al	-	-	0.3	-	-	-
Cu	-	0.1	0.1	-	-	-
Ni	0.1	0.1	0.2	0.1	0.1	0.2
Si	0.1	0.7	0.2	0.1	0.1	0.1
F	-	0.1	0.1	-	-	-
Na	0.3	0.2	0.2	0.1	0.1	0.1

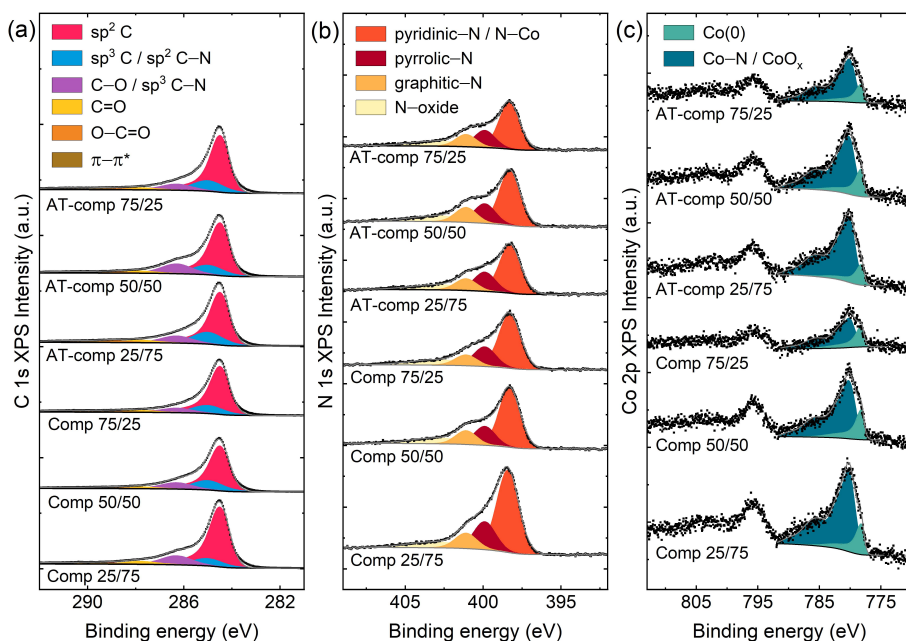


Figure 4.25. XPS spectra of the RM2/rGO composite samples a) C 1s region, b) N 1s region and c) Co 2p region.

The initial electrochemical characterisation was done using RDE method towards the ORR in O₂ saturated 0.1 M KOH solution (Figure 4.26a). As a baseline comparison, the performance of *N*-RM2 and *N*-rGO was first evaluated. *N*-RM2 exhibited the lowest activity towards the ORR with $E_{onset} = 0.852$ V vs. RHE and $E_{1/2} = 0.727$ V vs. RHE, while the addition of rGO increased all performance metrics significantly as can be seen from table 4.13. *N*-RM2 lower ORR catalytic ability comes from the lower surface area than all other catalysts, which restrict the number of active sites as well as hinders the mass transport efficiency. Conversely, *N*-rGO, with its higher SSA and enhanced porosity, provided a larger number of accessible active sites, leading to improved ORR activity, with E_{onset} of 0.897 V vs. RHE and $E_{1/2}$ of 0.780 V vs. RHE. Out of the composites studied in this section, the *AT-Comp* 50/50 had the best ORR activity with the E_{onset} of 0.912 V vs. RHE and an $E_{1/2}$ of 0.820 V vs. RHE, accompanied by a limiting current density of 4.63 mA cm⁻². The non-acid treated counterpart had slightly lower ORR activity with E_{onset} of 0.895 V vs. RHE, $E_{1/2}$ of 0.792 V vs. RHE and $j = 4.45$ mA cm⁻², which demonstrates the beneficial effect of acid treatment for this catalyst. Polarisation curves at different rotating speeds and Koutecky-Levich plots of RM2/rGO composites can be found from the supporting info of paper [III]. The value of n (Table 4.13) for all RM2/rGO composites were in between 3.2 and 3.9 which indicates that the ORR mechanism is 2+2 e⁻ with some formation of H₂O₂, which is undesirable for efficient ORR performance. *Comp* 25/75, *AT-Comp* 25/75, *Comp* 75/25 and *AT-Comp* 75/25 had very similar E_{onset} and $E_{1/2}$ values, although the limiting current density varied. Regarding the N- and Co-doped carbon materials ORR activity, the pyridinic-N and Co-N coordination sites are considered as the most effective active sites. As per XPS, the ratio of N-species was similar to all composites, while the doping level varied. In the *AT-Comp* series catalysts, the *AT-Comp* 50/50 retained the most nitrogen while also containing the most Co and Co-N sites.

According to TEM (Figure 4.21) and SEM (Figure 4.20) micrographs this catalyst contained the most bamboo carbon nanotubes and onion-like carbon species, which encapsulated the metal nanoparticles, thereby enhancing the stability of active sites. This structural stability translated into the highest ORR electrocatalytic performance. In contrast, *Comp* 25/75 showed a reduction in ORR activity after acid treatment, likely due to the loss of unprotected metal and nitrogen species, as the active sites were not sufficiently encapsulated. On the other hand, *Comp* 75/25 exhibited improved ORR performance following acid treatment, which can be attributed to the removal of excess, non-contributing metal species and the presence of partially encapsulated Co, which provided some protection against leaching and degradation of the active sites.

To demonstrate the catalyst materials bifunctional abilities towards oxygen reactions, the OER was also studied in N_2 saturated 1 M KOH solution (Figure 4.26b). E_{OER} (V) @ 10 $mA\ cm^{-2}$ served as the primary metric. As can be seen from the Table 4.13, the *Comp*-series catalysts had better OER activity compared to their *AT-Comp* counterparts. Among the *Comp*-series catalysts, the *Comp* 50/50 achieved $E_{OER} = 1.621$ V vs RHE, slightly better than *Comp* 75/25 ($E_{OER} = 1.624$ V vs RHE) and *Comp* 25/75 ($E_{OER} = 1.631$ V vs RHE). Within the *AT-Comp* series, *AT-Comp* 75/25 had the lowest $E_{OER} = 1.632$ V vs RHE. *AT-Comp* 50/50 and *AT-Comp* 25/75 also performed well, with $E_{OER} = 1.639$ V vs RHE and $E_{OER} = 1.634$ V vs RHE, respectively. It is well established that the dominant active sites for OER are transition metals and metal oxides, particularly in combination with better porosity and higher SSA to host active sites. As described before, the *Comp*-series catalysts had greater concentration of transition metal sites in them, therefore increasing their OER activity, while within the *AT-Comp* some of the metal species were leached out, slightly diminishing the OER activity. Specifically, the superior OER activity of *Comp* 50/50 can be attributed to the presence of Co and Mn species, some of which were partially removed in *AT-Comp* 50/50. Furthermore, a portion of the metal species in both series may be encapsulated within graphitic or carbon shell structures, reducing their accessibility and availability for catalysing the OER. Despite this, the overall OER activity of the composite catalysts remained significantly better than that of the individual *N-RM2* and *N-rGO* materials. This underscores the importance of metal incorporation and the formation of synergistic nitrogen–metal active sites within the composite structures.

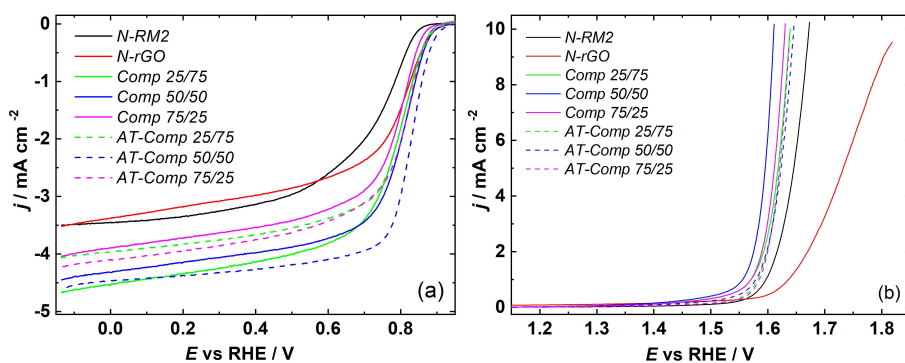


Figure 4.26. (a) ORR polarisation curves at 1600 rpm in O_2 saturated 0.1 M KOH solution, (b) OER curves at 1600 rpm in N_2 saturated 1 M KOH solution for the *N-RM2*, *N-rGO* and *RM2/rGO* composites.

Table 4.13. Electrochemical properties for RM2/rGO composite catalysts, N-RM2 and N-rGO.

Catalyst	ORR				OER	ΔE
	E_{onset} (V vs. RHE)	$E_{1/2}$ (V vs. RHE)	j (mA cm ⁻²)	n	E_{OER} (V) @ 10 mA cm ⁻²	
N-RM2	0.852	0.727	4.25	-	1.674	0.885
N-rGO	0.897	0.780	3.52	-	-	-
Comp 25/75	0.887	0.777	4.67	3.6	1.631	0.853
Comp 50/50	0.895	0.792	4.45	3.9	1.621	0.828
Comp 75/25	0.875	0.777	4.05	3.4	1.624	0.846
AT-Comp 25/75	0.895	0.790	4.06	3.2	1.634	0.842
AT-Comp 50/50	0.912	0.820	4.63	3.6	1.639	0.818
AT-Comp 75/25	0.887	0.797	4.22	3.5	1.632	0.834

The bifunctionality parameter ΔE value for these materials was the lowest for the AT-Comp 50/50 $\Delta E=0.818$ V, indicating the best overall bifunctional electrocatalytic performance out of the RM2/rGO materials. While the performance is slightly lower compared to the BR50-CNT50-N ($\Delta E = 0.799$ V) material discussed in the previous section, the substitution of CNTs with battery-derived rGO offers a more sustainable alternative, thereby aligning this approach with the principles of circular economy and resource efficiency. Table 4.14 compares the catalyst materials developed in this thesis with the best-performing SLIB-derived catalysts reported in the literature, as previously discussed in Section 1.4.2. While direct comparisons are affected by differences in catalyst loading, catalytic activity values nonetheless provide a useful benchmark for performance comparison. The monofunctional ORR catalysts reported in the literature do not always outperform the bifunctional oxygen electrocatalysts developed in this thesis. For instance, the best-performing ORR catalyst, Co@NG-800, achieved an $E_{1/2}$ of 0.880 V vs RHE, whereas BR50-CNT50-N from this work exhibited an $E_{1/2}$ of 0.830 V vs RHE—only a difference of 50 mV—despite BR50-CNT50-N being tested with a lower catalyst loading. In the case of OER performance, the top-performing SLIB-derived material, r-Co(OH)₂, exhibited an E_{OER} of 1.361 V vs RHE, but this was achieved using an unusually high catalyst loading of 15 mg cm⁻², far above the typical 0.2–0.5 mg cm⁻² used in most electrochemical studies. Furthermore, r-Co(OH)₂ was synthesised from manually extracted cathode material (LiCoO₂), a valuable resource typically prioritised for reuse in new LIB production—posing limitations to its industrial scalability and sustainability. Most reported SLIB-derived catalysts, particularly for OER, are based on cathode active materials. Their use on larger scale could potentially compete with LIB recyclers, particularly for high-value metals like cobalt and lithium. In contrast, the materials developed in this thesis utilise the graphite-rich leach residue—an industrial waste byproduct of hydrometallurgical LIB recycling that is otherwise discarded. While the bifunctional activity of these materials is

somewhat lower than that of the best-performing literature example (N/NMCO, $\Delta E = 0.705$ V), our approach offers a more sustainable and circular solution by valorising a waste stream rather than consuming critical raw materials. The catalyst materials which demonstrated the best catalytic activity in each of the studies were chosen to further evaluate in the practical zinc-air battery applications.

Table 4.14. The electrochemical characteristics of ORR, OER and bifunctional oxygen electrocatalysts based on EoL LIBs reported in the literature.

Catalyst material	Catalyst loading (mg cm ⁻²)	ORR $E_{1/2}$ (V vs RHE)	E_{OER} (V vs RHE @ $j = 10$ mA cm ⁻²)	ΔE (V)	Reference
HT-Bat-res-BM-N	0.4	0.795	1.648	0.853	This work
BR25-CNT75-N	0.2	0.811	1.628	0.817	This work
BR50-CNT50-N	0.2	0.830	1.629	0.799	This work
AT-Comp 50/50	0.4	0.820	1.632	0.818	This work
NG-Bat	0.4	~0.710	-	-	[58]
N-Co/rGO-AT	0.4	0.860	-	-	[117]
Co ₃ O ₄ /rGO	0.5	0.865	-	-	[183]
Co@NG-800	0.5	0.880	-	-	[184]
LNCM-G/CC	-	-	1.550	-	[187]
G-PANI-Fe	0.5	0.800	-	-	[181]
ND-rGO	-	0.810	-	-	[182]
Co ₉ S ₈ /Co ₃ O ₄	1.0	-	1.504	-	[185]
M-CoO	0.255	-	1.569	-	[186]
NCMB-2	-	-	1.482	-	[188]
r-Co(OH) ₂	~15	-	1.361	-	[189]
Co@NCW-4	0.2 (ORR) / 0.4 (OER)	0.823	1.580	0.757	[190]
RCA-30	~0.3	0.740	1.610	0.870	[191]
N/NMCO	0.35 (ORR) / 2.1 (OER)	0.810	1.515	0.705	[192]
Ni-Co-Mn oxides	0.4	0.740	1.597	0.857	[208]
Bat-N-rGO	0.4	0.849	1.666	0.812	[57]
NG7	0.25	0.840	1.640	0.800	[193]

4.5 Black mass leach residue derived oxygen electrocatalysts for zinc-air battery applications

To evaluate the practical applicability of the catalyst materials developed in this thesis [I–III], they were employed as air electrode catalysts in zinc–air batteries. This allowed for direct assessment of their bifunctional oxygen electrocatalytic performance under realistic device conditions. For benchmarking purposes, a commercial catalyst composed of 20 wt% PtRu/C was used as a reference air electrode material. While the half-cell reactions will offer a valuable insight into the catalyst materials performance towards ORR and OER, their performance in practical application might not be completely inter-changeable. Figure 4.27 shows the OCP values for the catalyst materials studied in this thesis. OCP is an indicator of ORR activity under equilibrium conditions, whereas the ideal OCP value for ZABs is approximately 1.65 V, representing the theoretical cell voltage. In practical systems, however, lower OCP values are typically observed due to overpotentials and kinetic losses. The catalysts with poor ORR activity generally exhibit an OCP value under 1.4 V [61]. The *RM2/rGO* composite catalysts maintained an average OCP values exceeding 1.45 V (except for *Comp 75/25*) for at least 1800 s, while the materials studied in [I] and [II] had OCP value in between 1.40 V and 1.42 V. This shows an improved ORR activity of *RM2/rGO* composite catalyst materials, even though they did not outperform the *RM1/CNT* composites in ORR half-cell reactions.

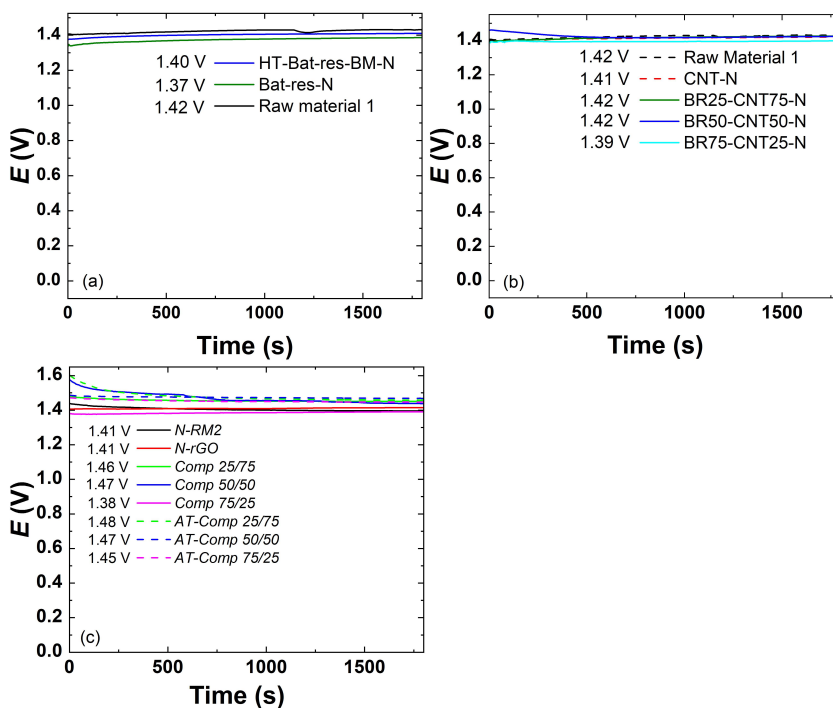


Figure 4.27. OCP values for (a) HT-Bat-res-BM-N, Bat-res-N and Raw Material 1, (b) RM1/CNT composites and CNT-N, and (c) RM2/rGO composites, N-RM2 and N-rGO catalysts. The numerical values given are an average value of 1800 s.

The charge and discharge polarisation curves were recorded to further assess the bifunctional performance of the catalyst materials (Figure 4.28). While the charge polarisation curves exhibited relatively small differences among catalysts studied, more pronounced variations were observed in the discharge polarisation curves. On Figure 4.28a, the *HT-Bat-res-BM-N* exhibited the highest potential values from discharge polarisation curves, showing superior ORR activity over other studied materials. On Figure 4.28b for the CNT composite materials similar discharge polarisation curve values were shown for *BR50-CNT50-N*, *BR25-CNT75-N* and for *CNT-N*, while in charge polarisation curves the *BR50-CNT50-N* and *BR75-CNT25-N* demonstrated the best values. Finally, for the *RM2/rGO* (Figure 4.28c) composite catalysts the best polarisation curve values were shown by the *AT-Comp 50/50* catalyst material. Overall, these results are consistent half-cell reactions (results presented in Tables 4.6, 4.9, 4.13 and 4.14), where the same catalyst materials exhibited the highest electrocatalytic activity.

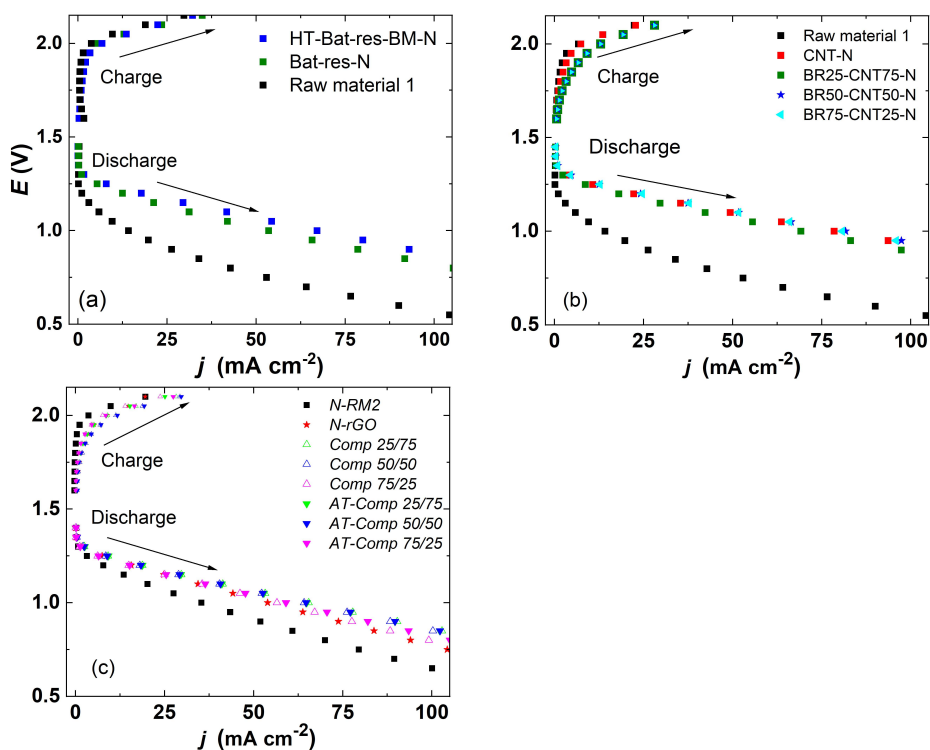


Figure 4.28. ZAB charge and discharge polarisation curves for (a) *HT-Bat-res-BM-N*, *Bat-res-N* and Raw Material 1, (b) *RM1/CNT* composites and *CNT-N*, and (c) *RM2/rGO* composites, *N-RM2* and *N-rGO* catalysts.

One of the key indicators of ZAB efficiency is the power density (Pd) generated by the assembled ZAB. For benchmarking purposes, ZABs assembled with commercially available 20% PtRu/C catalysts were used for comparison. In the first study [I] (Figure 4.29a), the battery-derived catalyst *HT-Bat-res-BM-N* achieved a maximum Pd of 104 mW cm^{-2} , surpassing the 95 mW cm^{-2} obtained with the 20% PtRu/C benchmark. In the second study [II] (Figure 4.29b), the highest Pd was recorded for *BR50-CNT50-N*

(97 mW cm⁻²), closely followed by *BR25-CNT75-N* and *CNT-N*, whereas *BR75-CNT25-N* exhibited lower power output. These results highlight the importance of porosity and with the optimal *RM1* to CNT ratio being at 50:50 wt%. Nonetheless, all composites exceeded the maximum *Pd* of 20% PtRu/C material which achieved *Pd* of 70 mW cm⁻². Similarly, in the third study [III] (Figure 4.29c), all composites composed of *RM2* and rGO exceeded the benchmark catalyst, with *Comp 25/75*, *AT-Comp 25/75*, and *AT-Comp 50/50* each achieving *Pd* values of 100 mW cm⁻². *Comp 75/25* and *AT-Comp 75/25* showed slightly lower performance. Acid treatment had a beneficial effect for composites with higher *RM2* content (*Comp 75/25* and *Comp 50/50*), likely due to the removal of inactive species that otherwise blocked access to the catalytic sites. In contrast, the structure of *Comp 25/75* remained largely unchanged after acid treatment, which aligns with the negligible change in its *Pd*. When comparing the maximum *Pd* values across the three studies, the variations are relatively modest: *HT-Bat-res-BM-N* (104 mW cm⁻²), *BR50-CNT50-N* (97 mW cm⁻²), and *Comp 25/75*, *AT-Comp 25/75* and *AT-Comp 50/50* (100 mW cm⁻²).

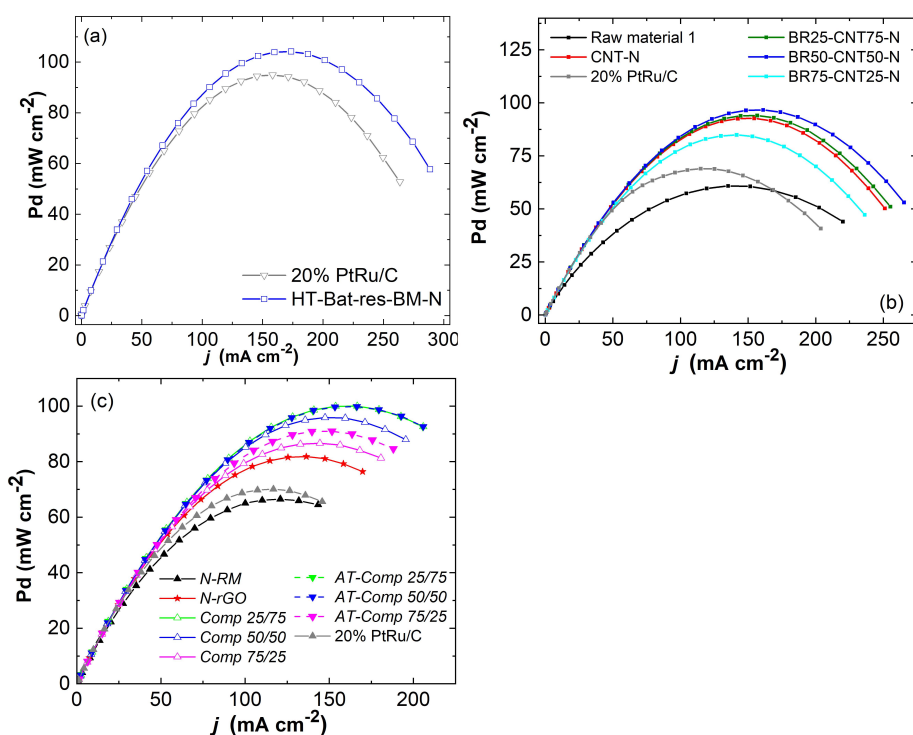


Figure 4.29. ZAB power density values for (a) *HT-Bat-res-BM-N* and 20% PtRu/C (b) *RM1/CNT* composites, *CNT-N*, and 20% PtRu/C, and (c) *RM2/rGO* composites, *N-RM2*, *N-rGO*, and 20% PtRu/C catalysts.

However, direct comparisons of absolute *Pd* values can be misleading due to variations in experimental setup. To allow for more meaningful comparison, the relative improvement over the commercial catalyst (20% PtRu/C) was calculated for each study. This normalisation revealed that *Comp 25/75*, *AT-Comp 25/75*, and *AT-Comp 50/50*

outperformed the commercial benchmark by 43%, *BR50-CNT50-N* by 38.5%, and *HT-Bat-res-BM-N* by 9.5%. These findings indicate that the *RM2/rGO* composites are the most effective bifunctional electrocatalysts among the materials studied in this thesis. Table 4.15 summarises the performance data of LIB-derived ZAB catalysts reported in the literature and those developed in this work. Relative improvement over the commercial catalyst was used to account for differences in testing conditions, providing a more consistent basis for comparison. When benchmarked against other SLIB-derived bifunctional oxygen catalysts—such as N/NMCO [192], Bat-N-rGO [57], and NG7 [193] the *RM2/rGO* composites similarly surpass the power density of commercial catalyst, while RCA-30 [191] and Ni-Co-Mn oxides [208] have lower *Pd* values than for the commercial catalysts. Only the Bat-N-rGO was synthesised from a similar waste fraction than catalysts developed in this thesis, while all the other benchmark catalyst materials were derived from manually extracted LIB-materials. This comparative assessment further highlights the superior performance and sustainability potential of the *RM2/rGO* composites, which are synthesised from industrial waste fractions of LIB recycling.

Table 4.15. The catalyst loading and power density values of zinc-air batteries for bifunctional oxygen electrocatalysts based on EoL LIBs studied in this thesis and reported in the literature.

Catalyst material	Catalyst loading (mg cm ⁻²)	ZAB Pd (mW cm ⁻²)	Power density in % vs commercial catalyst	Reference
<i>HT-Bat-res-BM-N</i>	1.0	104	9.5 %	This work
<i>BR50-CNT50-N</i>	1.0	97	38.5 %	This work
<i>AT-Comp 50/50</i>	1.0	100	43 %	This work
Co@NCW-4	2.0	225	7.5 %	[190]
RCA-30	0.4	92	-20 %	[191]
N/NMCO	-	137	30 %	[192]
Ni-Co-Mn oxides	6.37	85	-25 %	[208]
Bat-N-rGO	1.0	112.8	21 %	[57]
NG7	5.0	120	~20 %	[193]

For the evaluation of specific capacity and specific energy the complete discharge tests were conducted for selection of catalysts from each study (Figure 4.30). Specific capacity (mAh g⁻¹) reflects how long the battery can operate before complete oxidation of the zinc anode, while specific energy (Wh kg⁻¹) indicates the total amount of usable energy delivered per kilogram of zinc. Both parameters are key indicators of the electrochemical efficiency of the catalyst materials, with higher values signifying superior performance. For the materials studied in section 4.2 the complete discharge tests were conducted at 25 mA cm⁻² shown at Figure 4.30a. *HT-Bat-res-BM-N* exhibited the highest specific capacity of 765 mAh g⁻¹, surpassing the commercial 20% PtRu/C benchmark by 77 mAh g⁻¹. The *Bat-res-N* and Raw Material 1 achieved specific capacities of 729 mAh g⁻¹ and 762 mAh g⁻¹, respectively. *HT-Bat-res-BM-N* also recorded the highest values, with $E_{sp} = 780$ Wh kg⁻¹. The complete discharge tests for *BR50-CNT-50-N* (Figure 4.30b, conducted at 5 mA cm⁻²) showed that it delivered a specific capacity of 684 mAh g⁻¹ and $E_{sp} = 817$ Wh kg⁻¹, both exceeding the corresponding values obtained with 20% PtRu/C (650 mAh g⁻¹ and 759 Wh kg⁻¹, respectively). Finally, the *AT-Comp 50/50* was chosen for

complete discharge tests in the [III] study (section 4.4) shown on Figure 4.30c. Even though the Pd values (Figure 4.29c) were same for *Comp 25/75* and *AT-Comp 25/75*, the *AT-Comp 50/50* was chosen for complete discharge tests in the [III] study section 4.4 due to it having higher concentration of *RM2*, therefore enhancing the sustainability and having more unique structure which could enhance the stability of catalyst. The *AT-Comp 50/50* had a specific capacity of 679 mAh g^{-1} and $E_{sp} = 806 \text{ Wh kg}^{-1}$, similarly to catalysts in other studies it exceeded the benchmark values for 20% PtRu/C. Overall, the highest specific capacity and specific energy were achieved by the *BR50-CNT50-N* catalyst, closely followed by *AT-Comp 50/50*, demonstrating the efficient utilisation of zinc and effective delivery of stored energy in both systems.

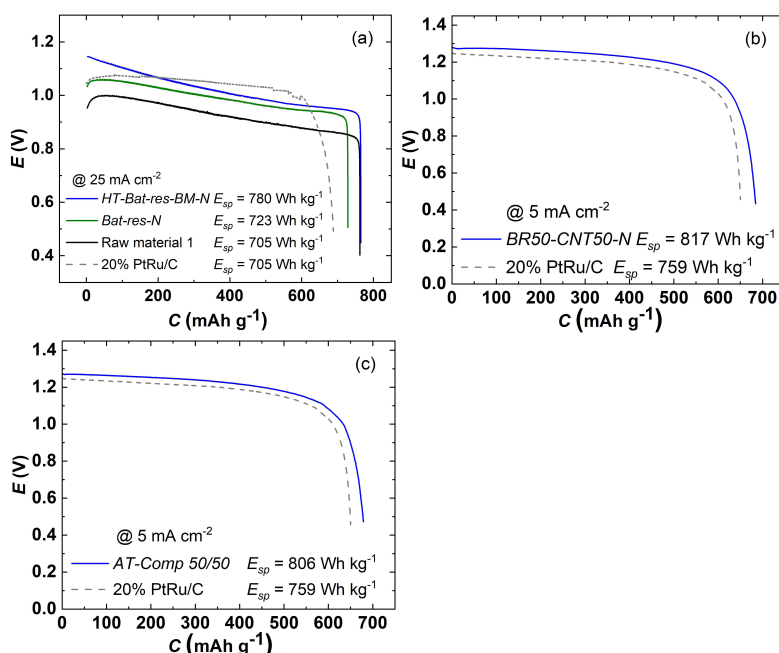


Figure 4.30. ZAB complete discharge test results for (a) *HT-Bat-res-BM-N*, *Bat-res-N*, Raw Material 1, and 20% PtRu/C (b) *BR50-CNT50-N* and 20% PtRu/C, and (c) *AT-Comp 50/50* and 20% PtRu/C catalysts.

Finally, the stability of the catalyst materials was tested using the charge-discharge cycling method with 30-minute charge and 30-minute discharge time, each benchmarked against the 20% PtRu/C catalyst material (Figure 4.31). The discharge currents were 10 mA cm^{-2} in studies [I] and [II]. Testing at lower current densities simulates low-load applications and helps evaluate catalyst longevity under mild conditions, while higher current densities impose greater oxidative and reductive stress on the test system [61]. Therefore, for the [III] study the current density was lowered to 5 mA cm^{-2} to focus more specifically on the intrinsic stability of the catalyst material, minimising the influence of other components in the cell, such as zinc reversibility, which may also limit overall system performance. Under these conditions, the battery-derived *HT-Bat-res-BM-N* catalyst demonstrated superior cycling stability compared to the commercial 20% PtRu/C

(Figure 4.31a), remaining stable for approximately 80 hours at 10 mA cm^{-2} . The initial potential window of charge-discharge cycling (ΔE_{ZAB}) for *HT-Bat-res-BM-N* was 0.94 V, while at 60 hours mark it had only decayed 0.03 V to 0.97 V. Similarly, *BR50-CNT50-N* (Figure 3.31b) exhibited good durability with 70 hours of stable cycling under the same conditions. The initial ΔE_{ZAB} value for the same material was 0.86 V, while at 60 hour mark it had decayed to 1.18 V, showing lower stability than *HT-Bat-res-BM-N*. In study [III] (Figure 4.31c), the comparison was further evaluated using other catalyst materials demonstrating similar *Pd* values. There the *AT-Comp 50/50* catalyst outperformed all others, maintaining stable operation for over 120 hours with initial ΔE_{ZAB} value of 0.75 V, while at 60 hours mark it had decayed to 0.9 V, while still showing lower values than all other studied catalysts at the same time. This demonstrates an exceptional performance of *AT-Comp 50/50*, which is attributed to its unique structural features—specifically, the encapsulation of metal species within graphitic carbon shells, which protect the active sites from leaching under harsh alkaline conditions. Although the best-performing LIB-derived catalyst reported in the literature (Table 4.15)—based on LCO and wood-derived Co–N–C [190]—achieved 160 hours of stable operation at 10 mA cm^{-2} while having higher loading than the LIB-derived catalysts developed in this thesis. *HT-Bat-res-BM-N*, *BR50-CNT50-N*, and *AT-Comp 50/50*, nonetheless demonstrated outstanding cycling performance and durability. These results highlight the robustness and viability of hydrometallurgical LIB recycling leach residue-derived bifunctional oxygen electrocatalysts for zinc–air batteries. However, further optimisation and exploration of alternative leach residues remain necessary, as the use of industrial LIB recycling waste as a catalyst precursor is still in the early stages of research and development.

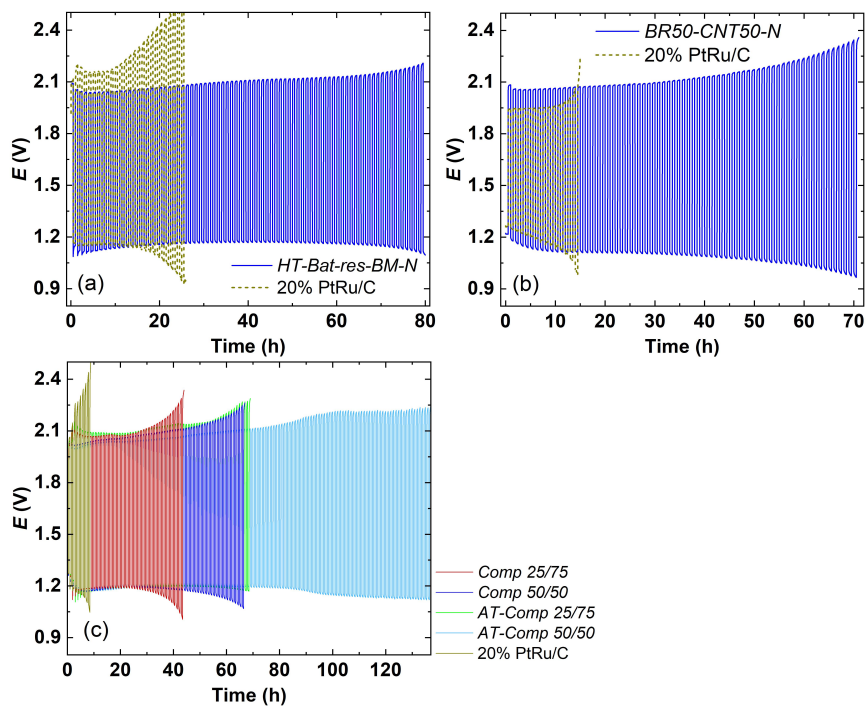


Figure 4.31. ZAB charge-discharge cycling stability test results for (a) HT-Bat-res-BM-N and 20% PtRu/C at 10 mA cm^{-2} , (b) BR50-CNT50-N and 20%PtRu/C at 10 mA cm^{-2} , and (c) Comp 25/75, Comp 50/50, AT-Comp 25/75, AT-Comp 50/50 and 20% PtRu/C at 5 mA cm^{-2} .

Conclusions

This thesis presents an innovative and sustainable approach to valorise industrial process waste generated during the hydrometallurgical recycling of Li-ion battery black mass. High-value bifunctional oxygen electrocatalysts were developed from a heterogeneous leach residue – an underutilised byproduct from hydrometallurgical recycling process. Two different leach residues (Raw material 1 and Raw material 2) were investigated, differentiated by their residual Co content. The nitrogen doped materials structure, and chemical composition was analysed using different physical characterisation methods while their electrochemical activity was investigated by utilising a rotating disc electrode method and practical application in zinc-air batteries.

In the first study, the direct nitrogen doping of Raw Material 1 was performed using ball-milling and pyrolysis. The resulting catalyst, *HT-Bat-res-BM-N*, demonstrated promising bifunctional oxygen electrocatalytic activity, with a bifunctionality parameter ΔE of 0.853 V. The *in-situ* Co doping from the Raw Material 1 and the formation of bamboo carbon nanotubes was proved by physical characterisation. Furthermore, X-ray photoelectron spectroscopy analysis revealed that 55% of the nitrogen was in the electrochemically active pyridinic-N form, which is known to enhance oxygen electroreactions.

The second study focused on improving the electrical conductivity and porosity of the catalyst by integrating Raw material 1 with carbon nanotubes. Following a similar synthesis protocol, including ball-milling and pyrolysis, various heat-treated Raw material 1 to carbon nanotubes ratios were tested. The optimal composition was demonstrated by *BR50-CNT50-N*, which exhibited a bifunctionality parameter ΔE of 0.799 V. This improvement in electrocatalytic performance was attributed to enhanced conductivity and porosity, as well as to the formation of additional Co-catalysed bamboo carbon nanotubes, which increased the stability of the active sites.

The third and final study adopted a fully circular approach by combining a second leach residue (Raw material 2), containing a higher residual Co content, with reduced graphene oxide synthesised from manually extracted spent graphite from end-of-life Li-ion batteries. The synthesis route remained consistent, employing ball-milling and pyrolysis, but was further enhanced with an acid leaching step to remove excess, less active metal species and refine the catalyst structure. By varying the ratio of heat-treated Raw material 2 to reduced graphene oxide, the *AT-Comp 50/50* composite was identified as the most promising bifunctional electrocatalyst, achieving a ΔE of 0.818 V. Characterisation results showed that the addition of rGO significantly improved the specific surface area and porosity, facilitating more efficient mass transport and active site formation. As with the previous studies, bamboo carbon nanotubes and onion-like carbon structures encapsulating Co nanoparticles were observed by transmission electron microscopy with energy dispersive spectroscopy, enhancing the stability and performance of the catalyst under harsh electrochemical conditions.

All catalyst materials developed in this work were subsequently tested in zinc-air battery application. While the *BR50-CNT50-N* catalyst demonstrated the best bifunctional activity in rotating disc electrode tests, the *AT-Comp 50/50* outperformed all others in zinc-air battery testing. It achieved a 43% higher power density than the commercial 20% PtRu/C benchmark catalyst. *BR50-CNT50-N* also showed excellent performance, exceeding the commercial benchmark by 38.5%. In terms of stability, the *AT-Comp 50/50* catalyst demonstrated the most extended operation, maintaining stable charge-discharge

cycling for over 120 hours with an initial potential window of 0.75 V. The results obtained in zinc-air battery testing showed very good activity and excellent stability compared to the other Li-ion battery derived bifunctional oxygen electrocatalysts.

In conclusion, the aims of the studies were achieved by demonstrating, that the Raw Material 1 and 2 both were suitable for the in-situ metal doping of the carbon materials to produce active sites for the oxygen reduction and oxygen evolution reactions. Thanks to the encapsulation of metallic Co into the carbon shells, the stability of the catalyst materials was improved, which was proved by the zinc-air battery testing results. Overall, this research demonstrates a novel and effective method for converting the waste stream of hydrometallurgical Li-ion battery recycling into functional and high-performance bifunctional electrocatalysts. The work not only adds value to materials that would otherwise be discarded or incinerated but also aligns with the broader principles of circular economy and critical raw material circularity. These findings highlight the potential of leach residues as sustainable precursors for advanced energy materials and provide a foundation for future studies on scalable waste-to-resource technologies in battery recycling.

Novelty and further research

Novelty:

- This work demonstrates that the metal content present in the leach residue of industrially processed black mass from hydrometallurgical LIB recycling can be effectively repurposed for *in situ* Co doping of carbon-based electrocatalyst materials.
- It was shown that cobalt nanoparticles present in the leach residue can catalyse the formation of bamboo and onion-like carbon nanostructures, which encapsulate the metal species, thereby enhancing the structural stability and electrochemical performance of the catalyst materials.
- The valorisation of hydrometallurgical recycling waste not only adds functional value to an underutilised industrial byproduct but also supports circular economy principles, by reducing waste and enhancing the circularity of critical raw materials.

Future research directions:

- Further studies are required to systematically investigate how variations in leach residue composition influence the *in situ* metal doping, the type and distribution of active sites, and the electrocatalytic performance.
- The potential of black mass leach residue should also be explored for alternative applications, such as catalysts for environmental applications (e.g. water purification), or as a feedstock for reduced graphene oxide synthesis and its related applications (e.g. in sensors, composites, or capacitors).
- A comprehensive life-cycle assessment is necessary to evaluate the environmental impact and sustainability of catalyst synthesis (or any other material synthesis) using leach residues. Such analysis will provide a clearer understanding of the ecological and economic benefits of using waste-derived materials in comparison to conventional methods relying on pure materials.

References

- [1] IEA, World Energy Outlook, Paris, 2024. <https://www.iea.org/reports/world-energy-outlook-2024>, Licence: CC BY 4.0 (report); CC BY NC SA 4.0 (Annex A).
- [2] IEA, Global EV Outlook 2024, Paris, 2024. <https://www.iea.org/reports/global-ev-outlook-2024>.
- [3] I. European Commission: Directorate-General for Internal Market Entrepreneurship and SMEs, M. Grohol, C. Veeh, Study on the critical raw materials for the EU 2023 – Final report, Publications Office of the European Union, 2023. <https://doi.org/doi/10.2873/725585>.
- [4] IEA, Global Critical Minerals Outlook 2024, Paris, 2024. <https://www.iea.org/reports/global-critical-minerals-outlook-2024>.
- [5] D. Walter, W. Atkinson, S. Mohanty, K. Bond, C. Gulli, A. Lovins, The Battery Mineral Loop – The path from extraction to circularity, 2024. <https://rmi.org/insight/the-battery-mineral-loop>.
- [6] J. Neumann, M. Petranikova, M. Meeus, J.D. Gamarra, R. Younesi, M. Winter, S. Nowak, Recycling of Lithium-Ion Batteries—Current State of the Art, Circular Economy, and Next Generation Recycling, *Adv. Energy Mater.* 12 (2022) 2102917. <https://doi.org/10.1002/AENM.202102917>.
- [7] IEA, Recycling of Critical Minerals, Paris, 2024. <https://www.iea.org/reports/recycling-of-critical-minerals>, Licence: CC BY 4.0.
- [8] J.B. Goodenough, K.S. Park, The Li-ion rechargeable battery: A perspective, *J Am Chem Soc* 135 (2013) 1167–1176. <https://doi.org/10.1021/JA3091438>
- [9] M. Weiss, R. Ruess, J. Kasnatscheew, Y. Levartovsky, N.R. Levy, P. Minnmann, L. Stolz, T. Waldmann, M. Wohlfahrt-Mehrens, D. Aurbach, M. Winter, Y. Ein-Eli, J. Janek, Fast Charging of Lithium-Ion Batteries: A Review of Materials Aspects, *Adv Energy Mater* 11 (2021) 2101126. <https://doi.org/10.1002/AENM.202101126>.
- [10] A.K. Koech, G. Mwandila, F. Mulolani, P. Mwaanga, Lithium-ion battery fundamentals and exploration of cathode materials: A review, *S Afr J Chem Eng* 50 (2024) 321–339. <https://doi.org/10.1016/J.SAJCE.2024.09.008>.
- [11] C. Julien, A. Mauger, K. Zaghib, H. Groult, Optimization of Layered Cathode Materials for Lithium-Ion Batteries, *Materials* 2016, 9 (2016) 595. <https://doi.org/10.3390/MA9070595>
- [12] S. Natarajan, M.L. Divya, V. Aravindan, Should we recycle the graphite from spent lithium-ion batteries? The untold story of graphite with the importance of recycling, *J. Energy Chem.* 71 (2022) 351–369. <https://doi.org/10.1016/J.JEChem.2022.04.012>.
- [13] A.W. Golubkov, D. Fuchs, J. Wagner, H. Wiltsche, C. Stangl, G. Fauler, G. Voitic, A. Thaler, V. Hacker, Thermal-runaway experiments on consumer Li-ion batteries with metal-oxide and olivin-type cathodes, *RSC Adv* 4 (2013) 3633–3642. <https://doi.org/10.1039/C3RA45748F>.
- [14] T. Hettesheimer, A. Thielmann, C. Neef, A. Durand, Preparatory Study on Ecodesign and Energy Labelling of rechargeable electrochemical batteries with internal storage under FWC ENER/C3/2015-619-Lot -1 Task 4, Brussels, 2019. <https://ecodesignbatteries.eu/>
- [15] A. Mayyas, K. Moawad, A. Chadly, E. Alhseinat, Can circular economy and cathode chemistry evolution stabilize the supply chain of Li-ion batteries?, *Extr Ind Soc* 14 (2023) 101253. <https://doi.org/10.1016/J.EXIS.2023.101253>.

- [16] M.C. Etude, A.I. Ikeuba, C.N. Njoku, E. Yakubu, H.C. Uzoma, C.E. Mgbemere, D.I. Udunwa, Recycling lithium-ion batteries: A review of current status and future directions, *Sustain Chem One World* 4 (2024) 100027. <https://doi.org/10.1016/J.SCOWO.2024.100027>.
- [17] Y. Lan, L. Tan, N. Wu, J. Wen, W. Yao, Y. Tang, H.M. Cheng, Current status and outlook of recycling spent lithium-ion batteries, *J Energy Storage* 110 (2025) 115374. <https://doi.org/10.1016/J.EST.2025.115374>.
- [18] Z.J. Baum, R.E. Bird, X. Yu, J. Ma, Lithium-Ion Battery Recycling—Overview of Techniques and Trends, *ACS Energy Lett* 7 (2022) 712–719. <https://doi.org/10.1021/ACSENERGYLETT.1C02602>
- [19] P. Li, S. Luo, L. Zhang, Q. Liu, Y. Wang, Y. Lin, C. Xu, J. Guo, P. Cheali, X. Xia, Progress, challenges, and prospects of spent lithium-ion batteries recycling: A review, *J Energy Chem* 89 (2024) 144–171. <https://doi.org/10.1016/J.JECHEM.2023.10.012>.
- [20] A. Pražanová, Z. Plachý, J. Kočí, M. Fridrich, V. Knap, Direct Recycling Technology for Spent Lithium-Ion Batteries: Limitations of Current Implementation, *Batteries* 2024, 10 (2024) 81. <https://doi.org/10.3390/BATTERIES10030081>.
- [21] X. Wu, Y. Liu, J. Wang, Y. Tan, Z. Liang, G. Zhou, Toward Circular Energy: Exploring Direct Regeneration for Lithium-Ion Battery Sustainability, *Adv Mater* 36 (2024) 2403818. <https://doi.org/10.1002/ADMA.202403818>
- [22] Y. Liu, Z. Shu, Y.F. Ding, T. Yan, Q. Xu, L. Chen, A. Wang, M. Li, Y. Ma, J. Jiang, J. Wu, A comprehensive review of pre-treatment discharge of the spent lithium-ion cells, *J Energy Storage* 112 (2025) 115497. <https://doi.org/10.1016/J.EST.2025.115497>.
- [23] R. Sommerville, P. Zhu, M.A. Rajaeifar, O. Heidrich, V. Goodship, E. Kendrick, A qualitative assessment of lithium ion battery recycling processes, *Resour Conserv Recycl* 165 (2021) 105219. <https://doi.org/10.1016/J.RESCONREC.2020.105219>.
- [24] L. Brückner, J. Frank, T. Elwert, Industrial Recycling of Lithium-Ion Batteries—A Critical Review of Metallurgical Process Routes, *Metals* 2020, 10 (2020) 1107. <https://doi.org/10.3390/MET10081107>.
- [25] H. Deng, B. Wang, J. Xu, G. Yang, Z. Shi, H. Zhu, W. He, G. Li, A comprehensive review of whole process typical hydrometallurgical technologies for recycling waste lithium-ion batteries, *Sep Purif Technol* 363 (2025) 132234. <https://doi.org/10.1016/J.SEPPUR.2025.132234>.
- [26] H. Wang, Y. Huang, C. Huang, X. Wang, K. Wang, H. Chen, S. Liu, Y. Wu, K. Xu, W. Li, Reclaiming graphite from spent lithium ion batteries ecologically and economically, *Electrochim Acta* 313 (2019) 423–431. <https://doi.org/10.1016/J.ELECTACTA.2019.05.050>.
- [27] P. Engels, F. Cerdas, T. Dettmer, C. Frey, J. Hentschel, C. Herrmann, T. Mirfabrikar, M. Schueler, Life cycle assessment of natural graphite production for lithium-ion battery anodes based on industrial primary data, *J Clean Prod* 336 (2022) 130474. <https://doi.org/10.1016/J.JCLEPRO.2022.130474>.
- [28] J. Keeling, Graphite: properties, uses and South Australian resources, *MESA J* 84 (2017) 28–41. https://minedocs.com/17/Sivour_Deposit_2017.pdf
- [29] A.D. Jara, A. Betemariam, G. Woldetinsae, J.Y. Kim, Purification, application and current market trend of natural graphite: A review, *Int J Min Sci Technol* 29 (2019) 671–689. <https://doi.org/10.1016/J.IJMST.2019.04.003>.

- [30] U.S. Geological Survey, 2022 Final List of Critical Minerals, Reston, VA, 2022. <https://www.federalregister.gov/documents/2022/02/24/2022-04027/2022-final-list-of-critical-minerals>
- [31] REGULATION (EU) 2023/1542 OF THE EUROPEAN PARLIAMENT AND OF THE COUNCIL, Concerning batteries and waste batteries, amending Directive 2008/98/EC and Regulation (EU) 2019/1020 and repealing Directive 2006/66/EC, 2023.
- [32] Z. Shang, W. Yu, J. Zhou, X. Zhou, Z. Zeng, R. Tursun, X. Liu, S. Xu, Recycling of spent lithium-ion batteries in view of graphite recovery: A review, *ETransportation* 20 (2024) 100320. <https://doi.org/10.1016/J.ETRAN.2024.100320>.
- [33] P. Xu, D.H.S. Tan, B. Jiao, H. Gao, X. Yu, Z. Chen, P. Xu, D.H.S. Tan, Z. Chen, B. Jiao, H. Gao, X. Yu, A Materials Perspective on Direct Recycling of Lithium-Ion Batteries: Principles, Challenges and Opportunities, *Adv Funct Mater* 33 (2023) 2213168. <https://doi.org/10.1002/ADFM.202213168>.
- [34] A. Chernyaev, J. Partinen, L. Klemettinen, B.P. Wilson, A. Jokilaakso, M. Lundström, The efficiency of scrap Cu and Al current collector materials as reductants in LIB waste leaching, *Hydrometallurgy* 203 (2021) 105608. <https://doi.org/10.1016/J.HYDROMET.2021.105608>.
- [35] A. Chernyaev, B.P. Wilson, M. Lundström, Study on valuable metal incorporation in the Fe–Al precipitate during neutralization of LIB leach solution, *Sci Rep* 11 (2021) 1–8. <https://doi.org/10.1038/s41598-021-02019-2>.
- [36] S. Rothermel, M. Evertz, J. Kasnatscheew, X. Qi, M. Grütze, M. Winter, S. Nowak, Graphite Recycling from Spent Lithium-Ion Batteries, *ChemSusChem* 9 (2016) 3473–3484. <https://doi.org/10.1002/SSC.201601062>.
- [37] H. Lv, H. Huang, C. Huang, Q. Gao, Z. Yang, W. Zhang, Electric field driven delithiation: A strategy towards comprehensive and efficient recycling of electrode materials from spent lithium ion batteries, *Appl Catal B* 283 (2021) 119634. <https://doi.org/10.1016/J.APCATB.2020.119634>.
- [38] J. Shen, M. Zhou, W. Liu, Y. Shi, W. Tang, Y. Deng, R. Liu, Y. Zuo, J. Zhang, Advanced direct recycling technology enables a second life of spent lithium-ion battery, *Energy Storage Mater* 74 (2025) 103964. <https://doi.org/10.1016/J.ENSME.2024.103964>.
- [39] S.H. Zheng, X.T. Wang, Z.Y. Gu, H.Y. Lü, S. Li, X.Y. Zhang, J.M. Cao, J.Z. Guo, X.L. Wu, Direct and rapid thermal shock for recycling spent graphite in lithium-ion batteries, *J Colloid Interface Sci* 667 (2024) 111–118. <https://doi.org/10.1016/J.JCIS.2024.04.058>.
- [40] L. Huang, L. Liu, L. Lu, X. Feng, X. Han, W. Li, M. Zhang, D. Li, X. Liu, D.U. Sauer, M. Ouyang, A review of the internal short circuit mechanism in lithium-ion batteries: Inducement, detection and prevention, *Int J Energy Res* 45 (2021) 15797–15831. <https://doi.org/10.1002/ER.6920>.
- [41] J.R. Wang, D.H. Yang, Y.J. Xu, X.L. Hou, H.A. Edison, D.Z. Wang, L. Zhang, Z.D. Zhu, X.Y. Feng, X.H. Song, H.F. Xiang, Recent developments and the future of the recycling of spent graphite for energy storage applications, *New Carbon Mater* 38 (2023) 787–803. [https://doi.org/10.1016/S1872-5805\(23\)60777-2](https://doi.org/10.1016/S1872-5805(23)60777-2).
- [42] J. Wang, J. Ma, K. Jia, Z. Liang, G. Ji, Y. Zhao, B. Li, G. Zhou, H.M. Cheng, Efficient Extraction of Lithium from Anode for Direct Regeneration of Cathode Materials of Spent Li-Ion Batteries, *ACS Energy Lett* 7 (2022) 2816–2824. <https://doi.org/10.1021/ACSENERGYLETT.2C01539>

- [43] Y. Zhao, Y. Kang, M. Fan, T. Li, J. Wozny, Y. Zhou, X. Wang, Y.L. Chueh, Z. Liang, G. Zhou, J. Wang, N. Tavajohi, F. Kang, B. Li, Precise separation of spent lithium-ion cells in water without discharging for recycling, *Energy Storage Mater* 45 (2022) 1092–1099. <https://doi.org/10.1016/J.ENSME.2021.11.005>.
- [44] S.S. Jayasree, B. Gangaja, D.S. Baji, A. V. Nair, S. Nair, D. Santhanagopalan, Energy efficient lattice and surface chemical regeneration of graphite from failed Li-ion batteries and its use as ultra-long cycling Na-ion battery anodes, *Resour Conserv Recycl* 190 (2023) 106841. <https://doi.org/10.1016/J.RESCONREC.2022.106841>.
- [45] H. Duc Pham, C. Padwal, J.F.S. Fernando, T. Wang, T.Y. Kim, D. Golberg, D.P. Dubal, Back-Integration of Recovered Graphite from Waste-Batteries as Ultra-High Capacity and Stable Anode for Potassium-Ion Battery, *Batter Supercaps* 5 (2022) e202100335. <https://doi.org/10.1002/BATT.202100335>.
- [46] Q. Xu, Y. Wang, X. Shi, Y. Zhong, Z. Wu, Y. Song, G. Wang, Y. Liu, B. Zhong, X. Guo, The direct application of spent graphite as a functional interlayer with enhanced polysulfide trapping and catalytic performance for Li–S batteries, *Green Chem* 23 (2021) 942–950. <https://doi.org/10.1039/D0GC04033A>.
- [47] M. Abdollahifar, S. Doose, H. Cavers, A. Kwade, Graphite Recycling from End-of-Life Lithium-Ion Batteries: Processes and Applications, *Adv Mater Technol* 8 (2023) 2200368. <https://doi.org/10.1002/ADMT.202200368>.
- [48] M.L. Divya, S. Natarajan, Y.S. Lee, V. Aravindan, Achieving high-energy dual carbon Li-ion capacitors with unique low- and high-temperature performance from spent Li-ion batteries, *J Mater Chem A Mater* 8 (2020) 4950–4959. <https://doi.org/10.1039/C9TA13913C>.
- [49] P.G. Schiavi, P. Altimari, R. Zanoni, F. Pagnanelli, Full recycling of spent lithium ion batteries with production of core-shell nanowires//exfoliated graphite asymmetric supercapacitor, *Journal of Energy Chemistry* 58 (2021) 336–344. <https://doi.org/10.1016/J.JEACHEM.2020.10.025>.
- [50] J.S. Ribeiro, M.B.J.G. Freitas, J.C.C. Freitas, Recycling of graphite and metals from spent Li-ion batteries aiming the production of graphene/CoO-based electrochemical sensors, *J Environ Chem Eng* 9 (2021) 104689. <https://doi.org/10.1016/J.JEACE.2020.104689>.
- [51] T. Zhao, Y. Yao, M. Wang, R. Chen, Y. Yu, F. Wu, C. Zhang, Preparation of MnO₂-Modified Graphite Sorbents from Spent Li-Ion Batteries for the Treatment of Water Contaminated by Lead, Cadmium, and Silver, *ACS Appl Mater Interfaces* 9 (2017) 25369–25376. <https://doi.org/10.1021/ACSAMI.7B07882>.
- [52] Y. Tong, C. Qin, L. Zhu, S. Chen, Z. Lv, J. Ran, From Spent Lithium-Ion Batteries to Low-Cost Li₄SiO₄ Sorbent for CO₂ Capture, *Environ Sci Technol* 56 (2022) 5734–5742. <https://doi.org/10.1021/ACS.EST.1C08625>.
- [53] S. Natarajan, H.C. Bajaj, V. Aravindan, Template-free synthesis of carbon hollow spheres and reduced graphene oxide from spent lithium-ion batteries towards efficient gas storage, *J Mater Chem A Mater* 7 (2019) 3244–3252. <https://doi.org/10.1039/C8TA11521D>.
- [54] J. Guan, Z. Li, S. Chen, W. Gu, Zero-valent iron supported on expanded graphite from spent lithium-ion battery anodes and ferric chloride for the degradation of 4-chlorophenol in water, *Chemosphere* 290 (2022) 133381. <https://doi.org/10.1016/J.CHEMOSPHERE.2021.133381>.

- [55] D. Song, J. Yu, J. Wu, B. Zhang, J. Li, In situ enhanced catalytic degradation behavior of antibiotics by graphite anodes from spent lithium-ion batteries: The unique role of self-doped metals, *J Clean Prod* 486 (2025) 144495. <https://doi.org/10.1016/J.JCLEPRO.2024.144495>.
- [56] Z. Xu, J. Wang, S. Sun, Y. Shi, Z.H.I. Sun, H. Cao, Y. Xie, Simple Route for Graphite Recycling from Waste Lithium-Ion Batteries to Environmental Functional Materials, *ACS Sustain Chem Eng* 10 (2022) 13435–13443. <https://doi.org/10.1021/ACSSUSCHEMENG.2C04090>
- [57] K. Liivand, J. Sainio, B.P. Wilson, I. Kruusenberg, M. Lundström, Overlooked residue of Li-ion battery recycling waste as high-value bifunctional oxygen electrocatalyst for Zn-air batteries, *Appl. Catal. B: Environ.* 332 (2023) 122767. <https://doi.org/10.1016/J.APCATB.2023.122767>.
- [58] K. Liivand, M. Kazemi, P. Walke, V. Mikli, M. Uibu, D.D. Macdonald, I. Kruusenberg, Spent Li-Ion Battery Graphite Turned Into Valuable and Active Catalyst for Electrochemical Oxygen Reduction, *ChemSusChem* 14 (2021) 1103–1111. <https://doi.org/10.1002/CSSC.202002742>.
- [59] Y. Xu, M. Shao, M. Mavrikakis, R.R. Adzic, Recent Developments in the Electrocatalysis of the O₂ Reduction Reaction, in: *Fuel Cell Catalysis: A Surface Science Approach*, John Wiley & Sons, Ltd, 2008: pp. 271–315. <https://doi.org/10.1002/9780470463772.CH9>.
- [60] J. Larminie, A. Dicks, M. McDonald, *Fuel cell systems explained*, 2003.
- [61] R.K. Gupta, *Metal-Air Batteries: Principles, Progress, and Perspectives*, 1st ed., CRC Press, Boca Raton, 2023. <https://doi.org/10.1201/9781003295761>.
- [62] M.R. Tarasevich, A. Sadkowsky, E. Yeager, Oxygen Electrochemistry, in: B.E. Conway, J.O. Bockris, E. Yeager, S.U.M. Khan, R.E. White, *Comprehensive Treatise of Electrochemistry*, Springer, Boston, MA, 1983: pp. 301–398. https://doi.org/10.1007/978-1-4613-3584-9_6.
- [63] T.W. Chen, G. Anushya, S.M. Chen, P. Kalimuthu, V. Mariyappan, P. Gajendran, R. Ramachandran, Recent Advances in Nanoscale Based Electrocatalysts for Metal-Air Battery, Fuel Cell and Water-Splitting Applications: An Overview, *Mater* 15 (2022) 458. <https://doi.org/10.3390/MA15020458/S1>.
- [64] P. Ganesan, A. Ishihara, A. Staykov, N. Nakashima, Recent Advances in Nanocarbon-Based Nonprecious Metal Catalysts for Oxygen/Hydrogen Reduction/Evolution Reactions and Zn-Air Battery, *Bull Chem Soc Jpn* 96 (2023) 429–443. <https://doi.org/10.1246/BCSJ.20230051>.
- [65] Z. Feng, C. Dai, P. Shi, X. Lei, R. Guo, B. Wang, X. Liu, J. You, Seven mechanisms of oxygen evolution reaction proposed recently: A mini review, *Chemical Engineering Journal* 485 (2024) 149992. <https://doi.org/10.1016/J.CEJ.2024.149992>.
- [66] Y. Irmawati, F. Balqis, F. Destyorini, C.G. Adios, R. Yudianti, F. Iskandar, A. Sumboja, Cobalt Nanoparticles Encapsulated with N-Doped Bamboo-Like Carbon Nanofibers as Bifunctional Catalysts for Oxygen Reduction/Evolution Reactions in a Wide pH Range, *ACS Appl Nano Mater* 6 (2022). <https://doi.org/10.1021/ACSANM.2C05091>.
- [67] S. Lu, Z. Zhang, C. Cheng, B. Zhang, Y. Shi, S. Lu, Unveiling the Aggregation of M–N–C Single Atoms into Highly Efficient MOOH Nanoclusters during Alkaline Water Oxidation, *Angew Chem Int Ed* 64 (2025) e202413308. <https://doi.org/10.1002/ANIE.202413308>.

- [68] A. Singh, R. Sharma, A. Gautam, B. Kumar, S. Mittal, A. Halder, Chemistry in rechargeable zinc-air battery: A mechanistic overview, *Catal Today* 445 (2025) 115108. <https://doi.org/10.1016/J.CATTOD.2024.115108>.
- [69] D. Stock, S. Dongmo, J. Janek, D. Schröder, Benchmarking Anode Concepts: The Future of Electrically Rechargeable Zinc-Air Batteries, *ACS Energy Lett* 4 (2019) 1287–1300. <https://doi.org/10.1021/ACSENERGYLETT.9B00510>.
- [70] S. Tharani, D. Durgalakshmi, A.K. Kunhiraman, S. Balakumar, R.A. Rakesh, Hybrid zinc-air battery (ZAB) with transition metal-based electrocatalysts—A step toward next-generation electrochemical energy storage, *Wiley Interdiscip Rev Energy Environ* 12 (2023) e472. <https://doi.org/10.1002/WENE.472>.
- [71] D. Yang, L. Zhang, X. Yan, X. Yao, Recent Progress in Oxygen Electrocatalysts for Zinc–Air Batteries, *Small Methods* 1 (2017) 1700209. <https://doi.org/10.1002/SMTD.201700209>.
- [72] H. Ooka, J. Huang, K.S. Exner, The Sabatier Principle in Electrocatalysis: Basics, Limitations, and Extensions, *Front Energy Res* 9 (2021) 654460. <https://doi.org/10.3389/FENRG.2021.654460>.
- [73] D. Borodin, I. Rahinov, P.R. Shirhatti, M. Huang, A. Kandratsenka, D.J. Auerbach, T. Zhong, H. Guo, D. Schwarzer, T.N. Kitsopoulos, A.M. Wodtke, Following the microscopic pathway to adsorption through chemisorption and physisorption wells, *Sci* (1979) 369 (2020) 1461–1465. <https://doi.org/10.1126/SCIENCE.ABC9581>.
- [74] T. Naito, T. Shinagawa, T. Nishimoto, K. Takanabe, Recent advances in understanding oxygen evolution reaction mechanisms over iridium oxide, *Inorg Chem Front* 8 (2021) 2900–2917. <https://doi.org/10.1039/D0QI01465F>.
- [75] L. Negahdar, F. Zeng, S. Palkovits, C. Broicher, R. Palkovits, Mechanistic Aspects of the Electrocatalytic Oxygen Evolution Reaction over Ni–Co Oxides, *ChemElectroChem* 6 (2019) 5588–5595. <https://doi.org/10.1002/CELC.201901265>.
- [76] W. Guan, H. Shao, C. Zhang, X. Qiu, J. Zhao, Y. Wang, L. Zhang, M. Shao, J. Hu, Strategies for the regulation of specific active sites in metal–nitrogen–carbon, *Nano Energy* 120 (2024) 109149. <https://doi.org/10.1016/J.NANOEN.2023.109149>.
- [77] S. Cao, F.F. Tao, Y. Tang, Y. Li, J. Yu, Size- and shape-dependent catalytic performances of oxidation and reduction reactions on nanocatalysts, *Chem Soc Rev* 45 (2016) 4747–4765. <https://doi.org/10.1039/C6CS00094K>.
- [78] X.X. Wang, M.T. Swihart, G. Wu, Achievements, challenges and perspectives on cathode catalysts in proton exchange membrane fuel cells for transportation, *Nat Catal* 2 (2019) 578–589. <https://doi.org/10.1038/S41929-019-0304-9>.
- [79] K. Shah, R. Dai, M. Mateen, Z. Hassan, Z. Zhuang, C. Liu, M. Israr, W.-C. Cheong, B. Hu, R. Tu, C. Zhang, X. Chen, Q. Peng, C. Chen, Y. Li, K. Shah, R. Dai, Z. Hassan, Z. Zhuang, C. Liu, M. Israr, B. Hu, R. Tu, C. Zhang, Q. Peng, C. Chen, Y. Li, X. Chen, M. Mateen, W. Cheong, Cobalt Single Atom Incorporated in Ruthenium Oxide Sphere: A Robust Bifunctional Electrocatalyst for HER and OER, *Angew Chem Int Ed* 61 (2022) e202114951. <https://doi.org/10.1002/ANIE.202114951>.
- [80] Y. Qin, R. Zhao, J. Sun, M. Xu, Q. Wang, Self-supported iridium-ruthenium oxides catalysts with enriched phase interfaces for boosting oxygen evolution reaction in acid, *Appl Surf Sci* 622 (2023) 156945. <https://doi.org/10.1016/J.APSUSC.2023.156945>.

- [81] H. Sun, W.C. Jung, Recent advances in doped ruthenium oxides as high-efficiency electrocatalysts for the oxygen evolution reaction, *J Mater Chem A Mater* 9 (2021) 15506–15521. <https://doi.org/10.1039/D1TA03452A>.
- [82] H. Liu, R. Xiong, S. Ma, R. Wang, Z. Liu, T. Yao, B. Song, Recent advances in noble-metal-free bifunctional oxygen electrode catalysts, *Energy Adv* 4 (2025) 55–83. <https://doi.org/10.1039/D4YA00551A>.
- [83] Y. Zhong, X. Xu, W. Wang, Z. Shao, Recent Advances in Metal-Organic Framework Derivatives as Oxygen Catalysts for Zinc-Air Batteries, *Batter Supercaps* 2 (2019) 272–289. <https://doi.org/10.1002/BATT.201800093>.
- [84] L. Yang, D. Wang, Y. Lv, D. Cao, Nitrogen-doped graphitic carbons with encapsulated CoNi bimetallic nanoparticles as bifunctional electrocatalysts for rechargeable Zn–Air batteries, *Carbon* 144 (2019) 8–14. <https://doi.org/10.1016/J.CARBON.2018.12.008>.
- [85] T. Liu, S. Cai, Z. Gao, S. Liu, H. Li, L. Chen, M. Li, H. Guo, Facile synthesis of the porous FeCo@nitrogen-doped carbon nanosheets as bifunctional oxygen electrocatalysts, *Electrochim Acta* 335 (2020) 135647. <https://doi.org/10.1016/J.ELECTACTA.2020.135647>.
- [86] Z. Meng, N. Chen, S. Cai, R. Wang, W. Guo, H. Tang, Co-N-doped hierarchically ordered macro/mesoporous carbon as bifunctional electrocatalyst toward oxygen reduction/evolution reactions, *Int J Energy Res* 45 (2021) 6250–6261. <https://doi.org/10.1002/ER.6247>.
- [87] D. Liu, Y. Tong, X. Yan, J. Liang, S.X. Dou, Recent Advances in Carbon-Based Bifunctional Oxygen Catalysts for Zinc-Air Batteries, *Batter Supercaps* 2 (2019) 743–765. <https://doi.org/10.1002/BATT.201900052>.
- [88] J. Sun, N. Wang, Z. Qiu, L. Xing, L. Du, Recent Progress of Non-Noble Metal Catalysts for Oxygen Electrode in Zn-Air Batteries: A Mini Review, *Catalysts* 12 (2022) 843. <https://doi.org/10.3390/CATAL12080843>.
- [89] Y. Kumar, M. Mooste, K. Tammeveski, Recent progress of transition metal-based bifunctional electrocatalysts for rechargeable zinc–air battery application, *Curr Opin Electrochem* 38 (2023) 101229. <https://doi.org/10.1016/J.COEELEC.2023.101229>.
- [90] J. Pan, X.L. Tian, S. Zaman, Z. Dong, H. Liu, H.S. Park, B.Y. Xia, Recent Progress on Transition Metal Oxides as Bifunctional Catalysts for Lithium-Air and Zinc-Air Batteries, *Batter Supercaps* 2 (2019) 336–347. <https://doi.org/10.1002/BATT.201800082>.
- [91] G. Fu, Z. Cui, Y. Chen, L. Xu, Y. Tang, J.B. Goodenough, Hierarchically mesoporous nickel-iron nitride as a cost-efficient and highly durable electrocatalyst for Zn-air battery, *Nano Energy* 39 (2017) 77–85. <https://doi.org/10.1016/J.NANOEN.2017.06.029>.
- [92] C. Zhu, Z. Yin, W. Lai, Y. Sun, L. Liu, X. Zhang, Y. Chen, S.-L. Chou, C. Zhu, L. Liu, Y. Chen, Z. Yin, Y. Sun, W. Lai, S. Chou, X. Zhang, Fe-Ni-Mo Nitride Porous Nanotubes for Full Water Splitting and Zn-Air Batteries, *Adv Energy Mater* 8 (2018) 1802327. <https://doi.org/10.1002/AENM.201802327>.
- [93] J. Cai, H. Liu, Y. Luo, Y. Xiong, L. Zhang, S. Wang, K. Xiao, Z.Q. Liu, Single-phase bimetal sulfide or metal sulfide heterojunction: Which one is better for reversible oxygen electrocatalyst?, *J Energy Chem* 74 (2022) 420–428. <https://doi.org/10.1016/J.JEACHEM.2022.07.023>.

- [94] X. Shu, M. Yang, D. Tan, K.S. Hui, K.N. Hui, J. Zhang, Recent advances in the field of carbon-based cathode electrocatalysts for Zn–air batteries, *Mater Adv* 2 (2021) 96–114. <https://doi.org/10.1039/D0MA00745E>.
- [95] D. Chen, L. Pan, P. Pei, X. Song, P. Ren, L. Zhang, Cobalt-based oxygen electrocatalysts for zinc-air batteries: Recent progress, challenges, and perspectives, *Nano Res* 2022 15:6 15 (2022) 5038–5063. <https://doi.org/10.1007/S12274-022-4154-4>.
- [96] X. Zou, M. Tang, Q. Lu, Y. Wang, Z. Shao, L. An, Carbon-based electrocatalysts for rechargeable Zn–air batteries: design concepts, recent progress and future perspectives, *Energy Environ Sci* 17 (2024) 386–424. <https://doi.org/10.1039/D3EE03059H>.
- [97] R. Jasinski, A New Fuel Cell Cathode Catalyst, *Nat* 201 (1964) 1212–1213. <https://doi.org/10.1038/2011212a0>.
- [98] R. Jasinski, Cobalt Phthalocyanine as a Fuel Cell Cathode, *J Electrochem Soc* 112 (1965) 526. <https://doi.org/10.1149/1.2423590>.
- [99] S. Gupta, D. Tryk, I. Bae, W. Aldred, E. Yeager, Heat-treated polyacrylonitrile-based catalysts for oxygen electroreduction, *J Appl Electrochem* 19 (1989) 19–27. <https://doi.org/10.1007/BF01039385>.
- [100] C. Hu, L. Dai, Carbon-Based Metal-Free Catalysts for Electrocatalysis beyond the ORR, *Angew Chem Int Ed* 55 (2016) 11736–11758. <https://doi.org/10.1002/ANIE.201509982>.
- [101] E. Davari, D.G. Ivey, Bifunctional electrocatalysts for Zn–air batteries, *Sustain Energy Fuels* 2 (2017) 39–67. <https://doi.org/10.1039/C7SE00413C>.
- [102] Z. Liang, H. Zheng, R. Cao, Recent advances in Co-based electrocatalysts for the oxygen reduction reaction, *Sustain Energy Fuels* 4 (2020) 3848–3870. <https://doi.org/10.1039/D0SE00271B>.
- [103] H.J. Kim, H.Y. Kim, J. Joo, S.H. Joo, J.S. Lim, J. Lee, H. Huang, M. Shao, J. Hu, J.Y. Kim, B.J. Min, S.W. Lee, M. Kang, K. Lee, S. Choi, Y. Park, Y. Wang, J. Li, Z. Zhang, J. Ma, S. Il Choi, Recent advances in non-precious group metal-based catalysts for water electrolysis and beyond, *J Mater Chem A Mater* 10 (2021) 50–88. <https://doi.org/10.1039/D1TA06548C>.
- [104] H.M. Xu, H.R. Zhu, C.J. Huang, Z.J. Zhang, T.Y. Shuai, Q.N. Zhan, G.R. Li, Recent advances in Fe-N-C- and Co-N-C-based materials as bifunctional electrocatalysts for oxygen reduction and oxygen evolution, *Sci China Chem* 67 (2023) 1137–1160. <https://doi.org/10.1007/S11426-023-1863-8>.
- [105] Y.-J. Wang, R. Yuan, A. Ignaszak, D.P. Wilkinson, J. Zhang, *Advanced Bifunctional Electrochemical Catalysts for Metal-Air Batteries*, 1st ed., CRC Press, Vancouver, 2021.
- [106] Z. Shi, W. Yang, Y. Gu, T. Liao, Z. Sun, Z. Shi, W. Yang, Y. Gu, T. Liao, Z. Sun, Metal-Nitrogen-Doped Carbon Materials as Highly Efficient Catalysts: Progress and Rational Design, *Adv Sci* 7 (2020) 2001069. <https://doi.org/10.1002/ADVS.202001069>.
- [107] S. Ratso, A. Zitolo, M. Käärik, M. Merisalu, A. Kikas, V. Kisand, M. Rähn, P. Paiste, J. Leis, V. Sammelselg, S. Holdcroft, F. Jaouen, K. Tammeveski, Non-precious metal cathodes for anion exchange membrane fuel cells from ball-milled iron and nitrogen doped carbide-derived carbons, *Renew Energy* 167 (2021) 800–810. <https://doi.org/10.1016/J.RENENE.2020.11.154>.

- [108] C.W. Ye, L. Xu, Recent advances in the design of a high performance metal–nitrogen–carbon catalyst for the oxygen reduction reaction, *J Mater Chem A Mater* 9 (2021) 22218–22247. <https://doi.org/10.1039/D1TA05605K>.
- [109] Y. Huang, Y. Chen, M. Xu, A. Ly, A. Gili, E. Murphy, T. Asset, Y. Liu, V. De Andrade, C.U. Segre, A.L. Deriy, F. De Carlo, M. Kunz, A. Gurlo, X. Pan, P. Atanassov, I. V. Zenyuk, Catalysts by pyrolysis: Transforming metal-organic frameworks (MOFs) precursors into metal-nitrogen-carbon (M-N-C) materials, *Mater Today* 69 (2023) 66–78. <https://doi.org/10.1016/J.MATTOD.2023.08.007>.
- [110] A.H. Lu, W.C. Li, E.L. Salabas, B. Spliethoff, F. Schüth, Low temperature catalytic pyrolysis for the synthesis of high surface area, nanostructured graphitic carbon, *Chem Mater* 18 (2006) 2086–2094. <https://doi.org/10.1021/CM060135P>.
- [111] L. Zhang, J. Lu, Y. Wang, X. Li, Pyrolysis of Copper Phthalocyanine as Non-noble Metal Electrocatalysts for Oxygen Reduction Reaction, *J Wuhan Univ of Technol Mater Sci Ed* 39 (2024) 1087–1092. <https://doi.org/10.1007/S11595-024-2974-7>.
- [112] N. Cui, K. Bi, W. Sun, Q. Wu, Y. Li, T. Xu, B. Lv, S. Zhang, Effect of Pyrolysis Conditions on the Performance of Co-Doped MOF-Derived Carbon Catalysts for Oxygen Reduction Reaction, *Catalysts* 2021, 11 (2021) 1163. <https://doi.org/10.3390/CATAL11101163>.
- [113] P. Li, Z. Jin, Y. Qian, Z. Fang, D. Xiao, G. Yu, Supramolecular confinement of single Cu atoms in hydrogel frameworks for oxygen reduction electrocatalysis with high atom utilization, *Mater Today* 35 (2020) 78–86. <https://doi.org/10.1016/J.MATTOD.2019.10.006>.
- [114] J.Y. Choi, L. Yang, T. Kishimoto, X. Fu, S. Ye, Z. Chen, D. Banham, Is the rapid initial performance loss of Fe/N/C non precious metal catalysts due to micropore flooding?, *Energy Environ Sci* 10 (2017) 296–305. <https://doi.org/10.1039/C6EE03005J>.
- [115] S. Ratso, I. Kruusenberg, A. Sarapuu, M. Kook, P. Rauwel, R. Saar, J. Aruväli, K. Tammeveski, Electrocatalysis of oxygen reduction on iron- and cobalt-containing nitrogen-doped carbon nanotubes in acid media, *Electrochim Acta* 218 (2016) 303–310. <https://doi.org/10.1016/J.ELECTACTA.2016.09.119>.
- [116] I. Kruusenberg, N. Alexeyeva, K. Tammeveski, J. Kozlova, L. Matisen, V. Sammelselg, J. Solla-Gullón, J.M. Feliu, Effect of purification of carbon nanotubes on their electrocatalytic properties for oxygen reduction in acid solution, *Carbon* 49 (2011) 4031–4039. <https://doi.org/10.1016/J.CARBON.2011.05.048>.
- [117] M. Kazemi, K. Liivand, M. Prato, P. Vacek, J. Walmsley, S. Dante, G. Divitini, I. Kruusenberg, Graphite and Cobalt Recycled from Li-Ion Batteries: A Valuable Raw Material for Oxygen Reduction Reaction Electrocatalysts, *Energy & Fuels* 38 (2023) 659–670. <https://doi.org/10.1021/ACS.ENERGYFUELS.3C03495>.
- [118] L. Wei, Y. Zhang, Y. Yang, M. Ye, C.C. Li, L. Wei, Y. Zhang, Y. Yang, M. Ye, C.C. Li, Manipulating the Electronic Structure of Graphite Intercalation Compounds for Boosting the Bifunctional Oxygen Catalytic Performance, *Small* 18 (2022) 2107667. <https://doi.org/10.1002/SMLL.202107667>.
- [119] M.J. Wang, J. Yang, L. Wang, Q. Li, Y. Cao, Q. Wu, Y. Han, D. Wang, C. Wang, H.M. Zhang, L. Peng, Engineering charge redistribution on high-density RuCo nanoclusters loaded on N-doped graphite carbon as robust bifunctional oxygen electrocatalysts for rechargeable Zn-air batteries, *J Alloys Compd* 967 (2023) 171813. <https://doi.org/10.1016/J.JALLCOM.2023.171813>.

- [120] J. Duan, S. Chen, M. Jaroniec, S.Z. Qiao, Heteroatom-Doped Graphene-Based Materials for Energy-Relevant Electrocatalytic Processes, *ACS Catal* 5 (2015) 5207–5234. <https://doi.org/10.1021/ACSCATAL.5B00991>.
- [121] Y. Qin, H.H. Wu, L.A. Zhang, X. Zhou, Y. Bu, W. Zhang, F. Chu, Y. Li, Y. Kong, Q. Zhang, D. Ding, Y. Tao, Y. Li, M. Liu, X.C. Zeng, Aluminum and Nitrogen Codoped Graphene: Highly Active and Durable Electrocatalyst for Oxygen Reduction Reaction, *ACS Catal* 9 (2019) 610–619. <https://doi.org/10.1021/ACSCATAL.8B04117>.
- [122] K. Zhang, C. Qu, Z. Liang, S. Gao, H. Zhang, B. Zhu, W. Meng, E. Fu, R. Zou, Highly Dispersed Co-B/N Codoped Carbon Nanospheres on Graphene for Synergistic Effects as Bifunctional Oxygen Electrocatalysts, *ACS Appl Mater Interfaces* 10 (2018) 30460–30469. <https://doi.org/10.1021/ACSAMI.8B11726>.
- [123] J.M. Luque-Centeno, M. V. Martínez-Huerta, D. Sebastián, V. Baglio, M.J. Lázaro, Bifunctional TiCo electrocatalysts based on N-doped graphene cryogels for the oxygen evolution and reduction reactions, *Carbon* 218 (2024) 118615. <https://doi.org/10.1016/J.CARBON.2023.118615>.
- [124] A. Ali, P.K. Shen, Recent Progress in Graphene-Based Nanostructured Electrocatalysts for Overall Water Splitting, *Electrochemical Energy Reviews* 3 (2020) 370–394. <https://doi.org/10.1007/S41918-020-00066-3>.
- [125] Y. Wang, F. Yan, X. Ma, C. Zhu, X. Zhang, Y. Chen, Hierarchically 3D bifunctional catalysts assembled with 1D MoC core/branched N-doped CNT arrays for zinc-air batteries, *Electrochim Acta* 367 (2021) 137522. <https://doi.org/10.1016/J.ELECTACTA.2020.137522>.
- [126] D.M. Morales, M.A. Kazakova, S. Dieckhöfer, A.G. Selyutin, G. V. Golubtsov, W. Schuhmann, J. Masa, Trimetallic Mn-Fe-Ni Oxide Nanoparticles Supported on Multi-Walled Carbon Nanotubes as High-Performance Bifunctional ORR/OER Electrocatalyst in Alkaline Media, *Adv Funct Mater* 30 (2020) 1905992. <https://doi.org/10.1002/ADFM.201905992>.
- [127] X. Zhao, F. Li, R. Wang, J.M. Seo, H.J. Choi, S.M. Jung, J. Mahmood, I.Y. Jeon, J.B. Baek, Controlled Fabrication of Hierarchically Structured Nitrogen-Doped Carbon Nanotubes as a Highly Active Bifunctional Oxygen Electrocatalyst, *Adv Funct Mater* 27 (2017) 1605717. <https://doi.org/10.1002/ADFM.201605717>.
- [128] C. Chen, H. Su, L.N. Lu, Y.S. Hong, Y. Chen, K. Xiao, T. Ouyang, Y. Qin, Z.Q. Liu, Interfacing spinel NiCo₂O₄ and NiCo alloy derived N-doped carbon nanotubes for enhanced oxygen electrocatalysis, *J Chem Eng* 408 (2021) 127814. <https://doi.org/10.1016/J.CEJ.2020.127814>.
- [129] Q.C. Wang, J. Wang, Y.P. Lei, Z.Y. Chen, Y. Song, S. Bin Luo, Research progress on carbon nanotubes in noble-metal-free electrocatalytic oxygen reduction reaction, *Chinese J Inorg Chem* 34 (2018) 807–822. <https://doi.org/10.11862/CJIC.2018.101>.
- [130] S. Chandrasekaran, P.G. Campbell, T.F. Baumann, M.A. Worsley, Carbon aerogel evolution: Allotrope, graphene-inspired, and 3D-printed aerogels, *J Mater Res* 32 (2017) 4166–4185. <https://doi.org/10.1557/JMR.2017.411>.
- [131] M. Asim, A. Hussain, M. Samanci, N.K. Janjua, A. Bayrakçeken, Carbon aerogel supported Ni–Fe catalysts for superior oxygen evolution reaction activity, *Carbon Lett* 34 (2024) 1779–1801. <https://doi.org/10.1007/S42823-024-00730-4>.

- [132] G. Fu, X. Yan, Y. Chen, L. Xu, D. Sun, J.-M. Lee, Y. Tang, G. Fu, X. Yan, Y. Chen, L. Xu, D. Sun, Y. Tang, J. Lee, Boosting Bifunctional Oxygen Electrocatalysis with 3D Graphene Aerogel-Supported Ni/MnO Particles, *Adv Mater* 30 (2018) 1704609. <https://doi.org/10.1002/ADMA.201704609>.
- [133] L. Zong, X. Chen, S. Liu, K. Fan, S. Dou, J. Xu, X. Zhao, W. Zhang, Y. Zhang, W. Wu, F. Lu, L. Cui, X. Jia, Q. Zhang, Y. Yang, J. Zhao, X. Li, Y. Deng, Y. Chen, L. Wang, Ultrafine Fe/Fe₃C decorated on Fe-Nx-C as bifunctional oxygen electrocatalysts for efficient Zn-air batteries, *J Energy Chem* 56 (2021) 72–79. <https://doi.org/10.1016/J.JEchem.2020.07.048>.
- [134] X. Wang, Z. Zhang, H. Gai, Z. Chen, Z. Sun, M. Huang, An efficient pH-universal electrocatalyst for oxygen reduction: defect-rich graphitized carbon shell wrapped cobalt within hierarchical porous N-doped carbon aerogel, *Mater Today Energy* 17 (2020) 100452. <https://doi.org/10.1016/J.MTENER.2020.100452>.
- [135] R. Wang, J. Cao, S. Cai, X. Yan, J. Li, W.M. Yourey, W. Tong, H. Tang, MOF@Cellulose Derived Co-N-C Nanowire Network as an Advanced Reversible Oxygen Electrocatalyst for Rechargeable Zinc-Air Batteries, *ACS Appl Energy Mater* 1 (2018) 1060–1068. <https://doi.org/10.1021/ACSAEM.7B00204>.
- [136] S. Ott, A. Bauer, F. Du, T.A. Dao, M. Klingenhof, A. Orfanidi, P. Strasser, Impact of Carbon Support Meso-Porosity on Mass Transport and Performance of PEMFC Cathode Catalyst Layers, *ChemCatChem* 13 (2021) 4759–4769. <https://doi.org/10.1002/CCTC.202101162>.
- [137] Z. Wei, Z. Yanfei, W. Jiao, Mesoporous carbon materials: synthesis methods, properties, and advanced applications, *Front Mater* 12 (2025) 1548671. <https://doi.org/10.3389/FMATS.2025.1548671>.
- [138] S. He, M. Wu, S. Li, Z. Jiang, H. Hong, S.G. Cloutier, H. Yang, S. Omanovic, S. Sun, G. Zhang, Research Progress on Graphite-Derived Materials for Electrocatalysis in Energy Conversion and Storage, *Molecules* 27 (2022) 8644. <https://doi.org/10.3390/MOLECULES27248644>.
- [139] H. Liu, Y. Zhang, R. Li, X. Sun, S. Désilets, H. Abou-Rachid, M. Jaidann, L.S. Lussier, Structural and morphological control of aligned nitrogen-doped carbon nanotubes, *Carbon* 48 (2010) 1498–1507. <https://doi.org/10.1016/J.CARBON.2009.12.045>.
- [140] P.S. Shiv Charan, S. Shanmugam, V. Kamaraj, Carbon Nanotubes—Synthesis and Application, *Trans Indian Ceram Soc* 68 (2009) 163–172. <https://doi.org/10.1080/0371750X.2009.11082170>.
- [141] Y. Cheng, S.P. Jiang, Advances in electrocatalysts for oxygen evolution reaction of water electrolysis-from metal oxides to carbon nanotubes, *Prog Nat Sci Mater* 25 (2015) 545–553. <https://doi.org/10.1016/J.PNSC.2015.11.008>.
- [142] S. Ratso, M. Käärik, M. Kook, P. Paiste, V. Kisand, S. Vlassov, J. Leis, K. Tammeveski, Iron and Nitrogen Co-doped Carbide-Derived Carbon and Carbon Nanotube Composite Catalysts for Oxygen Reduction Reaction, *ChemElectroChem* 5 (2018) 1827–1836. <https://doi.org/10.1002/CELC.201800132>.
- [143] V. Likodimos, T.A. Steriotis, S.K. Papageorgiou, G.E. Romanos, R.R.N. Marques, R.P. Rocha, J.L. Faria, M.F.R. Pereira, J.L. Figueiredo, A.M.T. Silva, P. Falaras, Controlled surface functionalization of multiwall carbon nanotubes by HNO₃ hydrothermal oxidation, *Carbon* 69 (2014) 311–326. <https://doi.org/10.1016/J.CARBON.2013.12.030>.

- [144] A.M. Dimiev, S. Eigler, Graphene Oxide: Fundamentals and Applications, John Wiley and Sons, InC, Chichester, 2017.
- [145] S. Morales-Torres, A. Jiříčková, O. Jankovský, Z. Sofer, D. Sedmidubský, Synthesis and Applications of Graphene Oxide, *Mater* 15 (2022) 920. <https://doi.org/10.3390/MA15030920>.
- [146] S. Choi, C. Kim, J.M. Suh, H.W. Jang, Reduced graphene oxide-based materials for electrochemical energy conversion reactions, *Carbon Energy* 1 (2019) 85–108. <https://doi.org/10.1002/CEY2.13>.
- [147] S. Ratso, I. Kruusenberg, M. Vikkisk, U. Joost, E. Shulga, I. Kink, T. Kallio, K. Tammeveski, Highly active nitrogen-doped few-layer graphene/carbon nanotube composite electrocatalyst for oxygen reduction reaction in alkaline media, *Carbon* 73 (2014) 361–370. <https://doi.org/10.1016/J.CARBON.2014.02.076>.
- [148] G. Wu, A. Santandreu, W. Kellogg, S. Gupta, O. Ogoke, H. Zhang, H.L. Wang, L. Dai, Carbon nanocomposite catalysts for oxygen reduction and evolution reactions: From nitrogen doping to transition-metal addition, *Nano Energy* 29 (2016) 83–110. <https://doi.org/10.1016/J.NANOEN.2015.12.032>.
- [149] H. Bin Yang, J. Miao, S.F. Hung, J. Chen, H.B. Tao, X. Wang, L. Zhang, R. Chen, J. Gao, H.M. Chen, L. Dai, B. Liu, Identification of catalytic sites for oxygen reduction and oxygen evolution in N-doped graphene materials: Development of highly efficient metal-free bifunctional electrocatalyst, *Sci Adv* 2 (2016). <https://doi.org/10.1126/SCIADV.1501122>.
- [150] J. Feng, C. Ma, Y. Zhang, C. Du, Y. Chen, H. Dong, L. Yu, L. Dong, Enhancing oxygen reduction and evolution reactions on multi-metal N-doped graphene catalysts through catalytic activity and selectivity tuning, *Appl Surf Sci* 651 (2024) 159219. <https://doi.org/10.1016/J.APSUSC.2023.159219>.
- [151] H. Fan, Y. Wang, F. Gao, L. Yang, M. Liu, X. Du, P. Wang, L. Yang, Q. Wu, X. Wang, Z. Hu, Hierarchical sulfur and nitrogen co-doped carbon nanocages as efficient bifunctional oxygen electrocatalysts for rechargeable Zn-air battery, *J Energy Chem* 34 (2019) 64–71. <https://doi.org/10.1016/J.JEACHEM.2018.09.003>.
- [152] K. Qu, Y. Zheng, S. Dai, S.Z. Qiao, Graphene oxide-polydopamine derived N, S-codoped carbon nanosheets as superior bifunctional electrocatalysts for oxygen reduction and evolution, *Nano Energy* 19 (2016) 373–381. <https://doi.org/10.1016/J.NANOEN.2015.11.027>.
- [153] X. Cui, Z. Chen, Z. Wang, M. Chen, X. Guo, Z. Zhao, Tuning Sulfur Doping for Bifunctional Electrocatalyst with Selectivity between Oxygen and Hydrogen Evolution, *ACS Appl Energy Mater* 1 (2018) 5822–5829. <https://doi.org/10.1021/ACSAEM.8B01186>.
- [154] R. Zhao, B. Ni, L. Wu, P. Sun, T. Chen, Carbon-based iron-cobalt phosphate FeCoP/C as an effective ORR/OER/HER trifunctional electrocatalyst, *Colloids Surf A Physicochem Eng Asp* 635 (2022) 128118. <https://doi.org/10.1016/J.COLSURFA.2021.128118>.
- [155] J. Zhang, L. Dai, Nitrogen, Phosphorus, and Fluorine Tri-doped Graphene as a Multifunctional Catalyst for Self-Powered Electrochemical Water Splitting, *Angew Chem Int Ed* 55 (2016) 13296–13300. <https://doi.org/10.1002/ANIE.201607405>.

- [156] H.T. Larijani, M. Khorshidian, Theoretical insight into the role of pyridinic nitrogen on the catalytic activity of boron-doped graphene towards oxygen reduction reaction, *Appl Surf Sci* 492 (2019) 826–842. <https://doi.org/10.1016/J.APSUSC.2019.05.149>.
- [157] J. Chattopadhyay, T.S. Pathak, D. Pak, Heteroatom-Doped Metal-Free Carbon Nanomaterials as Potential Electrocatalysts, *Molecules* 27 (2022) 670. <https://doi.org/10.3390/MOLECULES27030670>.
- [158] I.Y. Jeon, H.J. Noh, J.B. Baek, Nitrogen-Doped Carbon Nanomaterials: Synthesis, Characteristics and Applications, *Chem Asian J* 15 (2020) 2282–2293. <https://doi.org/10.1002/ASIA.201901318>.
- [159] B. Wu, H. Meng, D.M. Morales, F. Zeng, J. Zhu, B. Wang, M. Risch, Z.J. Xu, T. Petit, Nitrogen-Rich Carbonaceous Materials for Advanced Oxygen Electrocatalysis: Synthesis, Characterization, and Activity of Nitrogen Sites, *Adv Funct Mater* 32 (2022) 2204137. <https://doi.org/10.1002/ADFM.202204137>.
- [160] J. Liang, Q. Yuan, Effects of graphitic- and pyridinic-N co-doping on structure regulation and ORR activity of N-doped graphene, *Appl Surf Sci* 648 (2024) 159025. <https://doi.org/10.1016/J.APSUSC.2023.159025>.
- [161] J. Liu, P. Song, W. Xu, Structure-activity relationship of doped-nitrogen (N)-based metal-free active sites on carbon for oxygen reduction reaction, *Carbon* 115 (2017) 763–772. <https://doi.org/10.1016/J.CARBON.2017.01.080>.
- [162] F. Yu, Q. Ying, S. Ni, C. Li, D. Xue, Y. Yang, Enhanced activity towards oxygen electrocatalysis for rechargeable Zn–air batteries by alloying Fe and Co in N-doped carbon, *Dalton Trans* 50 (2021) 16185–16190. <https://doi.org/10.1039/D1DT02787E>.
- [163] B. Wu, J.L. Mi, H. Hu, Z.Y. Zu, L. Liu, Fe-, S-, and N-Doped Carbon Nanotube Networks as Electrocatalysts for the Oxygen Reduction Reaction, *ACS Appl Nano Mater* 3 (2020) 12297–12307. <https://doi.org/10.1021/ACSANM.0C02789>.
- [164] Z. Li, H. Sun, L. Wei, W.J. Jiang, M. Wu, J.S. Hu, Lamellar Metal Organic Framework-Derived Fe-N-C Non-Noble Electrocatalysts with Bimodal Porosity for Efficient Oxygen Reduction, *ACS Appl Mater Interfaces* 9 (2017) 5272–5278. <https://doi.org/10.1021/ACSAMI.6B15154>.
- [165] D. Lyu, Y. Du, S. Huang, B.Y. Mollamahale, X. Zhang, S.W. Hasan, F. Yu, S. Wang, Z.Q. Tian, P.K. Shen, Highly Efficient Multifunctional Co-N-C Electrocatalysts with Synergistic Effects of Co-N Moieties and Co Metallic Nanoparticles Encapsulated in a N-Doped Carbon Matrix for Water-Splitting and Oxygen Redox Reactions, *ACS Appl Mater Interfaces* 11 (2019) 39809–39819. <https://doi.org/10.1021/ACSAMI.9B11870>.
- [166] H. Liu, S. Yi, Y. Wu, H. Wu, J. Zhou, W. Liang, J. Cai, H. Xu, An efficient Co-N/C electrocatalyst for oxygen reduction facilely prepared by tuning cobalt species content, *Int J Hydrogen Energy* 45 (2020) 16105–16113. <https://doi.org/10.1016/J.IJHYDENE.2020.04.024>.
- [167] M. Li, X. Bo, Y. Zhang, C. Han, A. Nsabimana, L. Guo, Cobalt and nitrogen co-embedded onion-like mesoporous carbon vesicles as efficient catalysts for oxygen reduction reaction, *J Mater Chem A Mater* 2 (2014) 11672–11682. <https://doi.org/10.1039/C4TA01078G>.

- [168] X. Zhang, K. Zhang, W. Zhang, X. Zhang, L. Wang, Y. An, X. Sun, C. Li, K. Wang, Y. Ma, Carbon Nano-Onion-Encapsulated Ni Nanoparticles for High-Performance Lithium-Ion Capacitors, Batteries 9 (2023) 102. <https://doi.org/10.3390/BATTERIES9020102/S1>.
- [169] Y. Yao, H. Chen, C. Lian, F. Wei, D. Zhang, G. Wu, B. Chen, S. Wang, Fe, Co, Ni nanocrystals encapsulated in nitrogen-doped carbon nanotubes as Fenton-like catalysts for organic pollutant removal, J Hazard Mater 314 (2016) 129–139. <https://doi.org/10.1016/J.JHAZMAT.2016.03.089>.
- [170] L. Yang, D. Wang, Y. Lv, D. Cao, Nitrogen-doped graphitic carbons with encapsulated CoNi bimetallic nanoparticles as bifunctional electrocatalysts for rechargeable Zn–Air batteries, Carbon 144 (2019) 8–14. <https://doi.org/10.1016/J.CARBON.2018.12.008>.
- [171] Z.Y. Wu, W.B. Ji, B.C. Hu, H.W. Liang, X.X. Xu, Z.L. Yu, B.Y. Li, S.H. Yu, Partially oxidized Ni nanoparticles supported on Ni-N co-doped carbon nanofibers as bifunctional electrocatalysts for overall water splitting, Nano Energy 51 (2018) 286–293. <https://doi.org/10.1016/J.NANOEN.2018.06.071>.
- [172] L. Wei, L. Qiu, Y. Liu, J. Zhang, D. Yuan, L. Wang, Mn-Doped Co-N-C Dodecahedron as a Bifunctional Electrocatalyst for Highly Efficient Zn-Air Batteries, ACS Sustain Chem Eng 7 (2019) 14180–14188. <https://doi.org/10.1021/ACSSUSCHEMENG.9B02884>.
- [173] S. Gupta, S. Zhao, X.X. Wang, S. Hwang, S. Karakalos, S. V. Devaguptapu, S. Mukherjee, D. Su, H. Xu, G. Wu, Quaternary FeCoNiMn-Based Nanocarbon Electrocatalysts for Bifunctional Oxygen Reduction and Evolution: Promotional Role of Mn Doping in Stabilizing Carbon, ACS Catal 7 (2017) 8386–8393. <https://doi.org/10.1021/ACSCATAL.7B02949>.
- [174] M. Ohtsuka, F. Kitamura, On the Formal Redox Potential of Oxygen Reduction Reaction at Iron Phthalocyanine/Graphene Composite Electrode in Alkaline Media, Electrochemistry 83 (2015) 376–380. <https://doi.org/10.5796/ELECTROCHEMISTRY.83.376>.
- [175] S. Kattel, G. Wang, A density functional theory study of oxygen reduction reaction on Me–N₄ (Me = Fe, Co, or Ni) clusters between graphitic pores, J Mater Chem A Mater 1 (2013) 10790–10797. <https://doi.org/10.1039/C3TA12142A>.
- [176] X. Wang, S. Jie, Z. Liu, The influence of encapsulated cobalt content within N-doped bamboo-like carbon nanotubes catalysts for arylalkanes oxidation, Mater Chem Phys 232 (2019) 393–399. <https://doi.org/10.1016/J.MATCHEMPHYS.2019.04.088>.
- [177] J.H. Kim, S.K. Park, Y.J. Oh, Y.C. Kang, Hierarchical hollow microspheres grafted with Co nanoparticle-embedded bamboo-like N-doped carbon nanotube bundles as ultrahigh rate and long-life cathodes for rechargeable lithium-oxygen batteries, Chem Eng J 334 (2018) 2500–2510. <https://doi.org/10.1016/J.CEJ.2017.12.018>.
- [178] H. Yang, S. Gao, D. Rao, X. Yan, Designing superior bifunctional electrocatalyst with high-purity pyrrole-type CoN₄ and adjacent metallic cobalt sites for rechargeable Zn-air batteries, Energy Storage Mater 46 (2022) 553–562. <https://doi.org/10.1016/J.ENSMT.2022.01.040>.
- [179] Abhilash, M. Uma Maheswari, K. Raghava Reddy, T.M. Aminabhavi, V. Aravindan, P. Meshram, Recycling strategies for renewable graphite and other carbon nanomaterials from used batteries: A review, J Clean Prod 493 (2025) 144871. <https://doi.org/10.1016/J.JCLEPRO.2025.144871>.

- [180] J. Liu, H. Shi, X. Hu, Y. Geng, L. Yang, P. Shao, X. Luo, Critical strategies for recycling process of graphite from spent lithium-ion batteries: A review, *Sci. Total Environ.* 816 (2022) 151621. <https://doi.org/10.1016/J.SCITOTENV.2021.151621>.
- [181] D. Ruan, K. Zou, K. Du, F. Wang, L. Wu, Z. Zhang, X. Wu, G. Hu, Recycling of Graphite Anode from Spent Lithium-ion Batteries for Preparing Fe-N-doped Carbon ORR Catalyst, *ChemCatChem* 13 (2021) 2025–2033. <https://doi.org/10.1002/CCTC.202001867>.
- [182] D. Ruan, Z. Zhang, X. Wu, L. Wu, F. Wang, K. Zou, K. Du, G. Hu, Synthesizing High-quality Graphene from Spent Anode Graphite and Further Functionalization Applying in ORR Electrocatalyst, *ChemistrySelect* 6 (2021) 90–95. <https://doi.org/10.1002/SLCT.202004230>.
- [183] K.S. Bejigo, S. Natarajan, K. Bhunia, V. Elumalai, S.J. Kim, Recycling of value-added products from spent lithium-ion batteries for oxygen reduction and methanol oxidation reactions, *J Clean Prod* 384 (2023) 135520. <https://doi.org/10.1016/J.JCLEPRO.2022.135520>.
- [184] K. Serbara Bejigo, K. Bhunia, J. Kim, C. Lee, S. Back, S.J. Kim, Upcycling end of lithium cobalt oxide batteries to electrocatalyst for oxygen reduction reaction in direct methanol fuel cell via sustainable approach, *J Energy Chem* 82 (2023) 148–157. <https://doi.org/10.1016/J.JECHEM.2023.03.042>.
- [185] H. Bian, W. Wu, Y. Zhu, C.H. Tsang, Y. Cao, J. Xu, X. Liao, Z. Lu, X.Y. Lu, C. Liu, Z. Zhang, Waste to Treasure: Regeneration of Porous Co-Based Catalysts from Spent LiCoO₂ Cathode Materials for an Efficient Oxygen Evolution Reaction, *ACS Sustain Chem Eng* 11 (2023) 670–678. <https://doi.org/10.1021/ACSSUSCHEMENG.2C05534>.
- [186] S.Y. Lei, L.B. Liu, S. Liu, W. Sun, Y. Yang, J.L. Luo, Constructing defect-rich CoO post smart Li extraction from spent Li-ion battery toward efficient oxygen evolution reaction, *Chem Eng J* 503 (2025) 158325. <https://doi.org/10.1016/J.CEJ.2024.158325>.
- [187] R. Cui, S. Wang, J. Kong, Y. Ming, T. Sun, J. Miao, Z. Lv, R. Yan, Z. Wang, Mixed cathode and anode materials from spent lithium-ion battery for high-stability oxygen evolution reaction electrode, *J Alloys Compd* 934 (2023) 167847. <https://doi.org/10.1016/J.JALLCOM.2022.167847>.
- [188] Z. Chen, W. Zou, R. Zheng, W. Wei, W. Wei, B.J. Ni, H. Chen, Synergistic recycling and conversion of spent Li-ion battery leachate into highly efficient oxygen evolution catalysts, *Green Chemistry* 23 (2021) 6538–6547. <https://doi.org/10.1039/D1GC01578H>.
- [189] A. Kotkar, S. Dash, P. Bhanja, S. Sahu, A. Verma, A. Mukherjee, M. Mohapatra, S. Basu, Microwave assisted recycling of spent Li-ion battery electrode material into efficient oxygen evolution reaction catalyst, *Electrochim Acta* 442 (2023) 141842. <https://doi.org/10.1016/J.ELECTACTA.2023.141842>.
- [190] Y. Wang, K. Sheng, R. Xu, Z. Chen, K. Shi, W. Li, J. Li, Efficient bifunctional 3D porous Co–N–C catalyst from spent Li–ion batteries and biomass for Zinc–Air batteries, *Chem Eng Sci* 268 (2023) 118433. <https://doi.org/10.1016/J.CES.2022.118433>.
- [191] Y. Liu, X. Zhuge, T. Liu, Z. Luo, K. Luo, Y. Li, Y. Ren, M. Bayati, X. Liu, Cold-plasma activation converting conductive agent in spent Li-ion batteries to bifunctional oxygen reduction/evolution electrocatalyst for zinc-air batteries, *J Colloid Interface Sci* 665 (2024) 793–800. <https://doi.org/10.1016/J.JCIS.2024.03.169>.

- [192] X. Zheng, X. Zhao, J. Lu, J. Li, Z. Miao, W. Xu, Y. Deng, A.L. Rogach, Regeneration of spent cathodes of Li-ion batteries into multifunctional electrodes for overall water splitting and rechargeable Zn-air batteries by ultrafast carbothermal shock, *Sci China Mater* 65 (2022) 2393–2400. <https://doi.org/10.1007/S40843-021-1984-8>.
- [193] K.S. Bejigo, B. Fikadu, A.S. Raaju Sundhar, R. Alphonse Raj, J. Lee, S.J. Kim, Waste to Wealth: Upgrading spent graphite towards defect-rich nitrogen-doped graphene for lithium storage and oxygen electrocatalysis, *Carbon* 238 (2025) 120261. <https://doi.org/10.1016/J.CARBON.2025.120261>.
- [194] S. Balachandran, K. Forsberg, T. Lemaître, N. Vieceli, G. Lombardo, M. Petranikova, Comparative Study for Selective Lithium Recovery via Chemical Transformations during Incineration and Dynamic Pyrolysis of EV Li-Ion Batteries, *Metals* 11 (2021) 1240. <https://doi.org/10.3390/MET11081240>.
- [195] W. Wang, Y. Zhang, X. Liu, S. Xu, A simplified process for recovery of Li and Co from spent LiCoO₂ cathode using Al foil as the in situ reductant, *ACS Sustain Chem Eng* 7 (2019) 12222–12230. <https://doi.org/10.1021/ACSSUSCHEMENG.9B01564>.
- [196] A.C. Ferrari, J. Robertson, Interpretation of Raman spectra of disordered and amorphous carbon, *Phys Rev B* 61 (1999) 14095–14107.
- [197] P.T. Araujo, M. Terrones, M.S. Dresselhaus, Defects and impurities in graphene-like materials, *Mater Today* 15 (2012) 98–109. [https://doi.org/10.1016/S1369-7021\(12\)70045-7](https://doi.org/10.1016/S1369-7021(12)70045-7).
- [198] S.S. Li, J.K. Wang, Q. Zhu, X.W. Zhao, H.J. Zhang, Fabrication of Graphitic Carbon Spheres via a Hydrothermal Carbonization Combined Catalytic Graphitization Method Using Cobalt as Catalysts, *Solid State Phenomena* 281 (2018) 807–812. <https://doi.org/10.4028/WWW.SCIENTIFIC.NET/SSP.281.807>.
- [199] Y. Wang, Y. Nie, W. Ding, S.G. Chen, K. Xiong, X.Q. Qi, Y. Zhang, J. Wang, Z.D. Wei, Unification of catalytic oxygen reduction and hydrogen evolution reactions: highly dispersive Co nanoparticles encapsulated inside Co and nitrogen co-doped carbon, *Chem Commun* 51 (2015) 8942–8945. <https://doi.org/10.1039/C5CC02400E>.
- [200] A. Holewinski, S. Linic, Elementary Mechanisms in Electrocatalysis: Revisiting the ORR Tafel Slope, *J Electrochem Soc* 159 (2012) H864–H870. <https://doi.org/10.1149/2.022211JES>.
- [201] K. Kisand, A. Sarapuu, A. Kikas, V. Kisand, M. Rähn, A. Treshchalov, M. Käärik, H.-M. Piirsoo, J. Aruväli, P. Paiste, J. Leis, V. Sammelselg, A. Tamm, K. Tammeveski, NC-ND license Bifunctional multi-metallic nitrogen-doped nanocarbon catalysts derived from 5-methylresorcinol, *Electrochem Commun* 124 (2021) 106932. <https://doi.org/10.1016/j.elecom.2021.106932>.
- [202] K.S.W. Sing, D.H. Everett, R.A.W. Haul, L. Moscou, R.A. Pierotti, J. Rouquerol, T. Siemieniewska, Reporting Physisorption Data for Gas/Solid Systems with Special Reference to the Determination of Surface Area and Porosity, *Pure Appl Chem* 57 (1985) 603–619. <https://doi.org/10.1351/PAC198557040603>.
- [203] Y. Zhang, Y. Yu, X. Fu, Z. Liu, Y. Liu, S. Li, Light-switchable catalytic activity of Cu for oxygen reduction reaction, *Front Mater Sci* 14 (2020) 481–487. <https://doi.org/10.1007/S11706-020-0521-9/METRICS>.

- [204] Z. Lu, G. Chen, S. Siahrostami, Z. Chen, K. Liu, J. Xie, L. Liao, T. Wu, Di. Lin, Y. Liu, T.F. Jaramillo, J.K. Nørskov, Y. Cui, High-efficiency oxygen reduction to hydrogen peroxide catalysed by oxidized carbon materials, *Nat Catalysis* 2018 156–162. <https://doi.org/10.1038/s41929-017-0017-x>.
- [205] H.W. Kim, H. Park, J.S. Roh, J.E. Shin, T.H. Lee, L. Zhang, Y.H. Cho, H.W. Yoon, V.J. Bukas, J. Guo, H.B. Park, T.H. Han, B.D. McCloskey, Carbon Defect Characterization of Nitrogen-Doped Reduced Graphene Oxide Electrocatalysts for the Two-Electron Oxygen Reduction Reaction, *Chemistry of Materials* 31 (2019) 3967–3973. <https://doi.org/10.1021/ACS.CHEMMATER.9B00210>.
- [206] S. Perumbilavil, P. Sankar, T. Priya Rose, R. Philip, White light Z-scan measurements of ultrafast optical nonlinearity in reduced graphene oxide nanosheets in the 400-700 nm region, *Appl Phys Lett* 107 (2015) 051104. <https://doi.org/10.1063/1.4928124/29691>.
- [207] A.C. Ferrari, D.M. Basko, Raman spectroscopy as a versatile tool for studying the properties of graphene, *Nat Nanotechnol* 2013 235–246. <https://doi.org/10.1038/nnano.2013.46>.
- [208] F. Balqis, Y. Irmawati, D. Geng, F.A.A. Nugroho, A. Sumboja, Nanostructured Ball-Milled Ni-Co-Mn Oxides from Spent Li-Ion Batteries as Electrocatalysts for Oxygen Evolution Reaction, *ACS Appl Nano Mater* 7 (2024) 18138–18145. <https://doi.org/10.1021/ACSANM.3C02092>

Acknowledgements

First and foremost, I would like to express my deepest gratitude to my supervisors, Dr. Kerli Liivand and Dr. Ivar Kruusenberg, for their support and guidance throughout my PhD journey.

I am also sincerely thankful to all co-authors of the research papers upon which this thesis is based: Dr. Mari Lundström, Dr. Benjamin P. Wilson, Dr. Jani Sainio, Dr. Alexander Chernyaev, Dr. Milla Vikberg and Dr. Lassi Klemettinen. Their input to the successful finishing of this work has been enormous.

A big thank you goes to all my colleagues in National Institute of Chemical Physics and Biophysics, but I would like to particularly acknowledge Dr. Kätlin Kaare, Dr. Sander Ratso and Martin Jantson, with whom I've shared many valuable discussions—both scientific and otherwise.

This research was funded by the Estonian Research Council (PUTJD1029, PSG312, EAG248, PSG926), the Environmental Investment Centre (KIK 17988), Business Finland BatCircle2.0 project (Grant Number 44886/31/2020), as well as Business Finland BatCircle3.0 project (Grant Number 1754/31/2024). In addition, this work was funded by the Ministry of Education and Research through the Centre of Excellence in Circular Economy for Strategic Mineral and Carbon Resources (01.01.2024–31.12.2030, TK228). Additionally, the Research Council of Finland RawMatTERS Infrastructure (RAMI), JUST Materials Research Infrastructure (RI) both based at Aalto University and the OtaNano - Nanomicroscopy Center (Aalto-NMC) were utilized as part of this research. Hua Jiang is acknowledged for their assistance with the HR-TEM measurements. This work has been partially supported by ASTRA “TUT Institutional Development Programme for 2016–2022” Graduate school of Functional Materials and Technologies (2014–2020.4.01.16-0032) and Kristjan Jaak short study visits scholarship.

Kristjan, Richard, Hendrik, Kätlin, Sietse, Andres, Karl Rene, Hans, and Villem—thank you for your companionship and for helping me make stressful times a bit less stressful.

Lastly, and most importantly, I say thank you to my family: mom Maire, mother-in-law Vilve, furry friends Kohvi and Sidrun, but above all my deepest gratitude goes to my partner and greatest supporter Laura, who has been by my side through highs and lows of this journey.

Abstract

Upcycling Li-ion battery waste into sustainable electrocatalysts for Zinc-air battery application

The global energy crisis and growing environmental concerns have intensified the need for sustainable energy technologies as alternatives to fossil fuel-based systems. Among these, Li-ion batteries (LIBs) have experienced rapid growth in both research and commercial deployment. However, the increasing volume of end-of-life LIBs presents significant environmental and resource challenges. While industrial-scale LIB recycling processes have made progress in recovering valuable metals such as cobalt and nickel, other components—particularly graphite, the primary anode material—are commonly discarded or incinerated.

This thesis presents a novel upcycling approach that repurposes the leach residue generated from the hydrometallurgical recycling of industrial black mass. This residue, which is typically treated as waste, contains a mixture of graphite and impurities of materials still present from previous recycling steps. Instead of attempting to purify the graphite, this work exploits the heterogeneous composition of the residue to synthesize bifunctional oxygen electrocatalysts, which are essential components in emerging electrochemical energy devices. By introducing nitrogen as a heteroatom, catalytically active nitrogen species—such as pyridinic-N—were incorporated into the carbon matrix. Concurrently, residual metals from the leach residue, particularly cobalt, facilitated the formation of nanostructured carbon species such as bamboo and onion-like carbon nanotubes. These structures encapsulated cobalt nanoparticles, improving the stability and activity of the resulting catalysts.

The initial electrocatalytic performance of the synthesized materials was evaluated for both the oxygen reduction reaction and oxygen evolution reaction using rotating disc-electrode method. To demonstrate practical viability, the catalysts were further tested in zinc-air batteries—a promising energy storage technology. Compared to the commercial benchmark catalyst (20% PtRu/C), the top-performing waste-derived catalysts exceeded the power density by 43% and 38.5%, respectively, while also demonstrating excellent specific capacity and cycling stability.

This work establishes a sustainable route for converting hydrometallurgical LIB recycling waste into value-added, high-performance bifunctional electrocatalysts. By doing so, it not only reduces the environmental effect of battery recycling but also contributes to critical raw material circularity and supports the transition toward a circular energy economy.

Lühikokkuvõte

Liitiumioonakude jäätmete väärindamine ressursitõhusateks katalüsaatormaterjalideks tsink-õhk akude tarvis

Globaalne energiakriis ja süvenevad keskkonnaprobleemid on suurendanud vajadust jätkusuutlike energiatehnoloogiate järele, mis pakuksid alternatiivi traditsioonilistele fossiilkütustel põhinevatele lahendustele. Üheks selliseks alternatiiviks on Li-ioonakud, mis tänaseks päevaks on enimkasutatud energiasalvestustehnoloogia. Seetõttu tõstatab oma elutsükli lõppu jõudnud akude kasvav maht olulist keskkonna- ja ressursiprobleemi. Kuigi tööstuslikud Li-ioonakude ümbertöötlemise protsessid on võimaldanud edukalt taaskasutusse suunata väärtuslikke metalle nagu koobalt ja nikkel, siis teised komponendid – eriti grafiit, mis on aku anoodimaterjal – sageli kas ladustatakse prügilates või põletatakse.

Käesolevas doktoritöös esitati uudet lähenemist, mille käigus väärindatakse Li-ioonakude hüdrometallurgilisel ümbertöötlemisel tekkinud musta massi leostamisjääki, mida seni on käsitletud vaid väärindamata lõppjäätmena. Must mass sisaldab grafiiti, kuid ka muid ebapuhtusi eelnevatest ümbertöötlemise protsessidest. Selle asemel, et keskenduda grafiidi puhastamisele, kasutati antud töös selle heterogeenset koostist ära kahefunktsionaalsete hapniku elektrokatalüsaatorite sünteesiks, mida saab rakendada uutes elektrokeemilistes energiasüsteemides.

Lämmastiku lisamine katalüsaatormaterjalide sünteesis võimaldas süsinikstruktuuri sisse viia elektrokeemiliselt aktiivseid lämmastiku vorme, nagu püriidiinne lämmastik. Samal ajal soodustasid leostamise jäägis leiduvad metallid (eriti koobalt) bambusekujuliste süsinikkanotorude ja sibulakujuliste süsinikstruktuuride teket, mis koos süsinikstruktuuri kapseldunud koobalti nanoosakestega tõstis elektrokatalüsaatorite stabiilsust ja aktiivsust.

Sünteesitud materjalide elektrokatalüütilist aktiivsust hinnati hapniku redutseerimisreaktsiooni ja hapniku eraldumise reaktsiooni suhtes, kasutades pöörleva ketaselektroodi meetodit. Lisaks testiti neid katalüsaatormaterjale uudse energiasalvestustehnoloogia Zn-õhk aku õhk elektroodi katalüsaatormaterjalina. Võrreldes kommersiaalse 20% PtRu/C katalüsaatoriga saavutasid parimad Li-ioonakude ümbertöötlemise jääkidest valmistatud katalüsaatorid vastavalt 43% ja 38,5% kõrgema võimsustiheduse. Lisaks demonstreerisid need materjalid ka kõrget mahutavust ja head tsüklilist stabiilsust.

Käesolevas doktoritöös tutvustati uudet meetodit liitiumioonakude jäätmete vähendamiseks, sünteesides neist jäätmetest kahefunktsionaalseid hapniku elektrokatalüsaatormaterjale ja edendades samal ajal ka uudeid energiasalvestustehnoloogiaid metall-õhk akude näol. Käesolev doktoritöö aitab vähendada Li-ioonakude kasutamisest tulenevat keskkonnamõju, edendab kriitiliste toorainete taaskasutust ning seega soodustab üleminekut ringmajandusele.

Appendix 1

Publication I

R. Praats, A. Chernyaev, J. Sainio, M. Lundström, I. Kruusenberg, K. Liivand, Supporting critical raw material circularity – upcycling graphite from waste LIBs to Zn–air batteries, *Green Chemistry* 26 (2024) 2874–2883.



Cite this: *Green Chem.*, 2024, **26**, 2874

Supporting critical raw material circularity – upcycling graphite from waste LIBs to Zn–air batteries†

Reio Praats,^a Alexander Chernyaev,^b Jani Sainio,^c Mari Lundström,^b Ivar Kruusenberg^a and Kerli Liivand^{id} ^{*,a}

The use of Li-ion batteries (LIBs) is continuously growing, leading to a corresponding increase in the volume of end-of-life LIBs. Recycling of LIBs not only ensures the safe management of hazardous waste, but also minimizes the losses of valuable materials. While for some battery metals, such as Co, Ni, and Cu, industrial recovery processes have already been established, graphite is currently discarded as waste. This research introduces an innovative approach to create a bifunctional oxygen electrocatalyst by using the graphite waste fraction from hydrometallurgical recycling. Notably, we strategically utilized the residual metals left in the graphite fraction to achieve high electrocatalytic activity for both the ORR and OER under alkaline conditions. Our novel black mass-derived oxygen electrocatalyst was used as an air cathode catalyst in Zn–air batteries and demonstrated a high power density of 104 mW cm^{−2} with outstanding long-term stability of 80 hours. This work unlocks new opportunities for repurposing overlooked graphite waste in energy conversion and storage applications.

Received 7th November 2023,
Accepted 10th January 2024

DOI: 10.1039/d3gc04315k

rsc.li/greenchem

Introduction

Lithium-ion batteries (LIBs) have widespread uses in our everyday life, from portable devices to electric vehicles and even heavy machinery. The International Energy Agency (IEA) predicts that there will be a 40-fold increase in LIB usage from 2020 to 2040, which will correspondingly increase the volume of end-of-life batteries required to be recycled.¹ Already in 2019, around 0.2 million tons of spent LIBs (SLIBs) were globally available to be recycled.² Sustainably recovering secondary resources from SLIBs through recycling not only guarantees cost-effective and safe end-of-life management, but also safeguards critical materials from being lost. In addition, this process plays a crucial role in fortifying the battery value chain by recycling secondary resources and keeping them in a loop. The majority of LIB recycling pathways primarily prioritize the high recovery of cathode-active materials (Co, Ni, Li), due to their higher value.^{3,4} However, it is worth noting that natural

graphite (NG) holds significant importance in energy technologies and the steelmaking industry. Recognizing its potential supply risks, the European Commission classified NG as a critical raw material as early as 2011.⁵ In addition, the United States has listed graphite as a critical and strategic mineral.⁶ Graphite holds immense significance across various industries owing to its unique combination of metallic and non-metallic properties, excellent electrical and heat conductivity, good strength, chemical inertness, and heat tolerance up to 3600 °C.⁷ All these beneficial properties lead to diverse applications of graphite in sectors such as the steel industry, aerospace and defence, electronics, transportation, construction, and renewable energy.^{4,5} Therefore, it is imperative to prioritize the recycling of this critical material to ensure its sustained availability and utilization across these vital industries. In the industrial LIB recycling process, graphite is incorporated within the black mass, which is produced during the mechanical pre-treatment step, where batteries are crushed and sieved to form a mixture of small particles composed of all LIB components.⁸ In the hydrometallurgical recycling of black mass, the process typically involves leaching out most of the cathode metals from the black mass. The remaining undissolved fraction, known as the leach residue, is typically treated as waste, and disposed of. The leach residue consists of graphite and other undissolved battery materials, like polymer binder, conducting agent (carbon black), current collectors (Al and Cu), and some undissolved cathode metals.⁹ LIBs typically

^aNational Institute of Chemical Physics and Biophysics, Akadeemia tee 23, 12618 Tallinn, Estonia. E-mail: kerli.liivand@kbfi.ee

^bDepartment of Chemical and Metallurgical Engineering, School of Chemical Engineering, Aalto University, P.O. Box 16200, 00076 Aalto, Finland

^cDepartment of Applied Physics, School of Science, Aalto University, P.O. Box 15100, 00076 Aalto, Finland

†Electronic supplementary information (ESI) available. See DOI: <https://doi.org/10.1039/d3gc04315k>

contain approximately 20 wt% of graphite, which is presently not recycled or recovered. Instead, it is discarded as a waste fraction at the end of the recycling process.⁴ Handling critical resources in this manner cannot be deemed sustainable or economically viable. Several research groups have demonstrated that the quality and structure of spent graphite may undergo only slight changes after its initial use in a battery, rendering it as a potentially valuable resource for the development of new batteries or other applications.^{4,10–14}

The escalating energy consumption and the climate crisis have amplified focus on alternative green energy technologies, such as fuel cells and metal–air batteries.^{15–17} However, these systems require active electrocatalysts to enhance the oxygen reduction reaction (ORR) and the oxygen evolution reaction (OER) taking place in these devices. Currently, expensive Pt or Pt alloys on carbon carriers and RuO₂ or IrO₂ are considered the best commercial catalysts for the ORR and the OER, respectively.^{18,19} Even though noble metal-based catalysts are very efficient, their expensiveness and low durability make them commercially undesirable.^{20–22} Therefore, there is urgency to develop low-cost, durable, and active multifunctional catalyst materials that can catalyse simultaneously both the ORR and OER. Some of the most promising candidates for substituting expensive noble metal-based catalysts are carbon-based materials that are co-doped with nitrogen and transition metal(s), like Fe and Co.^{23–26} Furthermore, carbon-based materials are excellent catalyst supports, due to their low cost, good electrical conductivity, durable structure, resistance to acids and bases, and good adjustability.^{16,20,26–28} However, the synthesis of a multifunctional catalyst material, which catalyses both reactions simultaneously, can be a great challenge due to the need for different catalytic sites and mechanisms. Pioneering work on M–N–C-type catalysts was conducted by Jasinski, who demonstrated that introducing transition metals with nitrogen into the carbon lattice through pyrolysis significantly enhances the activity of ORR electrocatalysts.^{29,30} Nowadays, M–N–C-type catalysts are typically prepared by mixing nitrogen sources, high purity metal salt/oxides, and carbon materials. Subsequently, the mixture is pyrolyzed to introduce metal and nitrogen species into the carbon structure. This process leads to the formation of N–C and M–Nx-type bonds, which are recognized as active sites for the ORR and the OER.^{31–38} In addition to nitrogen species, metal nanoparticles encapsulated by carbon or metal oxides are well-known OER active centres.^{39–42} The ability to catalyse both oxygen reactions, good capacity, and long-term stability are required characteristics for promising bifunctional oxygen electrocatalysts that could be applied in rechargeable Zn–air batteries (ZABs) as air cathode catalyst materials.³² Co–N–C-type catalysts have shown high peak power densities and long-term stabilities in ZABs, which make them favourable candidates to be used commercially.^{39,42–48} In addition, carbon-supported multi-metallic catalyst materials, such as Co–Fe or Co–Ni, have shown promising results. However, the precise mechanism underlying the synergistic effects of multiple metals in enhancing oxygen reduction reactions (ORRs) and oxygen evol-

ution reactions (OERs) remains unclear.^{49–53} These intelligently designed materials often require multi-stage synthesis steps and expensive reagents as carbon support materials and/or metal complexes, which limit the commercialisation possibilities of these materials. To date, there have only been a few studies where recycled materials from SLIBs were used to synthesise electrocatalysts for the ORR and the OER. In most of these studies, the cathode or anode is manually extracted from the used LIB and individually processed to extract Co salt or used graphite. Yang *et al.*⁵⁴ and Bian *et al.*⁵⁵ recovered Co salt from the SLIB cathode layer to synthesize a bifunctional oxygen electrocatalyst. Graphite recovered from the anode layer has been used as a precursor material for reduced graphene oxide (rGO)-based catalyst materials.^{14,56–58} Liivand *et al.* successfully synthesised a graphene-like bifunctional oxygen electrocatalyst from black mass leach residue.⁵⁸

This research presents a novel approach utilizing the leach residue from hydrometallurgical recycling as a cost-effective raw material for oxygen electrocatalyst production. This residue, containing graphite and residual transition metals (Co, Ni, Mn, and Cu), served as a source of carbon and metals, enabling the synthesis of a highly active and stable bifunctional electrocatalyst for enhancing both the ORR and OER. Moreover, this synthesized catalyst exhibited exceptional performance as an air electrode catalyst material in rechargeable zinc–air batteries. This work aligns with the main purposes of the circular economy, reducing the waste generated from battery recycling while contributing to the development of next-generation green energy technologies.

Experimental section

Procurement of leach residue and synthesis of the catalyst material

LIBs from used laptops and mobile phones were subjected to industrial crushing, whereupon magnetic separation and sieving processes were used to generate a Co-rich black mass. Before our research, this black mass had previously undergone hydrometallurgical treatment, as reported by Chernyaev *et al.*,⁵⁹ which effectively leached out the majority of cathode metals, leaving behind the graphite-rich waste fraction. This graphite-rich leach residue was used as the starting material in this research, referred to as the raw material. The raw material consists mainly of graphite with additional impurities such as plastics (separator and binder) and traces of undissolved metals (Co, Ni, Al, Mn, Cu).⁵⁹ To synthesize the catalyst material, we used the raw material directly or subjected it to a heat treatment process to eliminate the organic impurities and binder. For the heat treatment, the raw material underwent flash pyrolysis at 800 °C for 1 hour under an argon atmosphere (99.999%, Elme Messer), resulting in a material referred to as HT-Bat-res. To introduce nitrogen into the raw material or HT-Bat-res, we employed dicyandiamide (DCDA, Sigma-Aldrich, Germany) and polyvinylpyrrolidone (PVP, Sigma Aldrich, Germany, *M_w*: 40 000) in a ratio of 1:20:0.1, respectively. To

obtain a homogeneous raw material: DCDA:PVP mixture in ethanol, 2 hours of sonication was applied. In the case of the heat-treated raw material, a mixture of HT-Bat-res:DCDA:PVP was subjected to ball milling (BM) for two rounds of 30 min each using 4 g of 0.5 mm ZrO₂ balls in a mixture of ethanol and water (2:1) as the medium. Subsequently, the dried mixtures were subjected to flash pyrolysis for 2 hours at 800 °C under an argon atmosphere, resulting in a catalyst known as Bat-res-N (N-doped raw material) or HT-Bat-res-BM-N (ball-milled and N-doped HT-Bat-res). An emphasis was placed on ensuring the repeatability of the synthesis process; therefore, at least three distinct syntheses per catalyst material were performed, and good repeatability was achieved.

Physical characterisation

Scanning electron microscopy (SEM, Mira 3, Tescan, Czech Republic) combined with an energy dispersive X-ray spectrometer (UltraDry Silicon Drift) and NSS microanalysis software (EDS, Thermo Fisher Scientific, USA) was used to analyse the surface morphology and bulk phase composition of the studied materials. The crystallinity and phase composition of these materials were analysed by powder X-ray diffraction (XRD) using a PANalytical X'Pert3 powder XRD instrument (CuK α radiation, $\lambda = 1.54182$ Å), with step size of 0.04° at 45 kV and 40 A. Raman spectra for the analysis of carbon structures of the materials were recorded using a confocal Raman microscope (Renishaw inViaTM, UK) with a 532 nm wavelength laser beam. Data analysis and fitting were performed by applying the Voigt function in the OriginPro (OriginLab Corporation, USA) program. N₂ adsorption-desorption analysis was used to determine the porosity and specific surface area at nitrogen boiling temperature (77 K). The specific surface area was measured by using the Brunauer-Emmett-Teller (BET) method and the pore size distribution was determined with DFT calculations. X-ray photoelectron spectroscopy (XPS) was carried out with a Kratos Axis Ultra spectrometer with monochromated Al K α radiation using a pass energy of 40 eV, an X-ray power of 75 W and an analysis area of approximately 700 $\mu\text{m} \times 300 \mu\text{m}$. The sp² carbon 1s peak at 284.5 eV was used as a charge reference. The elemental composition was determined from the peak areas of high-resolution core level spectra after Shirley background subtraction using equipment-specific sensitivity factors.

Electrochemical measurements

The ORR and the OER were studied with the rotating disk electrode (RDE) method using a Gamry potentiostat/galvanostat Interface 1010E instrument with a three-electrode system, where Ag/AgCl₂ (3 M KCl) was used as the reference electrode, a graphite rod was used as the counter electrode, and a 0.2 cm² glassy carbon (GC) electrode coated with the catalyst was used as the working electrode. An Orignalys speed control unit and a rotator were used for the RDE method with rotation rates from 3600 to 400 rpm. The prepared catalyst ink has a concentration of 4 mg ml⁻¹ in ethanol containing 1 μl mg_{catalyst}⁻¹ of 5 wt% NafionTM solution. The suspension was

previously sonicated for 1 h and, thereafter, 4 \times 5 μl of catalyst ink was pipetted onto clean GC electrodes, resulting in 0.4 mg cm⁻² catalyst loading. For easier comparison, all measured potentials were recalculated to values vs. reversible hydrogen electrode (RHE) by using the Nernst equation:

$$E(\text{RHE}) = E_{\text{Ag/AgCl}} + 0.059 \text{ pH} + E_{\text{Ag/AgCl}}^{\circ} \quad (1)$$

where $E_{\text{Ag/AgCl}}$ is the experimentally measured potential vs. Ag/AgCl and $E_{\text{Ag/AgCl}}^{\circ} = 0.210$ V at 25 °C. ORR measurements were performed in 0.1 M KOH solution at room temperature, saturated with O₂ (Elme Messer, 5.0), and the gas flow was held constant over the solution throughout the experiment. Experiments were controlled with Gamry Instruments Framework software. OER measurements were carried out in N₂ (Elme Messer, 5.0)-saturated 1 M KOH solution at room temperature and the gas flow was held constant over the solution throughout the experiment. The *i*R-drop was eliminated from the OER polarization curves by compensating each of them through *i*R-drop elimination with respect to the solution's ohmic resistance. The ohmic resistance was determined from the EIS data obtained in the frequency range of 100 kHz–1 Hz (with 10 mV modulation) at the open circuit potential. The resistance value was obtained from the Nyquist plot by determining the real part of the impedance when the imaginary part was zero. For electrocatalytic activity assessment, a minimum of three separate RDE measurements, each with three electrodes, were conducted for each synthesized catalyst material.

Zinc-air battery (ZAB) experiments were conducted by using a custom-made test cell. An air electrode with active surface area of 0.79 cm² consisting of a gas diffusion layer (GDL, Sigracet 28BC by SGLCarbon, Germany) and a catalyst layer coated on the GDL, with a final loading of 1 mg cm⁻², was used. Ti mesh was used as an air electrode current collector. For comparison, a commercial catalyst of 20% PtRu (1:1 ratio) on a carbon support (FuelCellstore, USA) was also used as an air electrode catalyst material. A 6 M KOH + 0.2 M Zn(Ac)₂ electrolyte and a polished Zn plate (1 mm, 99.9%) were used to complete the ZAB cell. All measurements were conducted at room temperature. A PGSTAT30 potentiostat/galvanostat (Metrohm Autolab, The Netherlands), controlled by the NOVA 2.1.5 program, was used to control the ZAB tests. Galvanostatic charge-discharge cycling curves were obtained using 30 min charge and 30 min discharge processes at a current density of 10 mA cm⁻². The specific energy density and capacity were obtained with a complete discharge test and calculated based on the mass of consumed Zn. At least three different ZAB cells were tested to evaluate the maximum discharge power density for each synthesized catalyst material.

Results and discussion

Physicochemical characterisation of the samples

The starting material in this research was black mass leach residue (Fig. 1a), primarily comprised of graphite. However, it

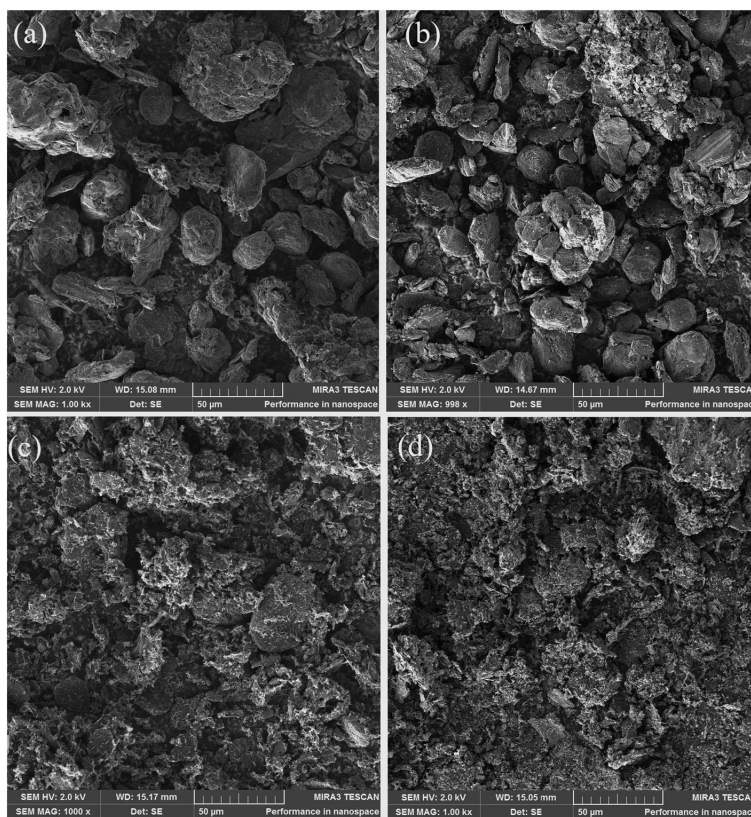


Fig. 1 SEM micrographs of (a) the raw material (black mass leach residue) and the (b) HT-Bat-res, (c) Bat-res-N and (d) HT-Bat-res-BM-N catalyst materials at 1000 \times magnification.

also contained remnants of other battery materials from the cathode (Co, Li, Mn, Ni), the current collectors (Cu and Al), and the binder material (PVDF, a source of F). These components were confirmed through SEM-EDX analysis (Table 1 and Fig. S1 in the ESI †) and XRD (Fig. S2 †). The XRD diffractogram confirmed the presence of a high intensity peak at around 26.5 $^\circ$ for graphite (ICDD: 96-901-1578). In addition, the residue contained $\text{Li}_{1.44}\text{Co}_3\text{O}_6$ (ICDD: 96-155-0393),

LiMn_2O_3 (ICDD: 96-151-3968), SiO_2 (ICDD: 96-900-5033), Cu (ICDD: 96-901-2044), CoO (ICDD: 96-900-8619) and Al_2O_3 (ICDD: 00-010-0173), based on peaks in the XRD diffractogram. This is a typical composition for the black mass leach residue, which has traditionally been found to be very heterogeneous.^{58,59} The heat treatment of leach residue successfully removed the PVDF, as demonstrated by the absence of elemental F in the treated materials, based on SEM-EDX mapping (Fig. S3 † and Table 1). In addition, the results in Table 1 and Fig. S1, S3–S5 † show that the relative concentrations of metals in the bulk increased with the heat treatment(s), showing the removal of organic phases. The removal of the binder played a role in breaking down the larger graphite chunks into smaller and more uniformly sized particles, as observed in Fig. 1a and b. Initially, the sizes of particles in the raw material were between 25 and 50 μm and exhibited a relatively roundish shape with a smooth surface (Fig. 1a). The introduction of nitrogen doping resulted in the development of compact and rough structures on the surface of the catalyst material, indicating the successful nitrogen doping of the graphite surface (as shown in Fig. 1c and d and Fig. S6 †). In

Table 1 Elemental composition of the studied materials based on SEM-EDX mapping (Fig. S1 †)

Element	Raw material (wt%)	HT-Bat-res (wt%)	Bat-res-N (wt%)	HT-Bat-res-BM-N (wt%)
C	79.6	82.88	80.77	75.84
O	15.05	13.43	15.33	18.63
Co	0.77	1.99	2.28	3.42
Mn	0.04	0.24	0.26	0.38
Ni	—	—	0.17	0.21
Al	0.39	0.39	0.46	0.45
Cu	0.43	0.52	0.51	0.49
F	3.05	—	—	—

the case of HT-Bat-res-BM-N, the ball-milling treatment led to a reduction in the size of the supporting graphite particles. In addition, these graphite particles appeared less roundish, instead displaying a flatter and thinner structure compared to the supporting material of the original raw material sample (Fig. S6†). XRD analyses of the pyrolyzed materials revealed that the undissolved active cathode material has undergone reduction, resulting in the formation of metal oxides and/or metallic species. These findings suggest that the graphite present in the leach residue can function as a reductive agent during the thermal treatment. Furthermore, in addition to graphite, it has been shown that aluminium in the presence of a carbon source can facilitate the thermal reduction of the cathode material.⁶⁰ Hu *et al.* have demonstrated that when subjected to higher temperature roasting in the presence of graphite, both Co and Ni exhibit a greater tendency for reduction into metallic species as compared to Mn, which predominantly remains in the oxide state at 900 °C.⁶¹ Based on the transition metal traces, it was observed that Co exhibited the highest relative metal content (3.42%) in the HT-Bat-res-BM-N sample (Table 1). This finding suggests the potential formation of more stable Co–N–C active centres within the bulk of the material, which could enhance the stability of metallic Co.⁶²

This observation was further corroborated by the XRD analysis (Fig. S7†), which revealed the disappearance of the CoO peak and a noticeable increase in the intensity of the Co(0) peak after N-doping. Subsequent to the heat treatment of the materials, distinct metallic Co (Co(0), ICDD: 96-901-1624) peaks became evident in the XRD patterns of the HT-Bat-res, Bat-res-N and HT-Bat-res-BM-N samples, indicating the successful decomposition of $\text{Li}_{1.44}\text{Co}_3\text{O}_6$. In the case of the Bat-res-N and HT-Bat-res-BM-N materials, the majority of Co existed in the Co(0) form, while for HT-Bat-res, Co was predominantly present as either Co_4O_4 or Co(0), as discerned from the XRD diffractograms. These results confirm that a substantial proportion of Co is reduced into its metallic form during the N-doping process, presumably integrated into the Co–N–C active centres within the material's bulk. Moreover, the diffractograms of Bat-res-N and HT-Bat-res-BM-N also indicate the presence of cobalt carbide ($\text{Co}_{0.01}\text{Co}$, ICDD: 98-061-7394). The incorporation of Co nanoparticles into the carbon support material poses a significant challenge. However, it has been established that carbon nanotubes (CNTs) can form in the presence of cobalt nanoparticles and DCDA during the pyrolysis of carbon-based materials. The initiation of CNT growth on carbon is catalysed by metallic Co, which is often subsequently encapsulated within the CNTs. Our previous research has documented the growth of these CNTs under similar conditions.^{58,63} In addition, XRD analysis identified Cu peaks (ICDD: 96-901-2044) in the diffractograms of the HT-Bat-res, Bat-res-N and HT-Bat-res-BM-N materials. The I_D/I_G ratio, determined from the Raman spectra (Fig. S8†) of the studied materials, revealed that with every process step, a higher graphitization rate and a lower surface defect level in the carbon lattice were achieved. It is important to note that the D-band

intensity is influenced not only by vacancies and topological defects, but also by the presence of impurities.⁶⁴ It is believed that the removal of various impurities from the graphite fraction is the key factor in this work that influences the intensity of the D-band. The I_D/I_G ratio decreased from 0.72 to 0.50 with the removal of binder and organic phases. This effect can be attributed to the greater abundance of diverse oxygen groups that become attached to both the surface and edges of graphite following the acidic treatment (leaching) of the black mass. With N-doping of the samples, even lower I_D/I_G ratios were achieved, *i.e.* 0.40 and 0.28 for the Bat-res-N and HT-Bat-res-BM-N materials, respectively. These observations indicate that the introduction of N- and Co- into the carbon support material framework enhances the degree of graphitization, as corroborated by prior research that has been conducted. The introduction of graphitic nitrogen into the carbon framework after N-doping can contribute to the stabilization of graphitic planes in the carbon material, and thus promotes a more ordered and crystalline structure.⁶⁵ In addition, the cobalt and cobalt oxides present in the sample may also serve as catalysts for the transformation of amorphous carbon into graphitized carbon.⁶⁶ Furthermore, the combination of various treatment steps increased the specific surface area (S_{BET}) and porosity of the materials in the following order: raw material < HT-Bat-res < Bat-res-N < HT-Bat-res-BM-N, as shown in Fig. S9†. The removal of binder and organic phases from the leach residue increased the specific surface area from 2.4 to 9.9 $\text{m}^2 \text{g}^{-1}$. Notably, ball milling of the HT-Bat-res material has a pronounced impact on the surface area of the HT-Bat-res-BM-N material, which reached 46.8 $\text{m}^2 \text{g}^{-1}$. This outcome is favourable, as an increased surface area and porosity of the catalyst support material enhance mass transport within the material and introduce additional defects on the carbon surface. These defects can serve as anchoring sites for N- and metal species.^{14,38,42} In order to obtain further insights into the possible extent of N-doping of the graphite support material, XPS analysis of the Bat-res-N and HT-Bat-res-BM-N materials was performed. Carbon, oxygen, nitrogen, and various Li-ion battery metals (Co, Li, Mn, Ni, Al, and Cu) were found in the samples by XPS analysis. The atomic concentrations are given in Table S1†. Fig. 2 shows the obtained and deconvoluted carbon, nitrogen and cobalt spectra of the two samples. The C 1s spectrum consists of a main asymmetric peak at 284.5 eV, which can be assigned to the sp^2 carbon. At binding energies between 285 and 289 eV, there will be some additional contributions from other types of carbon–carbon, carbon–oxygen and carbon–nitrogen bonds,^{67–69} and N-peak fitting results for Bat-res-N and HT-Bat-res-BM-N (fitting parameters shown⁵⁸) are presented in Table 2. The difference in the N-doping level, 5.6 at% for Bat-res-N vs. 6.4 at% for HT-Bat-res-BM-N, agrees well with the conclusion that ball milling leads to a reduction in the graphite particle size, resulting in a higher specific surface area and a greater number of defects in the carbon lattice. The Co 2p spectra (Fig. 2c) have been fitted with two components: metallic Co and Co(II).⁵⁸ The Co(II) component can contain contributions from both the CoO and Co–N

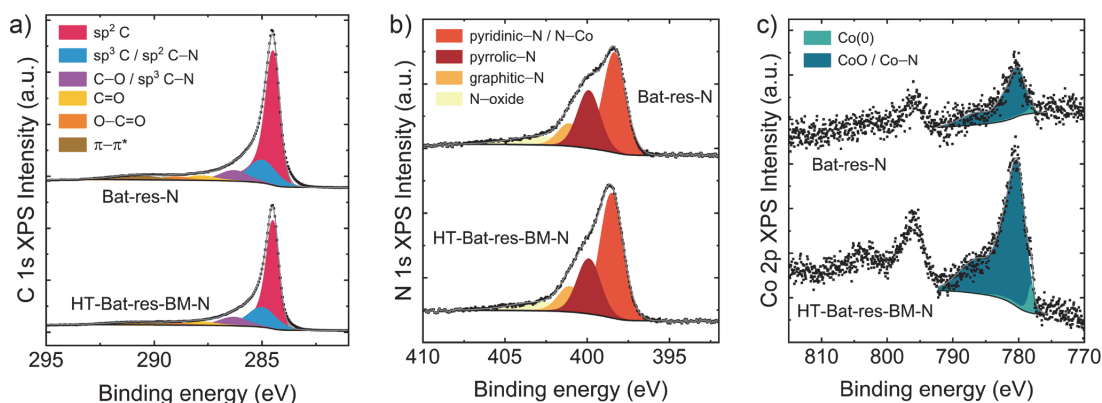


Fig. 2 X-ray photoelectron spectra of the Bat-res-N and HT-Bat-res-BM-N samples: (a) C 1s region, (b) N 1s region and (c) Co 2p region.

Table 2 N-peak fitting results based on XPS analysis (data from Fig. 2)

Name of the sample	Pyridinic N/N-Co	Pyrrolic N	Graphitic N	N oxide
Bat-res-N	50%	29%	11%	10%
HT-Bat-res-BM-N	55%	24%	11%	9%

bonds.^{70,71} These defects provide more favourable sites for nitrogen groups to attach during the doping process. Pyridinic N, which is considered to be the most efficient nitrogen group for enhancing the ORR and OER,⁷² has a concentration of 50% for the Bat-res-N catalyst and 55% for the HT-Bat-res-BM-N catalyst. The surface concentrations of Co were 0.1% and 0.4%, for Mn they were 0.5% and 0.9% and for Li they were 1.4% and 0.6%, respectively, for Bat-res-N and HT-Bat-res-BM-N. The concentration of battery metals on the catalyst surface, as determined through XPS analysis, exhibits a marked disparity compared to their concentration in the bulk of the studied materials, as determined from the EDX data. Concentrations are notably different especially for Co (0.4 at% vs. 3.42 wt%) and Al (2.1 at% vs. 0.45 wt%) in the case of the HT-Bat-res-BM-N sample. This variation in measurements is likely attributed to the inherent distinctions between the analysis methodologies. XPS captures data exclusively from the material's surface, penetrating to only a few atomic layers (typically up to 10 nm). In contrast, EDX analysis delves deeper, characterizing the material's bulk, with a penetration depth of approximately one μm . These findings suggest that the residues of Al, Mn, and Li are more prevalent on the surface of catalyst materials. In contrast, Co appears to be primarily integrated into the carbon support material, possibly forming bonds with active Co-N-C centres. This phenomenon could be related to the distinct reduction behaviours observed during the roasting process. It appears that Co undergoes reduction primarily to its metallic form, while other elements tend to remain in their oxide states, as discussed with respect to XRD analysis.

Electrocatalyst activity towards the ORR and OER

The modifications carried out on the black mass leach residue have increased its surface area and porosity, potentially leading to the formation of Co-N-C active centres that could promote the ORR and OER. The electrocatalytic activity of the synthesised materials as catalysts was first tested with regard to the ORR in 0.1 M KOH solution. The linear sweep voltammetry (LSV) curves and the determined electrochemical characteristics of the catalyst materials are presented in Fig. 3a and Table 3, respectively. The E_{onset} value increased with every following treatment step, showing that the N-doping of the material enhanced the electrochemical activity, with the highest values being for the Bat-res-N and HT-Bat-res-BM-N catalysts, at 0.875 V and 0.890 V, respectively. The half-wave potential ($E_{1/2}$) and limiting current density (j) of the HT-Bat-res-BM-N catalyst were 0.795 V and 4.81 mA cm^{-2} , respectively, demonstrating its excellent ORR performance. The formation of these active centres and the increased surface area were corroborated through a comprehensive analysis involving XRD, SEM-EDX, XPS and N_2 adsorption/desorption analyses. Notably, the HT-Bat-res-BM-N catalyst exhibited the highest specific surface area, a crucial attribute for enhancing the ORR because it allows for a greater capacity to host active centres.³⁸ The LSV polarization curves at different rotation rates for the Bat-res-N and HT-Bat-res-BM-N catalysts can be seen in Fig. S10a and S10b,[†] respectively. The Koutecky-Levich (K-L) plots (Fig. S10c and S10d[†]) were derived from the LSV curves. These plots exhibit a consistent linearity and parallelism across all the examined potentials, implying that the reaction is predominantly limited by mass transport. Based on the K-L plots, the number of electrons (n) transferred per O_2 molecule (Fig. S10b and S10d[†]) was calculated. The results indicated that the oxygen was reduced mainly *via* a $4e^-$ pathway, where O_2 is directly transformed into H_2O without forming intermediate H_2O_2 .⁷³ The Tafel plots in Fig. S10e[†] show that the HT-Bat-Res-BM-N and Bat-res-N catalysts exhibit similar slopes of -52 mV dec^{-1} and -60 mV dec^{-1} , respectively. Remarkably,

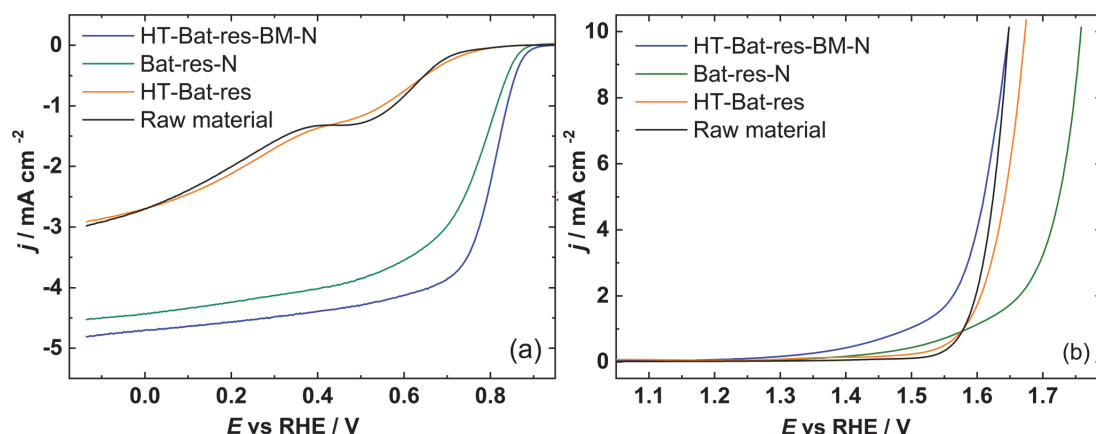


Fig. 3 RDE electrochemical characteristics of the studied materials: (a) ORR polarization curves at 1600 rpm in O_2 -saturated 0.1 M KOH solution and (b) OER polarization curves at 1600 rpm in N_2 -saturated 1 M KOH solution.

Table 3 Electrochemical characteristics of the raw material and different catalysts

Catalyst	ORR E_{onset} (V vs. RHE)	OER $E_{1/2}$ (V vs. RHE)	j (mA cm^{-2})	E (V)@ 10 mA cm^{-2}
Raw material	0.745	0.327	2.98	1.648
HT-Bat-res	0.767	0.370	2.92	1.675
Bat-res-N	0.875	0.755	4.53	1.759
HT-Bat-res-BM-N	0.890	0.795	4.81	1.648

these values align with those commonly observed for Pt-based catalysts. This suggests that the rate-determining step in the reaction mechanism is primarily associated with the initial reduction of O_2 .⁷⁴ A comparison of the OER activity between the studied materials is shown in Fig. 3b and Table 3. Again, HT-Bat-res-BM-N showed the highest activity with E (V) @10 mA cm^{-2} = 1.648 V vs. RHE, while HT-Bat-res and Bat-res-N showed higher potentials of 1.675 V and 1.759 V vs. RHE. The untreated raw material also demonstrated good activity towards the OER with E (V)@10 mA cm^{-2} = 1.648 V vs. RHE, which can be attributed to traces of metal oxides in the bulk raw material. XRD analyses demonstrated the presence of Co_3O_4 in the raw material (Fig. S2†). Co_3O_4 implies a compound with a combination of cobalt atoms in different oxidation states, including cobalt(II) and cobalt(III). The presence of multiple oxidation states suggests a mixed valency, which tends to be effective in catalysing the OER.⁷⁵ The N-doped materials exhibit a Tafel slope (Fig. S10†) of 140 mV dec^{-1} and 119 mV dec^{-1} for Bat-res-N and HT-Bat-res-BM-N, respectively, while the undoped materials exhibit Tafel slopes of 71 mV dec^{-1} (raw material) and 97 mV dec^{-1} (HT-Bat-res). The increase of Tafel slopes for the N-doped materials could indicate that mass transfer is the rate limiting step and the effective electrode surface area is lower.⁴⁰ HT-Bat-res-BM-N showed excellent activity and stability towards both the ORR

and OER due to the formation of electrochemically active Co-N-C and Co(0) species. Multi-metal catalyst materials have good ORR/OER bifunctional electrocatalytic activity due to the synergistic effect of the metals, but the concrete effects of multi-metallic catalyst materials are still under debate.^{49,50,76}

Performance as an air electrode catalyst in zinc-air batteries

To assess the synthesized catalyst's viability for end application, we constructed a zinc-air battery (ZAB) (Fig. S11a†). This allowed us to evaluate the catalyst's bifunctional performance when employed as an air cathode catalyst material. For comparison purposes, we also employed a commercial catalyst consisting of 20% PtRu/C as the air electrode catalyst material. All the studied catalyst materials showed very similar open circuit potential values (Fig. S11b†) of 1.40 V for HT-Bat-res-BM-N and 1.45 V for PtRu/C. The peak power density (Fig. 4a) for HT-Bat-res-BM-N was 104 mW cm^{-2} at a current density of 173 mA cm^{-2} , which is 32 mW higher than what was achieved with a 20% PtRu/C catalyst-based ZAB. By comparing the charging and discharging polarization curves of the catalysts, HT-Bat-res-BM-N has the higher discharge voltage; however, all catalyst materials have similar charge voltages, as can be seen from Fig. 4b. Complete discharge tests were carried out to calculate the specific capacity and energy of the constructed ZAB (Fig. 4c and Table 4). The highest specific capacity of 765 mA h g^{-1} was achieved with the HT-Bat-res-BM-N catalyst. Both the N-doped catalysts demonstrated higher power density than the raw material-based catalyst, showing the enhancement effects of nitrogen doping and the increased surface area, which provides a greater number of active centres for both the ORR and OER. The stability of the catalyst materials was tested during charge-discharge cycling at a current of 10 mA cm^{-2} with a 30 min charge and discharge time, as can be seen in Fig. 4d. The HT-Bat-res-BM-N catalyst showed outstanding stability up to 80 cycles with an average round-trip efficiency of 55% and a

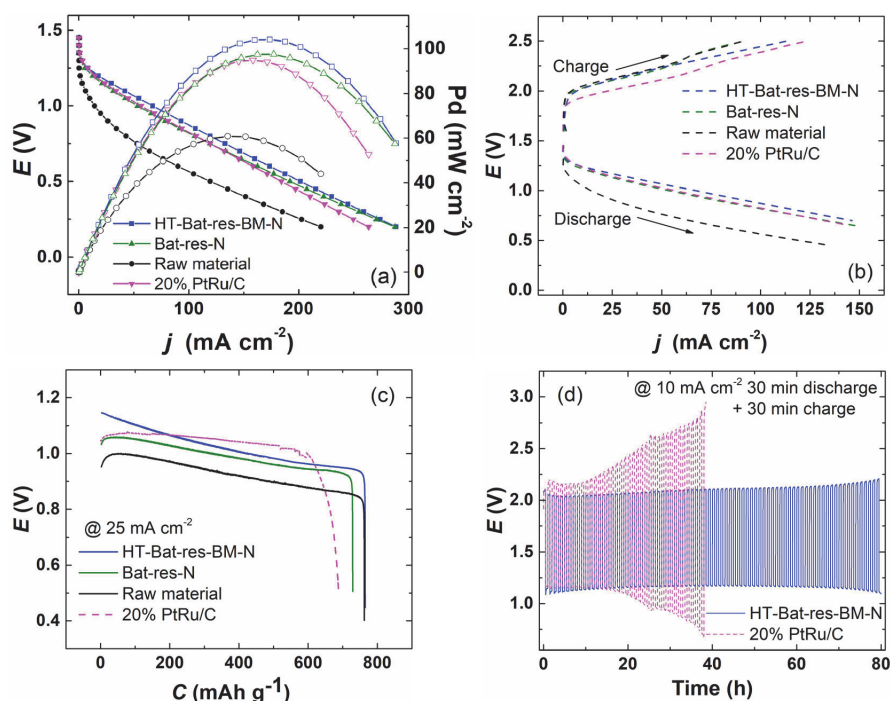


Fig. 4 ZAB results of the studied catalysts and the 20% PtRu/C catalyst: (a) discharge polarization curves and power density curves, (b) charge and discharge polarization curves, (c) complete discharge test, (d) galvanostatic charge/discharge cycling.

Table 4 Specific capacity and specific energy of the studied catalysts and PtRu/C

Name of the sample	Raw material	Bat-res-N	HT-Bat-res-BM-N	20% PtRu/C
Specific capacity ($mA\ h\ g^{-1}$)	762	729	765	688
Specific energy ($W\ h\ kg^{-1}$)	705	723	780	705

voltage gap of 0.95 V. In contrast, 20% PtRu/C showed an initially higher round-trip efficiency (60%) and a smaller voltage gap (0.79 V), but its performance started to decrease quickly after 10 potential cycles showing the superior cycling stability and efficiency of the HT-Bat-res-BM-N catalyst.

The performance and stability of HT-Bat-res-BM-N do not currently surpass those of the top catalysts employed in ZABs.^{38,42,46,47,51,53} However, it is important to note that all these reference catalysts were synthesized using costly and precious pure materials and complicated synthesis routes. Table S2† provides a comparative overview of bi- or trimetallic bifunctional N-doped carbon catalysts for ZABs.

The catalysts developed in this research offer a significant advantage, as they are synthesized from industrial recycling waste, facilitating the responsible and sustainable use of criti-

cal resources. Furthermore, this approach introduces an innovative, straightforward, and economically efficient method for repurposing waste graphite derived from LIBs.

Conclusions

In this study, we revealed the undiscovered potential of the Li-ion battery black mass leach residue, typically discarded as industrial hydrometallurgical recycling waste, as a valuable raw material for synthesis of electrocatalytically active bifunctional oxygen electrocatalysts. By taking advantage of the metal impurities present in the black mass leach residue, we incorporated nitrogen and Co into the graphite support material through a ball milling and pyrolysis modification process. The resulting material, HT-Bat-res-BM-N, exhibited high electrocatalytic activity for both the ORR and OER.

This remarkable performance can be attributed to the development of electrocatalytically active nitrogen and cobalt centres, as well as an increased surface area compared to that of the original material. We further assessed the applicability of these battery waste-derived catalysts by employing them as air electrode catalyst materials in a zinc-air battery. HT-Bat-res-BM-N demonstrated an impressive power density of $104\ mW\ cm^{-2}$ and outstanding stability, withstanding

80 hours of charge–discharge cycling at 10 mA cm^{−2}. Notably, it outperformed the commercial 20% PtRu/C catalyst in this application. This research highlights the previously undiscovered value of the Li-ion battery leach residue as a valuable resource for the preparation of transition metal-doped carbon-based materials, which holds great promise for enhancing energy conversion and storage devices. The catalysts developed in this research provide notable advantages by utilizing industrial recycling waste and promoting responsible resource use. In addition, this approach presents an innovative, cost-effective method for repurposing waste graphite from LIBs.

Author contributions

R. P.: conceptualization, investigation, and writing – original draft. A. C.: investigation (SEM-EDX and Raman) and writing – original draft. J. S.: investigation (XPS) and writing – original draft. M. L.: resources and writing – original draft. I. K.: resources, supervision, and writing – original draft. K. L.: conceptualization, funding acquisition, investigation, project administration, and writing – original draft.

Conflicts of interest

The authors declare that there are no conflicts of interest.

Acknowledgements

This research was supported by the Estonian Research Council (PSG312, PSG926, EAG248), the Environmental Investment Centre (KIK 17988), and the Business Finland BatCircle2.0 project (Grant Number 44886/31/2020). Additionally, the Academy of Finland's RawMatTERS Finland Infrastructure (RAMI) based at Aalto University and the OtaNano – Nanomicroscopy Center (Aalto-NMC) were utilized as part of this research.

References

- 1 IEA, *The Role of Critical Minerals in Clean Energy Transitions*, Paris, 2021.
- 2 H. E. Melin, *The Lithium-Ion Battery Life Cycle Report*, London, 2021.
- 3 O. Velázquez-Martínez, J. Valio, A. Santasalo-Aarnio, M. Reuter and R. Serna-Guerrero, *Batteries*, 2019, **5**, 68.
- 4 S. Natarajan, M. L. Divya and V. Aravindan, *J. Energy Chem.*, 2022, **71**, 351–369.
- 5 European Commission, *Critical Raw Materials Resilience: Charting a Path towards greater Security and Sustainability*, European Commission, Brussels, 2020.
- 6 U.S. Geological Survey, *2022 Final List of Critical Minerals*, Reston, VA, 2022.
- 7 A. D. Jara, A. Betemariam, G. Woldetinsae and J. Y. Kim, *Int. J. Min. Sci. Technol.*, 2019, **29**, 671–689.
- 8 J. Neumann, M. Petranikova, M. Meeus, J. D. Gamarra, R. Younesi, M. Winter and S. Nowak, *Adv. Energy Mater.*, 2022, **12**, 2102917.
- 9 A. Chernyaev, J. Partinen, L. Klemettinen, B. P. Wilson, A. Jokilaakso and M. Lundström, *Hydrometallurgy*, 2021, **203**, 105608.
- 10 M. Abdollahifar, S. Doose, H. Cavers and A. Kwade, *Adv. Mater. Technol.*, 2022, 2200368.
- 11 J. Liu, H. Shi, X. Hu, Y. Geng, L. Yang, P. Shao and X. Luo, *Sci. Total Environ.*, 2022, **816**, 151621.
- 12 Q. Cheng, Y. Han, Y. You, C. Hou, P. Perumal, B. Raj, M. Mohapatra and S. Basu, *J. Phys. Energy*, 2022, **4**, 045003.
- 13 H. Wang, Y. Huang, C. Huang, X. Wang, K. Wang, H. Chen, S. Liu, Y. Wu, K. Xu and W. Li, *Electrochim. Acta*, 2019, **313**, 423–431.
- 14 K. Liivand, M. Kazemi, P. Walke, V. Mikli, M. Uibu, D. D. Macdonald and I. Kruusenberg, *ChemSusChem*, 2021, **14**, 1103–1111.
- 15 W. Fang, J. Zhao, W. Zhang, P. Chen, Z. Bai and M. Wu, *J. Alloys Compd.*, 2021, **869**, 158918.
- 16 J. Sun, N. Wang, Z. Qiu, L. Xing and L. Du, *Catalysts*, 2022, **12**, 843.
- 17 I. Staffell, D. Scamman, A. Velazquez Abad, P. Balcombe, P. E. Dodds, N. Shah and K. R. Ward, *Energy Environ. Sci.*, 2019, **12**, 463–491.
- 18 H. J. Kim, H. Y. Kim, J. Joo, S. H. Joo, J. S. Lim, J. Lee, H. Huang, M. Shao, J. Hu, J. Y. Kim, B. J. Min, S. W. Lee, M. Kang, K. Lee, S. Choi, Y. Park, Y. Wang, J. Li, Z. Zhang, J. Ma and S. Il Choi, *J. Mater. Chem. A*, 2021, **10**, 50–88.
- 19 S. Ghosh and R. N. Basu, *Nanoscale*, 2018, **10**, 11241–11280.
- 20 X. X. Wang, M. T. Swihart and G. Wu, *Nat. Catal.*, 2019, **2**, 578–589.
- 21 Z. Liang, H. Zheng and R. Cao, *Sustainable Energy Fuels*, 2020, **4**, 3848–3870.
- 22 B. Mohanty, P. Bhanja and B. K. Jena, *Mater. Today Energy*, 2022, **23**, 100902.
- 23 Y. J. Wu, X. H. Wu, T. X. Tu, P. F. Zhang, J. T. Li, Y. Zhou, L. Huang and S. G. Sun, *Appl. Catal., B*, 2020, **278**, 119259.
- 24 F. Yu, Q. Ying, S. Ni, C. Li, D. Xue and Y. Yang, *Dalton Trans.*, 2021, **50**, 16185–16190.
- 25 C. Zhu, Q. Shi, B. Z. Xu, S. Fu, G. Wan, C. Yang, S. Yao, J. Song, H. Zhou, D. Du, S. P. Beckman, D. Su and Y. Lin, *Adv. Energy Mater.*, 2018, **8**, 1801956.
- 26 J. Zhang, Z. Xia and L. Dai, *Sci. Adv.*, 2015, **1**, 1500564.
- 27 T. W. Chen, G. Anushya, S. M. Chen, P. Kalimuthu, V. Mariyappan, P. Gajendran and R. Ramachandran, *Materials*, 2022, **15**, 458.
- 28 H. Pourfarzad, M. Shabani-Nooshabadi and M. R. Ganjali, *J. Power Sources*, 2020, **451**, 227768.
- 29 R. Jasinski, *Nature*, 1964, **201**, 1212–1213.
- 30 H. Jahnke, M. Schönborn and G. Zimmermann, *Top. Curr. Chem.*, 1976, **61**, 133–181.
- 31 P. Bogdanoff, I. Herrmann, M. Hilgendorff, I. Dorbandt, S. Fiechter and H. Tributsch, *J. New Mater. Electrochem. Syst.*, 2004, **7**, 85–92.

- 32 B. Chi, X. Zhang, M. Liu, S. Jiang and S. Liao, *Prog. Nat. Sci.: Mater. Int.*, 2020, **30**, 807–814.
- 33 R. Praats, M. Käärik, A. Kikas, V. Kisand, J. Aruväli, P. Paiste, M. Merisalu, A. Sarapuu, J. Leis, V. Sammelselg, J. C. Douglin, D. R. Dekel and K. Tammeveski, *J. Solid State Electrochem.*, 2021, **25**, 57–71.
- 34 R. Praats, M. Käärik, A. Kikas, V. Kisand, J. Aruväli, P. Paiste, M. Merisalu, J. Leis, V. Sammelselg, J. H. Zagal, S. Holdcroft, N. Nakashima and K. Tammeveski, *Electrochim. Acta*, 2020, **334**, 135575.
- 35 S. Ratso, M. Käärik, M. Kook, P. Paiste, V. Kisand, S. Vlassov, J. Leis and K. Tammeveski, *ChemElectroChem*, 2018, **5**, 1827–1836.
- 36 S. Ratso, A. Zitolo, M. Käärik, M. Merisalu, A. Kikas, V. Kisand, M. Rähn, P. Paiste, J. Leis, V. Sammelselg, S. Holdcroft, F. Jaouen and K. Tammeveski, *Renewable Energy*, 2021, **167**, 800–810.
- 37 T. Liu, S. Cai, Z. Gao, S. Liu, H. Li, L. Chen, M. Li and H. Guo, *Electrochim. Acta*, 2020, **335**, 135647.
- 38 Z. Meng, N. Chen, S. Cai, R. Wang, W. Guo and H. Tang, *Int. J. Energy Res.*, 2021, **45**, 6250–6261.
- 39 T. Yu, H. Xu, Z. Jin, Y. Zhang and H.-J. Qiu, *Appl. Surf. Sci.*, 2023, **610**, 155624.
- 40 L. Negahdar, F. Zeng, S. Palkovits, C. Broicher and R. Palkovits, *ChemElectroChem*, 2019, **6**, 5588–5595.
- 41 Q. Qin, P. Li, L. Chen and X. Liu, *ACS Appl. Mater. Interfaces*, 2018, **10**, 39828–39838.
- 42 D. Wang, P. Yang, H. Xu, J. Ma, L. Du, G. X. Zhang, R. Li, Z. Jiang, Y. Li, J. Zhang and M. An, *J. Power Sources*, 2021, **485**, 229339.
- 43 L. Yang, D. Wang, Y. Lv and D. Cao, *Carbon*, 2019, **144**, 8–14.
- 44 X. Wan, X. Guo, M. Duan, J. Shi, S. Liu, J. Zhang, Y. Liu, X. Zheng and Q. Kong, *Electrochim. Acta*, 2021, **394**, 139135.
- 45 H. Luo, W.-J. Jiang, S. Niu, X. Zhang, Y. Zhang, L.-P. Yuan, C. He, J.-S. Hu, H. Luo, C. He, W. Jiang, S. Niu, X. Zhang, Y. Zhang, L. Yuan and J. Hu, *Small*, 2020, **16**, 2001171.
- 46 B. Lv, S. Zeng, W. Yang, J. Qiao, C. Zhang, C. Zhu, M. Chen, J. Di and Q. Li, *J. Energy Chem.*, 2019, **38**, 170–176.
- 47 R. Wang, H. Yang, N. Lu, S. Lei, D. Jia, Z. Wang, Z. Liu, X. Wu, H. Zheng, S. Ali, F. Ma and S. Peng, *J. Chem. Eng.*, 2022, **433**, 134500.
- 48 R. Wang, J. Cao, S. Cai, X. Yan, J. Li, W. M. Yourey, W. Tong and H. Tang, *ACS Appl. Energy Mater.*, 2018, **1**, 1060–1068.
- 49 K. Kisand, A. Sarapuu, A. Kikas, V. Kisand, M. Rähn, A. Treshchalov, M. Käärik, H.-M. Piirsoo, J. Aruväli, P. Paiste, J. Leis, V. Sammelselg, A. Tamm and K. Tammeveski, *Electrochem. Commun.*, 2021, **124**, 106932.
- 50 D. M. Morales, M. A. Kazakova, S. Dieckhöfer, A. G. Selyutin, G. V. Golubtsov, W. Schuhmann and J. Masa, *Adv. Funct. Mater.*, 2020, **30**, 1905992.
- 51 R. Hao, J. Chen, Z. Wang, Y. Huang, P. Liu, J. Yan, K. Liu, C. Liu and Z. Lu, *J. Colloid Interface Sci.*, 2021, **586**, 621–629.
- 52 S. Guo, J. Hu, S. Luo, Y. Zhang, Z. Zhang, P. Dong, X. Zeng, M. Xu, L. Han, J. Yuan, C. Zhang and Y. Zhang, *Int. J. Hydrogen Energy*, 2022, **47**, 8348–8358.
- 53 M. Zhang, X. M. Hu, Y. Xin, L. Wang, Z. Zhou, L. Yang, J. Jiang and D. Zhang, *Sep. Purif. Technol.*, 2023, **308**, 122974.
- 54 C. Yang, Z. Jin, X. Zhang, X. Zheng and X. He, *ChemElectroChem*, 2022, **9**, e202101494.
- 55 H. Bian, W. Wu, Y. Zhu, C. H. Tsang, Y. Cao, J. Xu, X. Liao, Z. Lu, X. Y. Lu, C. Liu and Z. Zhang, *ACS Sustainable Chem. Eng.*, 2023, **11**, 670–678.
- 56 K. S. Bejigo, S. Natarajan, K. Bhunia, V. Elumalai and S. J. Kim, *J. Cleaner Prod.*, 2023, **384**, 135520.
- 57 D. Ruan, K. Zou, K. Du, F. Wang, L. Wu, Z. Zhang, X. Wu and G. Hu, *ChemCatChem*, 2021, **13**, 2025–2033.
- 58 K. Liivand, J. Sainio, B. P. Wilson, I. Kruusenberg and M. Lundström, *Appl. Catal., B*, 2023, **332**, 122767.
- 59 A. Chernyaev, J. Partinen, L. Klemettinen, B. P. Wilson, A. Jokilaakso and M. Lundström, *Hydrometallurgy*, 2021, **203**, 105608.
- 60 S. Ma, F. Liu, K. Li, Z. Chen, F. Chen, J. Wang, S. Zhong, B. P. Wilson and M. Lundström, *Hydrometallurgy*, 2022, **213**, 105941.
- 61 J. Hu, J. Zhang, H. Li, Y. Chen and C. Wang, *J. Power Sources*, 2017, **351**, 192–199.
- 62 D. Lyu, Y. Du, S. Huang, B. Y. Mollamahale, X. Zhang, S. W. Hasan, F. Yu, S. Wang, Z. Q. Tian and P. K. Shen, *ACS Appl. Mater. Interfaces*, 2019, **11**, 39809–39819.
- 63 M. Kazemi, K. Liivand, M. Prato, P. Vacek, J. Walmsley, S. Dante, G. Divitini and I. Kruusenberg, *Energy Fuels*, 2023, **38**, 659–670.
- 64 P. T. Araujo, M. Terrones and M. S. Dresselhaus, *Mater. Today*, 2012, **15**, 98–109.
- 65 J. Liang and Q. Yuan, *Appl. Surf. Sci.*, 2024, **648**, 159025.
- 66 S. S. Li, J. K. Wang, Q. Zhu, X. W. Zhao and H. J. Zhang, *Solid State Phenom.*, 2018, **281**, 807–812.
- 67 T. I. T. Okpalugo, P. Papakonstantinou, H. Murphy, J. McLaughlin and N. M. D. Brown, *Carbon*, 2005, **43**, 153–161.
- 68 NIST X-ray Photoelectron Spectroscopy (XPS) Database Number 20, Gaithersburg MD, 2000.
- 69 A. Kousar, I. Pande, L. F. Pascual, E. Peltola, J. Sainio and T. Laurila, *Anal. Chem.*, 2023, **95**, 2983–2991.
- 70 Y. Wang, Y. Nie, W. Ding, S. G. Chen, K. Xiong, X. Q. Qi, Y. Zhang, J. Wang and Z. D. Wei, *Chem. Commun.*, 2015, **51**, 8942–8945.
- 71 Y. Yao, H. Chen, C. Lian, F. Wei, D. Zhang, G. Wu, B. Chen and S. Wang, *J. Hazard. Mater.*, 2016, **314**, 129–139.
- 72 H. Jiang, J. Gu, X. Zheng, M. Liu, X. Qiu, L. Wang, W. Li, Z. Chen, X. Ji and J. Li, *Energy Environ. Sci.*, 2019, **12**, 322–333.
- 73 H. T. Larijani and M. Khorshidian, *Appl. Surf. Sci.*, 2019, **492**, 826–842.
- 74 A. Holewinski and S. Linic, *J. Electrochem. Soc.*, 2012, **159**, H864–H870.
- 75 X. Zhao, F. Li, R. Wang, J. M. Seo, H. J. Choi, S. M. Jung, J. Mahmood, I. Y. Jeon and J. B. Baek, *Adv. Funct. Mater.*, 2017, **27**, 1605717.
- 76 A. Sajeev, A. Sathyaseelan, K. Serbara Bejigo and S. Jae Kim, *J. Colloid Interface Sci.*, 2023, **637**, 363–371.

Appendix 2

Publication II

R. Praats, J. Sainio, M. Vikberg, L. Klemettinen, B.P. Wilson, M. Lundström, I. Kruusenberg, K. Liivand, Utilizing waste lithium-ion batteries for the production of graphite-carbon nanotube composites as oxygen electrocatalysts in zinc–air batteries, *RSC Sustainability* 3 (2025) 546–556.

PAPER

[View Article Online](#)
[View Journal](#) | [View Issue](#)Cite this: *RSC Sustainability*, 2025, 3, 546

Utilizing waste lithium-ion batteries for the production of graphite-carbon nanotube composites as oxygen electrocatalysts in zinc–air batteries†

Reio Praats,^a Jani Sainio,^{ib} Milla Vikberg,^c Lassi Klemettinen,^d Benjamin P. Wilson,^d Mari Lundström,^d Ivar Kruusenberg^a and Kerli Liivand^{ib} [✉]

The increasing global demand for energy has led to a rise in the usage of lithium-ion batteries (LIBs), which ultimately has resulted in an ever-increasing volume of related end-of-life batteries. Consequently, recycling has become indispensable to salvage the valuable resources contained within these energy storage devices. While various methods have been developed for the recovery of valuable cathode metals from spent LIBs, the anode's active material, graphite, is mostly lost from circulation. This study introduces an innovative method to valorize black mass leach residue, a waste product from industrial hydrometallurgical LIB recycling processes. Predominantly composed of graphite and minor metal residues, this material can be converted into a valuable bifunctional oxygen electrocatalyst. This transformation is achieved by doping the leach residue with nitrogen and through the incorporation of carbon nanotubes into the modified matrix, to enhance the surface area and conductivity of the produced electrocatalyst. These novel catalyst materials can enhance the oxygen reduction reaction and oxygen evolution reaction in zinc–air batteries (ZAB). The best catalyst material exhibited a commendable power density of 97 mW cm^{−2} in ZAB, demonstrating stable performance over 70 hours of continuous charge–discharge cycling. This research represents a significant advancement in the shrewd utilization of LIB recycling waste, which further enhances the goal of closed-loop materials circularity.

Received 29th August 2024
Accepted 16th December 2024

DOI: 10.1039/d4su00526k

rsc.li/rscsus

Sustainability spotlight

This study presents a novel approach to valorizing black mass leach residue, a waste product from lithium-ion battery (LIB) recycling, by converting it into a high-performance bifunctional oxygen electrocatalyst. This research advances global sustainability by recycling end-of-life LIBs into valuable materials, directly supporting SDG 12 (responsible consumption and production) through waste reduction and conservation of critical resources like graphite. By upcycling LIB leach residue into oxygen electrocatalysts for use in zinc–air batteries and fuel cells, the study also promotes SDG 7 (affordable and clean energy). Furthermore, it aligns with SDG 13 (climate action) and SDG 15 (life on land) by reducing waste, fostering green energy technologies, and minimizing environmental impacts associated with resource extraction.

Introduction

As the global production of Li-ion batteries (LIBs) continues to rise, driven by the escalating demand for electric vehicles (EVs),

portable electronics, and renewable energy storage solutions, the imperative for efficient end-of-life (EoL) LIB recycling practices has become increasingly pronounced. For example, the demand for LIBs in EVs increased to 550 GW h in 2022, which was equivalent to a year-on-year increase of approximately 65%.¹ Such a rapid rate of increase has raised concerns about the environmental impact related to all aspects of LIBs production, use and EoL management, where incorrect disposal or inefficient treatment methods can be potentially hazardous or lead to a loss of critical resources like Li, Co, Ni, Mn, Al, Cu, and graphite.^{2,3} In 2021, the global LIBs recycling capacity estimated to be 180 kT per year, of which 100 kT was based in China.² Currently LIB recycling typically comprises of mechanical pre-treatment (discharging, dismantling, crushing, sieving,

^aNational Institute of Chemical Physics and Biophysics, Akadeemia tee 23, 12618 Tallinn, Estonia. E-mail: kerli.liivand@kbfi.ee

^bDepartment of Applied Physics, School of Science, Aalto University, P. O. Box 15100, 00076 Aalto, Finland

^cDepartment of Chemistry and Materials Science (CMAT), School of Chemical Engineering, Aalto University, P. O. Box 16100, 00076 Aalto, Finland

^dDepartment of Chemical and Metallurgical Engineering (CMET), School of Chemical Engineering, Aalto University, P. O. Box 16200, 00076 Aalto, Finland

† Electronic supplementary information (ESI) available. See DOI: <https://doi.org/10.1039/d4su00526k>



magnetic separation *etc.*) followed by hydrometallurgical and/or pyrometallurgical processes to recover valuable metals from the black mass.^{3,4} In many cases, hydrometallurgical treatment of spent LIB (SLIB) waste results in a black mass leach residue, which is mainly comprised of graphite (used as an anode active material), Cu/Al from the current collectors as well as other insoluble materials like binder and separator, and some undissolved cathode active materials.⁵ There is about 20 wt% of graphite in LIBs which is often unrecovered and is discarded as waste after the recycling process. Recycling graphite is important for both preserving the environment and conserving resources.^{6,7} Both the European Commission and the US government have recently listed natural graphite (NG) as a critical material, recognizing its limited number of mining locations worldwide – with China responsible for about 67% of current global production.^{8–10} Synthetic graphite is produced from unsaturated carbons, which are heated to 2500 °C, making this process more CO₂ intensive and generally more expensive than production of NG.^{11,12} Therefore, there is an urgent need for the recovery and reuse of graphite from EoL LIBs to help reduce reliance on diminishing primary resources. The global transition towards more sustainable and environmentally responsible energy sources has sparked a growing interest in the development of efficient and eco-friendly energy conversion technologies like fuel cells and metal–air batteries. Within this domain the advancement of oxygen electrocatalysts plays a pivotal role in the development and commercialisation of these electrochemical devices.^{13–15} Presently, the most effective catalysts for enhancing the oxygen reduction reaction (ORR) are comprised of platinum (Pt) or Pt-alloys supported on carbon carriers.¹⁶ Similarly, for the oxygen evolution reaction (OER), metallic oxides such as RuO₂ and IrO₂ have demonstrated superior performance.¹⁷ While such catalysts exhibit high efficiency, they encounter challenges related to their stability under harsh conditions, which is compounded by reliance on expensive platinum-group metals (PGMs) that renders them commercially undesirable.^{17–19} Consequently, the need for more cost-effective and efficient bifunctional oxygen electrocatalysts has led the scientific community to explore alternative materials and methods for energy conversion and storage. Graphite-based and derived materials—including fullerenes, carbon nanotubes (CNTs), and graphene—have been the subject of intense investigation in recent years due to their potential applications as electrocatalysts or support materials for electrocatalysts. This interest can be attributed to their favourable electrical properties, high specific surface area, and the ability to undergo surface functionalisation.²⁰ For instance, metal–nitrogen–carbon (M–N–C) materials have emerged as highly promising oxygen electrocatalysts for the substitution of their PGM-based counterparts, due to their unique structural and compositional features.^{21,22} It is well known that C–N bonds exhibit good electrocatalytic activity towards ORR and this phenomenon derives from the more electronegative N-atoms, which distorts the associated electron cloud, making the C atoms relatively more positive. As a result of this electrochemical modification, the carbon can act as active O₂ adsorption site that leads to increased carbon disorder and enhanced electrical

conductivity.^{23,24} Typically, these active electrocatalysts incorporate not only carbon and nitrogen, but also transition metals, such as iron, cobalt, or manganese.^{23,25} The active centres for the ORR are primarily carbon-coordinated nitrogen atoms, and the presence of metals serve an important role in the formation of pyridinic nitrogen – which has been found to be one of the most active N-groups.²⁶ In contrast for OER, transition metals and metal oxides, together with pyridinic-N, are considered the active centres that drive the reaction.^{27,28} In addition, for bifunctional ORR/OER electrocatalysts, both types of reaction active sites are desirable, typically involving a combination of carbon–nitrogen and metal/metal oxides deposited within the carbon structure.^{22,23} One novel and promising avenue of new raw materials for the synthesis of bifunctional oxygen electrocatalysts lies in the upcycling of graphite from LIBs.^{6,29–33} In earlier studies, manually extracted graphite from SLIBs has been utilised as a raw material for the synthesis of different carbon support materials as well as nitrogen and metal doped electrocatalysts.^{31–33} Our research has previously demonstrated that industrial black mass leach residue can be used as a valuable precursor material for the synthesis of oxygen electrocatalysts.^{6,34} In the current study, we take this premise a step further by investigating the electrocatalytic activity of an oxygen electrocatalyst synthesised through the amalgamation of LIB leach residue (as a source of graphite and metals) with CNTs (that can act as spacers within the graphitic structure). To enhance the activity and durability of these catalyst materials, the introduction of different carbon structures as part of a composite is a viable approach that can be particularly effective when CNTs are used in conjunction with another carbon material.³⁵ The presence of CNTs not only act as conductive pathways, but also as an electron distributing agent on the surface through interaction with the support materials.³⁶ This concept is aimed at enhancing the specific surface area, porosity, and conductivity of the catalyst material, thereby improving electron mobility, and ultimately increasing the electrocatalytic activity towards both ORR and OER. The synthesis of oxygen electrocatalysts from leach residue presents a twofold advantage: it addresses the imperative for sustainable materials utilization by contributing to European raw material independency and answers to the demands of the new EU Battery Regulation about recycling a minimum of 65 wt% batteries by 2026, while concurrently advancing the development of efficient energy conversion technologies.³⁷

Experimental

Synthesis of the catalyst materials

The initial base material used in this research comprised of residue from an industrially produced battery black mass that had been subject to a hydrometallurgical process to extract the majority of cathode metals. Further details regarding the hydrometallurgical treatment of the black mass can be found elsewhere.⁷ The residual waste, known as black mass leach residue, served as the main starting material (*Raw Material*) for this study. This *Raw Material* primarily consists of graphite, with additional metal impurity remnants resulting from the



cathode active material and current collectors. For the synthesis of active catalysts, two different carbon materials were used, *Raw Material* and commercially available multi-walled carbon nanotubes (CNTs, >95%, XFM13, XFANO, China), to prepare the final composite materials. Both starting materials underwent a different pre-treatment step prior to their combination. The *Raw Material* went through pyrolysis at 800 °C for 1 hour under an Ar atmosphere (99.999%, Elme Messer Gaas, Estonia) to remove organics. The pyrolyzed *Raw Material* was named as *BR*. The CNTs were treated with a 1 : 1 mixture of 0.5 M H₂SO₄ and 0.5 M HNO₃ for 2 h at 50 °C and thereafter, 3 h at 80 °C. Finally, the CNTs were washed with Milli-Q water until a pH = 7 was achieved and then they were dried under vacuum. A mixture of carbon materials (*BR* + CNTs), nitrogen source dicyandiamide (DCDA, Sigma-Aldrich, Germany) and polyvinylpyrrolidone (PVP, Sigma Aldrich, Germany, *M_w*: 40 000), in a weight ratio of 1 : 20 : 0.1, in 3 ml of ethanol/water (2 : 1) was prepared and this mixture was then ball-milled with 5 mm ZrO₂ balls at 400 rpm for a total of one hour (in two separate 30 min sessions with a 5 min pause in between them). The resultant homogeneous material was then dried, before being pyrolyzed at 800 °C for 2 h under an Ar atmosphere. The ratio between carbon materials (*BR* to CNT) was varied: 25–75 wt%, 50–50 wt%, and 75–25 wt%. The acquired catalysts were named *BR25–CNT75–N*, *BR50–CNT50–N*, and *BR75–CNT25–N*, respectively. A detailed block flow diagram of the modification process is shown in Fig. 1. For comparison, pure *CNT–N* without the *BR* was also prepared and tested.

Physicochemical characterisation

The crystallinity and phase composition of the materials were assessed *via* powder X-ray diffraction analysis (XRD, Malvern Panalytical, UK) using a PANalytical X'Pert3 Powder XRD (Cu K α radiation, λ = 1.54182 Å), with step size 0.04 at 45 kV and 40 A. Microstructure images were taken with a MIRA3 scanning electron microscope (SEM, Tescan, Czech Republic) using secondary electrons (SE) at 5 kV acceleration voltage. Elemental mapping was conducted with an UltraDry Silicon Drift energy-dispersive spectrometer (EDS, Thermo Fisher Scientific, USA) at 10 kV acceleration voltage. HRTEM images were obtained with a double aberration-corrected microscope equipped with a 200 kV field-emission gun and X-ray EDS detector (JEOL JEM-2200FS, JEOL Ltd, Japan). Raman measurements were carried

out with a Renishaw inVia™ Confocal Raman Microscope (Renishaw, UK). The excitation laser (λ = 532 nm) was focused on the sample using a 50 \times objective of a Leica microscope. The scattered rays were collected at 180° and a diffraction grating 2400 gr mm^{−1} was applied to separate the wavelengths for detection with a Charge Coupled Device (CCD) detector. Spectral deconvolution was performed in OriginPro software by applying Voigt function. N₂ adsorption–desorption analysis (Anton Paar Novatouch LX4, Austria) was utilised to ascertain the specific surface area and porosity of samples cooled under liquid nitrogen conditions (77 K). Specific surface area was determined using the Brunauer–Emmett–Teller (BET) theory, whereas the pore size distribution was calculated using the Density Functional Theory (DFT) approach. X-ray photoelectron spectroscopy (XPS) was carried out with a Kratos Axis Ultra spectrometer with monochromated Al K α -radiation using a pass energy of 40 eV, X-ray power of 150 W and an analysis area of approximately 700 μ m \times 300 μ m. The sp² carbon 1s peak at 284.5 eV has been used as a binding energy reference. The elemental composition was determined from peak areas of high-resolution core level spectra after Shirley background subtraction using equipment specific sensitivity factors.

Electrochemical RDE testing

The ORR and OER were studied using rotating disc electrode (RDE) method utilizing a Gamry 1010E potentiostat/galvanostat, which employed a 3-electrode setup. The reference electrode used was Ag/AgCl (3 M KCl), with a graphite rod serving as the counter electrode for ORR and a Pt-wire for OER. A glassy carbon (GC, *S* = 0.2 cm²) electrode coated with selected catalyst material was used as a working electrode. The RDE setup used an Origalys speed control unit and rotator with rotation rates between 3600 and 400 rpm. The prepared catalyst ink had a catalyst concentration of 2 mg ml^{−1} in ethanol, containing 1 μ l mg_{catalyst}^{−1} of 5 wt% Nafion™ solution as an ionomer. Subsequently, 4 \times 5 μ l of catalyst ink was deposited onto cleaned GC electrodes, resulting in a catalyst loading of 0.2 mg cm^{−2}. For better comparison, both *Raw Material* and *CNT–N* were also subjected to testing; the loading for *CNT–N* was set at 0.1 mg cm^{−2} and all recorded potentials were converted to *vs.* the reversible hydrogen electrode (RHE) using the Nernst equation:

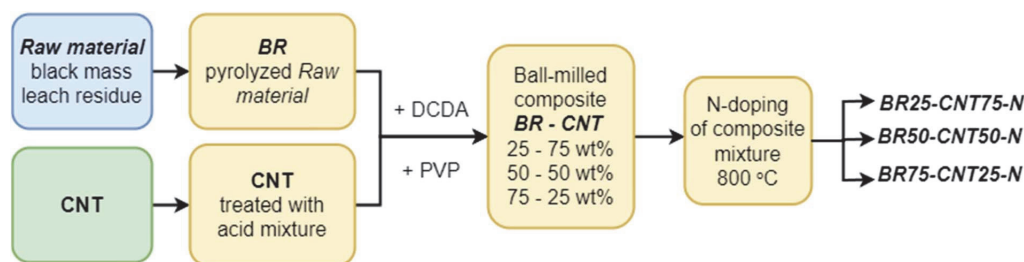


Fig. 1 Block flow diagram of the catalyst preparation.



$$E(\text{RHE}) = E_{\text{Ag/AgCl}} + 0.059\text{pH} + E_{\text{Ag/AgCl}}^0 \quad (1)$$

where $E_{\text{Ag/AgCl}}$ represents the experimentally measured potential vs. Ag/AgCl ($E_{\text{Ag/AgCl}}^0 = 0.210$ V at 25 °C).

The ORR tests were conducted in an oxygen (Elme Messer Gaas, 5.0) saturated 0.1 M KOH solution at room temperature with a constant O₂ gas flow over the solution and all experiments were controlled *via* Gamry Instruments Framework software. For OER measurements, N₂-saturated (Elme Messer Gaas, 5.0) 1 M KOH solution at room temperature was used, and like ORR, a constant gas flow over the solution was maintained. The *iR*-drop in the OER polarization curves was compensated by adjustment for the systems ohmic resistance that was determined from Electrochemical Impedance Spectroscopy data collected in the frequency range of 100 kHz to 0.01 Hz at the open circuit potential. The resistance was derived from the Nyquist plot by identifying the point where the imaginary part of the impedance reached zero, obtaining the real part as the resistance value. The OER overpotential (mV) was calculated by using $(E_{\text{experimental}}(\text{vs. RHE}) - 1.229 \text{ V}) \times 1000$. To evaluate the electrocatalytic activity, at least three sets of RDE measurements, each utilizing three electrodes, were performed for each catalyst material synthesized.

Zinc–air battery testing

For zinc–air battery (ZAB) experiments, a custom-made test cell was used. The air electrode, with an active surface area of 1.038 cm², comprised a gas diffusion layer (GDL, Sigracet 28BC by SGLCarbon, Germany) and a catalyst layer, with loading of 1 mg cm^{−2}, coated on the GDL. For comparison CNT-*N* material had a final loading of 0.5 mg cm^{−2}, matching the CNT loading used in the studies of the composite material. A Ti mesh served as the air electrode current collector. A commercial catalyst of 20% PtRu (1 : 1 ratio) on carbon support (FuelCellstore, USA) was utilized as an air electrode benchmark catalyst material. The ZAB cell used 6 M KOH + 0.2 M Zn(Ac)₂ as an electrolyte and a polished Zn plate (1 mm, 99.9%) as the other electrode. ZAB tests were carried out at room temperature using a PGSTAT30 potentiostat/galvanostat (Metrohm Autolab, The Netherlands) controlled by NOVA 2.1.5 software. Charge–discharge cycling involved alternating 30 minute charge and discharge processes at a current density of 10 mA cm^{−2}. Specific energy density and capacity were determined through complete discharge tests with a current density of 5 mA cm^{−2}, calculated based on the consumed Zn mass. At least three separate ZAB cells were tested for each catalyst material to evaluate the maximum discharge power density.

Results

Physicochemical characterisation of samples

XRD diffractogram (Fig. S1 in ESI† file) of the leach residue (*Raw Material*) prior to pyrolysis revealed a graphite-rich content with various residues from battery components: Li_{1.44}Co₃O₆, LiMn₂O₃, and CoO – originating from the cathode; Cu and Al₂O₃ – from current collectors and SiO₂ – from additions to anode

composition that are used to increase cell energy.³⁸ A similar combination of elements was also detected by SEM-EDS analysis (Fig. S2†), which additionally revealed the presence of F – resulting from the PVDF binder – and which was subsequently removed during the pyrolysis of the Raw Material. A more detailed description of the Raw Material composition can be found from our previous study.³⁴ Fig. 2 displays XRD diffractograms of the composite materials prepared from the *BR* and CNTs as well as pure CNT-*N* after the synthesis in comparison with standard cards. All diffractograms exhibited a prominent graphitic carbon peak at 26.5°, with the intensity of this peak diminishing as the CNT content increased, reaching its lowest in the pure CNT-*N* material, where no recycled material was added. This indicates that the graphitic carbon peaks are directly related to the *BR* concentration in the composite. CNT-*N* prepared from the commercial CNTs did not indicate any metal peaks within its diffractogram. The pyrolysis process reduced the metal oxides present in the *Raw Material* and thus *BR* displays the existence of more metallic forms, as evidenced, for example, by the emergence of metallic Co(0) peaks in the final composite materials with no indication of CoO. This transformation suggests the conversion of Co into Co–N–C active centres during the N-doping process.^{6,34}

Fig. S3† presents the SEM-SE micrographs of studied materials. CNT-*N* (Fig. S3a†) micrograph shows uniform CNT network. In the case of BR25–CNT75-*N* (Fig. S3b†), an extensive CNT network that includes the presence of some larger particles can be observed. In BR50–CNT50-*N* (Fig. S3c†) and BR75–CNT25-*N* (Fig. S3d†) materials the CNT network is less visible and lighter particles dispersed over the surface are noticeable. SEM-EDS analysis (Fig. S4–S6†) further reveals that a well dispersed mixture of CNT network and *BR* has been achieved in the case of

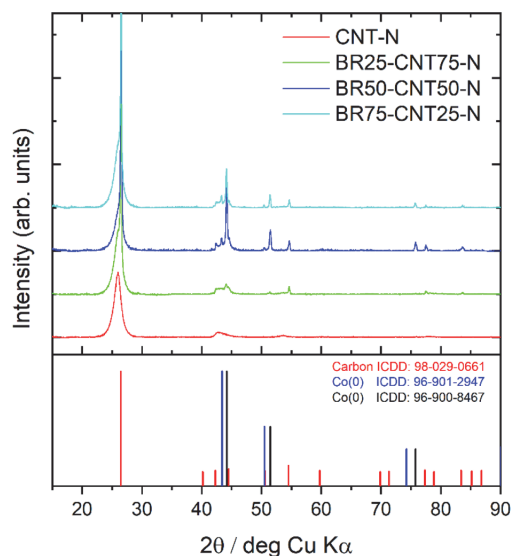


Fig. 2 XRD diffractograms of studied materials with standard cards.



the *BR50-CNT50-N* sample. In *BR75-CNT25-N* sample (Fig. S6†) larger metal agglomerates can be seen from the elemental mapping. From the battery metal residues Co has the highest content in all three composites, however, smaller amounts of Ni, Mn, Al, Cu and Zr were also detected, depending on the *BR* content in the final composite material.

The surface morphology and elemental composition of the prepared catalyst materials were also studied by TEM-EDS as shown in Fig. 3. TEM micrographs show extensive networks of CNTs with some metal and graphite agglomerates. Fig. 3a and S7† show that in the *CNT-N*, the CNT network is evenly distributed. In the case of composite materials (Fig. 3b–d and S8–S10†) some unevenly distributed larger, *ca.* 50–100 nm metal agglomerates as well as sizable graphite particles can be observed. The composite with the highest *BR* content (*BR75-CNT25-N*) had more areas with larger particles when compared to the other composite materials. TEM-EDS of *BR25-CNT75-N* in Fig. S8† shows evenly distributed CNTs with some 10–30 nm particles and several larger 50–100 nm particles also present. These larger particles in Fig. S8† EDS1 and EDS2 have a heterogeneous composition of C, O, Cu, Co, Fe originating from the *BR*. In contrast, Fig. S9† for *BR50-CNT50-N* shows encapsulated Co particles within the CNTs as well as a larger

50 nm Co and C area. Co particles can act as a catalyst during the nitrogen doping process for the formation of bamboo-structured carbon nanotubes with the Co particles being encapsulated into the nanotube (Fig. S9 location EDS1 and Fig. S10 location EDS1†).^{6,39} This demonstrates both the growth of bamboo CNTs as well as the distribution of metal residues and graphite particles. In the case of *BR75-CNT25-N* it was also possible to see bamboo nanotubes and encapsulated Co nanoparticles – as shown in Fig. S10† – but an additional dense population of *BR* metal and carbon fragments were also found to be present. The encapsulation of Co particles can increase the stability of Co particles in harsh environments which is necessary for good electrocatalysts.⁴⁰

For all samples displayed in Fig. S11,† the characteristic Raman modes of multiwalled carbon nanotubes can be distinguished.⁴¹ The three most prominent peaks are the first order G-band at approximately 1580 cm^{-1} , which are characteristic for graphitized sp^2 carbon materials, the defect induced D-band at around 1350 cm^{-1} originating from double resonant Raman process, and its overtone G'-band at approximately 2700 cm^{-1} . Additionally, a shoulder is observed on the G-band at approximately 1620 cm^{-1} associated as D'-band and a broad combination mode D + D' band at around 2950 cm^{-1} . Both are related

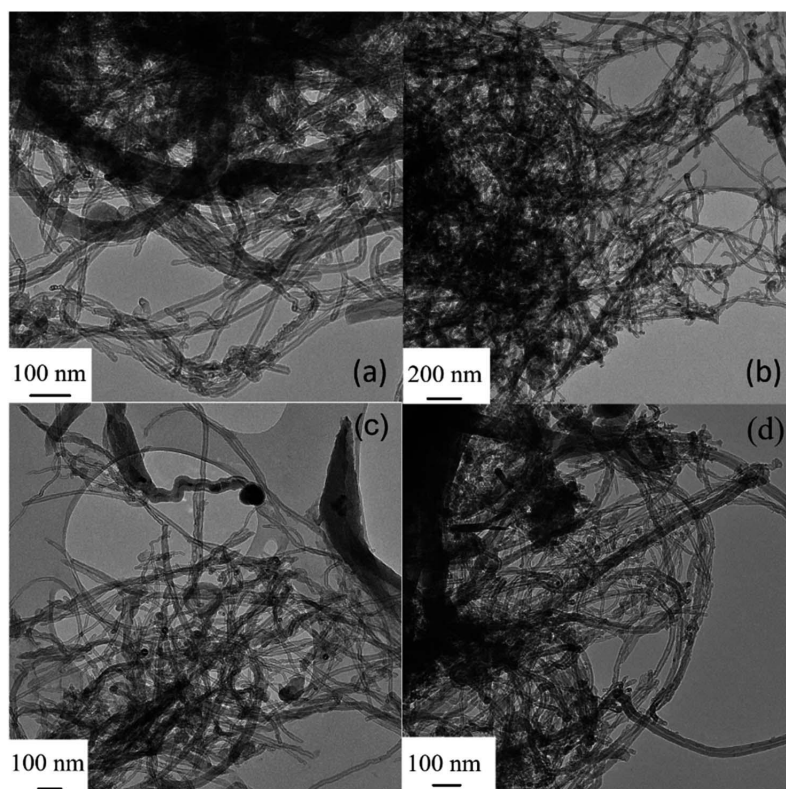


Fig. 3 TEM micrographs of (a) *CNT-N*, (b) *BR25-CNT75-N*, (c) *BR50-CNT50-N*, and (d) *BR75-CNT25-N* catalyst materials.



to defects.⁴¹ Acid treatment generally leads to a higher ratio between the intensities of the D- and G-bands (I_D/I_G).⁴¹ After a heat treatment, some of the graphitic structure is restored as can be observed from the I_D/I_G ratio decreasing from 0.89 for the acid treated CNT to 0.67 for the N-doped CNT-N. Doping by nitrogen most likely results in the observed downshift of the G- and D'-bands from 1580 cm^{-1} to 1575 cm^{-1} and from 1620 cm^{-1} to 1615 cm^{-1} , respectively.⁴² The I_D/I_G ratio for composite materials show that the degree of graphitization is slightly higher for materials with higher BR content as illustrated in Fig. S11,† but further changes in the Raman shifts are not observed for the composites with different BR ratios.

The specific surface area (SSA) of the composite catalyst materials exhibited a significant increase when compared to the initial *Raw Material*. Moreover, the SSA demonstrated an upward trend with increasing CNTs concentration within the composites, as indicated in Table 1. Fig. S12a† indicates that the composite catalysts have type IV isotherms with a narrow hysteresis loop indicating the presence of broad mesopores which continue to the macropores.⁴³ The pore size distribution in Fig. S12b† shows that the materials are mostly mesoporous with the pore sizes varying from 9 to 35 nm. The blending of CNTs into BR increases the ability to host more active centres and improves mass transport within the material.

XPS was used to study the chemical composition of the samples. Carbon, oxygen, nitrogen, and various metals (Co, Mn, Ni, Al, and Cu) were detected within the samples (Table 2). Fig. S13a† shows that the C 1s spectrum consists of a main asymmetric peak at 284.5 eV which can be assigned to sp^2 carbon. At binding energies between 285–289 eV there will be some additional contributions from other types of carbon-carbon, carbon-oxygen, and carbon-nitrogen bonding,^{44–46} although overall the C 1s spectra show no large variations between samples. Fig. 4 shows the N 1s and Co 2p spectra obtained for the samples. The N 1s spectra in Fig. 4a have been fitted assuming the presence of four types of N-functional groups: pyridinic-N, pyrrolic-N, graphitic-N and N-oxides (for fitting parameters see ref. 47 and 48). The pyridinic-N component will also contain contributions from N-Co bonds but due to the difference in concentrations of N and Co, the pyridinic-N will be more prominent. Based on the fitting, most of the nitrogen is either in pyridinic or pyrrolic form for all samples (Table S1†).

Comparison of the different nitrogen type ratios found within the samples show similar results, except for BR50–CNT50–N which has a higher concentration of graphitic-N and N-oxide and less pyrrolic-N. The Co 2p spectra (Fig. 4b) have been fitted with two components: one for metallic Co and one for Co-N which can also contain contributions from cobalt oxides and/or hydroxides.^{49–51} Due to the overlap of the Co-N

Table 2 Atomic concentrations (at%) of elements based on XPS data

Sample	C	O	N	Co	Mn	Ni	Al	Cu
N-CNT	88.0	3.2	8.1	0.3	—	—	0.2	—
BR25–CNT75–N	86.5	3.9	7.8	0.5	0.2	0.1	0.6	0.2
BR50–CNT50–N	87.2	5.6	4.7	0.8	0.3	0.1	0.8	0.3
BR75–CNT25–N	88.7	6.2	2.2	0.2	0.3	0.1	1.8	0.3

and CoO_x peaks they are represented by only one peak (with fitting parameters for Co(II) ⁴⁹). All Co 2p spectra measured can be explained almost solely with this peak. Since no cobalt oxide is observed in XRD for these samples, we attribute this peak to the presence of Co–N. Overall, some clear trends can be determined between the different samples: the amount of nitrogen decreases, and the amount of oxygen increases when going from CNT-N to BR75–CNT25–N. Additionally, the highest Co content on the composite surface was found to be for BR50–CNT50–N sample, following the same trend as shown with SEM-EDS and TEM analysis, higher BR content in the composites starts to favour larger agglomerates and limit the dispersion of Co. Uniformly distributed particles increase the active surface area of electrocatalysts.⁵²

Electrocatalytic activity towards ORR and OER

The electrocatalytic activity of the prepared catalyst materials were initially tested towards the ORR in O_2 saturated 0.1 M KOH solution (Fig. 5a). For a better comparison, *Raw Material* and CNT-N were also tested under same conditions and the electrochemical characteristics are shown in Table 3. The highest onset potential (E_{onset} , $j = 0.1 \text{ mA cm}^{-2}$) was demonstrated by the BR50–CNT50–N catalyst with a value of 0.914 V vs. RHE, followed by BR25–CNT75–N and BR75–CNT25–N catalyst materials. In comparison, CNT-N and *Raw Material* had an E_{onset} of 0.884 V and 0.757 V, respectively, proving the successful modification of the starting materials. The highest half-wave potential ($E_{1/2}$) was also recorded for BR50–CNT50–N material at 0.830 V and the limiting current density (j) of the same material was only surpassed by BR25–CNT75–N (5.41 mA cm^{-2} vs. 5.01 mA cm^{-2}). The presence of Ni, Mn, and Co in the *Raw Material* facilitated the formation of C–N_x and M–N_x moieties and the highest concentration of pyridinic-N was determined for the BR50–CNT50–N catalyst, as indicated by increased level of ORR activity.²³

BR25–CNT75–N and CNT-N had similar polarization curve profiles, which comes from the increased surface area and porosity compared to the other composite materials, leading to higher j and $E_{1/2}$ values. Fig. S14a, c, e and g† show the ORR polarization curves measured at different RDE rotation speeds and their related K–L plots (Fig. S14b, d, f and h†). Results

Table 1 SSA of the studied materials

Name of the sample	Raw material	CNT-N	BR25–CNT75–N	BR50–CNT50–N	BR75–CNT25–N
S_{BET} ($\text{m}^2 \text{ g}^{-1}$)	2.9	63.2	52.9	42.1	27.1



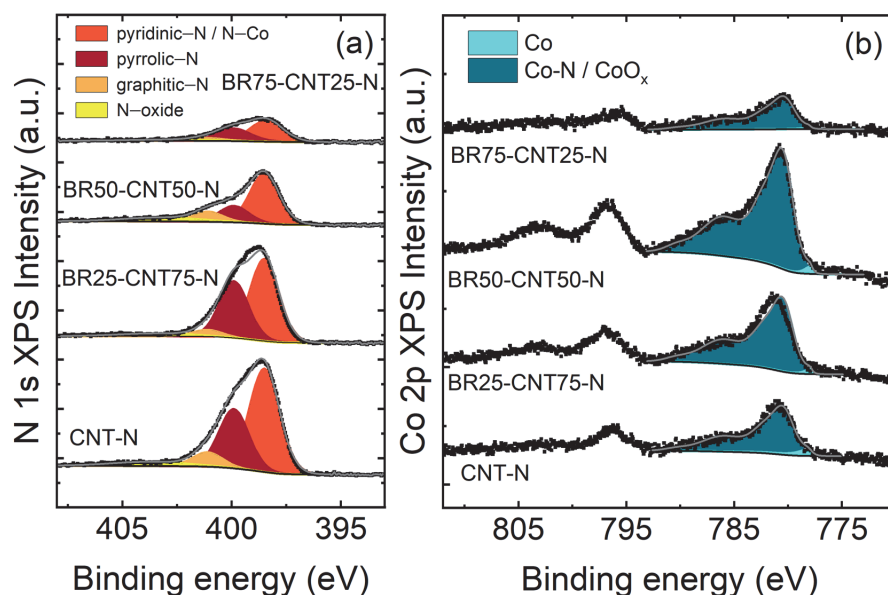


Fig. 4 X-ray photoelectron spectra of the samples: (a) N 1s region and (b) Co 2p region.

demonstrate that all are linear, parallel and have an intercept close to 0 indicating that the process is mass-transfer limited. The *BR50-CNT50-N* catalyst had an n -value close to 4 which was stable over the studied potential range – showing a $4e^-$ pathway for O_2 reduction. In contrast, for *BR25-CNT75-N* the n was over 4 and for *CNT-N* and *BR75-CNT25-N* the n values were below 4 and gradually decreased at higher potentials, which potentially led to hydrogen peroxide formation via $2e^-$ O_2 reduction. While there remains uncertainty regarding the specific sites that facilitate the 2-electron and/or 4-electron pathways for the ORR, it is suggested that defects within the carbon lattice, particularly those near the ether or carboxylic acid sites, tend to enhance hydrogen peroxide formation.^{53,54} Secondly, Co-moieties on the

other hand reduce the oxygen molecule directly through the $4e^-$ pathway to H_2O .²⁵ Cu and Al, which were also found in the *BR* containing materials, are usually not as active towards the ORR as Co, Fe and Ni.^{55,56} In addition, the lower catalytic activity measured for *BR75-CNT25-N* was attributed to the lack of CNT's spacers and insufficient surface area for active centre formation, as well as the higher amount and larger size of metal agglomerates, especially Al. The EIS measurements (Fig. S15a†) were performed on *BR50-CNT50-N*, *N-CNT*, and the *Raw Material* to investigate the influence of CNT addition on the conductivity of the carbon support material. The fitted and calculated charge transfer resistance values indicate that incorporating CNTs enhances the conductivity of the material

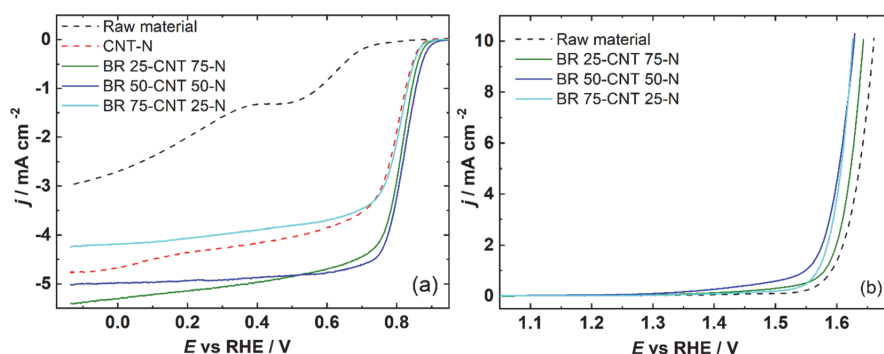


Fig. 5 Comparative (a) ORR polarization curves of studied catalyst materials at 1600 rpm in O_2 saturated 0.1 M KOH solution and (b) OER polarization curves of studied catalyst materials at 1600 rpm in N_2 saturated 1 M KOH solution.



Table 3 Electrochemical characteristics of studied catalyst materials

Catalyst	E_{onset} (V vs. RHE)	$E_{1/2}$ (V vs. RHE)	j (mA cm ⁻²)	OER η (mV)@10 mA cm ⁻²	$\Delta E = E_{\text{OER}}(@10 \text{ mA cm}^{-2}) - E_{\text{ORR}}(@E_{1/2})$ (V vs. RHE)
Raw material	0.757	0.342	2.96	431	1.318
CNT-N	0.884	0.797	4.76	—	—
BR75-CNT25-N	0.888	0.811	4.23	397	0.815
BR50-CNT50-N	0.914	0.830	5.02	398	0.799
BR25-CNT75-N	0.898	0.816	5.41	414	0.827

compared to the initial *Raw Material*. These findings support the hypothesis that the use of CNTs not only increases the conductivity of the material but also enhances surface area and porosity, enabling the hosting of more active centres and the inclusion of metals from the *BR*.

Fig. 5b shows the OER activity of the same catalyst material. As was the case for ORR, *BR50-CNT50-N* demonstrated the highest activity for OER with E (V)@10 mA cm⁻² = 1.627 V vs. RHE. Similar activity was also found for *BR75-CNT25-N* catalyst material, whilst all others were slightly lower. Such results were to be expected as in OER, the active centres comprise of metal oxides that are more prevalent in the materials with higher *BR* content. Nevertheless, the pure *Raw Material* demonstrated the lowest activity even though it has a high content of metals and metal oxides. However, as these metals/metal oxides are not incorporated within the carbon matrix they can be both easily

dissolved within the solution and have a very low surface area when compared to the other catalyst materials examined in this study. Co nanoparticles encapsulated into bamboo nanotubes are protected from corrosion; therefore, materials containing such structures can exhibit higher ORR/OER activity.

For all composite catalyst studied, the ΔE was calculated using formula $\Delta E = E_{\text{OER}}(@10 \text{ mA cm}^{-2}) - E_{\text{ORR}}(@E_{1/2})$ shown in Table 3. Out of all the studied catalysts, the *BR50-CNT50-N* showed the lowest ΔE value at 0.799 V, which shows good bifunctionality of the catalyst materials and even being comparable with some of the best performing catalyst materials shown in literature.⁵⁷ Overall, all the N-doped catalysts showed good activity towards the ORR and OER thanks to the synergistic effect of heteronuclear metal doping,⁵⁸ especially from the Co nanoparticles encapsulated into bamboo nanotubes.

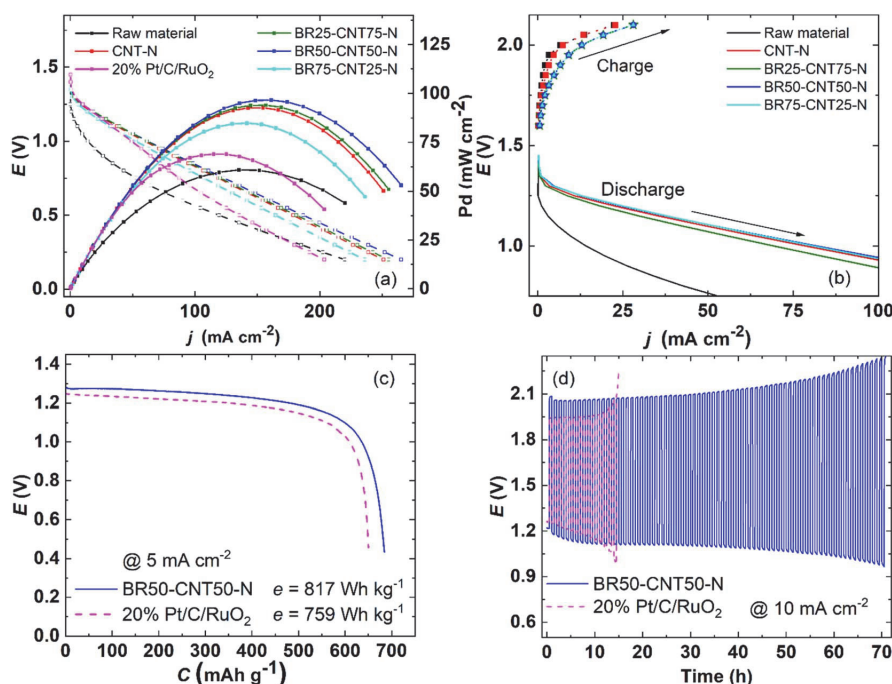


Fig. 6 ZAB results for studied catalysts: (a) discharge polarization curves and power density curves, (b) charge and discharge polarization curves, (c) complete discharge test at 5 mA cm⁻², (d) galvanostatic charge/discharge cycling at 10 mA cm⁻² with 30 min discharge and charge time.



Zinc-air battery air electrode catalyst performance

The prepared catalyst materials were also assessed for their bifunctionality towards oxygen reduction and evolution reaction by incorporation as an air electrode catalyst material in a zinc-air battery. For comparison, a commercial benchmark 20% PtRu/C catalyst was also used as an air electrode catalyst material. All the N-doped catalyst materials examined demonstrated superior discharge powers in comparison to the commercial catalyst (Fig. 6a). The highest power density of 97 mW cm^{-2} at $j = 161 \text{ mA cm}^{-2}$ was shown by *BR50-CNT50-N*, which was expected based on the half-cell test results. Moreover, the maximum power density also exceeded the commercial catalyst's performance by 28 mW cm^{-2} under the same conditions. The power density of all nitrogen-doped materials demonstrated notable performance, highlighting the enhancing capability of nitrogen centres. Additionally, the two composite catalysts (*BR50-CNT50-N* and *BR25-CNT75-N*) exhibited an even higher power density than *CNT-N*, highlighting the synergy between metal and nitrogen active centres. The open circuit potential (OCP) was consistent among all the investigated materials, with only *BR75-CNT25-N* exhibiting a slightly lower value, as illustrated in Fig. S16.† Fig. 6b illustrates the polarization curves for both discharge and charge processes. All examined materials exhibited nearly identical discharge polarization curves, except *Raw Material* which had lower discharge potential. Nevertheless, there was a slight discrepancy in the charge polarization curves, with *CNT-N* and the *Raw Material* displaying marginally higher charge voltages than the composite catalyst. This higher charge potential for the *Raw Material* can be attributed to the presence of non-stable metals in the harsh electrolyte environment, in contrast there are no added metals in the *CNT-N* material, therefore neither of these materials are suitable for the promotion of OER activity.²⁸ The specific capacity and energy were determined for both the commercial catalyst and *BR50-CNT50-N* catalyst based on data obtained during the complete discharge tests (Fig. 6c). For *BR50-CNT50-N*, the specific capacity and energy were 684 mA h g^{-1} and 817 W h kg^{-1} , respectively. In comparison, the 20% PtRu/C catalyst exhibited specific capacity and energy of 650 mA h g^{-1} and 759 W h kg^{-1} . *BR50-CNT50-N* showed outstanding stability during galvanostatic charge-discharge cycling test for 70 hours, compared to the commercial catalyst, which retained activity for just over 10 hours of continuous cycling as is shown in Fig. 6d. This significant difference in the observed stability and recorded activity between *BR50-CNT50-N* and the 20% PtRu/C catalyst results from the presence of the encapsulated Co particles and Co-N_x active centres within the composite catalyst material.

Conclusions

In this study, a methodology to repurpose lithium-ion battery hydrometallurgical recycling residue as a metal and carbon precursor for the synthesis of active bi-functional oxygen electrocatalysts is outlined. The metal residues in the recycling waste fraction are utilised to achieve *in situ* metal-doping of the

catalyst support material. To achieve this, the graphite rich *Raw Material* was combined with carbon nanotubes and nitrogen-doped through ball-milling and pyrolysis processes, to enhance electrocatalytic activity and stability by increasing surface area and through the formation of carbon-nitrogen and metal active centres within the resultant composite materials. Three different ratio combinations of *Raw Material* and CNTs were investigated, with the *BR50-CNT50-N* catalyst material demonstrating the highest electrocatalytic activity.

The notable ORR activity is attributed to the formation of pyridinic nitrogen groups in parallel with a larger surface area, which can host a higher concentration of these active centres. Enhanced activity toward the OER was accomplished by integrating metals into the carbon framework, particularly Co nanoparticles encapsulated within bamboo-like CNTs and through formation of Co-N_x active centres. This improved the activity and, notably, the stability of the catalyst materials, particularly under the harsh alkaline conditions encountered during electrochemical testing. Additionally, the practical applicability of the synthesized catalyst materials was demonstrated by their use as air-electrode catalysts in a rechargeable Zn-air battery. The *BR50-CNT50-N* catalyst exhibited the highest peak power density of 97 mW cm^{-2} and exceptional stability during charge-discharge cycling at a 10 mA cm^{-2} test for approximately 70 hours, significantly outperforming the commercial 20% PtRu/C catalyst. The research work detailed here further exhibits the value of Li-ion battery recycling residue as a resource for the preparation of active M-N-C catalyst materials. By utilizing industrial recycling waste and promoting responsible resource utilization, this approach introduces an innovative and cost-effective method that can repurpose the graphite-rich leach residue fraction from lithium-ion battery recycling process for the development of green energy conversion and storage devices.

Data availability

The data supporting this article has been included as part of the ESI.†

Author contributions

R. P.: conceptualization, investigation, and writing. J. S.: investigation (XPS) and writing. M. V.: investigation (Raman) and writing. L. K.: investigation (SEM-EDS) and writing. B. P. W.: resources and writing. M. L.: resources and writing. I. K.: supervision. K. L.: conceptualization, resources, investigation, supervision, and writing.

Conflicts of interest

There are no conflicts to declare.

Acknowledgements

This research was supported by the Estonian Research Council (PSG926, EAG248), and the Business Finland BatCircle3.0



project (Grant Number 1754/31/2024). In addition, this work was funded by the Ministry of Education and Research through the Centre of Excellence in Circular Economy for Strategic Mineral and Carbon Resources (01.01.2024–31.12.2030, TK228). Use of the facilities provided by Aalto University's OtaNano – Nanomicroscopy Center (Aalto-NMC) and RawMatters Research Infrastructure (RAMI) funded by the Research Council of Finland are also acknowledged as is Hua Jiang for their assistance with the TEM measurements.

References

- 1 IEA, *Global EV Outlook 2023*, Paris, 2023.
- 2 IEA, *The Role of Critical Minerals in Clean Energy Transitions*, Paris, 2021.
- 3 J. Neumann, M. Petranikova, M. Meeus, J. D. Gamarra, R. Younesi, M. Winter and S. Nowak, *Adv. Energy Mater.*, 2022, **12**, 2102917.
- 4 O. Velázquez-Martínez, J. Valio, A. Santasalo-Aarnio, M. Reuter and R. Serna-Guerrero, *Batteries*, 2019, **5**, 68.
- 5 A. Chernyaev, B. P. Wilson and M. Lundström, *Sci. Rep.*, 2021, **11**(1), 1–8.
- 6 K. Liivand, J. Sainio, B. P. Wilson, I. Kruusenberg and M. Lundström, *Appl. Catal., B*, 2023, **332**, 122767.
- 7 A. Chernyaev, J. Partinen, L. Klemettinen, B. P. Wilson, A. Jokilaakso and M. Lundström, *Hydrometallurgy*, 2021, **203**, 105608.
- 8 *Study on the Critical Raw Materials for the EU 2023 – Final Report*, Brussels, 2022.
- 9 U.S. Geological Survey, *2022 Final List of Critical Minerals*, Reston, VA, 2022.
- 10 *Critical Raw Materials Resilience: Charting a Path towards Greater Security and Sustainability*, Brussels, 2020.
- 11 J. Asenbauer, T. Eisenmann, M. Kuenzel, A. Kazzazi, Z. Chen and D. Bresser, *Sustain. Energy Fuels*, 2020, **4**, 5387–5416.
- 12 P. Engels, F. Cerdas, T. Dettmer, C. Frey, J. Hentschel, C. Herrmann, T. Mirfabrikar and M. Schueler, *J. Cleaner Prod.*, 2022, **336**, 130474.
- 13 W. Fang, J. Zhao, W. Zhang, P. Chen, Z. Bai and M. Wu, *J. Alloys Compd.*, 2021, **869**, 158918.
- 14 J. Sun, N. Wang, Z. Qiu, L. Xing and L. Du, *Catalysts*, 2022, **12**, 843.
- 15 I. Staffell, D. Scamman, A. Velazquez Abad, P. Balcombe, P. E. Dodds, P. Ekins, N. Shah and K. R. Ward, *Energy Environ. Sci.*, 2019, **12**, 463–491.
- 16 S. Ghosh and R. N. Basu, *Nanoscale*, 2018, **10**, 11241–11280.
- 17 D. Agrawal, N. Mahajan, S. A. Singh and I. Sreedhar, *Fuel*, 2024, **359**, 130131.
- 18 X. X. Wang, M. T. Swihart and G. Wu, *Nat. Catal.*, 2019, **2**, 578–589.
- 19 B. Mohanty, P. Bhanja and B. K. Jena, *Mater. Today Energy*, 2022, **23**, 100902.
- 20 S. He, M. Wu, S. Li, Z. Jiang, H. Hong, S. G. Cloutier, H. Yang, S. Omanovic, S. Sun and G. Zhang, *Molecules*, 2022, **27**, 8644.
- 21 H. Chang, S. Cong, L. Wang and C. Wang, *Nanomaterials*, 2022, **12**, 3834.
- 22 P. Stelmachowski, J. Duch, D. Sebastián, M. J. Lázaro and A. Kotarba, *Materials*, 2021, **14**, 4984.
- 23 G. Wu, A. Santandreu, W. Kellogg, S. Gupta, O. Ogoke, H. Zhang, H. L. Wang and L. Dai, *Nano Energy*, 2016, **29**, 83–110.
- 24 J. Duan, S. Chen, M. Jaroniec and S. Z. Qiao, *ACS Catal.*, 2015, **5**, 5207–5234.
- 25 Y. Zheng, D. S. Yang, J. M. Kweun, C. Li, K. Tan, F. Kong, C. Liang, Y. J. Chabal, Y. Y. Kim, M. Cho, J. S. Yu and F. Cho, *Nano Energy*, 2016, **30**, 443–449.
- 26 J. Liang and Q. Yuan, *Appl. Surf. Sci.*, 2024, **648**, 159025.
- 27 J. Heese-Gärtlein, A. Rabe and M. Behrens, *Z. Anorg. Allg. Chem.*, 2021, **647**, 1363–1372.
- 28 T. Naito, T. Shinagawa, T. Nishimoto and K. Takanabe, *Inorg. Chem. Front.*, 2021, **8**, 2900–2917.
- 29 L. Alcaraz, C. Díaz-Guerra, J. Calbet, M. L. López and F. A. López, *Materials*, 2022, **15**, 3246.
- 30 S. Natarajan, M. L. Divya and V. Aravindan, *J. Energy Chem.*, 2022, **71**, 351–369.
- 31 K. Liivand, M. Kazemi, P. Walke, V. Mikli, M. Uibu, D. D. Macdonald and I. Kruusenberg, *ChemSusChem*, 2021, **14**, 1103–1111.
- 32 M. Kazemi, K. Liivand, M. Prato, P. Vacek, J. Walmsley, S. Dante, G. Divitini and I. Kruusenberg, *Energy Fuels*, 2023, **38**(1), 659–670.
- 33 D. Ruan, K. Zou, K. Du, F. Wang, L. Wu, Z. Zhang, X. Wu and G. Hu, *ChemCatChem*, 2021, **13**, 2025–2033.
- 34 R. Praats, A. Chernyaev, J. Sainio, M. Lundström, I. Kruusenberg and K. Liivand, *Green Chem.*, 2024, **26**, 2874–2883.
- 35 B. Fang, J. Yang, C. Chen, C. Zhang, D. Chang, H. Xu and C. Gao, *ChemCatChem*, 2017, **9**, 4520–4528.
- 36 Q. C. Wang, J. Wang, Y. P. Lei, Z. Y. Chen, Y. Song and S. Bin Luo, *Chin. J. Inorg. Chem.*, 2018, **34**, 807–822.
- 37 *Regulation (EU) 2023/1542 of the European Parliament and of the Council of 12 July 2023 Concerning Batteries and Waste Batteries, Amending Directive 2008/98/EC and Regulation (EU) 2019/1020 and Repealing Directive 2006/66/EC*, 2023.
- 38 L. Brückner, J. Frank and T. Elwert, *Metals*, 2020, **10**, 1107.
- 39 X. Wang, S. Jie and Z. Liu, *Mater. Chem. Phys.*, 2019, **232**, 393–399.
- 40 S. Wang, S. Chen, L. Ma and J. A. Zapien, *Mater. Today Energy*, 2021, **20**, 100659.
- 41 V. Likodimos, T. A. Steriotis, S. K. Papageorgiou, G. E. Romanos, R. R. N. Marques, R. P. Rocha, J. L. Faria, M. F. R. Pereira, J. L. Figueiredo, A. M. T. Silva and P. Falaras, *Carbon*, 2014, **69**, 311–326.
- 42 H. Liu, Y. Zhang, R. Li, X. Sun, S. Désilets, H. Abou-Rachid, M. Jaidann and L. S. Lussier, *Carbon*, 2010, **48**, 1498–1507.
- 43 K. S. W. Sing, D. H. Everett, R. A. W. Haul, L. Moscou, R. A. Pierotti, J. Rouquerol and T. Siemieniowska, *Pure Appl. Chem.*, 1985, **57**, 603–619.
- 44 T. I. T. Okpalugo, P. Papakonstantinou, H. Murphy, J. McLaughlin and N. M. D. Brown, *Carbon*, 2005, **43**, 153–161.
- 45 *NIST X-Ray Photoelectron Spectroscopy (XPS) Database Number 20*, Gaithersburg MD, 2000.



- 46 A. Kousar, I. Pande, L. F. Pascual, E. Peltola, J. Sainio and T. Laurila, *Anal. Chem.*, 2023, **95**, 2983–2991.
- 47 T. Susi, T. Pichler and P. Ayala, *Beilstein J. Nanotechnol.*, 2015, **6**, 177–192.
- 48 C. Sheng Chen, J. Bi, Y. Zhao, L. Yang, C. Zhang, Y. Ma, Q. Wu, X. Wang, Z. Hu, S. Chen, J. Y. Bi, Y. Zhao, L. J. Yang, C. Zhang, Q. Wu, X. Z. Wang, Z. Hu and Y. W. Ma, *Adv. Mater.*, 2012, **24**, 5593–5597.
- 49 M. C. Biesinger, B. P. Payne, A. P. Grosvenor, L. W. M. Lau, A. R. Gerson and R. S. C. Smart, *Appl. Surf. Sci.*, 2011, **257**, 2717–2730.
- 50 Y. Wang, Y. Nie, W. Ding, S. G. Chen, K. Xiong, X. Q. Qi, Y. Zhang, J. Wang and Z. D. Wei, *Chem. Commun.*, 2015, **51**, 8942–8945.
- 51 Y. Yao, H. Chen, C. Lian, F. Wei, D. Zhang, G. Wu, B. Chen and S. Wang, *J. Hazard. Mater.*, 2016, **314**, 129–139.
- 52 Z. Li, H. Sun, L. Wei, W. J. Jiang, M. Wu and J. S. Hu, *ACS Appl. Mater. Interfaces*, 2017, **9**, 5272–5278.
- 53 Z. Lu, G. Chen, S. Siahrostami, Z. Chen, K. Liu, J. Xie, L. Liao, T. Wu, D. Lin, Y. Liu, T. F. Jaramillo, J. K. Nørskov and Y. Cui, *Nat. Catal.*, 2018, **1**(2), 156–162.
- 54 H. W. Kim, H. Park, J. S. Roh, J. E. Shin, T. H. Lee, L. Zhang, Y. H. Cho, H. W. Yoon, V. J. Bukas, J. Guo, H. B. Park, T. H. Han and B. D. McCloskey, *Chem. Mater.*, 2019, **31**, 3967–3973.
- 55 Y. Qin, H. H. Wu, L. A. Zhang, X. Zhou, Y. Bu, W. Zhang, F. Chu, Y. Li, Y. Kong, Q. Zhang, D. Ding, Y. Tao, Y. Li, M. Liu and X. C. Zeng, *ACS Catal.*, 2019, **9**, 610–619.
- 56 Y. Zhang, Y. Yu, X. Fu, Z. Liu, Y. Liu and S. Li, *Front. Mater. Sci.*, 2020, **14**, 481–487.
- 57 P. Ganesan, A. Ishihara, A. Staykov and N. Nakashima, *Bull. Chem. Soc. Jpn.*, 2023, **96**, 429–443.
- 58 J. Feng, C. Ma, Y. Zhang, C. Du, Y. Chen, H. Dong, L. Yu and L. Dong, *Appl. Surf. Sci.*, 2024, **651**, 159219.



Appendix 3

Publication III

Praats, R.; Sainio, J.; Vikberg, M.; Klemettinen, L.; Wilson, B. P.; Lundström, M.; Kruusenberg, I.; Liivand, K. A Pathway to Circular Economy-Converting Li-Ion Battery Recycling Waste into Graphite/rGO Composite Electrocatalysts for Zinc–Air Batteries, *Batteries* 11 (2025) 165.

Article

A Pathway to Circular Economy-Converting Li-Ion Battery Recycling Waste into Graphite/rGO Composite Electrocatalysts for Zinc–Air Batteries

Reio Praats ¹, Jani Sainio ² , Milla Vikberg ³ , Lassi Klemettinen ⁴ , Benjamin P. Wilson ⁴ , Mari Lundström ⁴, Ivar Kruusenberg ¹ and Kerli Liivand ^{1,*} 

¹ National Institute of Chemical Physics and Biophysics, Akadeemia tee 23, 12618 Tallinn, Estonia; reio.praats@kbfi.ee (R.P.)

² Department of Applied Physics, School of Science, Aalto University, P.O. Box 15100, 00076 Aalto, Finland; jani.sainio@aalto.fi

³ Department of Chemistry and Materials Science (CMAT), School of Chemical Engineering, Aalto University, P.O. Box 16100, 00076 Aalto, Finland

⁴ Department of Chemical and Metallurgical Engineering (CMET), School of Chemical Engineering, Aalto University, P.O. Box 16200, 00076 Aalto, Finland; ben.wilson@aalto.fi (B.P.W.)

* Correspondence: kerli.liivand@kbfi.ee

Abstract: Li-ion batteries (LIBs) are one of the most deployed energy storage technologies worldwide, providing power for a wide range of applications—from portable electronic devices to electric vehicles (EVs). The growing demand for LIBs, coupled with a shortage of critical battery materials, has prompted the scientific community to seek ways to improve material utilization through the recycling of end-of-life LIBs. While valuable battery metals are already being recycled on an industrial scale, graphite—a material classified as a critical resource—continues to be discarded. In this study, graphite waste recovered from the recycling of LIBs was successfully upcycled into an active graphite/rGO (reduced graphene oxide) composite oxygen electrocatalyst. The precursor graphite for rGO synthesis was also extracted from LIBs. Incorporating rGO into the graphite significantly enhanced the specific surface area and porosity of the resulting composite, facilitating effective doping with residual metals during subsequent nitrogen doping via pyrolysis. These composite catalysts enhanced both the oxygen reduction and oxygen evolution reactions, enabling their use as air electrode catalyst materials in zinc–air batteries (ZABs). The best-performing composite catalyst demonstrated an impressive power density of 100 mW cm^{−2} and exceptional cycling stability for 137 h. This research further demonstrates the utilization of waste fractions from LIB recycling to drive advancements in energy conversion technologies.

Keywords: energy storage; lithium-ion battery recycling; graphite; reduced graphene oxide; bifunctional oxygen electrocatalyst; oxygen reduction reaction; oxygen evolution reaction; zinc–air batteries



Academic Editors: Sake Wang, Nguyen Tuan Hung and Minglei Sun

Received: 26 March 2025

Revised: 17 April 2025

Accepted: 19 April 2025

Published: 21 April 2025

Citation: Praats, R.; Sainio, J.; Vikberg, M.; Klemettinen, L.; Wilson, B.P.; Lundström, M.; Kruusenberg, I.; Liivand, K. A Pathway to Circular Economy-Converting Li-Ion Battery Recycling Waste into Graphite/rGO Composite Electrocatalysts for Zinc–Air Batteries. *Batteries* **2025**, *11*, 165. <https://doi.org/10.3390/batteries11040165>

Copyright: © 2025 by the authors. Licensee MDPI, Basel, Switzerland. This article is an open access article distributed under the terms and conditions of the Creative Commons Attribution (CC BY) license (<https://creativecommons.org/licenses/by/4.0/>).

1. Introduction

Geopolitical factors, including wars, supply chain disruptions, and policy shifts, have intensified global energy insecurity in the years following the COVID-19 pandemic. This has underscored the urgent need for sustainable energy solutions, drawing heightened attention from the scientific community. One significant advancement is the rapid increase in the production and use of lithium-ion batteries (LIBs), which serve as the primary power source for portable electronic devices and electric vehicles (EVs). Until recently,

the LIB market has experienced exponential growth; however, the rate of increase has recently begun to slow [1]. LIBs are composed of various components, including graphite as the anode active material; layered transition metal oxides (e.g., LiCoO_2 , LiMn_2O_4 , LiNiMnCoO_2 , LiNiCoAlO_2) or LiFePO_4 as cathode active materials; aluminium and copper as current collectors; a polymer-based separator; and a lithium salt dissolved in an organic solvent as the electrolyte [2–4]. Therefore, the production of LIBs relies on critical and strategic raw materials such as Co, Li, Ni, Mn, Cu, and graphite [5,6]. Nevertheless, the supply growth of these essential resources has not kept pace with the surge in demand for new batteries, leading to potential shortages of these critical raw materials (CRMs) [7]. To address the shortage of CRMs and mitigate the environmental impact of mining new resources, the recycling and reuse of materials from end-of-life LIBs is essential. In 2023, global material recovery from LIB recycling reached 2100 kt, with approximately 80% of this capacity concentrated in China, while Europe and the USA each accounted for only about 4%. Under the Announced Pledges Scenario, the projected volume of end-of-life LIBs is expected to rise dramatically to approximately 35,000 kt by 2040, representing a recycling demand about 16 times greater than current global recycling capacity, demonstrating the need to increase the recycling capacity [8].

Graphite, a key material in LIBs, is largely overlooked in recycling processes and is often discarded as waste, either sent to landfills or incinerated [8,9]. On the other hand, spent graphite is a valuable resource which can be upcycled by synthesizing oxygen electrocatalysts, either being directly doped with heteroatoms to enhance its catalytic properties [10] or serving as a precursor for producing other carbon materials like reduced graphene oxide (rGO) [11]. These electrocatalysts are used in energy conversion technologies like metal-air batteries, fuel cells or electrolyzers [12]. Currently, the most effective oxygen electrocatalysts are noble metal-based materials, e.g., Pt/C for the oxygen reduction reaction (ORR) and IrO_2 or RuO_2 for the oxygen evolution reaction (OER) [13]. However, these catalysts rely on rare and expensive materials and exhibit insufficient stability for long-term, efficient use, particularly as bifunctional oxygen catalysts that simultaneously catalyze both the ORR and OER. [14]. Today, most of the research on bifunctional oxygen electrocatalysts focuses on the use of doped carbon nanomaterials incorporating non-precious metals such as Fe, Co, Mn, and Ni, as well as heteroatoms like N, S and O [15–19]. Among these are 2-dimensional carbon materials, such as rGO, which feature an optimal thickness-to-diameter ratio. This property enables short diffusion times and provides high surface areas capable of hosting active sites, thereby improving the activity of electrocatalysts [20]. Qin et al. developed a Co-N-C catalyst material for zinc–air batteries (ZAB) that demonstrated a notable power density of 155 mW cm^{-2} and a cycling stability of 63 h [21]. Similarly, Li et al. synthesized a bimetallic CoFe/SN-C catalyst, which served as an air electrode for ZAB, achieving an impressive power density of 169 mW cm^{-2} and a stability of 85 h at 10 mA cm^{-2} [22]. These examples highlight the potential of 2D carbon-based materials for active bifunctional catalyst synthesis. Still, a significant limitation of these approaches is the complex and costly synthesis process that relies on high purity chemical precursors.

An alternative and promising strategy involves using recycled materials as precursors for electrocatalyst synthesis. Graphite recovered from waste LIBs can serve as an excellent precursor for either rGO synthesis or can be directly utilized for electrocatalyst production [23,24]. Nonetheless, most research in this area relies on manually extracted materials from LIBs, a method that is not scalable; moreover, the produced electrocatalysts are usually only applicable for one reaction ORR or OER, as highlighted by earlier research [25–29]. A more scalable and efficient approach to utilizing waste materials involves repurposing hydrometallurgical LIB recycling leach residue. This primarily consists of graphite—but may also contain small amounts of other carbonaceous species to increase

the conductivity, like carbon black—residual battery metals such as Co, Ni, Al, Cu, and Mn, along with additives from the binder and electrolyte (e.g., F) [30]. Such metals can be incorporated into the carbon framework for the formation of active catalytic centres as demonstrated by our previous research that showcases the potential of this approach for sustainable and effective resource utilization [23,31,32].

In this study, we use waste from the hydrometallurgical treatment of LIBs along with manually extracted graphite from mobile phone batteries as precursors for synthesizing an active bifunctional graphite/rGO composite electrocatalyst. Building on our earlier findings that N-rGO derived from leach residue exhibits good electrocatalytic activity, we selected a purer rGO precursor to provide a clearer demonstration of metal incorporation, particularly Co, directly from the leach residue. Repurposing this waste material aligns with the EU Battery Regulation goal of recycling at least 65% of LIBs by 2026, while also contributing to the development of sustainable green energy conversion technologies [33].

2. Materials and Methods

2.1. Synthesis of the Catalyst Materials

The two starting materials for the composite catalyst synthesis were derived from spent battery graphite. Firstly, iPhone batteries (APN: 616-00036), utilizing LiCoO_2 as cathode active material, were collected from local repair shops, discharged, and manually dismantled. The anode, cathode, and separator were divided, and the anodes were submerged into water to remove the graphite from Cu-foil. This graphite was then filtered and dried prior to the GO synthesis by a classical Hummer's method, which included a thermal reduction at 800 °C for 1 h under Ar atmosphere to produce the rGO [23]. Additionally, black mass leach residue—an industrially processed battery material previously subjected to hydrometallurgical recycling process—was obtained for use in this study [30]. This residual waste, herein defined as Raw Material, served as one of the starting materials alongside the synthesised rGO for this study. Raw Material predominantly consists of graphite, along with traces of metals from the cathode active materials and current collectors, as well as the binder and some organic compounds. The Raw Material underwent pyrolysis at 800 °C for 1 h under Ar atmosphere (99.999%, Elme Messer Gaas, Estonia) to remove the organic compounds and binder, and the resulting material was named as RM.

To synthesize the catalyst, a mixture comprising RM, dicyandiamide (DCDA, Sigma-Aldrich, Hamburg, Germany) as the nitrogen source, and polyvinylpyrrolidone (PVP, Sigma-Aldrich, Germany, Mw: 40,000) was prepared in a weight ratio of 1:20:0.1 using 3 mL of an ethanol/water solution (2:1). The resulting mixture was subjected to ball milling with 5 mm ZrO_2 balls at 400 rpm for a total of one hour, carried out in two 30-min intervals with a 5-min pause in between. Afterward, a specific amount of rGO was added to the mixture, which was then placed in an ultrasonic bath for 2 h. The resulting homogeneous mixture was dried and pyrolyzed at 800 °C for 2 h under Ar atmosphere. The ratio of RM to rGO was varied, with compositions of 25 wt%/75 wt%, 50 wt%/50 wt%, and 75 wt%/25 wt%. The resulting catalysts were named *Comp 25/75*, *Comp 50/50*, and *Comp 75/25*, respectively. A similar synthesis method was used to prepare N-rGO, and N-RM materials for comparison. Additionally, *Comp 25/75*, *Comp 50/50*, and *Comp 75/25* underwent acid treatment with a 1:1 solution of 0.5 M H_2SO_4 and 0.5 M HNO_3 , first at 50 °C for 2 h, then at 80 °C for 3 h. The resultant catalyst materials were subsequently washed with Milli-Q water until a neutral pH was reached and dried under vacuum. Finally, the materials were re-pyrolyzed at 800 °C for 1 h under Ar atmosphere to remove any excess oxygen groups that resulted from the acid treatment. The final catalysts were named *AT-Comp 25/75*, *AT-Comp 50/50*, and *AT-Comp 75/25*. This process was performed to remove excess metals and unstable species, thereby ensuring the catalysts' stability under harsh electrochemical

testing conditions. A similar acid treatment process has been used in other studies to achieve the same purpose [34]. The flowsheet of catalyst material synthesis is shown in Figure 1.

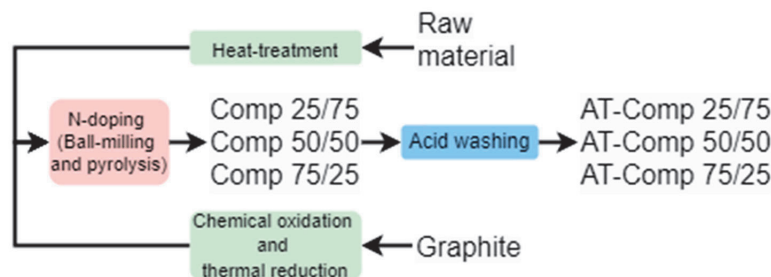


Figure 1. Flowsheet of catalyst material synthesis.

2.2. Physicochemical Characterisation

The crystallinity and phase composition of the materials were analyzed using powder X-ray diffraction (XRD) with a PANalytical X'Pert³ Powder XRD system (Malvern Panalytical, Malvern, UK). The measurements were conducted with Cu K α radiation ($\lambda = 1.54182 \text{ \AA}$), applying a step size of 0.04° at 45 kV and 40 mA. Atomic Absorption Spectroscopy (AAS; iCE 3000, Thermo Fisher Scientific Inc., Dreieich, Germany) was used to determine the battery metal residue content (wt%) in the Raw Material. Prior to analysis, the Raw Material was leached using aqua regia to prepare the solutions for AAS measurement. Microstructural images were captured using a JSM-IT800HL scanning electron microscope (SEM, JEOL Ltd., Tokyo, Japan) with secondary electron (SE) detection at an acceleration voltage of 5 kV and beam current of 54 pA. Elemental mapping was performed using an Aztec Live Premium Ultim Max 100 energy-dispersive spectrometer (EDS, Oxford Instruments, UK) at an acceleration voltage of 15 kV and beam current of 1.4 nA. Beam measurement was conducted using pure copper cathode as a reference material. The quantified maps were acquired at $400\times$ magnification with a resolution of 512 pixels, and the mapped area was scanned 8 times with $200 \mu\text{s}$ dwell time per pixel. Two maps were taken from each sample. HR-TEM micrographs were acquired using a double aberration-corrected microscope with a 200 kV field-emission gun and X-ray EDS detector (JEOL JEM-2200FS, JEOL Ltd., Tokyo, Japan).

Raman measurements were conducted using a Renishaw inViaTM Confocal Raman Microscope (Renishaw, Wotton-under-Edge, UK). A 532 nm excitation laser was focused on the sample through a $50\times$ objective lens of a Leica microscope. The scattered light was collected at a backscattering angle of 180° , and a 2400 L mm^{-1} diffraction grating was used to disperse the wavelengths for detection by a Charge Coupled Device (CCD) detector. Spectral deconvolution was carried out using OriginPro 2021 software, applying the Voigt function for peak fitting and analysis. Nitrogen adsorption–desorption analysis (Anton Paar Novatouch LX4, Anton Paar QuantaTec Inc., Graz, Austria) was performed to determine the specific surface area and porosity of the samples at liquid nitrogen boiling temperature (77 K). The specific surface area was determined by applying the Brunauer–Emmett–Teller (BET) method to the linear portion of the adsorption isotherm at relative pressures (P/P_0) between 0.05 and 0.3. Additionally, the density functional theory (DFT) surface area (S_{DFT}) was calculated using the Quenched Solid Density Functional Theory (QSDFT) equilibrium model for slit/cylindrical/spherical pore types calculated by using Quantachrome Instruments Touchwin 1.24 software (Anton Paar QuantaTec Inc., Graz, Austria). The pore size distribution (PSD) was evaluated using the Non-Local Density Functional Theory (NLDFT) method implemented in SAIEUS 3.0 software (Micromeritics,

Norcross, GA, USA). X-ray photoelectron spectroscopy (XPS) was carried out with a Kratos Axis Ultra spectrometer with monochromated Al K α -radiation using a pass energy of 40 eV, X-ray power of 195 W, and an analysis area of approximately 700 $\mu\text{m} \times 300 \mu\text{m}$. The sp² carbon 1 s peak at 284.5 eV has been used as a binding energy reference. The elemental composition was determined from peak areas of high-resolution core level spectra after Shirley background subtraction using equipment specific sensitivity factors. Peak fitting was done using Gaussian–Lorentzian peaks (GL (30) line shape in CasaXPS 2.3.25 software) with the positions of the peaks fixed to within ± 0.1 eV of given binding energies. For sp² carbon, an asymmetric line shape was used in CasaXPS [1]. The full widths at half-maximum (FWHMs) of the peaks were restricted to be equal within a fit except for sp² carbon and N-oxide peaks.

2.3. Electrochemical Characterisation

The ORR and OER were investigated by the rotating disc electrode (RDE) technique with a Gamry 1010E potentiostat/galvanostat, utilizing a three-electrode system. The reference electrode was Ag/AgCl (3 M KCl), while a graphite rod served as the counter electrode for ORR and a platinum wire for OER, respectively. A glassy carbon (GC, S = 0.2 cm²) electrode, coated with the catalyst material, was used as the working electrode. The RDE setup featured an Orignalys speed control unit and rotator, with rotation speeds ranging from 400 to 3600 rpm. The catalyst ink was prepared with a concentration of 4 mg mL^{−1} in ethanol, with 4 μL of 5 wt% NafionTM solution per mg of catalyst as an ionomer. Five 4 μL aliquots of the catalyst ink were applied to the cleaned GC electrodes, achieving a catalyst loading of 0.4 mg cm^{−2}. All recorded potentials were converted to reversible hydrogen electrode (RHE) values using the Nernst equation for the ORR and OER potential:

$$E(\text{RHE}) = E_{\text{Ag/AgCl}} + 0.059 \text{ pH} + E_{\text{Ag/AgCl}}^0$$

ORR tests were conducted in an O₂-saturated (Elme Messer Gaas, 5.0) 0.1 M KOH solution at room temperature, with a constant flow of O₂ gas over the solution. All experiments were controlled using Gamry Instruments Framework 7.10.0 software (Warminster, PA, USA). OER measurements were performed in a N₂-saturated (Elme Messer Gaas, 5.0) 1 M KOH solution at room temperature, with a constant gas flow similar to the ORR tests.

To account for the system's ohmic resistance, iR-drop compensation was applied to the OER polarization curves. The resistance was determined from electrochemical impedance spectroscopy (EIS) data collected over a frequency range of 100 kHz to 1 Hz at open circuit potential. The real part of the impedance, derived from the Nyquist plot at the point where the imaginary component was zero, was used as the resistance value. The OER overpotential (in mV) was calculated using the following equation:

$$E_{\text{experimental}}(\text{vs RHE}) - 1.229 \text{ V} \times 1000$$

To assess electrocatalytic activity, at least three sets of RDE measurements were performed for each synthesized catalyst material, with each set using three electrodes.

2.4. Zinc-Air Battery Testing

ZAB experiments were conducted using a custom-designed test cell. The air electrode, with an active surface area of 1.038 cm², consisted of a gas diffusion layer (GDL, Sigracet 28BC from SGLCarbon, Wiesbaden, Germany) and a catalyst layer loaded onto the GDL at 1 mg cm^{−2}. A titanium mesh functioned as the current collector for the air electrode. As a benchmark, a commercial catalyst 20% PtRu (in a 1:1 ratio) on carbon support (FuelCellstore, Bryan, TX, USA) was used for the air electrode. The electrolyte in the ZAB

cell was 6 M KOH mixed with 0.2 M Zn(Ac)₂, while a polished Zn plate (1 mm thick, 99.9% purity) served as the counter electrode.

All ZAB tests were performed at room temperature using a PGSTAT30 potentiostat/galvanostat (Metrohm Autolab, Utrecht, The Netherlands) controlled by NOVA 2.1.5 software. Charge–discharge cycling was conducted at a current density of 5 mA cm^{−2}, with alternating 30-min charge and discharge cycles. Specific energy density and capacity were measured through complete discharge tests at a current density of 5 mA cm^{−2}, calculated based on the Zn mass consumed. To ensure reliability, at least three separate ZAB cells were tested for each catalyst material to determine the maximum discharge power density.

3. Results and Discussion

3.1. Analysis of Materials Physicochemical Properties

3.1.1. Physicochemical Analysis of Precursor Materials

Initial characterization of the precursor materials and *N*-RM and *N*-rGO were performed using XRD analysis (Figure S1a,b in Supplementary Material). The XRD pattern in Figure S1a revealed that the Raw Material was primarily composed of graphite, indicated by the prominent (002) peak at 26.5°. Additionally, traces of unreacted cathode active material (LiCoO₂), metallic cobalt (Co(0)), and manganese oxide (MnO) were present, highlighting its heterogeneous nature. The presence of these metal components in the Raw Material, particularly cobalt, shows the significant potential for use as a precursor for electrocatalyst synthesis. The diffraction pattern for *N*-RM contained peaks at similar 2θ positions as the Raw Material, except that a majority of the LiCoO₂ peaks were no longer present. This suggests that oxidic cobalt had mostly reduced to metallic Co during the pyrolysis treatment at 800 °C. The reduction was most likely carbothermic [35] due to the high concentration of carbon present (Tables S1 and S2), but some aluminothermic reduction may also have taken place due to the presence of Al current collector residues in the Raw Material (Table S1) [36]. In addition, the heterogeneous nature of the Raw Material was confirmed by the AAS results presented in Table 1. Among the analyzed metals, Co showed the highest concentration at 18.6 ± 1.13 wt%, followed by Mn at 1.3 ± 0.03 wt%. The concentrations of all other detected elements were below 1 wt%. These values represent the average of three independent aqua regia leaching experiments, each with 2.5 g of Raw Material. Although the Raw Material is inherently heterogeneous, the low standard error of the mean values indicates good reproducibility and compositional stability of the leach residue used in this study. Figure S1b presents the XRD diffractograms of precursor graphite, GO, rGO, and *N*-rGO materials. The diffraction pattern of graphite showed no detectable metal impurities, as it displays only characteristic graphite peaks. In the GO sample, the disappearance of the graphitic (002) peak and the appearance of the typical GO (001) peak around 10–12° were observed, along with a low-intensity broad peak between 20° and 30°, which is indicative of an increased interlayer spacing due to oxidation [37]. Similar peaks were present in the rGO sample, but with a more pronounced 20–30° peak, suggesting partial re-stacking of graphene oxide sheets. The *N*-rGO sample exhibited comparable peaks to GO and rGO, but additionally, a distinct peak at 26.5° corresponding to the graphitic (002) plane was observed, confirming the partial re-stacking of graphene sheets following nitrogen doping.

Table 1. Metal content of the Raw Material (wt%).

Element	Li	Co	Mn	Ni	Cu	Fe
Concentration in Raw Material (wt%)	0.9	18.6	1.3	0.8	0.2	0.1
Standard error of mean (+/− wt%)	±0.02	±1.13	±0.03	±0.02	±0.01	±0.01

3.1.2. XRD, SEM-EDS, and TEM-EDS Analysis of Composites

The composite catalysts were also characterized by XRD (Figure 2). All composite samples exhibited a high intensity peak at 26.5° , characteristic of the (002) plane of graphitic carbon. This suggests that graphitic carbon contributes significantly to the carbon matrix within the composites. Moreover, the broad peak from 20 to 25° implies that also more amorphous phases of carbon are present, as a result of the rGO within the composite materials. Distinct peaks at 44.2° , 51.5° , and 75.8° corresponding to the (111), (002), and (022) planes of metallic Co(0), respectively, were evident in the XRD patterns for all studied samples, the presence of which confirms the successful incorporation of metallic Co within the composite materials.

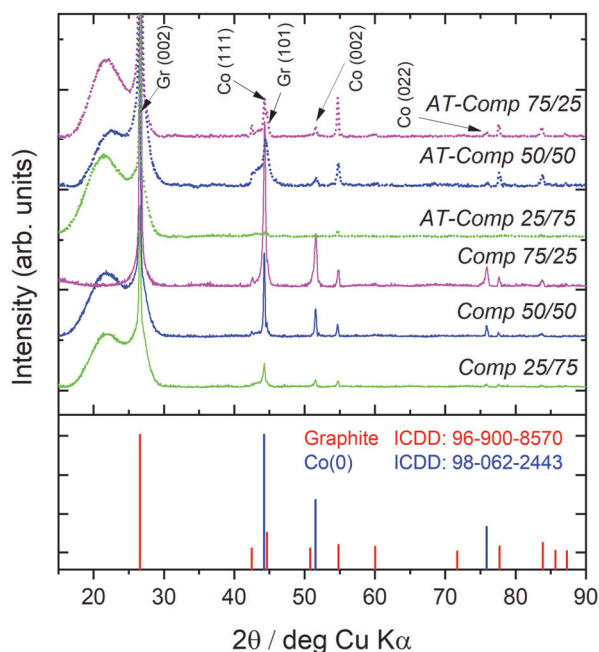


Figure 2. XRD patterns of studied composite materials together with standard cards.

Figure S2 displays the SEM micrographs of the studied materials. Figure S2a,d—corresponding to *Comp 25/75* and *AT-Comp 25/75*, respectively—reveal the characteristic layered structure of rGO. The surface of *Comp 25/75* exhibits greater roughness compared to its acid-treated counterpart, indicating the presence of nitrogen species on the surface of the material [32]. Figure S2b,c,e,f show more varying surface structures compared to the layered structure of rGO. Notably, *Comp 50/50* and *AT-Comp 50/50* show a significant presence of carbon nanotubes (CNTs), which are known to form in nitrogen doped carbon materials in the presence of Co or Ni nanoparticles during the pyrolysis process [23,32]. A similar structure is observed in *Comp 75/25* and *AT-Comp 75/25* (Figure S2c,f), but with a noticeably reduced CNT number. Quantified SEM-EDS mapping (Table S1) identified small amounts of various metals, including Co, Al, Si, Mn, and Ni, with Co being the most abundant on the surface of all composites. In the *Comp*-series catalysts, the Co content increased in relation to the proportion of RM within the material.

Nevertheless, for the *AT-Comp* series, the highest Co concentration was found in *AT-Comp 50/50* (Figure S3 demonstrates the quantified SEM-EDS elemental maps), probably as a result of Co(0) encapsulation within the CNTs. In contrast, *AT-Comp 75/25* material exhibited less distinct CNT formation, resulting in lower Co(0) encapsulation and a higher

level of Co species leaching during acid treatment. This highlights the beneficial role of acid treatment in enhancing the structural stability of the catalyst materials.

To further highlight the structural and compositional distinctions between the composite samples, related HR-TEM micrographs are displayed in Figure 3a–f. *Comp* 25/75 (Figure 3a) and *AT-Comp* 25/75 (Figure 3d) show minimal incorporation of Co nanoparticles, suggesting a lower metal content on the surface of these composites. In contrast, *Comp* 50/50 (Figure 3b) and *AT-Comp* 50/50 (Figure 3e, along with EDS data in Figure S4) display Co-catalysed bamboo-like CNTs, where Co nanoparticles (≈ 30 nm) are encapsulated within the nanotubes [23,32]. A similar—though less pronounced—effect is observed for *Comp* 75/25 (Figure 3c) and *AT-Comp* 75/25 (Figure 3f), where CNT formation occurs at a lower concentration. Beyond bamboo-like CNTs, larger (>100 nm) onion-like spherical carbonaceous regions are also visible, which form protective shells around Co(0) nanoparticles [38,39]. Both encapsulation mechanisms—within CNTs and spherical carbon shells—enhance the stability of Co(0) nanoparticles, making them more resistant to leaching under harsh conditions. Figure S4 presents the TEM-EDS spectra for *AT-Comp* 50/50 (Figure 3e), confirming the composition of the composite catalysts. Specifically, EDS 1 identifies a Co nanoparticle located at the end of a bamboo-like CNT, while EDS 2 reveals a Co nanoparticle fully encapsulated within a CNT. Furthermore, EDS 3 and 4 highlight onion-like spherical carbonaceous regions that serve as protective shells for Co. These Co-enriched carbon structures are absent in *Comp* 25/75 and *AT-Comp* 25/75. Acid treatment effectively removed unstable particles from all composites, refining their surface composition. The most significant structural modification is observed for *AT-Comp* 75/25, where the removal of non-stable Co species is particularly evident, as confirmed by both HR-TEM micrographs and SEM-EDS analysis.

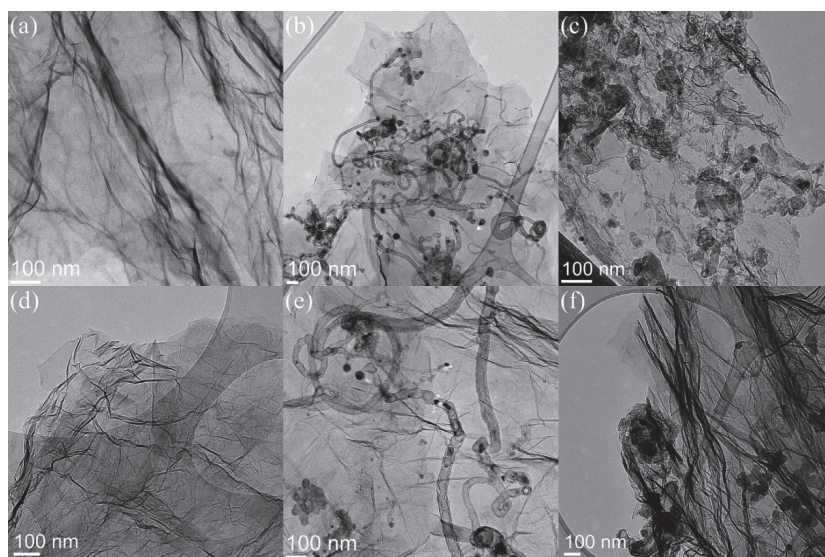


Figure 3. HRTEM micrographs of (a) *Comp* 25/75, (b) *Comp* 50/50, (c) *Comp* 75/25, (d) *AT-Comp* 25/75, (e) *AT-Comp* 50/50, and (f) *AT-Comp* 75/25.

3.1.3. Raman and N₂ Physisorption Analysis of Studied Materials

Raman analysis (Figure 4) provides more detail of the structural differences between the Raw Material, rGO, and the composite samples, highlighting the influence of rGO content and acid treatment on defect density and graphitic ordering. All composite materials exhibit two prominent peaks corresponding to the D-band at ~ 1350 cm^{−1} and the G-band

at $\sim 1580\text{ cm}^{-1}$, which are characteristic of carbon-based materials such as graphite and graphene oxide. The D-band is associated with structural defects and disordered carbon, while the G-band corresponds to the graphitic sp^2 -hybridized carbon network [40]. In rGO and the composite materials, the G-band is shifted to a slightly higher wavenumber, which can be attributed to the oxygenation of sp^2 carbon atoms, leading to the formation of sp^3 carbon bonds [41]. Additionally, the G' (2D) band appears at $\sim 2700\text{ cm}^{-1}$ in the Raw Material, and a broad signal indicative of a D + D' combination is observed around 2950 cm^{-1} , further reflecting the presence of structural irregularities. Analysis of the $I_{\text{D}}/I_{\text{G}}$ ratio reveals critical differences between the base materials. The Raw Material exhibits a lower $I_{\text{D}}/I_{\text{G}}$ ratio compared to rGO, indicating a higher degree of structural order in the Raw Material. This aligns with the hypothesis that Raw Material, primarily composed of graphite and has a more ordered graphitic structure, whereas rGO contains more defects, likely due to the presence of oxygen-containing functional groups introduced during the synthesis and reduction processes. The $I_{\text{D}}/I_{\text{G}}$ ratio of the composite materials shows a clear trend, with higher rGO content which corresponds to an increase in the number of defects and suggests that rGO contributes to the overall defect density of the composite. Acid treatment followed by the heat treatment of the composite materials resulted in a slight reduction in the $I_{\text{D}}/I_{\text{G}}$ ratio, implying a partial restoration of structural order, possibly due to the removal of oxygenated groups and non-stable forms of metals [42]. No additional Raman shifts were observed for the materials studied, indicating that no new functional groups or phases were introduced during synthesis or heat treatment.

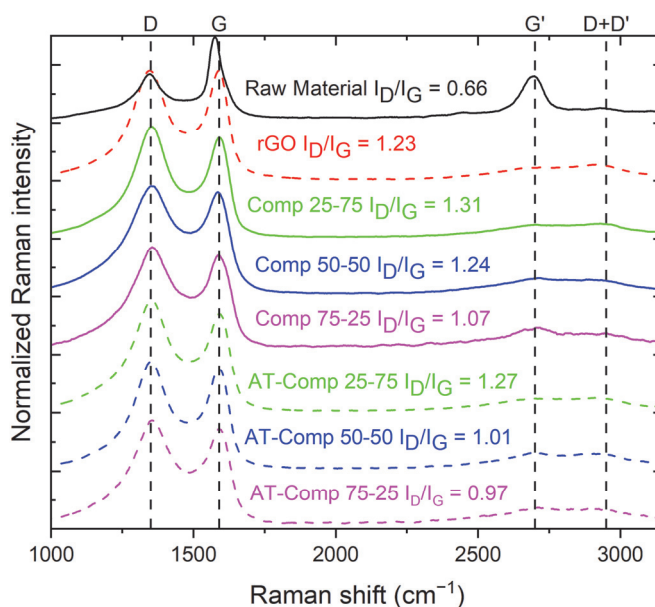


Figure 4. Raman spectra of Raw material, rGO, Comp 50/50, Comp 75/25, AT-Comp 25/75, AT-Comp 50/50, and AT-Comp 75/25 materials.

The specific surface area (SSA) and pore size distribution (PSD) of the materials were determined using N_2 adsorption–desorption isotherms, as illustrated in Figure S5 and Table 2. These isotherms exhibit a combination of type IV(a) and type II characteristics with H3-type hysteresis loops that reveal the presence of meso- and macroporous structures composed of slit-like pores and finer mesopores typically formed by plate-like particles or layered structures [43,44]. *N*-RM and Comp 75/25 display type II behaviour, which

indicates a higher prevalence of macroporosity compared to mesoporosity. The SSA of the materials increased with a higher rGO content and further improved following acid treatment due to leaching of unbonded metal species [45]. Among the composite materials studied, *AT-Comp 25/75* exhibited the highest BET surface area ($183.3\text{ m}^2\text{ g}^{-1}$). The observed differences between the BET and DFT surface areas suggest that adsorption predominantly occurs in meso/macropores rather than micropores [44]. The PSD data presented in Figure S5b and its inset reveal a diverse range of mesopores in the composite materials. While the volume of larger mesopores remains unchanged when the *Comp*-series are compared to their *AT-Comp* counterparts, the volume of smaller mesopores increases after acid treatment followed by pyrolysis. This observation suggests that the additional processing step enhances the structural refinement of the catalysts by removing unstable metal species. Furthermore, the increase in smaller mesopores and increase in the SSA indicates pore opening without significant degradation or collapse of the pore walls, thereby preserving the overall structural integrity of the material [46].

Table 2. Specific surface areas of the materials studied, measured with BET and DFT methods.

Sample Name	Raw Material	<i>N-RM</i>	rGO	<i>N-rGO</i>	<i>Comp 25/75</i>	<i>Comp 50/50</i>	<i>Comp 75/25</i>	<i>AT-Comp 25/75</i>	<i>AT-Comp 50/50</i>	<i>AT-Comp 75/25</i>
S_{BET} (m^2/g)	1.9	51.3	280.5	211.7	149.0	77.7	63.5	183.3	124.6	90.1
S_{DFT} (m^2/g)	2.7	37.9	239.8	188.5	126.5	64.5	52.9	156.0	105.6	75.0

3.1.4. Surface Composition and Chemical State Characterization of Materials via XPS

Chemical composition of the samples was studied by using the XPS (Table S2). In addition to carbon, oxygen, and nitrogen, various metals (Co, Mn, Ni, Si, Al, Cu, and Na) were detected in the samples, and the metal contents based on XPS were similar compared to the concentrations determined by SEM-EDS mapping (Table S1). Figure 5 presents the C 1 s, N 1 s, and Co 2p XPS spectra of the synthesized samples. The C 1 s spectrum displays a dominant asymmetric peak at 284.5 eV, corresponding to sp^2 -hybridized carbon. Additional signals observed in the 285–289 eV binding energy range are attributed to various carbon bonding environments, including C–C, C–O, and C–N interactions [47–49]. The C 1 s spectra, which do not show large differences between the studied samples, have been fitted to include contributions from all these species (for fitting details see [49]). The N 1 s spectra shown in Figure 5b were deconvoluted based on the presence of four nitrogen species: pyridinic-N, pyrrolic-N, graphitic-N, and N-oxides (see fitting parameters in [50,51]). The fitting results indicate that pyridinic-N is the dominant nitrogen configuration across all samples. Moreover, the relative distribution of the nitrogen species is consistent among the samples. While the pyridinic-N peak may include some contribution from N–Co bonding, the significantly higher nitrogen content compared to Co suggests that the signal is primarily due to pyridinic-N. Even though the nitrogen species have similar ratios between the studied materials, the doping levels show much more variation. In *Comp*-series materials, the at-% of N were 7.2%, 6.4%, and 6.2% for *Comp 25/75*, *Comp 50/50*, and *Comp 75/25*, respectively. For the *AT-comp* materials, the doping level decreased for all composite materials, showing the removal of less stable nitrogen species. Notably, the smallest decrease was observed in *AT-Comp 50/50*, suggesting a higher proportion of structurally stable nitrogen species. This stability is likely attributed to the formation of Co-catalyzed protective carbon structures, which provide an environment that also mitigates against nitrogen removal [34,38,52]. The Co 2p spectra (Figure 5c) were fitted using two main components: one corresponding to metallic Co and another representing

Co–N coordination, which may also include contributions from cobalt oxides and/or hydroxides [53–55]. Nonetheless, supporting evidence from the XRD diffractogram confirms the presence of metallic Co. Due to the spectral overlap, the Co–N and CoO_x species are represented by a single peak, fitted using standard parameters for Co(II) as referenced in [51]. Variations in the chemical state of cobalt are observed across the samples, with the proportion of metallic Co ranging from 28% to 44%. The atomic concentrations, peak fitting results, and additional spectra can be found in the Supplementary Information (Figure S6 and Table S2).

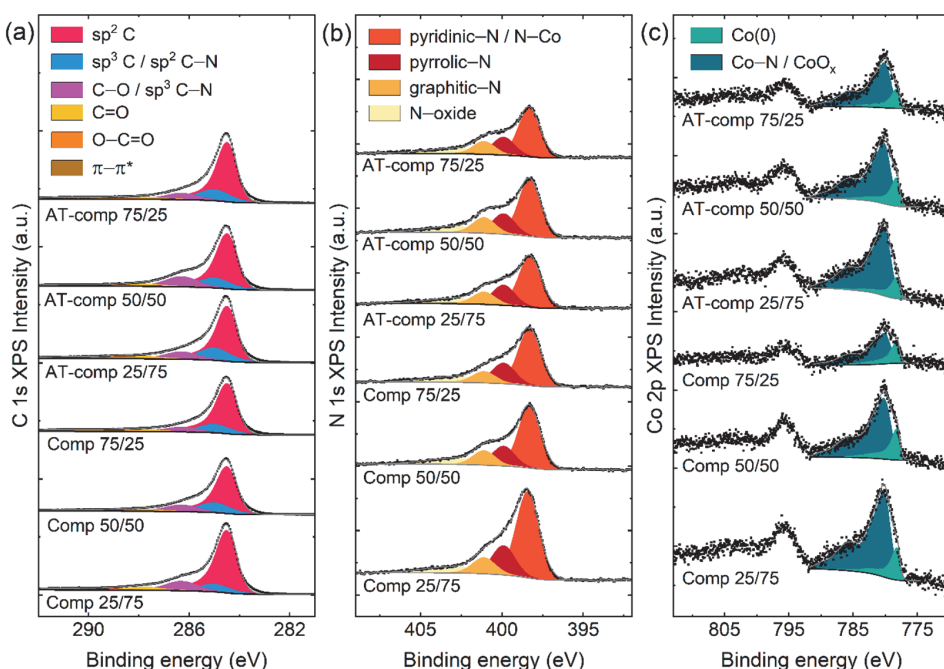


Figure 5. X-ray photoelectron spectra of the samples: (a) C 1s region, (b) N 1s region, and (c) Co 2p region.

3.2. Evaluation of Bifunctional Oxygen Electrocatalysis

The electrocatalytic performance of the synthesized catalyst materials was initially evaluated for the ORR in an O_2 -saturated 0.1 M KOH solution, as shown in Figure 6a. For a better comparison of the composite materials, both starting materials doped with nitrogen were also investigated. Among the tested materials, *AT-Comp 50/50* demonstrated the best performance with an E_{onset} ($j = 0.1 \text{ mA cm}^{-2}$) of 0.912 V vs. RHE and an $E_{1/2}$ of 0.820 V vs. RHE, accompanied by a limiting current density of 4.63 mA cm^{-2} . In comparison, the non-acid treated counterpart *Comp 50/50* showed slightly lower ORR activity, with an E_{onset} of 0.895 V vs. RHE and an $E_{1/2}$ of 0.792 V vs. RHE, though it still achieved similar current density of 4.45 mA cm^{-2} . *N-RM* had the lowest onset potential ($E_{\text{onset}} = 0.852 \text{ V}$ vs. RHE) and half-wave potential ($E_{1/2} = 0.727 \text{ V}$ vs. RHE), indicating lower ORR activity compared to the composite materials and *N-rGO*. This lower performance is attributed to its reduced SSA and porosity, which hinder effective mass transport within the catalyst. *N-rGO*, on the other hand, showed improved E_{onset} compared to *N-RM*, with an E_{onset} of 0.897 V vs. RHE and $E_{1/2}$ of 0.780 V vs. RHE, demonstrating higher catalytic activity. This enhanced activity of *N-rGO* is attributed to its higher SSA, which facilitates better mass transport and a higher concentration of electrocatalytically active nitrogen species [37].

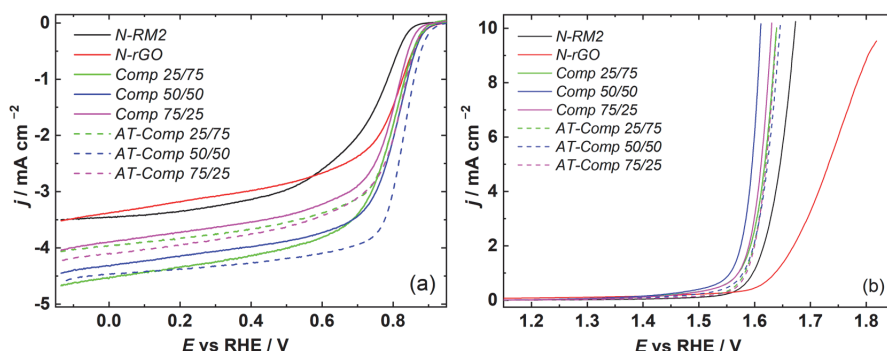


Figure 6. (a) ORR polarization curves at 1600 rpm in O₂ saturated 0.1 M KOH solution, and (b) OER curves at 1600 rpm in N₂ saturated 1 M KOH solution of the studied catalyst materials.

Figures S7 and S8 show the ORR polarization curves of studied composites on different rotating speeds as well as their Koutecky–Levich (K–L) analysis. The K–L plots for all studied materials are linear and parallel, indicating that the process is mass transport limited. Regarding the ORR activity of Co- and N-doped catalyst materials, pyridinic-N and Co-N species are recognized as the most effective active sites [56]. Notably, the ratio of pyridinic-N was similar in all studied catalysts, but the doping level varied. The highest ORR activity was observed for *AT-Comp 50/50*, which also retained the highest nitrogen concentration among the acid-treated materials while also containing the most Co and Co-N species on the surface of the catalyst. Additionally, TEM micrographs revealed the formation of Co-catalyzed bamboo-like carbon nanotubes and onion-like carbon species during the synthesis of *Comp 50/50* and *AT-Comp 50/50*. These types of structures enhance the overall morphology of the composites by functioning as spacers between rGO sheets, thus promoting efficient electron transfer and improved catalytic activity [23,57]. In contrast, for *Comp 25/75* and *AT-Comp 25/75*, the absence of a protective carbon layer around the catalytic centres was attributed to the lower metal content and lack of Co-catalysed carbon structures. As a result, some of the catalytic centres were leached out during acid treatment, leading to a reduction in ORR activity. In the case of *Comp 75/25*, some bamboo-CNTs and onion-like carbon shells were observed, which provided partial protection for the active centres during acid treatment. While some non-active metallic species were leached out, the retained structural stability contributed to an increase in catalytic activity after acid treatment observed for *AT-Comp 75/25*.

The OER performance was also studied, with the $E_{\text{OER}}(V)$ @ 10 mA cm⁻² serving as the primary metric. For OER, the primary active centres in metal and N-doped carbon nanomaterials are M-N species and oxidized metal species [58]. The non-acid-treated composite catalysts exhibited superior OER activity compared to their acid-treated counterparts (Figure 6b), which can be attributed to the higher concentration of M-N sites and presence of oxidized Co and Mn species. These active species play a crucial role in enhancing OER performance, as they facilitate oxygen evolution due to the presence of efficient catalytic sites. *Comp 50/50* achieved $E_{\text{OER}} = 1.621$ V vs. RHE, slightly better than *Comp 75/25* ($E_{\text{OER}} = 1.624$ V vs. RHE) and *Comp 25/75* ($E_{\text{OER}} = 1.631$ V vs. RHE). Among the acid-treated catalysts, *AT-Comp 75/25* had the lowest $E_{\text{OER}} = 1.632$ V vs. RHE. *AT-Comp 50/50* and *AT-Comp 25/75* also performed well, with $E_{\text{OER}} = 1.639$ V vs. RHE and $E_{\text{OER}} = 1.634$ V vs. RHE, respectively. The superior OER activity of *Comp 50/50* can be attributed to the presence of Co and Mn species, which were partially removed during acid treatment, as confirmed by SEM-EDS and XPS data (Tables S1 and S2). Nevertheless, both *N-RM* and *N-rGO* exhibited significantly higher E_{OER} values, highlighting the

enhanced activity of the composite catalysts over the single component materials due to the better incorporation of Co and formation of N-active species within the catalyst materials. The ΔE values (Table 3) for all the composite catalysts were determined using the following equation:

$$\Delta E = E_{OER} (@10 \text{ mA cm}^{-2}) - E_{ORR} (@E_{1/2})$$

Table 3. Summary of electrochemical properties of the studied catalyst materials.

Catalyst	ORR			OER	
	E_{onset} (V vs. RHE)	$E_{1/2}$ (V vs. RHE)	j (mA cm ^{−2})	E (V) @ 10 mA cm ^{−2}	ΔE
N-RM	0.852	0.727	4.25	1.674	0.885
N-rGO	0.897	0.780	3.52	-	-
Comp 25/75	0.887	0.777	4.67	1.631	0.853
Comp 50/50	0.895	0.792	4.45	1.621	0.828
Comp 75/25	0.875	0.777	4.05	1.624	0.846
AT-Comp 25/75	0.895	0.790	4.06	1.634	0.842
AT-Comp 50/50	0.912	0.820	4.63	1.639	0.818
AT-Comp 75/25	0.887	0.797	4.22	1.632	0.834

All the composite materials had smaller ΔE values than for the single component materials. Among the composite catalysts, *AT-Comp 50/50* catalyst achieved the smallest ΔE value of 0.818 V, highlighting its exceptional bifunctional performance. This performance is comparable to that of the most efficient Co–N–C catalysts reported in the literature, which are typically produced from high-purity precursors through multi-step synthesis procedures [19]. In contrast, our approach employs upcycled waste materials that would otherwise be discarded, significantly enhancing the sustainability and cost-effectiveness of the synthesis method while maintaining competitive catalytic performance.

3.3. Performance of Composite Catalysts as Air Electrodes in Zinc–Air Batteries

To demonstrate the practical application of the synthesised catalyst materials, several different zinc–air batteries were assembled using the as-synthesised catalyst materials and commercial 20% PtRu/C as zinc–air battery air electrode catalyst materials. In Figure 7a the open circuit potential (OCP) measurements are displayed. The OCP values of acid treated samples, *AT-Comp 50/50* and *AT-Comp 25/75*, exhibited not only slightly higher OCPs compared to their untreated counterparts, but also 40 to 50 mV higher values than measured for the commercial 20% PtRu/C catalyst material. The higher OCP values suggest improved catalytic activity, which probably results from enhanced surface area and better active-site exposure that facilitate oxygen adsorption and reduction. Figure 7b displays the charge and discharge polarization curves under different current densities, demonstrating both ORR and OER activity. The discharge polarization curves show that all the composite catalysts exhibit higher discharge potential than commercial 20% PtRu/C, suggesting better ORR activity in these conditions. The charge polarization curves highlight the lower potential recorded for the acid treated catalysts, although these values were similar to those of the commercial catalyst. Figure 7c illustrates the power density curves, where *AT-Comp 50/50*, *AT-Comp 25/75*, and *Comp 25/75* exhibited peak power densities of 100 mW cm^{−2}, outperforming the 20% PtRu/C based catalyst by 36%.

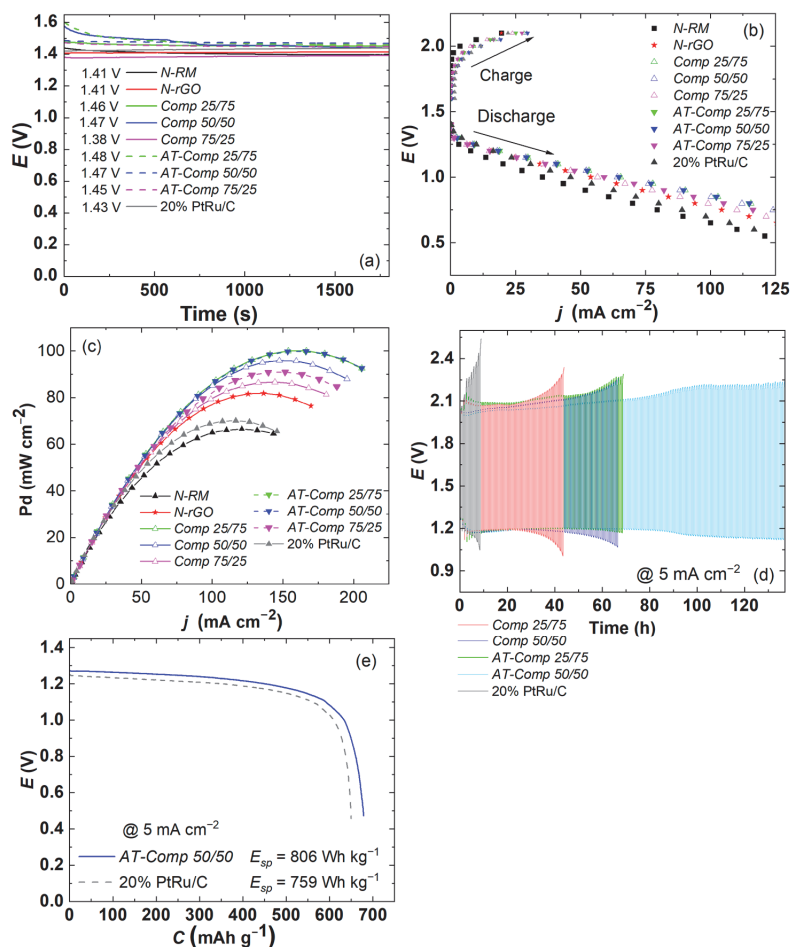


Figure 7. ZAB results for studied catalysts: (a) Open-circuit potential; (b) Charge and discharge polarization curves; (c) Power density curves; (d) Galvanostatic charge/discharge cycling with 30 min discharge and charge time; (e) Complete discharge test.

The stabilities of the best-performing catalysts were also explored using a charge-discharge cycling test (Figure 7d) with $j = 5 \text{ mA cm}^{-2}$. AT-Comp 50/50 catalyst demonstrated the longest stability of 137 h, which was of a noticeably extended duration when compared to the other catalysts. Moreover, 20% PtRu/C was outperformed by all the battery graphite derived catalysts tested during stability analysis, showing that the composite catalysts are significantly more stable in the harsh ZAB environment than the commercial catalyst. To evaluate the total energy storage capability, complete discharge tests were conducted, and the specific capacity (C) and specific energy density (E_{sp}) were calculated, as shown in Figure 7e. The AT-Comp 50/50 catalyst achieved a higher specific energy density ($E_{sp} = 806 \text{ Wh kg}^{-1}$) than the benchmark value for the commercial 20% PtRu/C catalyst ($E_{sp} = 759 \text{ Wh kg}^{-1}$). Composite optimizations enable more efficient utilization of active materials, thereby enhancing the energy density.

The high specific energy density, coupled with consistent discharge behaviour, establishes AT-Comp 50/50 as a highly promising material for ZAB applications where high energy density and stable long-term operation are desired. A comparison of all the synthesized catalysts demonstrates that AT-Comp 50/50 is the most promising due to its balanced

ORR and OER performance, high power density, excellent stability, and superior E_{sp} . The combination of RM with its metals, rGO with higher porosity and surface area with nitrogen species included in the carbon framework not only enhances the electrochemical properties, but also provides robustness under prolonged cycling conditions, outperforming both untreated catalysts and the commercial 20% PtRu/C reference material.

4. Conclusions

This study highlights the successful valorization of black mass leach residue—a by-product of lithium-ion battery recycling—as a promising precursor for electrocatalyst synthesis. By strategically combining graphite and cobalt recovered from the leach residue with rGO derived from waste graphite, an efficient bifunctional oxygen electrocatalyst was developed and implemented as an air electrode in zinc–air batteries. The composite catalysts were synthesized using ball milling for better mixing and reducing the particle size, followed by nitrogen doping via pyrolysis, with subsequent acid treatment to remove excess metals. Among the six synthesized composite materials, *AT-Comp 50/50* demonstrated the highest bifunctional activity and stability. The catalyst demonstrated outstanding performance as a zinc–air battery air electrode, reaching a power density of 100 mW cm^{-2} and maintaining excellent stability over 137 h of continuous charge–discharge cycling at a current density of 5 mA cm^{-2} . The enhanced catalytic performance of *AT-Comp 50/50* is primarily attributed to its increased specific surface area and optimized porosity, facilitating the effective incorporation and stabilization of active pyridinic-N and Co-N_x centers. Additionally, the formation of Co-catalyzed bamboo-like CNTs and onion-like spherical carbon species provided structural stability by encapsulating Co nanoparticles within the carbon shells, further promoting efficient electron transfer and enhancing catalyst stability. Notably, all tested composite catalysts outperformed the selected benchmark 20% PtRu/C catalyst. These findings underscore the viability of black mass leach residue as a sustainable feedstock for electrocatalyst development and demonstrate the effective use of waste graphite as a precursor for rGO synthesis. The study supports circular economy principles by promoting the smart reutilization of waste materials and contributes to the advancement of next-generation energy conversion technologies.

Supplementary Materials: The following supporting information can be downloaded at <https://www.mdpi.com/article/10.3390/batteries11040165/s1>, Figure S1: (a) XRD diffractogram of Raw Material and N-RM with standard cards; (b) XRD diffractograms of recovered graphite, GO, rGO and N-rGO with standard cards. Figure S2: SEM-SE micrographs of (a) *Comp 25/75*, (b) *Comp 50/50*, (c) *Comp 75/25*, (d) *AT-Comp 25/75*, (e) *AT-Comp 50/50*, and (f) *AT-Comp 75/25* catalyst materials. Figure S3: Quantified SEM-EDS elemental maps of sample *AT-Comp 50/50* and the map sum spectrum. Figure S4: TEM-EDS (a) micrograph with (b) EDS spectra of different locations. Figure S5: (a) N₂ adsorption–desorption Isotherms and (b) pore size distribution data of studied materials. Figure S6: X-ray photoelectron spectra of the samples: (a) O 1 s region and (b) survey spectra. Figure S7: (a,c,e) ORR polarization curves of studied catalyst materials for *Comp 25/75*, *Comp 50/50*, and *Comp 75/25*, respectively. (b,d,f,h) Koutecky–Levich plots derived from ORR data from the RDE data (a,c,e) for *Comp 25/75*, *Comp 50/50*, and *Comp 75/25*, respectively. The insets of (b,d,f) show the dependence of n vs. potential. Figure S8: (a,c,e) ORR polarization curves of studied catalyst materials for *AT-Comp 25/75*, *AT-Comp 50/50*, and *AT-Comp 75/25*, respectively. (b,d,f) and (h) Koutecky–Levich plots derived from ORR data from the RDE data (a,c,e) for *Comp 25/75*, *Comp 50/50*, and *Comp 75/25*, respectively. The insets of (b,d) and (f) show the dependence of n vs. potential. Table S1: Elemental compositions of the studied materials based on quantitative SEM-EDS mapping. Table S2: The atomic percentages (at-%) of the elements for all samples measured with XPS, including peak fitting results. The error associated with each value is roughly $\pm 10\%$ of the value.

Author Contributions: R.P.: conceptualization, investigation, and writing—original and reviewed draft. J.S.: investigation (XPS) and writing—original and reviewed draft. M.V.: investigation (Raman) and writing—original and reviewed draft. L.K.: investigation (SEM-EDS) and writing—original and reviewed draft. B.P.W.: resources and writing—original and reviewed draft. M.L.: resources and writing—original and reviewed draft. I.K.: resources and supervision. K.L.: conceptualization, funding acquisition, investigation, project administration, and writing—original and reviewed draft. All authors have read and agreed to the published version of the manuscript.

Funding: This research was supported by the Estonian Research Council (PSG926, EAG248), and the Business Finland BATCircle3.0 project (Grant Number 1754/31/2024). In addition, this work was funded by the Ministry of Education and Research through the Centre of Excellence in Circular Economy for Strategic Mineral and Carbon Resources (01.01.2024–31.12.2030, TK228). The Research Council of Finland funded JUST Materials Research Infrastructure (RI) based at Aalto University and the OtaNano—Nanomicroscopy Center (Aalto-NMC) were utilized as part of this research.

Data Availability Statement: The raw data supporting the conclusions of this article will be made available by the authors on request.

Acknowledgments: Hua Jiang is acknowledged for their assistance with the HR-TEM measurements. ChatGPT-4o by OpenAI was used to edit text and improve the writing of this paper. The authors have reviewed and edited the output and take full responsibility for the content of this publication.

Conflicts of Interest: The authors declare no conflict of interest.

References

- IEA. *Global EV Outlook 2024*; IEA: Paris, France, 2024.
- Goodenough, J.B.; Park, K.S. The Li-ion rechargeable battery: A perspective. *J. Am. Chem. Soc.* **2013**, *135*, 1167–1176. [[CrossRef](#)] [[PubMed](#)]
- Padhi, A.K.; Nanjundaswamy, K.S.; Goodenough, J.B. Phospho-olivines as Positive-Electrode Materials for Rechargeable Lithium Batteries. *J. Electrochem. Soc.* **1997**, *144*, 1188–1194. [[CrossRef](#)]
- Yu, Y.X. Can all nitrogen-doped defects improve the performance of graphene anode materials for lithium-ion batteries? *Phys. Chem. Chem. Phys.* **2013**, *15*, 16819–16827. [[CrossRef](#)] [[PubMed](#)]
- Directorate-General for Internal Market, Industry, Entrepreneurship and SMEs (European Commission); Grohol, M.; Veeh, C. European Commission: Directorate-General for Internal Market Entrepreneurship and SMEs, I. In *Study on the Critical Raw Materials for the EU 2023—Final Report*; Grohol, M., Veeh, C., Eds.; Publications Office of the European Union: Luxembourg, 2023.
- IEA. *Global Critical Minerals Outlook 2024*; IEA: Paris, France, 2024.
- IEA. *World Energy Outlook*; IEA: Paris, France, 2024.
- IEA. *Recycling of Critical Minerals*; IEA: Paris, France, 2024.
- Natarajan, S.; Divya, M.L.; Aravindan, V. Should we recycle the graphite from spent lithium-ion batteries? The untold story of graphite with the importance of recycling. *J. Energy Chem.* **2022**, *71*, 351–369. [[CrossRef](#)]
- He, S.; Wu, M.; Li, S.; Jiang, Z.; Hong, H.; Cloutier, S.G.; Yang, H.; Omanovic, S.; Sun, S.; Zhang, G. Research Progress on Graphite-Derived Materials for Electrocatalysis in Energy Conversion and Storage. *Molecules* **2022**, *27*, 8644. [[CrossRef](#)] [[PubMed](#)]
- Morales-Torres, S.; Jiříčková, A.; Jankovský, O.; Sofer, Z.; Sedmidubský, D. Synthesis and Applications of Graphene Oxide. *Materials* **2022**, *15*, 920. [[CrossRef](#)]
- Larminie, J.; Dicks, A.; McDonald, M. *Fuel Cell Systems Explained*; John Wiley & Sons Ltd.: Chichester, UK, 2003.
- Yang, D.; Zhang, L.; Yan, X.; Yao, X. Recent Progress in Oxygen Electrocatalysts for Zinc–Air Batteries. *Small Methods* **2017**, *1*, 1700209. [[CrossRef](#)]
- Sun, J.; Wang, N.; Qiu, Z.; Xing, L.; Du, L. Recent Progress of Non-Noble Metal Catalysts for Oxygen Electrode in Zn–Air Batteries: A Mini Review. *Catalysts* **2022**, *12*, 843. [[CrossRef](#)]
- Liu, T.; Cai, S.; Gao, Z.; Liu, S.; Li, H.; Chen, L.; Li, M.; Guo, H. Facile synthesis of the porous FeCo@nitrogen-doped carbon nanosheets as bifunctional oxygen electrocatalysts. *Electrochim. Acta* **2020**, *335*, 135647. [[CrossRef](#)]
- Meng, Z.; Chen, N.; Cai, S.; Wang, R.; Guo, W.; Tang, H. Co–N-doped hierarchically ordered macro/mesoporous carbon as bifunctional electrocatalyst toward oxygen reduction/evolution reactions. *Int. J. Energy Res.* **2021**, *45*, 6250–6261. [[CrossRef](#)]
- Yang, L.; Wang, D.; Lv, Y.; Cao, D. Nitrogen-doped graphitic carbons with encapsulated CoNi bimetallic nanoparticles as bifunctional electrocatalysts for rechargeable Zn–Air batteries. *Carbon* **2019**, *144*, 8–14. [[CrossRef](#)]

18. Ganesan, P.; Ishihara, A.; Staykov, A.; Nakashima, N. Recent Advances in Nanocarbon-Based Nonprecious Metal Catalysts for Oxygen/Hydrogen Reduction/Evolution Reactions and Zn-Air Battery. *Bull. Chem. Soc. Jpn.* **2023**, *96*, 429–443. [\[CrossRef\]](#)
19. Xu, H.M.; Zhu, H.R.; Huang, C.J.; Zhang, Z.J.; Shuai, T.Y.; Zhan, Q.N.; Li, G.R. Recent advances in Fe-N-C- and Co-N-C-based materials as bifunctional electrocatalysts for oxygen reduction and oxygen evolution. *Sci. China Chem.* **2023**, *67*, 1137–1160. [\[CrossRef\]](#)
20. Zou, X.; Tang, M.; Lu, Q.; Wang, Y.; Shao, Z.; An, L. Carbon-based electrocatalysts for rechargeable Zn-air batteries: Design concepts, recent progress and future perspectives. *Energy Environ. Sci.* **2024**, *17*, 386–424. [\[CrossRef\]](#)
21. Qin, J.; Liu, Z.; Wu, D.; Yang, J. Optimizing the electronic structure of cobalt via synergized oxygen vacancy and Co-N-C to boost reversible oxygen electrocatalysis for rechargeable Zn-air batteries. *Appl. Catal. B* **2020**, *278*, 119300. [\[CrossRef\]](#)
22. Li, C.; Zhou, E.; Yu, Z.; Liu, H.; Xiong, M. Tailor-made open porous 2D CoFe/SN-carbon with slightly weakened adsorption strength of ORR/OER intermediates as remarkable electrocatalysts toward zinc-air batteries. *Appl. Catal. B* **2020**, *269*, 118771. [\[CrossRef\]](#)
23. Liivand, K.; Sainio, J.; Wilson, B.P.; Kruusenberg, I.; Lundström, M. Overlooked residue of Li-ion battery recycling waste as high-value bifunctional oxygen electrocatalyst for Zn-air batteries. *Appl. Catal. B Environ.* **2023**, *332*, 122767. [\[CrossRef\]](#)
24. Liivand, K.; Kazemi, M.; Walke, P.; Mikli, V.; Uibu, M.; Macdonald, D.D.; Kruusenberg, I. Spent Li-Ion Battery Graphite Turned Into Valuable and Active Catalyst for Electrochemical Oxygen Reduction. *ChemSusChem* **2021**, *14*, 1103–1111. [\[CrossRef\]](#)
25. Ruan, D.; Zou, K.; Du, K.; Wang, F.; Wu, L.; Zhang, Z.; Wu, X.; Hu, G. Recycling of Graphite Anode from Spent Lithium-ion Batteries for Preparing Fe-N-doped Carbon ORR Catalyst. *ChemCatChem* **2021**, *13*, 2025–2033. [\[CrossRef\]](#)
26. Bian, H.; Wu, W.; Zhu, Y.; Tsang, C.H.; Cao, Y.; Xu, J.; Liao, X.; Lu, Z.; Lu, X.Y.; Liu, C.; et al. Waste to Treasure: Regeneration of Porous Co-Based Catalysts from Spent LiCoO₂ Cathode Materials for an Efficient Oxygen Evolution Reaction. *ACS Sustain. Chem. Eng.* **2023**, *11*, 670–678. [\[CrossRef\]](#)
27. Wang, Y.; Sheng, K.; Xu, R.; Chen, Z.; Shi, K.; Li, W.; Li, J. Efficient bifunctional 3D porous Co-N-C catalyst from spent Li-ion batteries and biomass for Zinc-Air batteries. *Chem. Eng. Sci.* **2023**, *268*, 118433. [\[CrossRef\]](#)
28. Kotkar, A.; Dash, S.; Bhanja, P.; Sahu, S.; Verma, A.; Mukherjee, A.; Mohapatra, M.; Basu, S. Microwave assisted recycling of spent Li-ion battery electrode material into efficient oxygen evolution reaction catalyst. *Electrochim. Acta* **2023**, *442*, 141842. [\[CrossRef\]](#)
29. Balqis, F.; Irmawati, Y.; Geng, D.; Nugroho, F.A.A.; Sumboja, A. Nanostructured Ball-Milled Ni-Co-Mn Oxides from Spent Li-Ion Batteries as Electrocatalysts for Oxygen Evolution Reaction. *ACS Appl. Nano Mater.* **2024**, *7*, 18138–18145. [\[CrossRef\]](#)
30. Chernyaev, A.; Partinen, J.; Klemettinen, L.; Wilson, B.P.; Jokilaakso, A.; Lundström, M. The efficiency of scrap Cu and Al current collector materials as reductants in LIB waste leaching. *Hydrometallurgy* **2021**, *203*, 105608. [\[CrossRef\]](#)
31. Praats, R.; Sainio, J.; Vikberg, M.; Klemettinen, L.; Wilson, B.P.; Lundström, M.; Kruusenberg, I.; Liivand, K. Utilizing waste lithium-ion batteries for the production of graphite-carbon nanotube composites as oxygen electrocatalysts in zinc-air batteries. *RSC Sustain.* **2025**, *3*, 546–556. [\[CrossRef\]](#)
32. Praats, R.; Chernyaev, A.; Sainio, J.; Lundström, M.; Kruusenberg, I.; Liivand, K. Supporting critical raw material circularity—Upcycling graphite from waste LIBs to Zn-air batteries. *Green Chem.* **2024**, *26*, 2874–2883. [\[CrossRef\]](#)
33. Regulation (EU) 2023/1542 of the European Parliament and of the Council of 12 July 2023 Concerning Batteries and Waste Batteries, Amending Directive 2008/98/EC and Regulation (EU) 2019/1020 and Repealing Directive 2006/66/EC (Text. with EEA Relevance); European Union: Brussels, Belgium, 2023.
34. Kazemi, M.; Liivand, K.; Prato, M.; Vacek, P.; Walmsley, J.; Dante, S.; Divitini, G.; Kruusenberg, I. Graphite and Cobalt Recycled from Li-Ion Batteries: A Valuable Raw Material for Oxygen Reduction Reaction Electrocatalysts. *Energy Fuels* **2023**, *38*, 659–670. [\[CrossRef\]](#)
35. Balachandran, S.; Forsberg, K.; Lemaître, T.; Vieceli, N.; Lombardo, G.; Petranikova, M. Comparative Study for Selective Lithium Recovery via Chemical Transformations during Incineration and Dynamic Pyrolysis of EV Li-Ion Batteries. *Metals* **2021**, *11*, 1240. [\[CrossRef\]](#)
36. Wang, W.; Zhang, Y.; Liu, X.; Xu, S. A simplified process for recovery of Li and Co from spent LiCoO₂ cathode using Al foil as the in situ reductant. *ACS Sustain. Chem. Eng.* **2019**, *7*, 12222–12230. [\[CrossRef\]](#)
37. Zhai, L.F.; Kong, S.Y.; Zhang, H.; Tian, W.; Sun, M.; Sun, H.; Wang, S. Facile synthesis of Co-N-rGO composites as an excellent electrocatalyst for oxygen reduction reaction. *Chem. Eng. Sci.* **2019**, *194*, 45–53. [\[CrossRef\]](#)
38. Kang, J.; Kim, Y.; Kim, H.M.; Hu, X.; Saito, N.; Choi, J.H.; Lee, M.H. In-situ one-step synthesis of carbon-encapsulated naked magnetic metal nanoparticles conducted without additional reductants and agents. *Sci. Rep.* **2016**, *6*, 38652. [\[CrossRef\]](#) [\[PubMed\]](#)
39. Zhang, X.; Zhang, K.; Zhang, W.; Zhang, X.; Wang, L.; An, Y.; Sun, X.; Li, C.; Wang, K.; Ma, Y. Carbon Nano-Onion-Encapsulated Ni Nanoparticles for High-Performance Lithium-Ion Capacitors. *Batteries* **2023**, *9*, 102. [\[CrossRef\]](#)
40. Ferrari, A.C.; Robertson, J. Interpretation of Raman spectra of disordered and amorphous carbon. *Phys. Rev. B* **1999**, *61*, 14095–14107. [\[CrossRef\]](#)
41. Perumbilavil, S.; Sankar, P.; Priya Rose, T.; Philip, R. White light Z-scan measurements of ultrafast optical nonlinearity in reduced graphene oxide nanosheets in the 400–700 nm region. *Appl. Phys. Lett.* **2015**, *107*, 051104. [\[CrossRef\]](#)

42. Gao, W.; Alemany, L.B.; Ci, L.; Ajayan, P.M. New insights into the structure and reduction of graphite oxide. *Nat. Chem.* **2009**, *1*, 403–408. [\[CrossRef\]](#)
43. Sing, K.S.W.; Everett, D.H.; Haul, R.A.W.; Moscou, L.; Pierotti, R.A.; Rouquerol, J.; Siemieniewska, T. Reporting Physisorption Data for Gas/Solid Systems with Special Reference to the Determination of Surface Area and Porosity. *Pure Appl. Chem.* **1985**, *57*, 603–619. [\[CrossRef\]](#)
44. Rouquerol, J.; Rouquerol, F.; Llewellyn, P.; Maurin, G.; Sing, K.S.W. *Adsorption by Powders and Porous Solids: Principles, Methodology and Applications*, 2nd ed.; Elsevier: Amsterdam, The Netherlands, 2013.
45. Wu, B.; Mi, J.L.; Hu, H.; Zu, Z.Y.; Liu, L. Fe-, S-, and N-Doped Carbon Nanotube Networks as Electrocatalysts for the Oxygen Reduction Reaction. *ACS Appl. Nano Mater.* **2020**, *3*, 12297–12307. [\[CrossRef\]](#)
46. Lu, A.H.; Li, W.C.; Salabas, E.L.; Spliethoff, B.; Schüth, F. Low temperature catalytic pyrolysis for the synthesis of high surface area, nanostructured graphitic carbon. *Chem. Mater.* **2006**, *18*, 2086–2094. [\[CrossRef\]](#)
47. Okpalugo, T.I.T.; Papakonstantinou, P.; Murphy, H.; McLaughlin, J.; Brown, N.M.D. High resolution XPS characterization of chemical functionalised MWCNTs and SWCNTs. *Carbon* **2005**, *43*, 153–161. [\[CrossRef\]](#)
48. *NIST X-Ray Photoelectron Spectroscopy (XPS) Database Number 20*; National Institute of Standards and Technology: Gaithersburg, MD, USA, 2000.
49. Kousar, A.; Pande, I.; Pascual, L.F.; Peltola, E.; Sainio, J.; Laurila, T. Modulating the Geometry of the Carbon Nanofiber Electrodes Provides Control over Dopamine Sensor Performance. *Anal. Chem.* **2023**, *95*, 2983–2991. [\[CrossRef\]](#)
50. Susi, T.; Pichler, T.; Ayala, P. X-ray photoelectron spectroscopy of graphitic carbon nanomaterials doped with heteroatoms. *Beilstein J. Nanotechnol.* **2015**, *6*, 177–192. [\[CrossRef\]](#) [\[PubMed\]](#)
51. Chen, S.; Bi, J.; Zhao, Y.; Yang, L.; Zhang, C.; Ma, Y.; Wu, Q.; Wang, X.; Hu, Z. Nitrogen-doped carbon nanocages as efficient metal-free electrocatalysts for oxygen reduction reaction. *Adv. Mater.* **2012**, *24*, 5593–5597. [\[CrossRef\]](#) [\[PubMed\]](#)
52. Cao, T.; Wang, D.; Zhang, J.; Cao, C.; Li, Y. Bamboo-Like Nitrogen-Doped Carbon Nanotubes with Co Nanoparticles Encapsulated at the Tips: Uniform and Large-Scale Synthesis and High-Performance Electrocatalysts for Oxygen Reduction. *Chem.—Eur. J.* **2015**, *21*, 14022–14029. [\[CrossRef\]](#) [\[PubMed\]](#)
53. Biesinger, M.C.; Payne, B.P.; Grosvenor, A.P.; Lau, L.W.M.; Gerson, A.R.; Smart, R.S.C. Resolving surface chemical states in XPS analysis of first row transition metals, oxides and hydroxides: Cr, Mn, Fe, Co and Ni. *Appl. Surf. Sci.* **2011**, *257*, 2717–2730. [\[CrossRef\]](#)
54. Wang, Y.; Nie, Y.; Ding, W.; Chen, S.G.; Xiong, K.; Qi, X.Q.; Zhang, Y.; Wang, J.; Wei, Z.D. Unification of catalytic oxygen reduction and hydrogen evolution reactions: Highly dispersive Co nanoparticles encapsulated inside Co and nitrogen co-doped carbon. *Chem. Commun.* **2015**, *51*, 8942–8945. [\[CrossRef\]](#)
55. Yao, Y.; Chen, H.; Lian, C.; Wei, F.; Zhang, D.; Wu, G.; Chen, B.; Wang, S. Fe, Co, Ni nanocrystals encapsulated in nitrogen-doped carbon nanotubes as Fenton-like catalysts for organic pollutant removal. *J. Hazard. Mater.* **2016**, *314*, 129–139. [\[CrossRef\]](#)
56. Xue, H.; Meng, A.; Lian, T.; Yang, T.; Gao, J.; Singh, C.V.; Geng, Z.; Chen, L.; Li, Z. Co-Pyridinic-N Bond Constructed at the Interface of CoxP and N-Doped Carbon to Effectively Facilitate Oxygen Reduction. *ACS Sustain. Chem. Eng.* **2023**, *11*, 5238–5249. [\[CrossRef\]](#)
57. Kim, J.H.; Park, S.K.; Oh, Y.J.; Kang, Y.C. Hierarchical hollow microspheres grafted with Co nanoparticle-embedded bamboo-like N-doped carbon nanotube bundles as ultrahigh rate and long-life cathodes for rechargeable lithium-oxygen batteries. *Chem. Eng. J.* **2018**, *334*, 2500–2510. [\[CrossRef\]](#)
58. Zhang, J.; Zhang, T.; Ma, J.; Wang, Z.; Liu, J.; Gong, X. ORR and OER of Co–N codoped carbon-based electrocatalysts enhanced by boundary layer oxygen molecules transfer. *Carbon* **2021**, *172*, 556–568. [\[CrossRef\]](#)

Disclaimer/Publisher’s Note: The statements, opinions and data contained in all publications are solely those of the individual author(s) and contributor(s) and not of MDPI and/or the editor(s). MDPI and/or the editor(s) disclaim responsibility for any injury to people or property resulting from any ideas, methods, instructions or products referred to in the content.

Curriculum vitae

Personal data

Name: Reio Praats
Date of birth: 04.11.1993
Place of birth: Estonia
Citizenship: Estonian

Contact data

E-mail: reio.praats@kbfi.ee

Education

2021–2025 Tallinn University of Technology, PhD
2017–2019 University of Tartu, MSc
2013–2016 University of Tartu, BSc
2010–2013 Hugo Treffner's Gymnasium

Language competence

English Fluent
Estonian Fluent
Russian Basic

Professional employment

2020– ... National Institute of Chemical Physics and Biophysics, Estonia,
Early-stage researcher
Aug 2020 – Nov 2020 Danish Power Systems®, Denmark, Research intern
2019–2020 Miina Härma Gümnaasium, Estonia, high-school chemistry
teacher
2014–2019 University of Tartu, Estonia, student researcher/chemist

Scientific publications

1. Praats, R.; Sainio, J.; Vikberg, M.; Klemettinen, L.; Wilson, B. P.; Lundström, M.; Kruusenberg, I.; Liivand, K. A Pathway to Circular Economy-Converting Li-Ion Battery Recycling Waste into Graphite/rGO Composite Electrocatalysts for Zinc–Air Batteries, *Batteries* 11 (2025) 165.
2. R. Praats, J. Sainio, M. Vikberg, L. Klemettinen, B.P. Wilson, M. Lundström, I. Kruusenberg, K. Liivand, Utilizing waste lithium-ion batteries for the production of graphite-carbon nanotube composites as oxygen electrocatalysts in zinc–air batteries, *RSC Sustainability* 3 (2025) 546–556.
3. R. Praats, A. Chernyaev, J. Sainio, M. Lundström, I. Kruusenberg, K. Liivand, Supporting critical raw material circularity – upcycling graphite from waste LIBs to Zn–air batteries, *Green Chemistry* 26 (2024) 2874–2883.
4. K. Kaare, A. Volperts, A. Plavniece, P. Walke, T. Käämbre, N. Noor, A. Foroozan, D.C. Higgins, R. Praats, K. Liivand, L. Tamasauskaitė-Tamasiunaite, L. Colmenares-Rausseo, J. Lilloja, K. Tammeveski, I. Kruusenberg, Heteroatom-Doped Carbon Nanomaterials Derived from Black Liquor for Electrochemical Oxygen Reduction Reaction, *ACS Sustainable Resource Management* 1 (2024) 1705–1716.

5. R. Praats, M. Käärrik, A. Kikas, V. Kisand, J. Aruväli, P. Paiste, M. Merisalu, A. Sarapuu, J. Leis, V. Sammelselg, J.C. Douglin, D.R. Dekel, K. Tammeveski, Electroreduction of oxygen on cobalt phthalocyanine-modified carbide-derived carbon/carbon nanotube composite catalysts, *J. Solid State Electrochem.* 25 (2021) 57–71.
6. R. Praats, M. Käärrik, A. Kikas, V. Kisand, J. Aruväli, P. Paiste, M. Merisalu, J. Leis, V. Sammelselg, J.H. Zagal, S. Holdcroft, N. Nakashima, K. Tammeveski, Electrocatalytic oxygen reduction reaction on iron phthalocyanine-modified carbide-derived carbon/carbon nanotube composite electrocatalysts, *Electrochim. Acta* 334 (2020) 135575.
7. R. Praats, I. Kruusenberg, M. Käärrik, U. Joost, J. Aruväli, P. Paiste, R. Saar, P. Rauwel, M. Kook, J. Leis, J.H. Zagal, K. Tammeveski, Electroreduction of oxygen in alkaline solution on iron phthalocyanine modified carbide-derived carbons, *Electrochim. Acta* 299 (2019) 999–1010.

Conference presentations

1. R. Praats, A. Chernyaev, J. Sainio, M. Lundström, I. Kruusenberg, K. Liivand, Supporting Critical Raw Material Circularity – Graphite from waste LIBs to Zn-air batteries, in 74th Annual meeting of ISE, September 2023.
2. R. Praats, A. Chernyaev, J. Sainio, M. Lundström, I. Kruusenberg, K. Liivand, Supporting Critical Raw Material Circularity – Graphite from waste LIBs to Zn-air batteries, in 8th Baltic Electrochemistry Conference: Finding New Inspiration 2, April 2024.

Elulookirjeldus

Isikuandmed

Nimi:	Reio Praats
Sünniaeg:	04.11.1993
Sünnikoht:	Eesti
Kodakondsus:	Eesti

Kontaktandmed

E-post:	reio.praats@kbfi.ee
---------	---------------------

Hariduskäik

2021–2025	Tallinn Tehnikaülikool, PhD
2017–2019	Tartu Ülikool, MSc
2013–2016	Tartu Ülikool, BSc
2010–2013	Hugo Treffneri gümnaasium

Keelteoskus

Inglise keel	Kõrgtase
Eesti keel	Kõrgtase
Vene keel	Algtase

Teenistuskäik

2020– ...	Keemilise ja Bioloogilise Füüsika instituut, Eesti, nooremteadur
Aug 2020 – Nov 2020	Danish Power Systems®, Taani, teaduspraktikant
2019–2020	Miina Härma Gümnaasium, Estonia, keemia õpetaja
2014–2019	Tartu Ülikool, Eesti, tudeng/keemik

Teadusartiklid

1. Praats, R.; Sainio, J.; Vikberg, M.; Klemettinen, L.; Wilson, B. P.; Lundström, M.; Kruusenberg, I.; Liivand, K. A Pathway to Circular Economy-Converting Li-Ion Battery Recycling Waste into Graphite/rGO Composite Electrocatalysts for Zinc–Air Batteries, *Batteries* 11 (2025) 165.
2. R. Praats, J. Sainio, M. Vikberg, L. Klemettinen, B.P. Wilson, M. Lundström, I. Kruusenberg, K. Liivand, Utilizing waste lithium-ion batteries for the production of graphite-carbon nanotube composites as oxygen electrocatalysts in zinc–air batteries, *RSC Sustainability* 3 (2025) 546–556.
3. R. Praats, A. Chernyaev, J. Sainio, M. Lundström, I. Kruusenberg, K. Liivand, Supporting critical raw material circularity – upcycling graphite from waste LIBs to Zn–air batteries, *Green Chemistry* 26 (2024) 2874–2883.
4. K. Kaare, A. Volperts, A. Plavniece, P. Walke, T. Käämbre, N. Noor, A. Foroozan, D.C. Higgins, R. Praats, K. Liivand, L. Tamasauskaitė-Tamasiunaite, L. Colmenares-Rausseo, J. Lilloja, K. Tammeveski, I. Kruusenberg, Heteroatom-Doped Carbon Nanomaterials Derived from Black Liquor for Electrochemical Oxygen Reduction Reaction, *ACS Sustainable Resource Management* 1 (2024) 1705–1716.

5. R. Praats, M. Käärrik, A. Kikas, V. Kisand, J. Aruväli, P. Paiste, M. Merisalu, A. Sarapuu, J. Leis, V. Sammelselg, J.C. Douglin, D.R. Dekel, K. Tammeveski, Electroreduction of oxygen on cobalt phthalocyanine-modified carbide-derived carbon/carbon nanotube composite catalysts, *J. Solid State Electrochem.* 25 (2021) 57–71.
6. R. Praats, M. Käärrik, A. Kikas, V. Kisand, J. Aruväli, P. Paiste, M. Merisalu, J. Leis, V. Sammelselg, J.H. Zagal, S. Holdcroft, N. Nakashima, K. Tammeveski, Electrocatalytic oxygen reduction reaction on iron phthalocyanine-modified carbide-derived carbon/carbon nanotube composite electrocatalysts, *Electrochim. Acta* 334 (2020) 135575.
7. R. Praats, I. Kruusenberg, M. Käärrik, U. Joost, J. Aruväli, P. Paiste, R. Saar, P. Rauwel, M. Kook, J. Leis, J.H. Zagal, K. Tammeveski, Electroreduction of oxygen in alkaline solution on iron phthalocyanine modified carbide-derived carbons, *Electrochim. Acta* 299 (2019) 999–1010.

Konverentside ettekanded

1. R. Praats, A. Chernyaev, J. Sainio, M. Lundström, I. Kruusenberg, K. Liivand, Supporting Critical Raw Material Circularity – Graphite from waste LIBs to Zn-air batteries, in 74th Annual meeting of ISE, September 2023.
2. R. Praats, A. Chernyaev, J. Sainio, M. Lundström, I. Kruusenberg, K. Liivand, Supporting Critical Raw Material Circularity – Graphite from waste LIBs to Zn-air batteries, in 8th Baltic Electrochemistry Conference: Finding New Inspiration 2, April 2024.

ISSN 2585-6901 (PDF)
ISBN 978-9916-80-370-7 (PDF)